UNIVERSITÀ DEGLI STUDI DI BERGAMO
DEPARTMENT OF ENGINEERING AND APPLIED SCIENCES
DOCTORAL PROGRAMME IN ENGINEERING AND APPLIED SCIENCES

CORROSION BEHAVIOUR OF METAL ALLOYS OBTAINED BY MEANS OF ADDITIVE MANUFACTURING

Doctoral dissertation of:
Testa Cristian

Tutor:
Prof. Pastore Tommaso
Supervisor:
Prof.ssa Cabrini Marina
The Chair of the Doctoral Program:
Prof. Re Valerio

XXXII Cycle

ABSTRACT

The additive manufacturing techniques to produce metallic parts are gaining lot of interest in different industrial fields due to several advantages mainly related to the possibility to produce near net shape parts with unique geometries, even impossible to be manufactured by using traditional subtractive technologies. It has been also demonstrated that this could also lead -in some cases- to both cost reduction and manufacturing time savings. The number of additive technologies for metals is increasing significantly and nowadays electron beam melting, selective laser melting and binder jetting as well as fusion deposition modelling are ready-on-the-market. Among them, techniques based on laser melting of powdered metal are surely considered the most promising, at least in the next few years. The industries that pushed such innovations are mainly automotive, aerospace, medical and energy production. The scientific community attention has also raised due to the opportunities coming from the use of this technologies. Several researches have been proposed mainly regarding the design strategies, topological optimisation, process parameters optimisation for tailoring mechanical properties and optimise surface finishing. In the field of material science and technology, the researchers are mainly focused on the process parameters optimisation to improve microstructure and density of the parts as well as the design of heat treatments to improve mechanical properties. One of the main topics related to the use of such innovative metallic materials is surely related to the material qualification strategies to grant products reliability and safety. Specially in very aggressive environments, the qualification procedures must also consider the corrosion behaviour of the material strictly depend upon the unique microstructure.

However, the scientific literature reports only few papers regarding the corrosion behaviour of metals produced by such a manufacturing technique, limited to few alloys of aluminium, titanium and stainless steel.

This thesis presents the research carried out on three different alloys with increasing corrosion resistance, such as aluminium, nickel, and titanium processed by Laser Powder Bed Fusion (LPBF). The industrial fields of application of these alloys are very wide, moving from automotive, aerospace, oil and gas, and biomedical, thanks to their lightness, biocompatibility and corrosion resistance, respectively.

The studies concerned the generalized corrosion, localized corrosion and the environmental assisted cracking comparing the results, were possible, with the tests carried out on the commercial traditional alloys. The effects of microstructure and post processing heat treatment on the corrosion resistance were investigated. The main goal of this research is the corrosion behaviour but with a focus on the need to the qualification process in order to insurance the performance of the build part.

The AlSi10Mg corrosion resistance decreases with increasing temperature of the heat treatment. The post processing heat treatments are not recommended in the case in which high corrosion resistance is required, if the post processing stress relieve treatment must be executed, coating or anodizing treatments should be developed in order to improve the corrosion resistance of the alloy. For the Alloy 625, electrochemical tests confirmed there were not differences between the 3D printed alloy in comparison with the hot worked alloy, instead, the resistance of intergranular corrosion was higher for the LPBF alloy. Titanium alloy showed a corrosion behaviour like the material produced via traditional way only after mechanical polishing or acid pickling.

This thesis is composed of the introductory part containing the description of the additive manufacturing technique, mainly highlighting the powder bed technology. The corrosion behaviour of the alloys is discussed in three different chapters and conclusive remarks are reported to summarise the most outstanding findings regarding the corrosion behaviour of 3D printed alloys.

CONTENT

TABLE OF SYMBOLS

AM	Additive Manufacturing
AB	As-built surface
AFM	Atomic force microscope
BJ	Binder jetting
CAD	Computer Aided design
DED	Direct Energy deposition
DSC	Differential scanning calorimetry
EBSD	Electron backscatter diffraction
Ecorr	Free corrosion potential
EDS	Energy dispersive x-ray spectrometry
EEE	Exo-electron emission
EIS	Electrochemical impedance spectroscopy
FESEM	Field emission scanning electron microscopy
GA	Gas atomization
HAZ	Heat affected zone
HT	Heat treatment sample
LPBF	Laser powder bed fusion
MP	Melt pool
P	Polished surface
PBF	Powder bed fusion
PD	Potentiodynamic
PREP	Plasma rotating electrode process
Ra	Arithmetical mean deviation of the assessed profile of roughness
Rz	Average distance between the highest peak and lowest valley in each sampling length
SBF	Simulated body solution
SCC	Stress corrosion cracking
SCE	Saturated calomel reference electrode

SEM	Scanning electron microscopy
SKPFM	Scanning kelvin probe force microscopy
UAM	Ultrasonic additive manufacturing
UT	Untreated sample
WA	Water atomization

TABLE OF FIGURES

TABLE OF TABLES

CHAPTER 1

INTRODUCTION AND AIM OF THESIS

Many scientific works deal with mechanical behaviour and microstructure characterization of 3D printed metal alloys. Many less works analyse the durability of these materials highlighting the concept of qualification. In fact, for the traditional process the qualification of feedstock materials is enough for guarantee the final properties of piece but for the additive manufacturing process this idea is completely wrong due to the strong microstructural metamorphosis during the process. The main point of the durability concept is focused on the design and realization of standard procedure with established parameters. The corrosion resistance of the alloys obtained by means of additive manufacturing techniques depends on different parameters, that can be divided in surface and microstructural effects (Table 1-1). About surface effect, the LPBF process produces high surface roughness, emerging porosities and the phenomenon of balling, as already presented in the previous paragraphs. In addition, the passive film protectiveness of the corrosion resistance alloys should be considered.

Table 1-1: Parameters affecting the corrosion behaviour of LPBF alloys

Effects of the surface:	**Effect of microstructure:**

• Passive film:
  • As build surfaces
  • Effect of the post processing heat treatment (in vacuum or air)
  • Chemical pickling
• Mechanical polishing
• Shoot penning
• Grinding
• Roughness
• Porosity and oxides
• Un-melted powder
	• Building direction
	• Not equilibrium phases
	• Differences in composition between centre and edge of the melt pool
	• Changes in microstructure due to the post processing heat treatments

The passive film, formed at high temperature and in deficit of oxygen, could be different from that spontaneously formed in air; in addition, the post processing heat treatments can further modify its structure and, as consequence, its corrosion resistance. Schematic representation of the process variables effect on the macro and microstructure is shown in Figure 1-1.

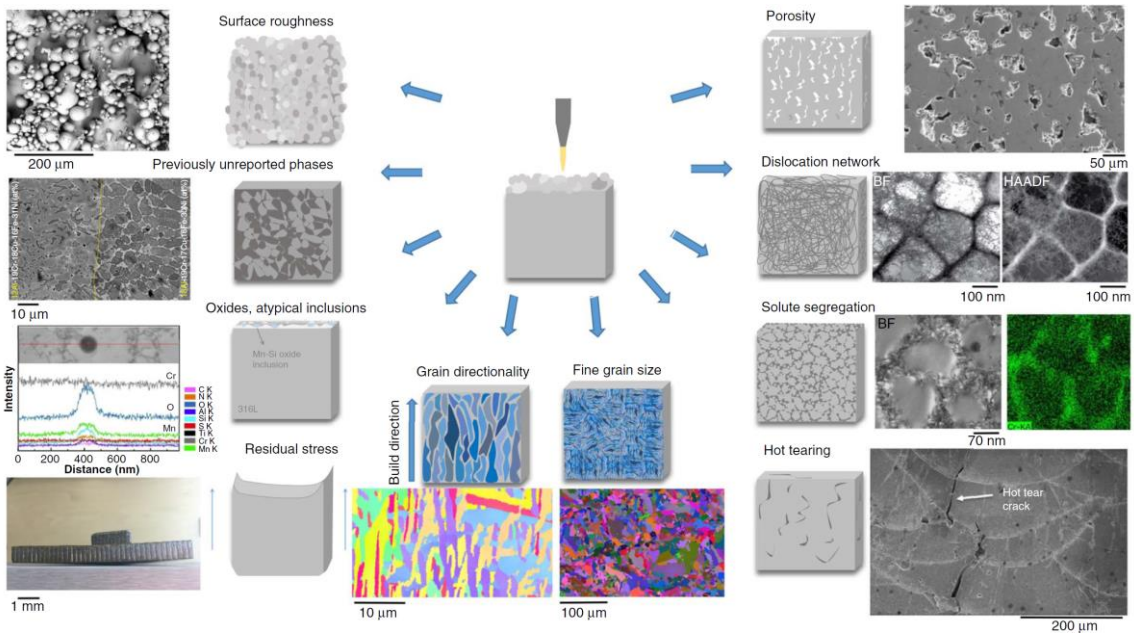

Figure 1-1: Processing variables that can affect the corrosion behaviour.[1]

The data about the aluminium LPBF alloys are in contrast demonstrating the confusion about this argument maybe due to the not comprehend effect of some printing parameters. The most of literature works is related to the Al-Si alloys because are the typical cast alloys. Revilla, et al study the corrosion of LPFB AlSi10Mg specimens monitoring the corrosion potential (E_{corr}). the cast and LPBF show similar behaviour, with values ranging between −0.7 $V_{Ag/AgCl}$ and −0.6 $V_{Ag/AgCl}$.[2] Leon et al. study the weight loss of AlSi10Mg produced by LPFB immersed in a 3.5 wt% NaCl. After 45 days of immersion, the LPFB AlSi10Mg presented slightly lower weight loss than cast AlSi10Mg.[3] The same author investigated the effect of surface finish on the corrosion behaviour of the same alloy. The corrosion rate of the polished sample was lower than the unpolished in all tests performed.[4] The aerated Harrison's solution that simulate the aggressive industrial atmosphere with acid rain, was used to study the corrosion of LPFB AlSi10Mg highlighting the surface finishing and heat treatment effects by Cabrini, et al.[5–7] The polished surface of the untreated specimen and heat treated at 300°C showed an

improvement of a passive range during the potentiodynamic polarization. Conversely, the specimen heat treated at 550 °C did not exhibit this improvement polishing the surface. Furthermore, the pitting potentials also increased after the shot peening treatment.

The corrosion behaviour of LPFB produced Al-12Si was investigated using weight loss test by Prashanth, et al. Cast and LPFB with rough surface increase the corrosion rate increasing the heat treatment temperature.[8]

Limited investigations have been performed on the corrosion behaviour of AM-produced alloys other than aluminium, iron, and titanium. In fact, no data are available for the alloy 625. Some works deals the corrosion behaviour of alloy 718 reporting an inferior corrosion resistance – regardless the building orientation – with comparison to the traditional ones.[1,9]

Thanks to the corrosion resistance, high mechanical properties and biocompatibility, the titanium alloys are most used in aerospace and biomedical fields also processed by AM leading to a many paper that study the corrosion behaviour. The LPBF Ti6Al4V shows high corrosion resistance in Hank's solution if compared to the wrought alloy, regardless the building direction.[1] Also the phosphate buffered solution at 37°C lead to similar corrosion rate between LPBF and wrought alloy.[10] Xu, et al. study the corrosion in simulated body solution and they correlated the corrosion behaviour of LPBF Ti6Al4V with the heat treatment temperature and they compared the behaviour with a traditional wrought alloy. The heat treated LPBF alloy was less susceptible to corrosion in simulated body solution than the untreated one. All the LPBF specimens had higher corrosion resistance that the traditional material.[11]

The aim of the thesis is to investigate the corrosion resistance of materials processed by additive manufacturing technique through the comparison with the performance of the traditional alloys with a similar chemical composition, studying the effect of post process treatment. Furthermore, the thesis aims to investigate the existence of the need to characterize the qualifying process for these materials to guarantee the final properties of the manufactured.

In this way, the following chapters are composed of the AM technique and of an experimental part that describes the test methodology, the presentation of the results and their discussion. The last chapter deals with the conclusions extrapolated from the research work carried out in this doctoral thesis.

CHAPTER 2

ADDITIVE MANUFACTURING PROCESS AND MICROSTRUCTURE OF MATERIALS

2.1 Metal Additive Manufacturing technique

Additive manufacturing (AM) is an innovative technology that can build parts by progressively adding thin layers of materials according to 3D CAD model. This technique leads to production of complex and customized form directly from the design without expensive machining. Furthermore, AM allows a significant reduction in the part number, deleting the necessity of assemble multiple components. In addition, parts can be produced in situ reducing the spare inventory and decreasing lead time for critical or old components. For these advantages, the AM is a technique adapted in many fields such as aerospace, medical, energy and automotive. Aerospace industry used the additive process in order to build new complex fuel injector nozzles. Thanks to AM customized prothesis and dental implants can be produced using medical images. Fast prototyping and race part can also achieve. Low cost industrial laser, high performance computer and metal powder technology have allowed the diffusion of additive manufacturing technique inside the industrial company as demonstrated by the growth in sales of commercial systems.

Only a few applications have reached fully certified production, but many other have only the certification of individual part type, material and process.[12] In order to ensure high performance of AM parts and avoid the influence of adopted parameters is necessary design a way for the qualification of these new parts. Metal AM is now able to produce hard to manufacture component that are normally difficult or impossible to produce via

conventional route. The increase number of articles and reviewer attest the strong interest for this new techniques.[13–22] However, some differences between traditional process are present, such as anisotropy, residual stress, porosity, rough surface and particular defect unique to additive manufacturing process that must be addressed for the critical application.

In the last years, many names provide by 3D printer manufacturers has been used to indicate the same technique (Table 2-1). Recently, the ASTM F2792 divides the AM in two macro sectors, the first is Directed Energy Deposition (DED) and the second is Powder Bed Fusion (PFB).

Table 2-1: AM metal equipment manufacturers and their specific process names [13]

Process	Process Name	Manufacturer	ASTM Category
DMLS®	Direct metal laser sintering	EOS	PBF-L
SLM®	Selective Laser Melting	SLM Solution	PBF-L
DMP®	Direct Metal Printing	3D System	PBF-L
LaserCUSING®	LaserCusing	Concept Laser	PBF-L
EBM®	Electron Beam Melting	Arcam AB	PFB-EB
EBAM®	Electron Beam Additive Manufacturing	Sciaky Inc.	DED-EB
LENS®	LENS	Optomec	DED-L
DMD®	Direct Metal Deposition	DM3D Technology LLC	DED-L

Another distinction is given by the heat source utilized such as laser (L), Electron Beam (EB), plasma arc (PA) etc. Furthermore, is possible classify the various technique between direct process, i.e. the process which starts from CAD model and produces directly net shape part; and indirect process, i.e. the process that using intermediate steps to complete the part. PBF AM processes and DED processes may be considered direct. Table 2-2 reports the common AM alloys and application.

Table 2-2: Common additive manufacturing alloys and applications [12]

	Aluminium	Maraging steel	Stainless steel	Titanium	Cobalt chrome	Nickel super alloy	Precious metal
Aerospace	✓		✓	✓	✓	✓	
Medical			✓	✓	✓		✓
Energy/ oil and gas			✓				
Automotive	✓		✓	✓			
Marine			✓	✓		✓	
Machinability and weldability	✓		✓	✓		✓	
Corrosion resistance			✓	✓	✓	✓	
High Temperature			✓	✓		✓	
Tools and molds		✓	✓				
Consumer products	✓		✓				✓

Figure 2-1-(a) shows a schematic representation of DED-L that used powder as raw material. DED-L is based on the powder placement into the right zone and the laser source melt the powder locally layer by layer.[23] Argon is used to protect the melt pool zone from oxidation as shielding gas and to carry the powder flow into the melt pool. DED-EB system uses an electron beam to melt a metal wire (Figure 2-1-(b)) and a vacuum chamber is necessary to eliminate all the contamination. The DED-PA and DED-GMA instead, are very similar to fusion welding (Figure 2-1-(c)).[24,25] All these techniques can be adopted to produce pieces with overhanging parts that require a specific structure to sustain their own weight. The supports will be removed after the printing process. At the end of the printing, the built can be mechanically separated from the building platform in order to receive the post processing treatment, such as heat treatment or mechanical finishing.
PBF, similarly as reported above, start with CAD model which is sliced into planar layers and send to the 3D machine setting the right printing parameters.[26]

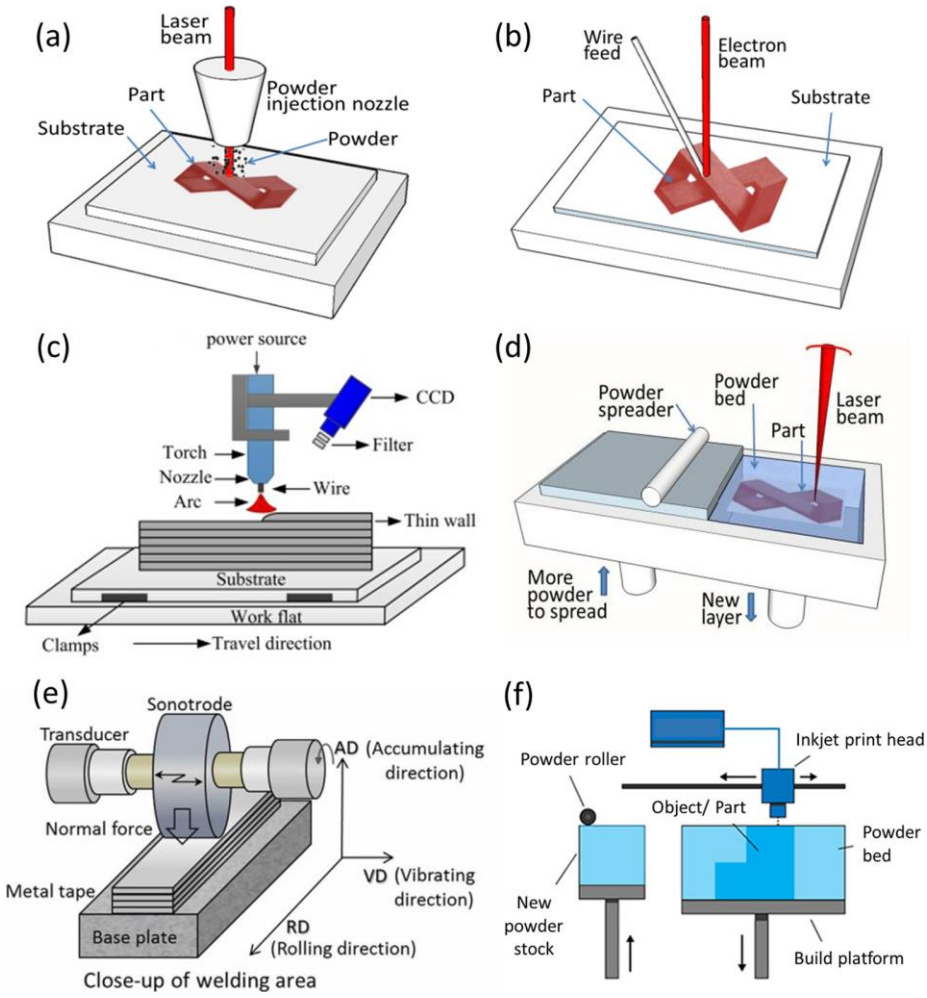

Figure 2-1: Schematic diagram of principal additive manufacturing techniques.[12,25,27,28]

The PBF is based on a powder bed with an energy source can be oriented inside the chamber in order to melt the powder where necessary. After the first layer of powder another layer is spread, and the process start again (Figure 2-1 (d)). A laser (L) or electron beam (EB) can be used as energy source. For PBF processes, the scanning strategy can follow different way in order to maximize the part density. The powders are often reused to avoid wastage that can lead to poor surface finish and mechanical properties of the final part.

A comparison of the main features between the LPBF and DED – that represent the principal players in the metal AM - is reported in Figure 2-2.

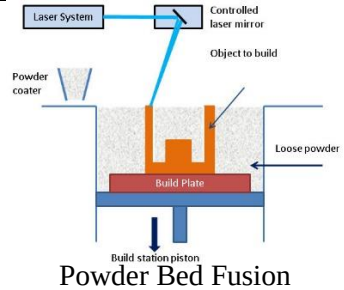

Powder Bed Fusion

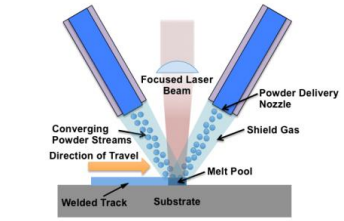

Direct Energy Deposition

Characteristics	DED	PBF
Materials	Large material diversity	Limited and lower experience in comparison to DED
Part dimensions	Limited by the handling system	Limited by process chamber (ϕ=250mm, height: 160mm)
Part complexity	Limited	Nearly unlimited
Dimensional accuracy	≥0.1 mm	≥0.1 mm
Build-up rate	10-40 cm^3/h	2-10 cm^3/h
Build up on	• 3D surface • On existing parts	• Flat surface • Flat preforms
Roughness Rz	60-100 µm	30-50 µm
Layer thickness	≥0.03-0.1 mm	≥ 0.03-0.1 mm

Figure 2-2: Characteristics of PBF and DED techniques[29–31]

The LPBF process produces samples with higher dimensional accuracy and lower roughness than DED process. On the other hand, the DED has a higher build-up rate and can create larger components than LPBF. The maximum dimensions of the LPBF components are limited by the building chamber.[29] However, the two processes can be complementary each other depending on the components characteristics.

Figure 2-1 (e) shows schematically the UAM process. It involves sheet metal joint together by means of ultrasonic vibrations that produce a solid-state jointed.[32]

Finally, in binder jet process, a liquid binder jet is selective sprayed by an inkjet printer on an alloy powder bed in Figure 2-1 (f).[26]

2.2 Powder Bed fusion technique

Process

In order to provide a baseline description of powder fusion processes, Laser Powder Bed Fusion will be described as shown in Figure 2-3. The LPBF fuses thin layers of powder which have been spread across the build area using a counter-rotating powder levelling roller. The building process takes place inside an enclosed chamber filled with nitrogen or argon gas to minimize oxidation and degradation of the powdered material. The building platform can be heated to avoid high temperature gradient during the printing process. Uniform temperature within the build platform is necessary to minimize the laser power requirements of the process (when the material is pre-heated, less laser energy is

required for fusion) and to prevent warping of the part during the build due to nonuniform thermal expansion and contraction (curling). Also the powder not already used can be maintained at elevated temperature. Once an appropriate powder layer has been formed a focused laser beam is directed onto the powder bed and it is moved according to the CAD model to melt the powder. Surrounding powder remains loose and serves as support for subsequent layers. After completing a layer, the building platform is lowered by one-layer thickness and a new layer of powder is laid and levelled using the counter-rotating roller. The beam scans the subsequent slice cross-section. This process repeats until the complete part is built. Finally, the parts are removed from the powder bed, loose powder is cleaned off the parts, and further finishing operations, are performed if necessary.[26]

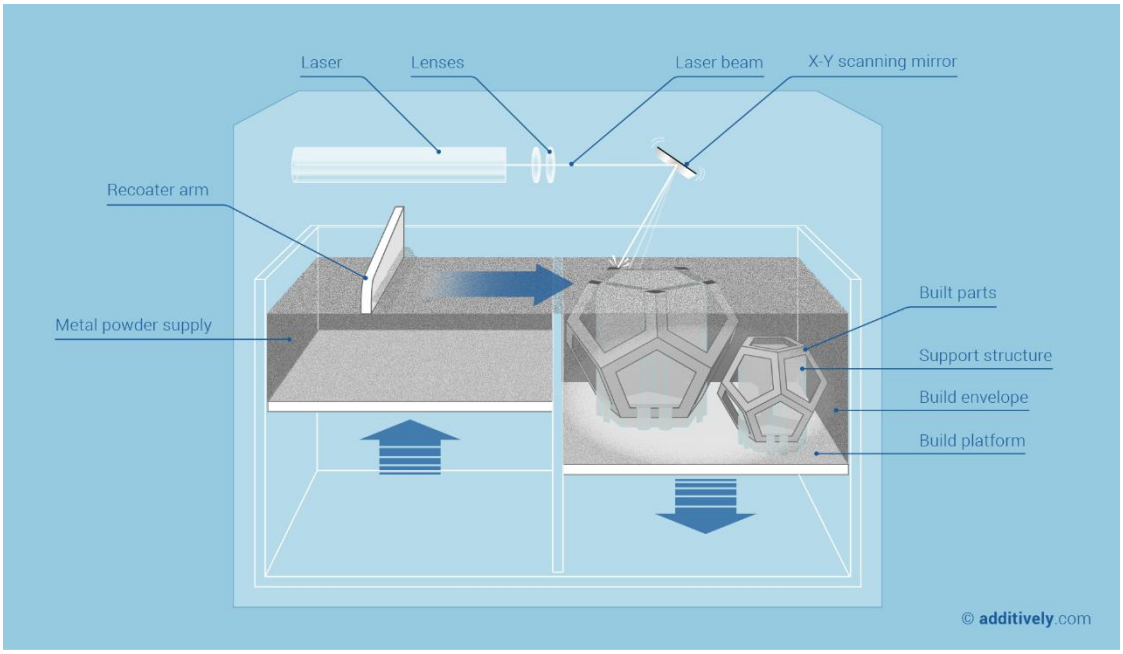

Figure 2-3: LPBF schematic process[33]

Powders

The commercially available powders is limited to pure titanium, Ti6Al4V, 316L stainless steel, 17-4PH stainless steel and 18Ni300 maraging steel, AlSi10Mg and AlSi7Mg, CoCrMo, and nickel based superalloys Inconel 718 and Inconel 625.[34–40] This range is continually expanding with new entrants to the materials supply market. Precious metals such as gold, silver or platinum are currently used in AM.

The quality of the 3D part depends strongly for the quality of the powders such as the shape, the size distribution, surface condition, composition, flowability etc. The LPFB powder has size range between 10 and 65 µm. Obviously, the quality of the powder is

related to the technology used to obtain the particles. In literature, four methods are presented to produce powder for AM.

In the gas atomization process (GA), the metal is atomized by the high pressure flow of argon and nitrogen gas (Figure 2-4-(a)).[41] This method forms powders with spherical morphology but the presence of the satellite particles increases the roughness of the surface. Moreover, the particles can contain trap gas that can lead to porosity in the 3D part. In rotary atomization (RA) process, the alloy is spilled on a rotary disk. Fine droplets of molten metal are flung from the disk, solidified and collected as powders that are not spherical. Plasma rotating electrode process (PREP) transforms a rotate metal bar into metal powder by means of electric arc or plasma using the centrifugal force to collect the solidified particles (Figure 2-4-(b)). This technique leads to perfectly spherical shape with smooth surfaces. High pressure water jet is used to atomize and solidify the liquid metal droplets as powders in water atomization (WA) process. The powders from the WA process are usually irregular shape with lower flowability.

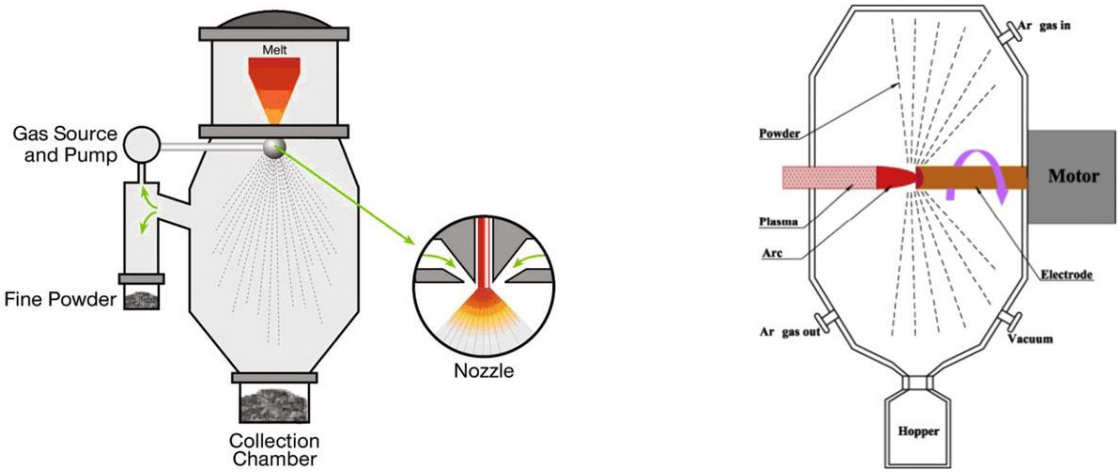

Figure 2-4: (a) GA system;[13] (b) PREP system[42]

Heat flow

The most used method to analyse the piece temperature involves the computer simulation because the measurement of temperature profile is very difficult because the source use high speed to move itself.

A rapid heating followed by a rapid cooling characterized this technique that leave a particular melt pool where the laser worked. Inside the melt pool, the temperature can be more degrees above the liquidus temperature of the alloy and it decreases moving to the edge of the melt pool (Figure 2-5). During the deposition, the substrate function as heat

dissipater. Hence, the ability of dissipate heat through the substrate decreases progressively with the increasing of the height of the part.

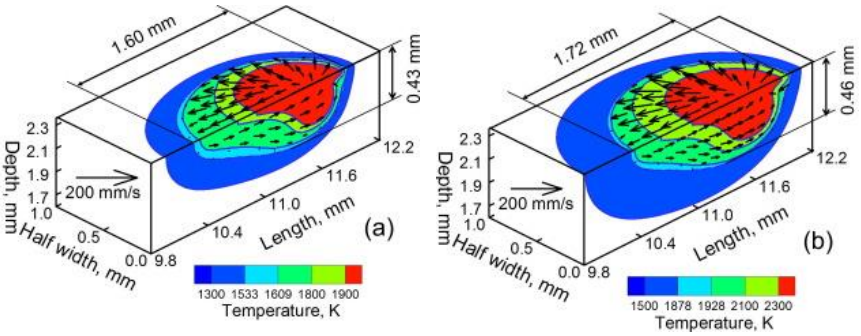

Figure 2-5: Gradient of temperature inside the melt pool for (a) alloy 718 and (b) Ti6Al4V by means of computational simulation[43]

The cooling rate is very high if compare to the welding, thus leading to a unique microstructure far from the thermodynamic equilibrium. Moreover, the high gradient temperature inside the melt pool, the partial reheating of the layers previous printed and the different thermal diffusion coefficient in the height are the main players in the inhomogeneous microstructure.

Defects

The AM technique involves peculiar defects linked with the process parameter and process type. During the deposition of alloys such as titanium or aluminium, the vaporization of some alloying element may occur if the melt pool temperature is too high. Due to the different volatility of some element, the change in the final composition of the printed alloy leads to different microstructure, corrosion behaviour and mechanical performance worsening the quality of the 3D component.[44] Authors reported that is possible decrease of 0.6-1.0 % Al and 0.4% Mg during the processing of titanium and aluminium alloys, respectively.[45–47]

The porosity strongly affects the mechanical behaviour and is very important minimized this phenomenon that is common in AM process (Figure 2-6).[48,49] Different factors are linked to the porosity. If high power is used during the process the melting zone can become unstable lead to a collapse of itself leaving a pore.

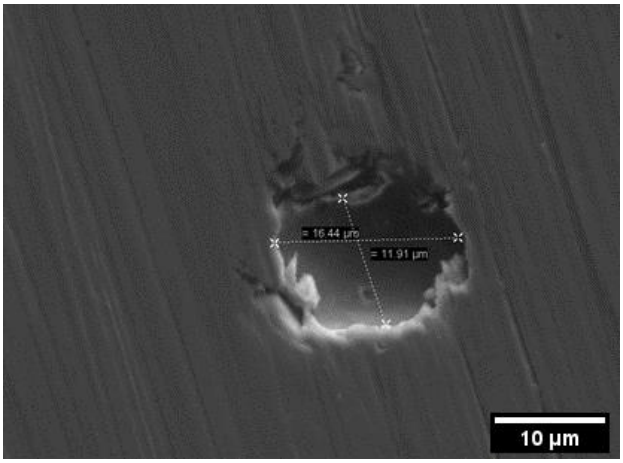

Figure 2-6: Pore inside the LPBF alloy 625 specimen

Even the gas inside the powder may induce porosity in the 3D component. Moreover, the shielding gas using to avoid the melt pool oxidation can be trapped and lead to porosity.
PBF process involve rough surface for the as fabricated part depending on the printing parameters. Powder quality (morphology and granulometry), process parameters (source power, scan speed, layer height, overhang angles, scan strategy, etc), design and material play an important role in the final roughness leading to partially fused powder, improper fusion or balling.[12] Nevertheless, post processing treatment such as surface machining, grinding, chemical polishing, and shot peening can mitigate the roughness.
The roughness is also embedded in the "stair step effect" due to the approximation of curve surface as shown in Figure 2-7. Therefore, the balancing between the build time and the accuracy and roughness is a main point during the set of the print parameters. Small layer thickness strongly reduces the surface roughness, but it takes more time for build the same volume. Another strategy to mitigate the problem is orient the part inside the chamber in a smart mode, avoiding high angles by complex edge and building direction.[50]
AM component can show crack due to the thermal contraction and shrinkage between the substrate and the melt pool causing a tensile stress in the new layer. If the magnitude of tensile stress exceeds the limit a crack can be detect at the grain boundaries. Moreover, in the partially melted zone can precipitates second phases inducing a tensile force due to the solidification shrinkage and thermal contraction during the cooling. In the AM product, the crack can be very long interesting many layer or limited at only one layer

with a maximum length equal to the layer height. Some materials such as Ti6Al4V and nickel superalloy are prone to this type of crack.[12]

At the end, if the residual stress between two consecutive layer overtake the mechanical resistance of the alloy, the delamination problem can affect the AM part.[43]

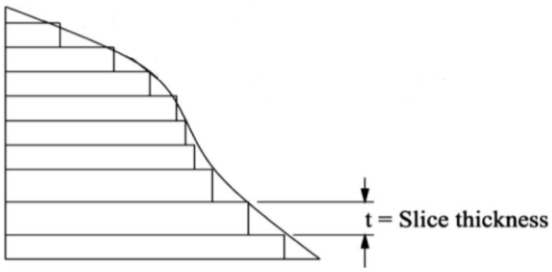

Figure 2-7: Rough surface caused by approximation of curve surface[50]

The rapid cooling rate and the deposition of a new liquid layer above one already solidified are the main concept of additive manufacture process but it can include the residual stress. This stress does not implicate only cracks but also distortion, bad tolerance, low fatigue and fracture resistance.[51,52] The residual stress distribution is non-uniform and may change during the process. Thus a quantitative study of the problem is necessary to reduce or eliminate it. Also a smart placement of the component into the chamber can limit the distortion.

Microstructure

The crystallographic orientation and grain shape depend on the thermal history.

The melt pool can have circular or keyhole cross-section in function of the power intensity. AM prefers the first form because the keyhole mode can be instable involving porosity.

The nucleation process occurs only during the deposition of the first layer when the building platform has dissimilar nature in comparison with the chemical composition of the first printed layer. In this case, it is necessary overcome the activation energy barrier at the liquid-solid interface. Conversely, the subsequent layers –having similar chemical composition– spontaneously grow epitaxially from the previous layer without any activation energy barrier.[12] Nevertheless, for these layers, the microstructure is dominated by competitive growth.[53] The competitive growth of the polycrystalline material concerns the dendrite that have crystallographic orientation parallel to the maximum heat flow

during the printing. Table 2-3 shows the preferentially growth directions for materials with various crystal structures.[54] Instead, columnar structures are developed when dendrites that are more aligned with the temperature gradient outgrow slower growing misaligned dendrites.[55]

Table 2-3: Preferential growth directions for materials with various crystal structures[54]

Crystal structure	Growth direction	Examples
Face-centred-cubic (fcc)	<100>	Aluminium alloys, austenitic stainless steels
Body-centred-cubic (bcc)	<100>	Carbon steels, ferritic stainless steels
Hexagonal-close-packed (hcp)	<1010>	Titanium, magnesium

The morphology of the grain obtain after the printing can affect the mechanical property; the PBF system is characterized by grain with the <001> build direction as shown in Figure 2-8.[56] Vertically oriented columnar grains are the main microstructure for several alloys processed by PBF.

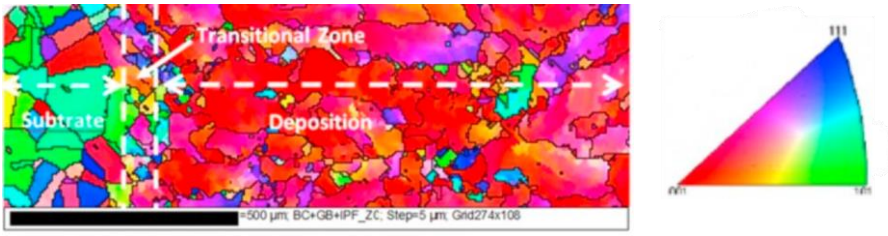

Figure 2-8: Microstructural morphology of LPBF alloy 625 [56]

Post-processing treatments

Most AM processes require post-processing after part building to prepare the part for its intended use.

One of the most common is support removal. Support material can be classified into two categories: the first is the material which surrounds the part and the second are the rigid structures which are designed and built to support the overhanging parts or connect the part with the building platform. In the PBF technique, the removal of the powder that surround the part is required. Nevertheless, it is necessary leave the powder around the piece during the cooling process in order to avoid distortion due to non-uniformly temperature distribution. After the cooling time, typically the entire build (melt part and powder) is removed from the machine as a block and transported to a station where the parts are removed manually from the surrounding powder material by means of brushes, compressed air, and light bead blasting. Some machine has an integrate system to take away the powder around the part (Figure 2-9).

Figure 2-9: Automated powder removal using vibratory and vacuum assist in a ZCorp 450 machine [26]

Obviously, internal channel or cavity is difficult to clean and may require significant post-processing time. The smart placement with respect to the building direction can limit the use of supports. The orientation can also affect the surface roughness and functionality. Where the supports are removed a typical marker is left such as small bumps and divots can compromise the surface. This effect may compromise the product functionality of small products. The supports are normally removed manually by hands or by mechanical cutting or by means of wire-EDM.[26]

The surface treatment is a common post processing treatment in order to improve the roughness. it can involve shot-penning, mechanical or electrochemical polishing etc. The process of shot-peening involves a mechanical surface treatment whereby small balls hit the surface of the component. The repeated impacts not only induce compressive residual stress but also refine the microstructure at the surface and sub-surface region (typically a few hundred micrometres in depth). The compressive residual stress field reduces the effective applied stresses of the component during application, which results in delayed crack initiation and retarded early crack propagation.[57] Regarding to the electrochemical polishing, the printed product is immersed into the electrolyte and a anodic current density is applicated. The electrochemical reaction slightly dissolves the metal surface, thereby smoothly polishing a very rough surface. Surface quality including roughness, splashed particle spots, smoothness, brightness, light reflection and corrosion resistance are improved by electrochemical polishing.[58]

Finally, hot isostatic pressing or heat treatment are used to minimize the residual stress and change/homogenise the microstructure. Traditional heat treatment developed for the specific metal alloy being employed are commonly used. However, special heat treatment methods have been studied to maintain the fine-grained microstructure within the AM part in order to retain high mechanical properties. The hot isostatic pressing process

combines high temperature and isostatic inert gas pressure (from to 100 to 3100 bar) in a high-pressure containment vessel. Heat and pressure, applied simultaneously, eliminate internal voids and residual porosity therefore improving fatigue resistance of fabricated parts and resulting in a very fine-grained structure.[59]

2.3 PBF metal alloys

PFB Aluminium alloy

High strength and stiffness, low weight, good formability, good corrosion resistance, and recycling possibility make aluminium alloys an ideal candidate to replace heavier materials (steel or copper) to satisfy the weight reduction demand in the automotive industry.[60] Authors reported that aluminium alloys exhibit an improvement in fuel economy of 5.5% for weight reduction of approximately 10%.[61]

The most common aluminium alloys processed by AM are the eutectic Al-Si and the heat treatable Al-Si-Mg alloys that are the main player in to as-cast and high pressure die cast techniques thanks to their high castability. The microstructure of Al-Si alloys usually consists of primary α-aluminium phase and eutectic, fully eutectic, or mixture of primary silicon phase and eutectic, depending on the composition and solidification condition (Figure 2-10).

LPBF AlSi10Mg parts have mechanical properties higher or at least comparable to the casted AlSi10Mg material. The Vickers hardness of the as built LPBF parts is much higher (almost 30HV) than the hardness of the high pressure die casted (HPDC) AlSi10Mg in the as-cast condition and almost comparable with the aged HPDC AlSi10Mg. The ultimate tensile strength of the as built LPFB AlSi10Mg parts is always higher than those of the HPDC. The elongation of the as-built AlSi10Mg parts is comparable with the HPDC parts (Table 2-4).[62]

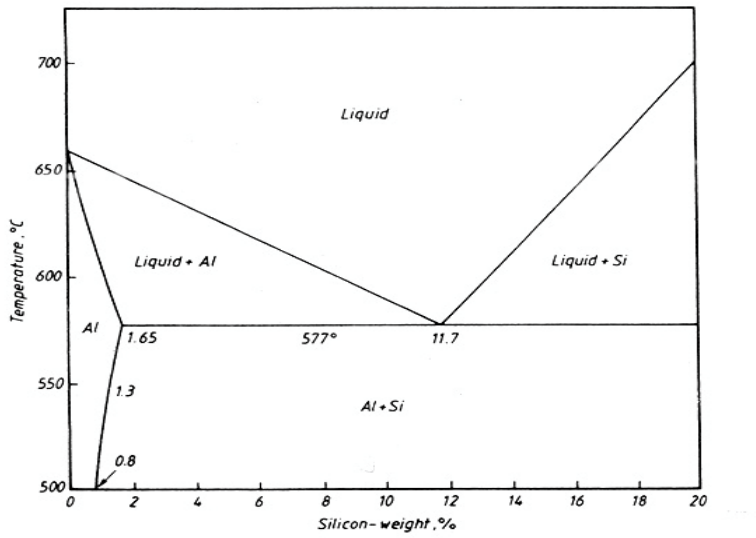

Equilibrium diagram: Aluminium–silicon. (*Courtesy Aluminium Federation.*)

Figure 2-10: Phase diagram of aluminium-silicon system.

Table 2-4: Mechanical properties of LPFB built parts and cast[62]

	E GPa	UTS MPa	ε %	HV
XY direction XZ direction	68±3	391±6 396±8	5.55±0.4 3.47±0.4	127
conventional cast and aged	71	300-317	2.5-3.5	86
high pressure die casting high pressure die casting T6	71 71	300-350 330-365	3-5 3-5	95-105 130-133

The macrostructure of the LPBF alloy printed rotating the scan strategy by 67° between consecutive layer shows the tracks of the laser scan along the building plane (XY) (Figure 2-11 (a)). The melt pool borders are elongated due to the variation of the laser scan direction. The temperature of the platform does not modify the alloy macrostructure. Along the direction perpendicular to the building direction (XZ), the macrostructure shows semi-circular shaped melt pools, partially overlapped on previous tracks (Figure 2-11 (b)). During the LPBF process, the underlying metal, which is only superficially melted, quickly remove the heat from the liquid and it ensures the adhesion of the track to the substrate. Each singular track could be considered as a small casting deposited on the previous one.[57]

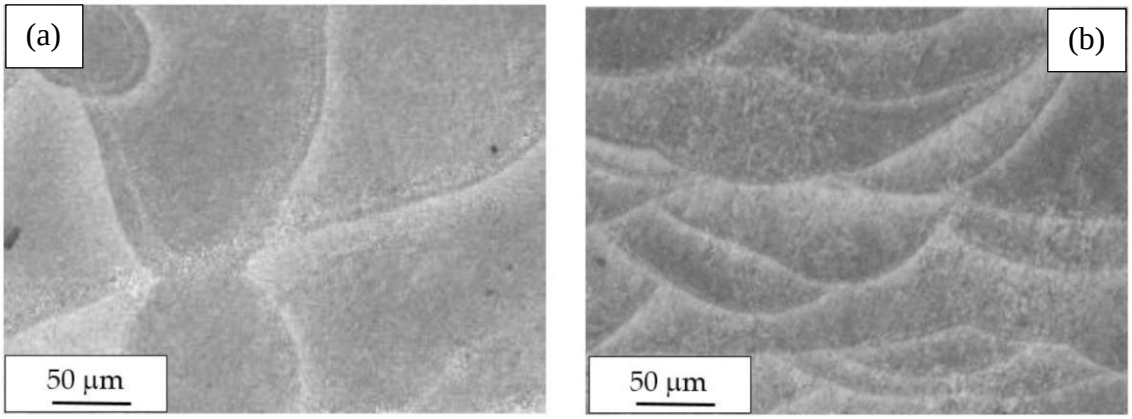

Figure 2-11: Optical images of microstructures of untreated (UT) specimen on (a) XY plane and (b) XZ plane[63]

The microstructure modification inside the melt pools depends on the rapid solidification process, building platform temperature and directional cooling. SEM analysis reveal cellular grains inside the melt pools and oriented dendrites. The rapid solidification inhibits segregation and precipitation of alloying elements from liquid and solid solution and produced a microstructure far from equilibrium. The directional cooling affects the grain growth perpendicularly with respect to the melt pool border towards the centre of the melt pool.[64] Smaller equiaxed grains are observed at the centre of the melt pool, while the border of the melt pool -where two tracks were overlapped- underwent double melting. Heat Affected Zone (HAZ) can be noticed just next to the melt pool border (Figure 2-12).

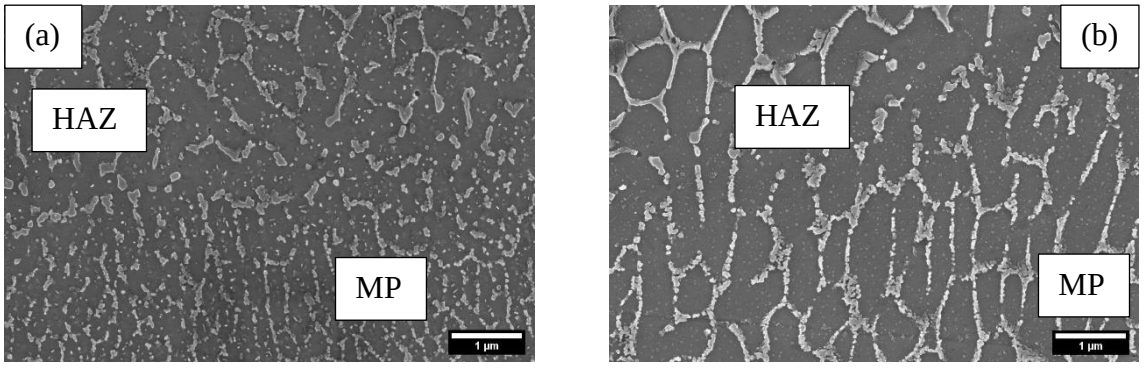

Figure 2-12: Microstructure of as-built specimens using different temperatures of the building platform (a) 35°C and (b) 100°C

The silicon distribution in the melt pool is regulated by the heating and cooling rate of the alloy. Owing to the high solidification rate, the α-Al phase inside the melt pool remains oversaturated in silicon.[65,66] According to Murray and McAlister, the maximum solubility of silicon in aluminium is about 1.5 wt % at the eutectic temperature but decreases to less

than 0.05 wt %. below 300 °C. Rapid cooling can maintain the silicon content into an α-Al phase at oversaturated level up to 11 wt %.[67]

The silicon does not fully remain in solid solution, but partially segregates on the columnar grains of the α-Al phase as fibrous particles that "decorate" the primary grain of α-Al phase (Figure 2-13(a)).[65]

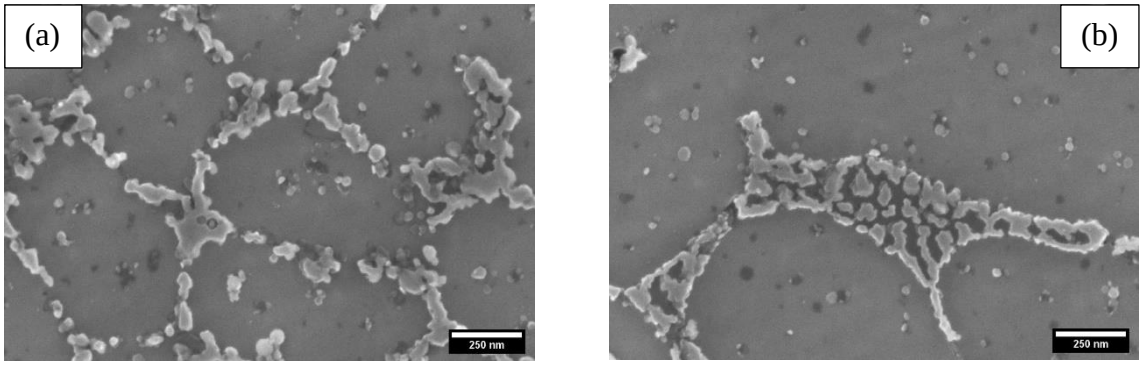

Figure 2-13: Close-up of the melt pool (MP) zones (a) of the silicon-isolated particles in HAZ; (b) of the UT specimens ($T_{platform}$ 35°C)

Thijs et al.[68] define the structure of silicon as "intercellular network".[68] At times, the silicon particles form a eutectic phase (Figure 2-13). The eutectic is more visible in specimens built with a platform temperature of 100°C compared to 35 °C (Figure 2-13 and Figure 2-14).

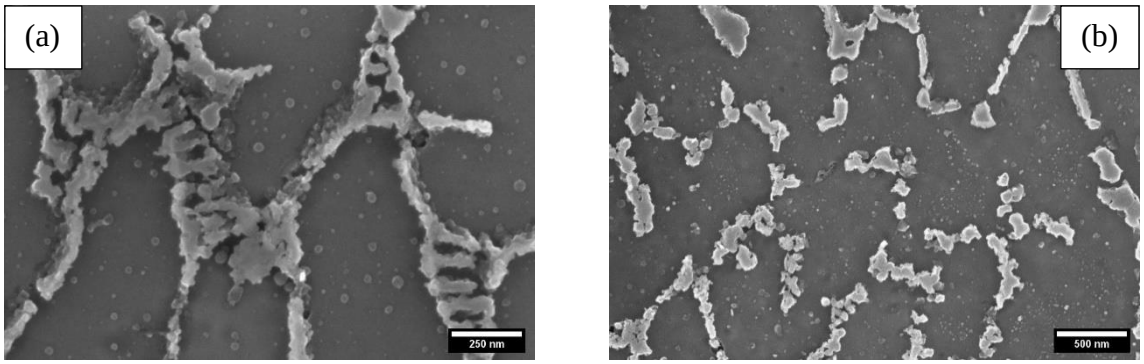

Figure 2-14: (a) Close-up of the eutectic-like phase on the border of α-Al grains and (b) idiomorphic crystal in the HAZ of the UT-specimens ($T_{platform}$ 100°C)

In the HAZ, the solid-state diffusion is promoted by thermal cycles and interruptions in intergranular network occur. Silicon particles coarsening could be noticed, which become idiomorphic crystals and some needle-like microparticles could be detected (Figure 2-15 (b)).[68] Moreover, during the printing the Mg_2Si can precipitate.[12,68]

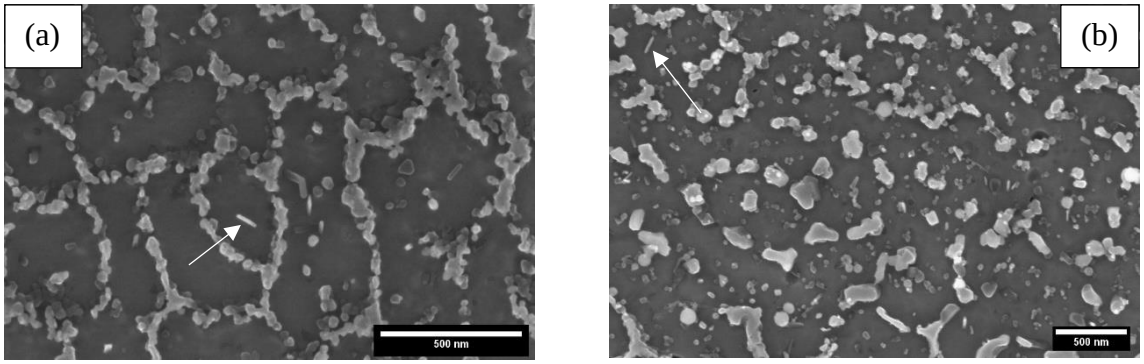

Figure 2-15: Microstructure of the AlSi10Mg specimen after stress relieved at 300°C (a) MP and (b) HAZ ($T_{platform}$ 35°C)

PFB Nickel alloy

Nickel superalloys are widely used in the aerospace applications,[69] marine environments including for the manufacture of heat exchangers,[70] in the Oil&Gas industry [71–73] and in nuclear plants [74–76] thanks to its high mechanical properties, good corrosion resistance and high performance at high temperatures. However they can underwent localized corrosion, such as crevice, pitting as well as intergranular corrosion and stress corrosion cracking (SCC) in very aggressive conditions.[77–79]

Alloy 625, also known as Inconel 625, is a nickel based solid solution strengthening superalloy, which is largely strengthened by Mo and Nb elements. The microstructure of the traditional alloy is formed by austenitic phase, with the possibility to have precipitation of intermetallic such as γ'-Ni_3(Ti-Al) and γ''-Ni_3Nb which can improve the mechanical properties. γ'-Ni_3(Ti-Al) phase is considered one of the most important strengthening phases in a significant number of Ni-Fe and Ni-based superalloys. γ′ is a Face Centred Cubic (FCC) intermetallic compound. Typically, γ′ phases are dispersed throughout the matrix, strengthening the alloys by means of Orowan mechanism. The same mechanism is also used by γ''-Ni_3Nb in order to strengthening the alloy. Carbides are commonly present in this superalloys, and they tend to form mainly along the grain boundaries and twin boundaries, generating fine inter/intragranular disperse carbides, during thermal exposures.[80] The LPFB alloy 625 show cellular and columnar grain of austenitic matrix phase γ, with γ′-[Ni_3TiAl], γ′′-[Ni_3Nb]. δ [Ni_3Nb] phases as well as dendrite formations can be found in the melt pool. [81–83]

The microstructure of the as-built samples shows columnar grains developing epitaxially, thus crossing several melt pools along the building direction (Figure 2-16). The marks

underline the different melt pool borders along both the building direction and perpendicular to the building platform. The melt pools are not all placed straight along the building direction due to the scan strategy which involves laser beam rotation of 67° between two consecutive layers.[84–86]

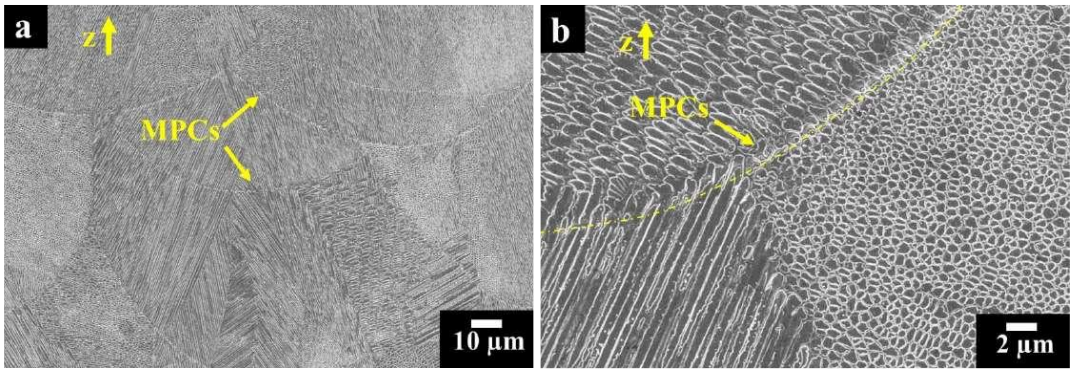

Figure 2-16: FESEM images at different magnification (a, b) exhibiting melt pools with columnar and cellular primary dendrites for as-built IN625 sample; Mixed acids reagent[87]

Figure 2-17 reveals the FESEM image of as-built alloy 625 samples performed by Politecnico di Torino along the building direction. The melt pools are made up of very fine primary dendritic structures which have both cellular and columnar shapes. The cellular dendrites structure is due to the alteration of columnar dendrite structures caused by very high cooling rates, as previously reported.[88] At higher magnification (Figure 2-17), very fine bright precipitates along the dendritic areas indicated by arrows 1 and bright elongated phases along the interdendritic regions pointed out by arrows 2 can be observed. Previous TEM investigations performed on as-built alloy 625 by Politecnico di Torino (produced with the same process parameters) reported a relatively high concentration of Nb and C for these precipitates, suggesting the early stage formation of fine MC carbides.[89]

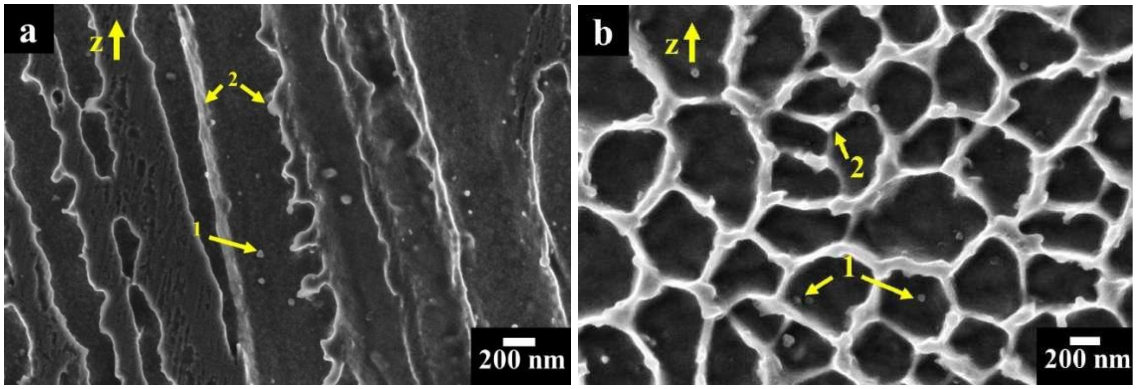

Figure 2-17: FESEM images of as-built IN625 sample at high magnification a) columnar dendritic structures with nanoprecipitates (1) and segregation of Nb and Mo within the interdendritic zones (2) b) cellular dendritic structures with nanoprecipitates (1) and segregation of Nb and Mo within the interdendritic areas (2)[87]

EDS results revealed enrichment in Nb and Mo within the interdendritic areas, indicated possible segregation of Nb and Mo due to their elevated tendency to segregate, as confirmed by the literature.[90,91]

The mechanical properties of printed alloy are higher or comparable with the traditional same alloy and are comply with the minimum requirements of the ASTM standard (Table 2-5).

Table 2-5: mechanical properties of alloy 625 [92,93]

	YS MPa	UTS MPa	ε %	Hardness
LPBF XY LPFB XZ	725 ± 50 615 ± 50	990 ± 50 900 ± 50	35 ± 5 42 ± 5	HRC 30
LPBF XY Heat treated at 870°C 1hours LPFB XZ Heat treated at 870°C 1hours	720 ± 100 650 ± 100	1040 ± 100 930 ± 100	35 ± 5 44 ± 5	
Cast	350	710	48	HV 266
Annealed	430	940	51.5	HV 145
ASTM B443, B444, B446 Annealed	414	827	> 30	

PFB Titanium alloy

Titanium and its alloys are among the most important metals in the biomedical field, thanks to their biocompatibility and mechanical properties, including a good strength-to-weight ratio due to their low specific weight and high tensile strength.[94] The Ti6Al4V alloy is mainly used for the realization of artificial joints.[95]

Ti6Al4V is dual phase alloy composed of a hexagonal α-phase and a body-centred-cubic β-phase at room temperature. Thijs et al.[96] noticed a fine- grained acicular martensitic structure in their investigations on AM alloy, and also identified from XRD the present phase as α'. In building direction, elongated grains with a size >>100 µm were found that

significantly exceed the layer thickness of 30 µm which was used in the experiment. An epitaxial growth occurred.[97]

Post processing heat treatment is usually needed to transform the martensite to α-phase in order to improve mechanical properties.[12] In general, AM processed Ti6Al4V also shows increased tensile strength compared with cast or wrought material. Conventionally processed (cast, wrought) α+β alloys, such as Ti6Al4V, exhibit lower elongation values than the commercial pure titanium due to the blocking of the twinning deformation process.[98] A comparison on the mechanical behaviour is given by the Table 2-6

Table 2-6: Mechanical properties of Ti6Al4V in relation with the process

Process	YS MPa	UTS MPa	ε %
Cast ASTM F1108	758	860	>8
Cast by[99]	896	1000	8
Wrought ASTM F1472	860	930	>10
Wrought by[99]	931	1055	9
XY LPBF by[100]	1137 ± 20	1206 ± 8	7.6 ± 2
XZ LPBF by[101]	1040 ± 10	1140 ± 10	8.2 ± 0.3
XY LPBF after stress relieving at 650°C for 3h[102]	1076 ± 14	1189 ± 16	13.6 ± 1.3

CHAPTER 3

EXPERIMENTAL STUDY OF AlSi10Mg

The following chapter deals of the experimental study of corrosion behaviour of Al-Si alloy processed by LPBF. Potentiodynamic test, electrochemical impedance spectroscopy and immerse tests were performed to characterize the localized corrosion and the selective corrosion. A microstructural characterization is also performed.

The tests were performed on specimens printed by Politecnico di Torino. Scanning Kelvin Probe Force Microscopy tests were carried out at the University of Udine. The Exo-electron emission tests were performed by the University of Riga.

The tests were carried out on AlSi10Mg specimens; Table 3-1 reports the alloy composition. The powders were processed by an Eos M270 Dual Mode machine equipped by powerful Yb (Ytterbium) fiber laser system with a continuous power up to 200 W operating in Ar atmosphere. The scanning strategy involves the rotation of laser beam of 67° between consecutive layers based on the EOS strategy. The combination of the process parameters and scanning strategy allows the production of parts with a residual porosity less than 0.1%.

Table 3-1: Nominal chemical composition of AlSi10Mg powder

Alloy (% weight)	Si	Fe	Cu	Mn	Mg	Zn	Ti
AlSi10Mg	9-11	≤0.55	≤0.05	≤0.45	0.2 - 0.4	≤0.1	0.01

The gas atomized AlSi10Mg powder was produced by EOS Gmbh (Krailling, Germany). FESEM observations reported in Figure 3-1 (a) of the as-received gas atomized aluminium powder revealed that the particles are spherical and quite regular in shape, ranging in dimensions from 0.5 to 40 µm, with a mean size of 25 µm. The smallest

particles tend to agglomerate on the surface of the bigger ones, creating some clusters of 50 to 80 µm. [57]

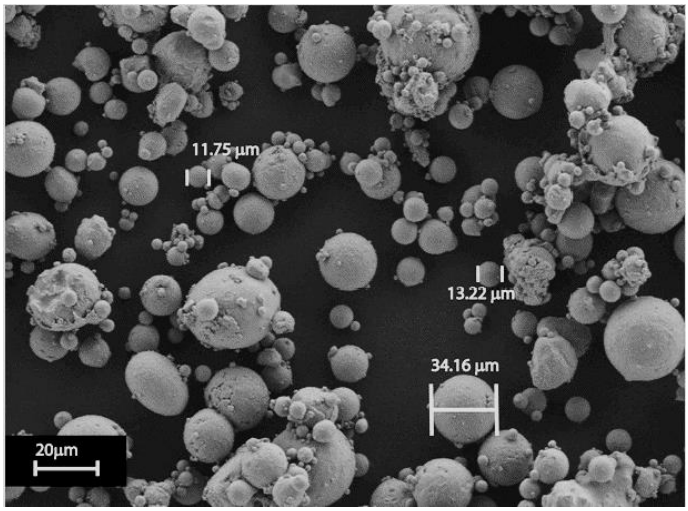

Figure 3-1: Field emission scanning electron microscope (FESEM) of AlSi10Mg powder [57]

The smallest particles are spherical, whereas the bigger ones possess an elongated shape. Some clusters are formed because of the agglomeration of the smallest particles on the surface of the bigger ones. Trevisan et al investigated the mean size distribution through laser granulometry (Fritsch model Analysette 22 Compact) using a frequency distribution based on a volumetric assumption, the diameters corresponding to 10% (d_{10}), 50% (d_{50}) and 90% (d_{90}) of the cumulative size distribution are 22, 34 and 53 µm, respectively. [103] Cylindrical specimens with 15 mm diameter and 5 mm height were used for the corrosion test. They were produced considering different orientations with respect to the building platform. Specimens were built both with the base parallel to the building platform (named XY, see Figure 3-2) and perpendicular to the building platform (named XZ, see Figure 3-2). Two different temperatures (35 °C and 100 °C) of the building platform during the production process were also considered.

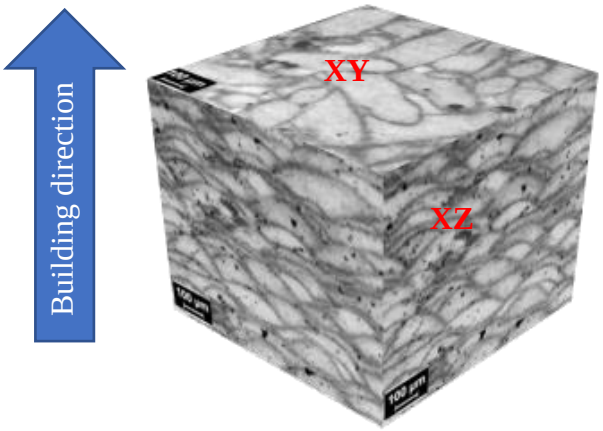

Figure 3-2: Macrostructure and orientation of AlSiMg samples

The specimens manufactured via LPBF were tested in two conditions: without heat treatment (named LPBF-UT specimens) and after different heat treatment and they are named LPBF-HT specimens. The post processing heat treatments were carried out at 200, 300, 400, and 500 °C for 2 h, followed by cooling in still air at room temperature.
The specimen used directly after the printing are marked with the initials AB (As Built). They present high roughness surface (Figure 3-3).

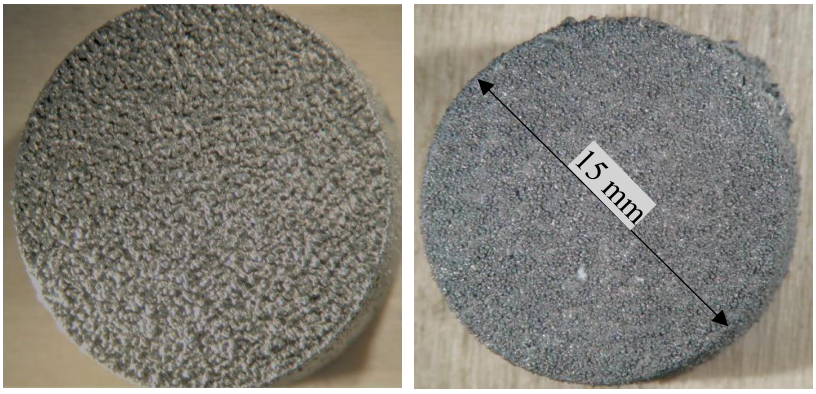

Figure 3-3: Macro image of the as produced surface

Calignano et al. reported that the roughness (Ra) of the AB specimens was 23 µm, with 153 µm of Rz -that is the distance between the highest peak and lowest valley. A residual emerging porosity of 0.7-0.8% was detected.[104]

The specimens marked as P (Polished) were grinded with abrasive paper until 4000 grit and polished with 0.3 μm colloidal alumina. They were passivated in air for 48 hours before tests. All specimens were degreased in acetone before the electrochemical tests.

Metallographic analysis and hardness tests

Metallographic analysis was carried out on specimens polished by means of abrasive papers up to 4000 grit, finished by 0.1 μm alumina aqueous suspension, and etched by means of Keller's reagent (2 mL HF (48%) + 3 mL HCl + 5 mL HNO_3 + 190 mL H_2O) for 15 seconds.

Vickers microhardness tests were executed according to UNI EN ISO 6507-1:2018 standard by using 100 g load and 15 s waiting time.

Selective corrosion test

Intergranular corrosion tests were carried out according to ISO 11846 standard. One side of the specimen was polished with emery paper up to 2400 grit, whereas the other side was left with the rough surface. According to the standard, the specimens were pickled in NaOH 8% at 55 °C for 3.5 min, rinsed in water, and dipped in 60% HNO_3 for 2 min. They were then rinsed in distilled water and dried. All the reagents were of analytical grade.

The intergranular corrosion tests were carried in 30 g/L of NaCl solution with 10 mL/L of HCl at room temperature for 24 h. After exposure, the specimens were rinsed, and the incoherent corrosion products were mechanically removed using a soft brush. They were then sectioned in order to analyse the morphology and depth of the attack.

Electrochemical test

Electrochemical tests were performed by using different instrument, such as Ivium Compastat, Metrohm Autolab PGSTAT302, Gamry REF600+, with a 1-L ASTM G5-82 glass cell on specimens printed at 100°C with building platform temperature. The cell was equipped with a saturated calomel reference electrode (SCE) placed in a Huber-Luggin capillary probe, and two graphite counter electrodes. The specimens were inserted into a PTFE sample holder with an exposed surface of 0.785 or 1 cm^2 (with a rubber gasket in order to avoid linkage of solution) and used as the working electrode.

For the potentiodynamic tests, the specimens were immersed in the solution and stabilized for 600 s. Then, the potentiodynamic test was conducted with a potential scan rate of 0.167 mV/s, from -10 mV *vs.* free corrosion potential (E_{corr}) to +800 mV *vs.* SCE or up to reach an anodic current of 1 mA/cm^2. This last value was chosen based on the experience, it is sufficient high to avoid any spontaneous repassivation of the specimen and not too high to fully destroy the specimens, permitting to evaluate the morphology of corrosion. The potential at the beginning of rapid current increase was assumed as pitting potential.

The tests were carried out at 23±2 °C in different aerated environmental reported below:

- 35 g/L (0.6 M) NaCl at pH 7
- 3.5 g/L (0.06 M) + 38.34 g/L Na_2SO_4 NaCl at pH 7
- 1 g/L (0.02 M) + 41.18 g/L Na_2SO_4 NaCl at pH 7
- 0.5 g/L (0.01 M) + 41.89 g/L Na_2SO_4 NaCl at pH 7

After the tests, the specimens were firstly washed with distilled water, rinsed with acetone in ultrasonic bath, and finally dried.

Corrosion morphologies were observed by means of optical and scanning electron microscopes.

The electrochemical impedance spectroscopy (EIS) tests were performed in the same cell and using the same condition/solution reported above for potentiodynamic tests. Initially, 600 seconds of equilibration time was recorded. A sinusoidal signal of 10 mV amplitude in the frequency range between 40000 and 0.01 Hz was used, with 5 frequencies for decade. Ivium Compastat, Metrohm Autolab PGSTAT302 and Gamry REF600+ were again used.

Surface characterization

The scanning Kelvin probe force microscopy (SKPFM) technique was used to obtain the surface potential (Volta potential) maps on polished AlSi10Mg specimens with $T_{platfotm}$ of 100°C by means of a Nanoscope III multimode atomic force microscope (AFM) equipped with an Extender TM electronic module. The SKPFM is a local technique to measure the Volta potential at the micro/nano scale, it permits to evaluate the energy to remove the electrons from the material Fermi level,[105] and this can be related to the different electrochemical nobility of the material phases.

The maps were acquired using n^+-silicon tips coated with $PtIr_5$ at 23 °C with a relative humidity of 40–65%. The topography and potential maps were sampled with a scan frequency of 0.1 Hz. To acquire potential maps, we used a scan height of 100 nm in the lift mode.

Exo-electron Emission (EEE) measurements

The exo-electron emission (EEE) measurements were carried out using a exo-electron spectrometer in a vacuum 10^{-3} Pa on AlSi10Mg specimens printed with $T_{platfotm}$ of 100°C. and this can be related to the corrosion resistance of the different material phases. The technique is based on the electron extraction work and can be highlight the effect of the heat treatment on the microstructure or phases precipitation.

The emitted electrons were detected using a secondary electron multiplier SEM-6M (VTC Baspik, Russia). During EEE measurements, the specimens were heated from the room temperature to 550 ºC at a rate of 10 ºC/min. Alongside the emitting surface of the specimens was irradiated with photons having an energy 4.67 eV. This energy was selected to be close to the electron work function of the tested material. These tests were performed by the University of Riga.

3.1 Result on Al-Si alloy

Intergranular tests results

The following images (Figure 3-4 and Figure 3-5) show the corrosion morphology of AlSi10Mg alloy in function of the heat treatment temperature for the both orientation of specimens, after the intergranular test.

The corrosion morphology is representative of the attacks that took place on all specimens. Preferential attacks at the melt pool borders can be evidenced especially for the XZ specimens. The depth of the attacks can be noticed by the metallographic sections. The specimens without any heat treatment did not show preferential attacks along the melt pools and the depth of penetration was negligible. The attack was deeper for specimens built at 35 °C compared to those built at 100 °C. This difference disappeared after the heat treatment. The samples heat treated at 200 °C showed penetrating attack along the border of the melting pools, which became deeper and wider on the specimens heat treated at 300 °C. Such penetrating attacks were evident on specimens built with the

base perpendicular to the building platform (XZ), whereas the attack on the XY planes achieved lower depth because they deviated through the different layers. During our intergranular tests, the corrosion attack took place on all building directions due to the fact that the specimens were fully dipped in the testing solution. However, the exposure of both XY and XZ polished specimens allowed for better analysis of the morphology of the attack and enhanced the preferential growth of the attack with respect to the melted pool border. On the specimens heat treated above 400 °C, marked general corrosion attack all the surfaces was observed independent of the building direction.[106]

AlSi10Mg specimen and building platform temperature 35°C		
	XZ	XY
No heat treatment	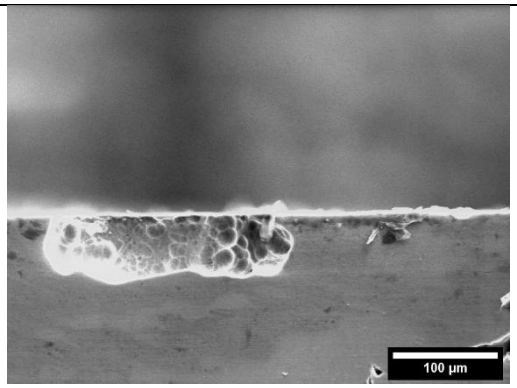	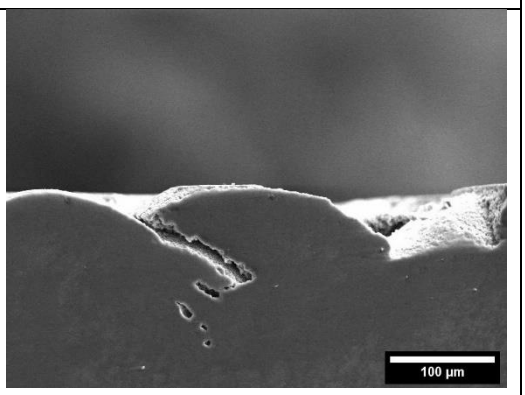
Heat treatment at 200°C	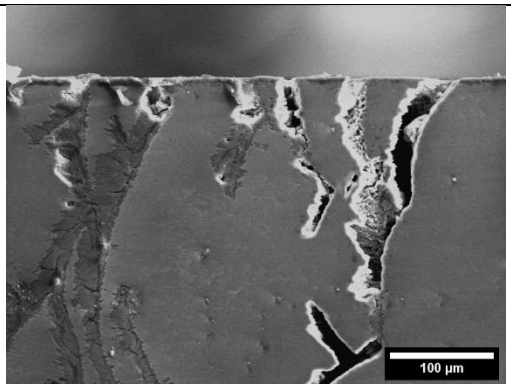	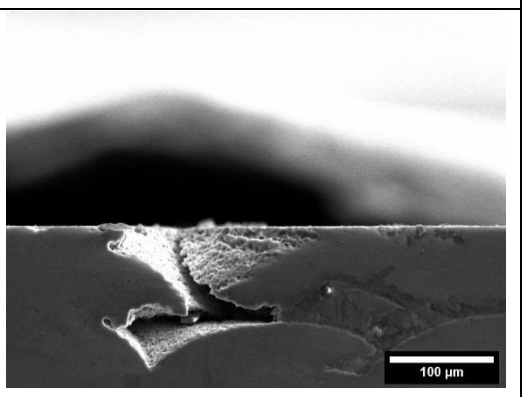

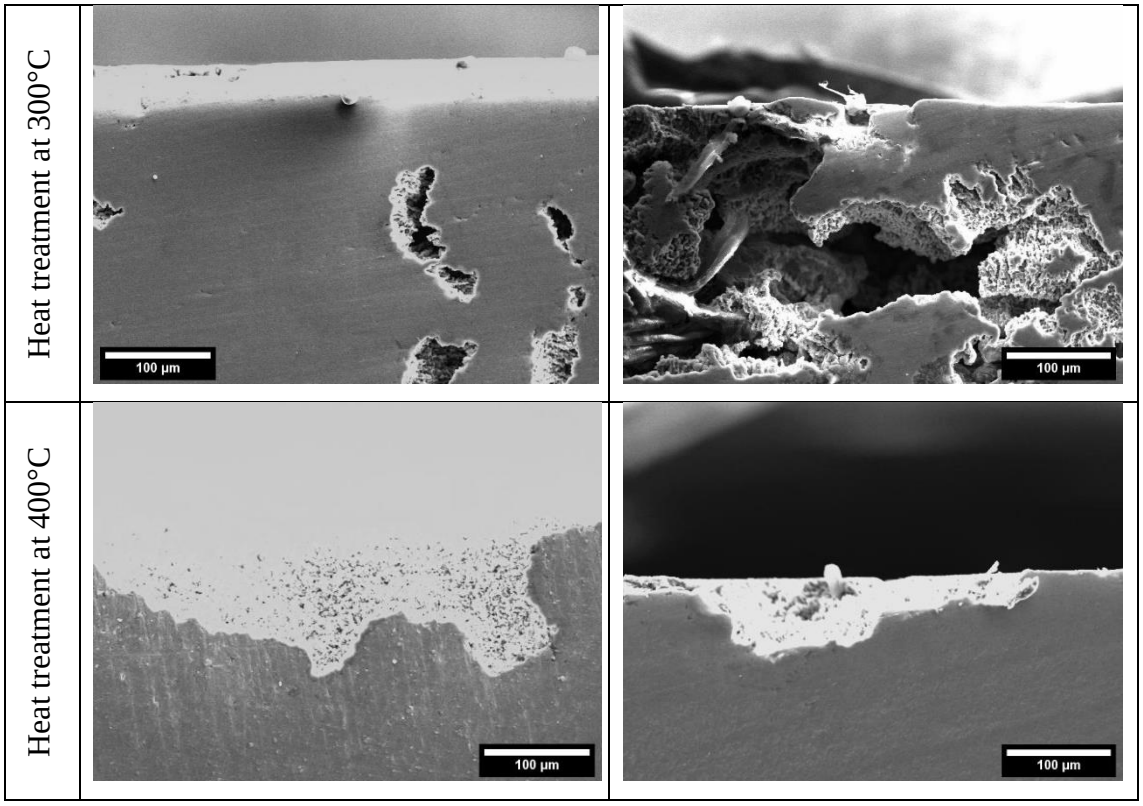

Figure 3-4: Metallography section of XY and XZ AlSi10Mg LPBF alloys (building platform set to 35°C) in acidified 30 g/L NaCl [61]

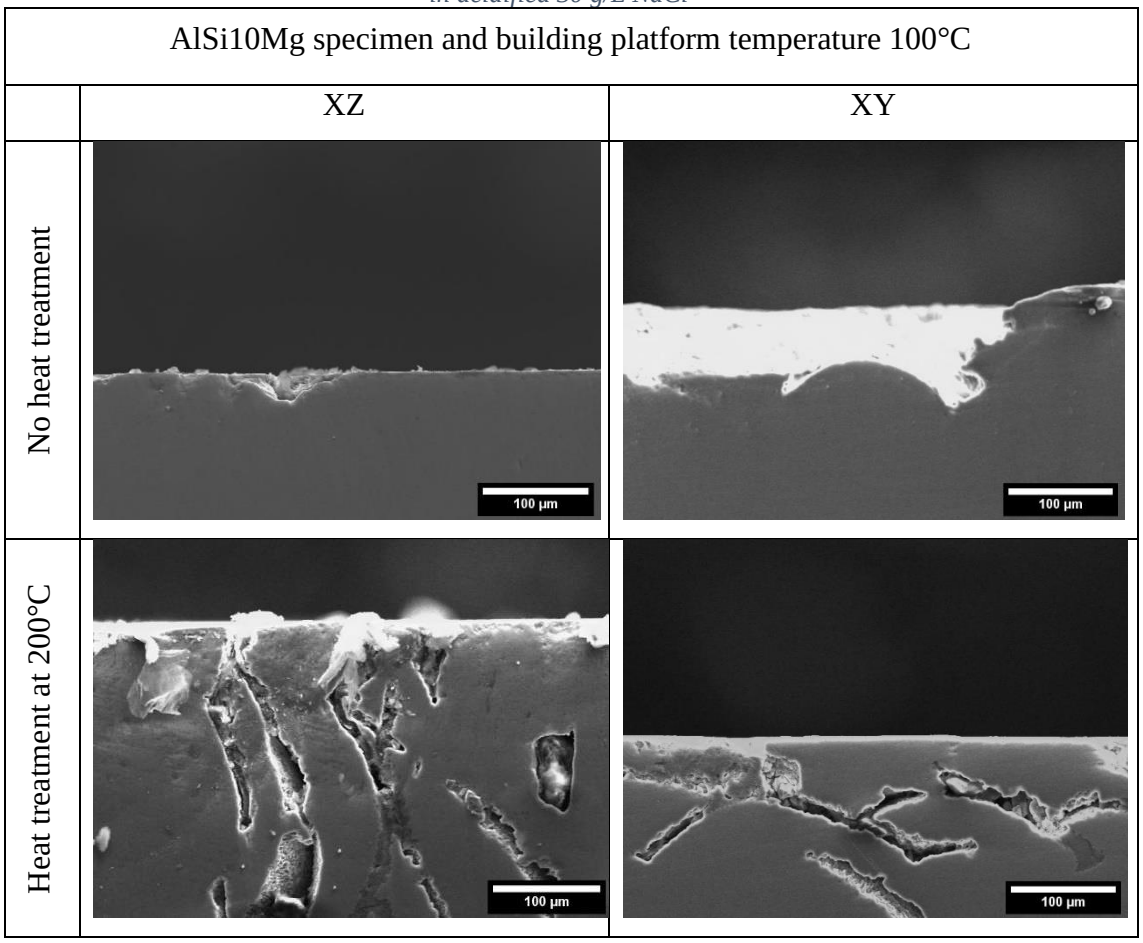

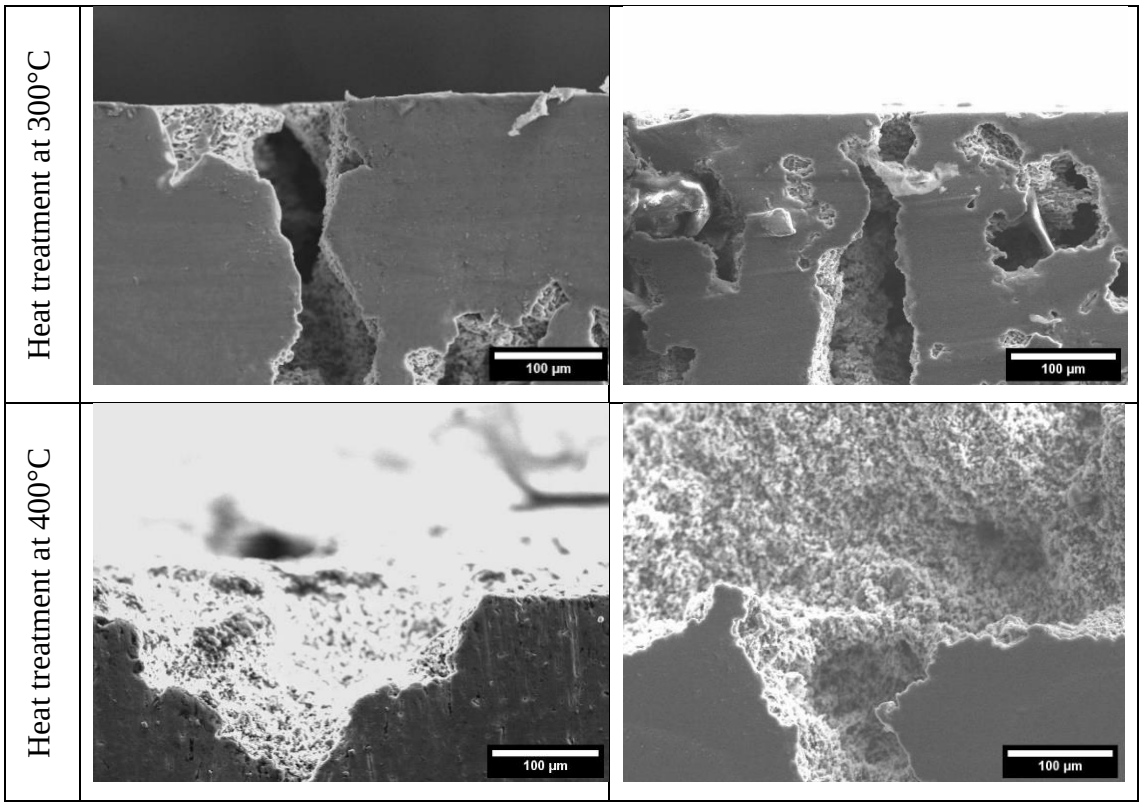

Figure 3-5: Metallography section of XZ and XY AlSi10Mg LPBF alloys in function of heat treatment temperature [61]

The Figure 3-6 reports the maximum depth of localized attack for the tested alloys as a function of metallurgical conditions – i.e. the post-processing heat treatment. Generally, the data confirmed as already descripted above.

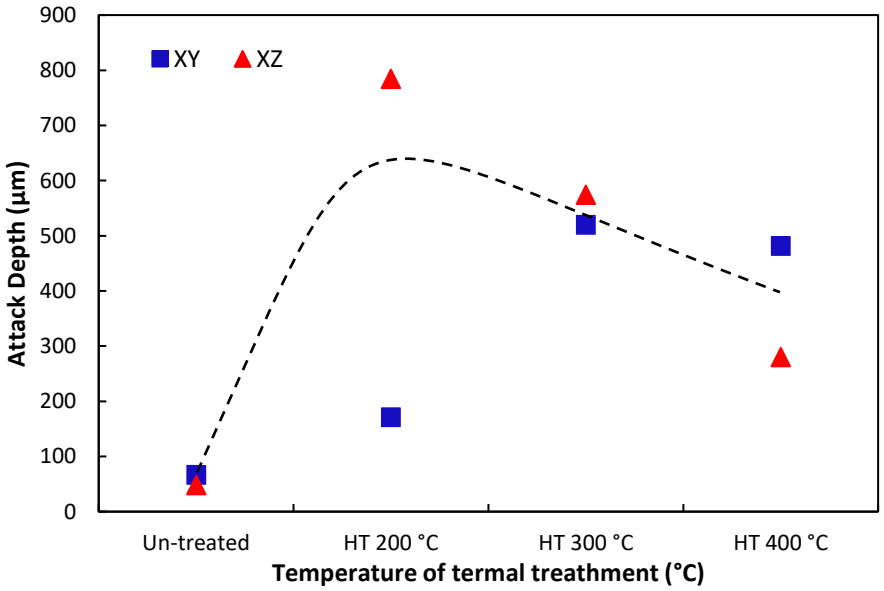

Figure 3-6: effect of post-processing heat treatment temperature on maximum localized corrosion depth of LPBF AlSi10Mg alloy[40]

Potentiodynamic tests

The potentiodynamic tests showed different trend in function of the chloride concentration, superficial condition and heat treatment temperature.

The tests on the as-built specimens were performed only using a 1 g/L NaCl solution. The Figure 3-7 and Figure 3-8 summarize the results, it was evidenced that the alloy almost had an active behaviour, with a corrosion potential close to -0.650 V *vs.* SCE for the XY specimens and between -0.750 V and -0.625 V *vs.* SCE for the XZ ones. The Figure 3-9 shows that the attack preferentially underwent along the border of the melt pools. Conversely, the specimens heat treated at 400°C presented a large damage.

The XY polished specimens showed corrosion potential between -0.475 V and -0.680 V *vs.* SCE in the solution with lower chloride concentration (Figure 3-10 and Figure 3-11). For the XZ ones in the same solution, E_{corr} was between -0.567 V and -0.715 V *vs.* SCE. The curves indicated a large range of passivity up to the anodic current increased rapidly indicating that the localized attack was started. The polished specimens immersed in the 35 g/L NaCl solution showed active behaviour for both orientations (Figure 3-12 and Figure 3-13).

The SEM analysis on the UT specimen highlighted a lot of attacks on the border of melt pools. The specimens heat treated at 200 and 300°C showed a pit attacks spread on different melt pools. The heat treatment at higher temperature showed large localized attack with an enrichment of silicon particles (Figure 3-14). Some curves and SEM images are reported in the Annex A.

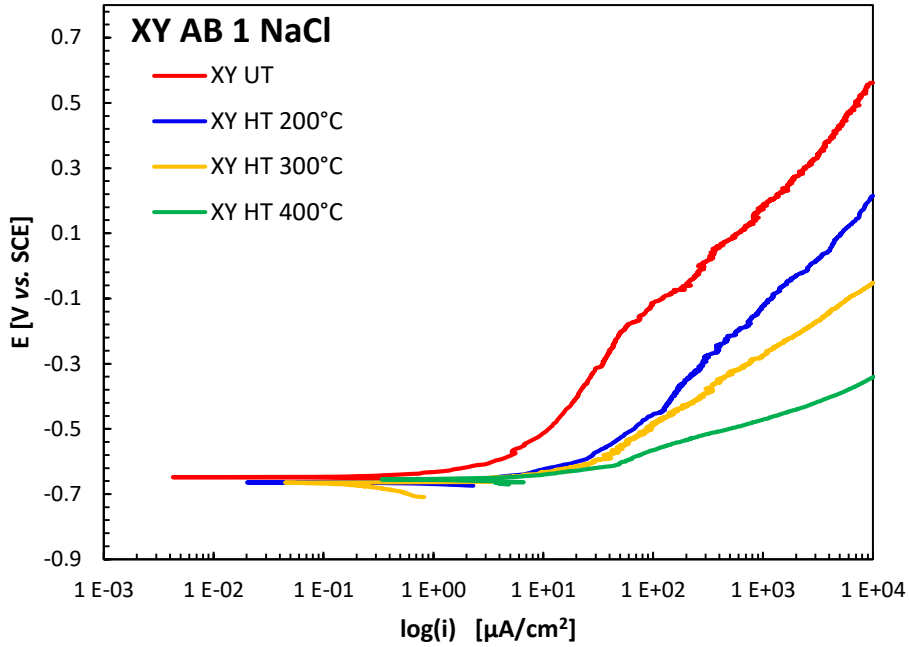

Figure 3-7: Potentiodynamic tests on XY as-built specimens in 0.5 g/L NaCl in function of the heat treatment temperature

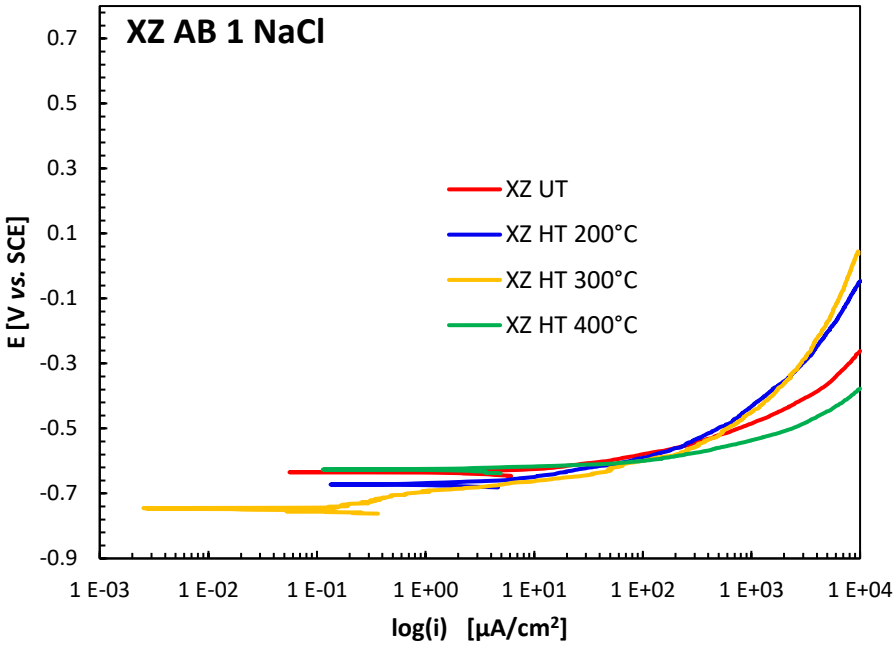

Figure 3-8: Potentiodynamic tests on XZ as-built specimens in 0.5 g/L NaCl in function of the heat treatment temperature

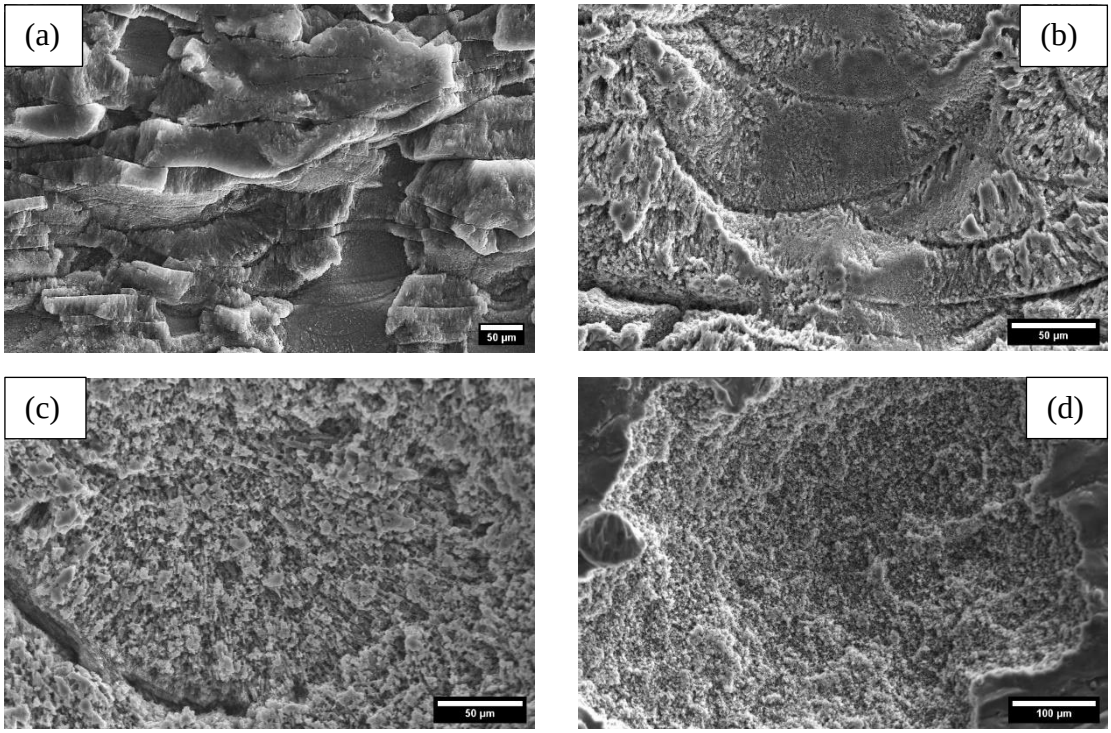

Figure 3-9: Localized attack on as-built surface exposed in 1 g/L NaCl for (a) the XZ un-treated specimen, (b) the XZ specimen heat treated at 200°C, (c) the XZ specimen heat treated at 300°C and (d) the XZ heat treated at 400°C.

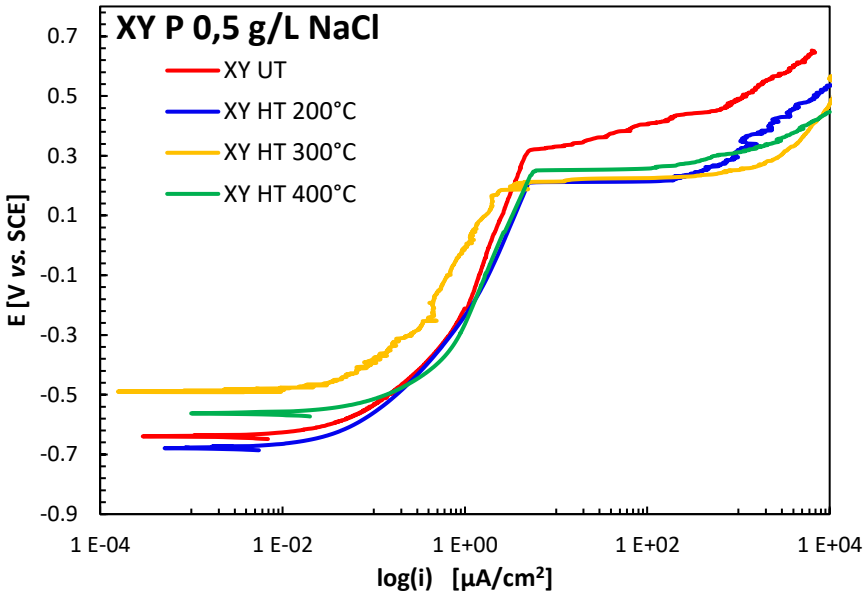

Figure 3-10: Potentiodynamic tests on XY polished specimens in 0.5 g/L NaCl in function of the heat treatment temperature

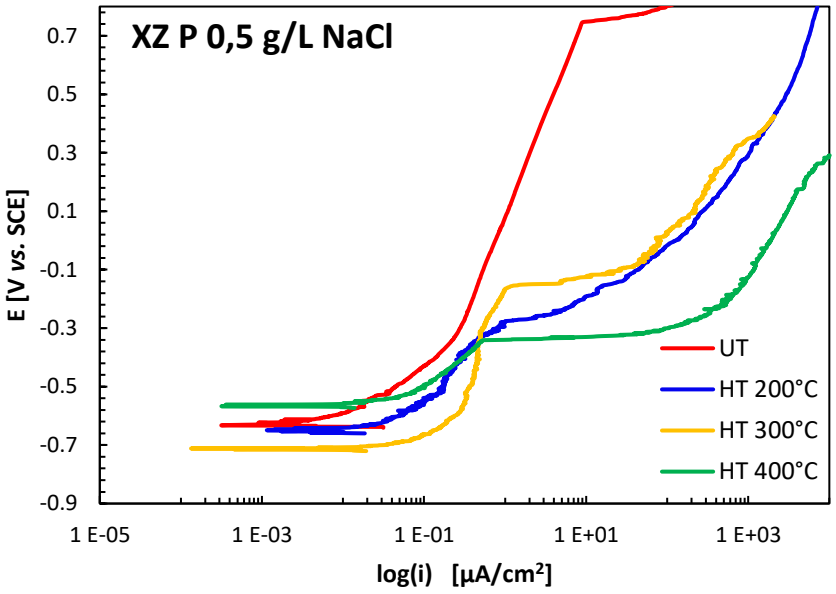

Figure 3-11: Potentiodynamic tests on XZ polished specimens in 0.5 g/L NaCl in function of the heat treatment temperature

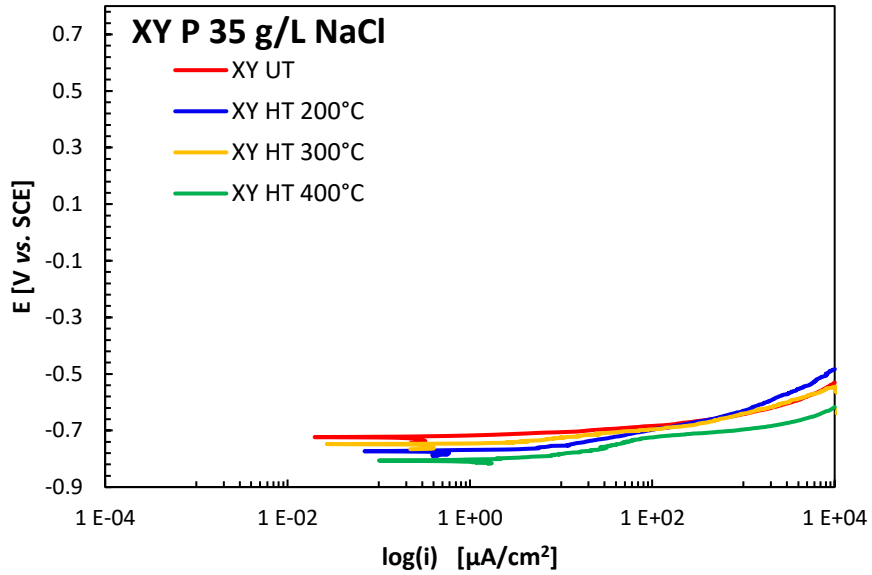

Figure 3-12: Potentiodynamic tests on XY polished specimens in 35 g/L NaCl in function of the heat treatment temperature

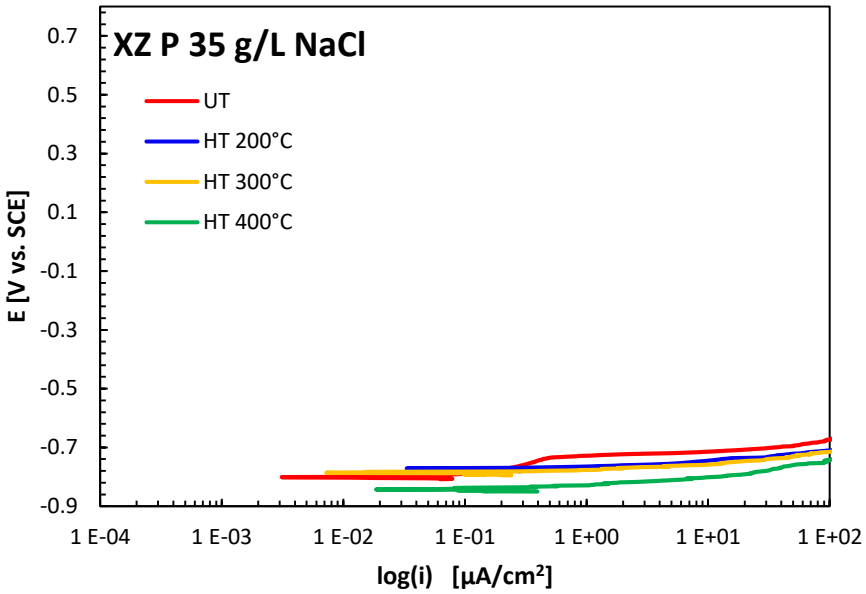

Figure 3-13: Potentiodynamic tests on XZ polished specimens in 35 g/L NaCl in function of the heat treatment temperature

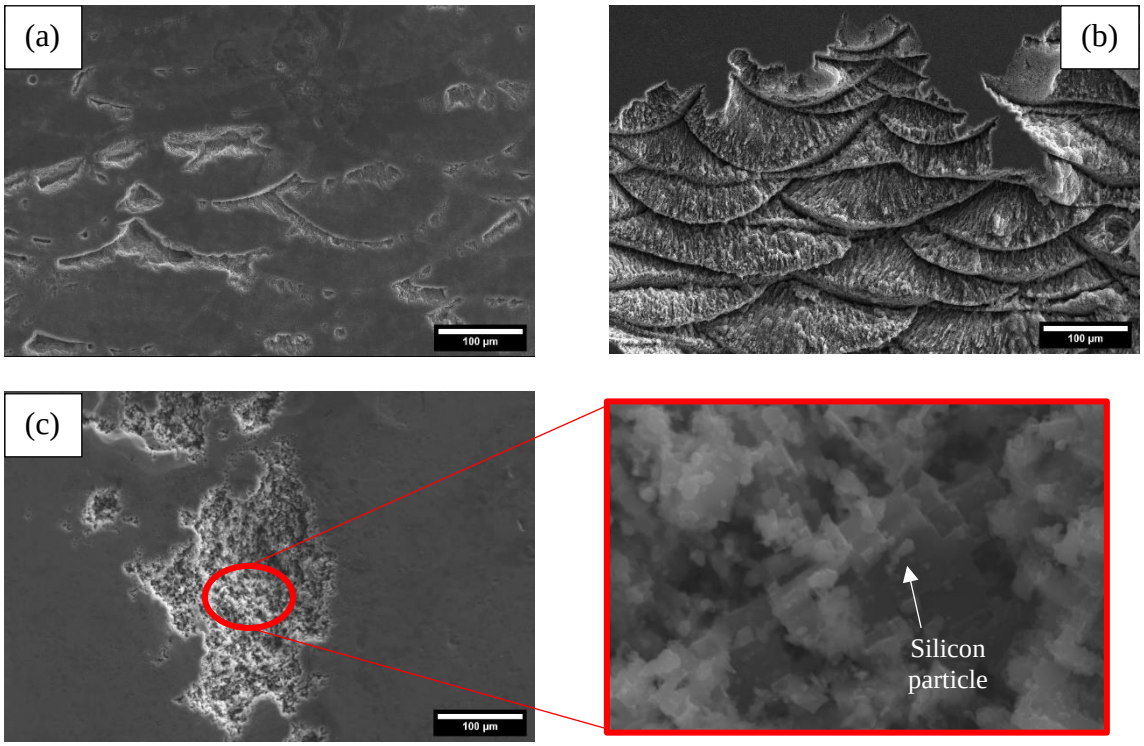

Figure 3-14: Localized attack in 35 g/L NaCl for (a) the XZ un-treated specimen, (b) the XZ heat treated at 200°C and (C) the XZ heat treated at 400°C.

Electrochemical Impedance spectroscopy

Figure 3-15 and Figure 3-16 show the EIS curves obtained on AlSi10Mg-XY specimens with as-built surface exposed to the solution with 1 g/L of NaCl. The trend of the curves at high frequencies denotes a similar constant value for all the specimens, decreasing the frequency, the specimens achieved a module value of 10000 Ωcm^2 for the UT and heat treated at 200°C and about 2200 Ωcm^2 for the specimens heat treated at 400°C.

It is possible note that increasing the heat treatment temperature, the phase peak was lowered and moved to higher frequencies. The XZ surface had similar behaviour.

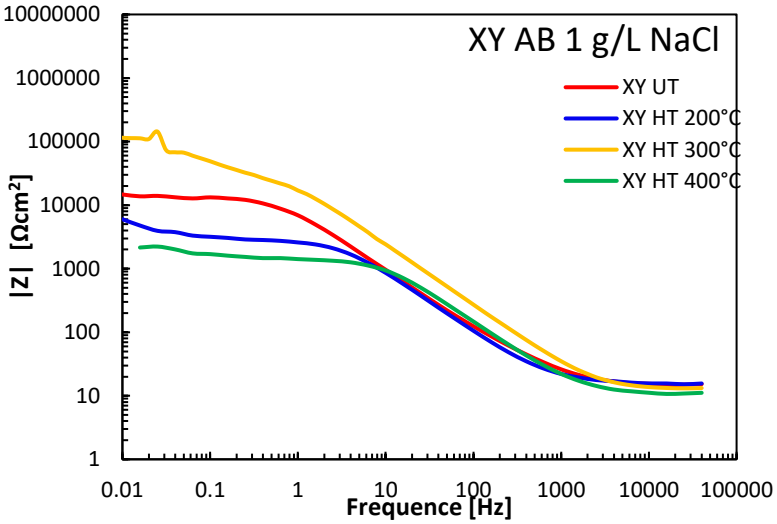

Figure 3-15: Bode-impedance diagram of XY AB specimens

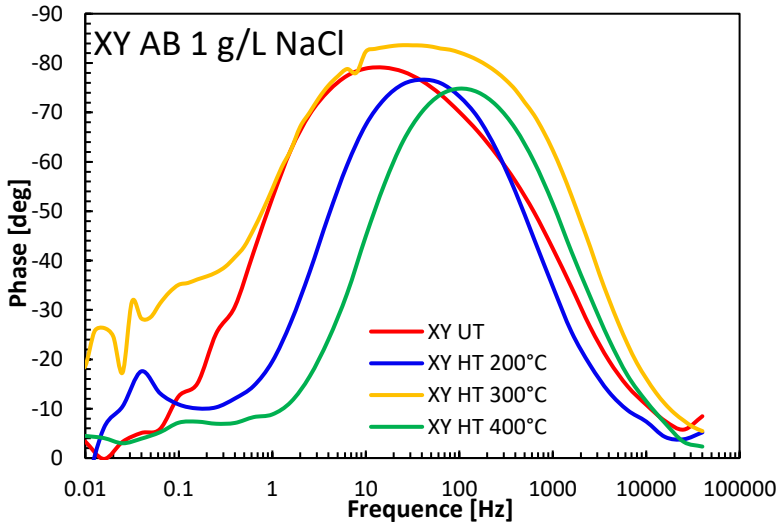

Figure 3-16: Bode-phase diagram of XY AB specimens

The Figure 3-17 shows the EIS spectra for the polished XY specimens in relation with the heat treatment temperature. Only one curve for each condition is reported in order to avoid confusion. In low chloride solution, the specimens with polished surface showed a trend that grow up to impedance value equal to $10^6\ \Omega cm^2$. The phase diagram showed a large peak that remain near to 90° for a long frequency period. Increasing the chloride content, the impedance modulus had a plateau at low frequencies achieving an impedance value equal to $10^5\ \Omega cm^2$. In high chloride solution (35 g/L NaCl) the impedance curves achieved $10^4\ \Omega cm^2$. The phase curves reduced the large peak achieving a value close to 0° at low frequencies.

A similar decreasing of the impedance modules at low frequencies was detected increasing the heat treatment temperature.

The XZ surface had similar behaviour and the curves are reported in the Annex A.

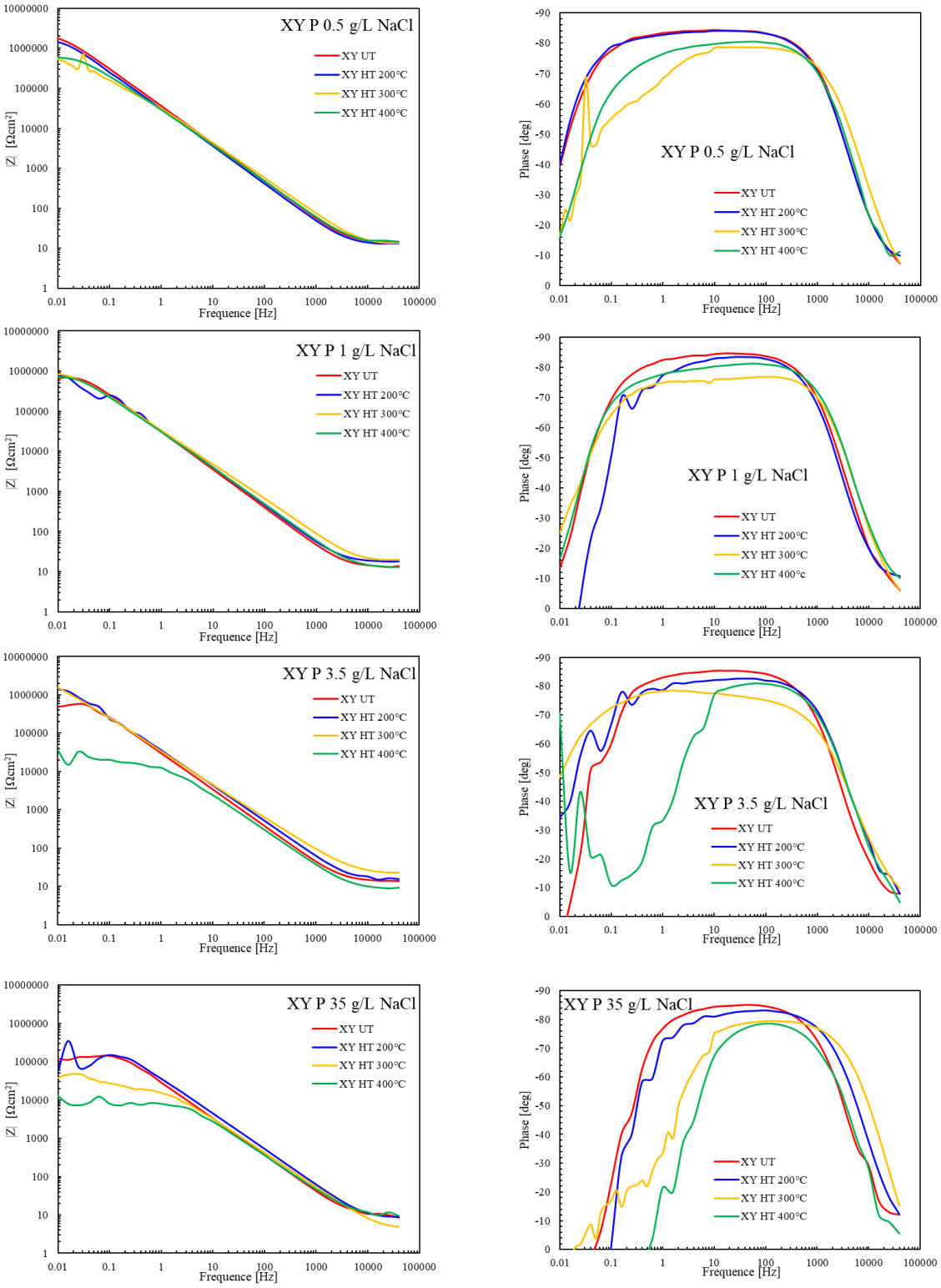

Figure 3-17: Bode diagram of XY P specimens in function of chloride content

Microstructural and mechanical characterization

Figure 3-18 shows the microstructures of the XY and XZ specimens as a function of the heat treatment. The melt pool microstructures were maintained up to 400 °C heat treatment temperature. At 300 °C, the edge of the melting well was more clearly marked, and there were also isolated silicon clusters. By increasing the heat treatment temperature up to 400 °C, the melt pool practically disappears, and α-Al matrix was present with dispersed silicon particles located at the old edge of the melt pool.

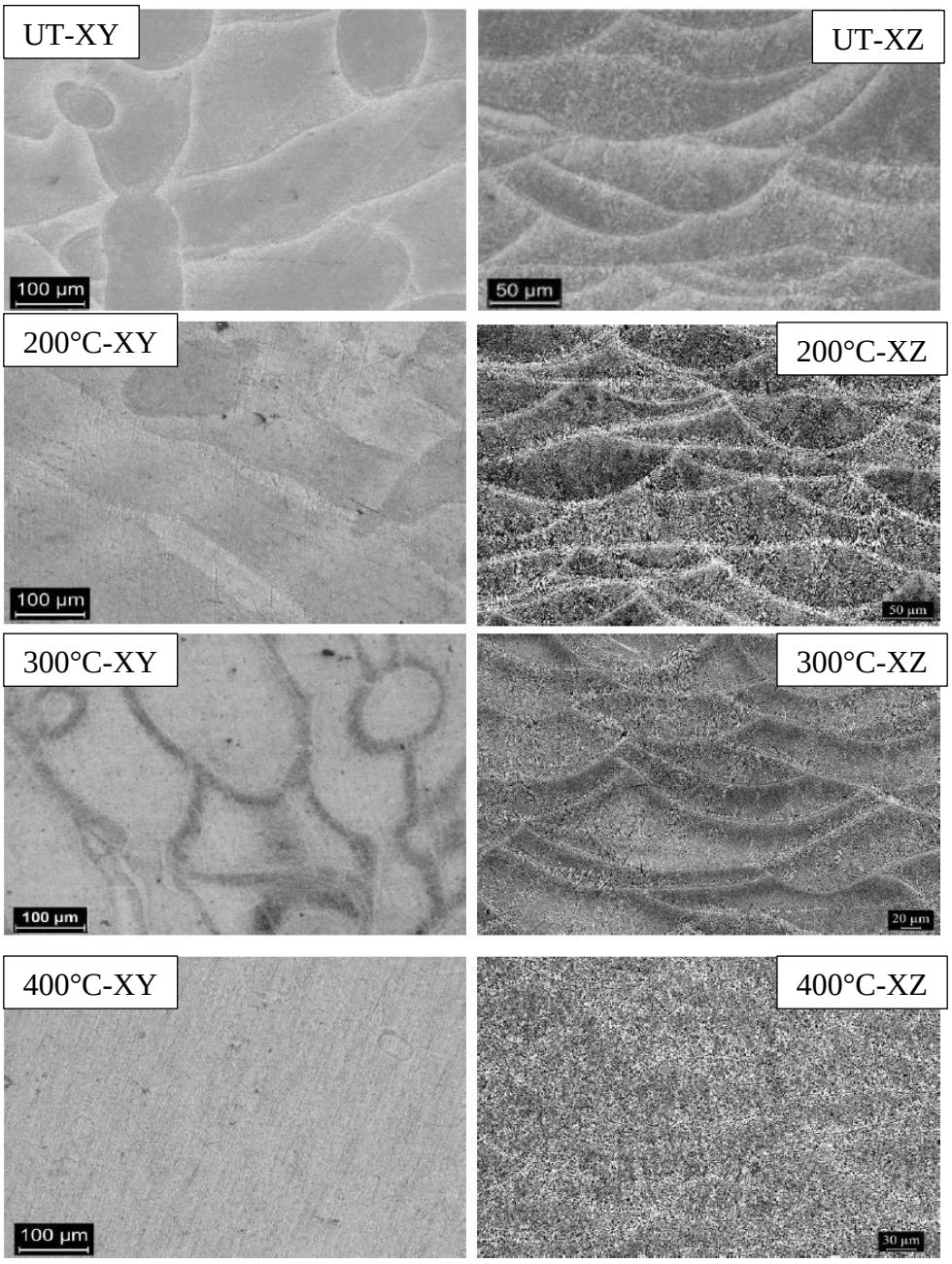

Figure 3-18: Optical images of microstructure for XY & XZ after etching in function of heat treatments [106]

The Figure 3-19 shows the micro-hardness values obtained using 100 g of load. The specimen hardness decreases as temperature increases, regardless the building platform temperature or the building plain. The minimum value was achieved after the heat treatment at 400 °C for 2 hours.

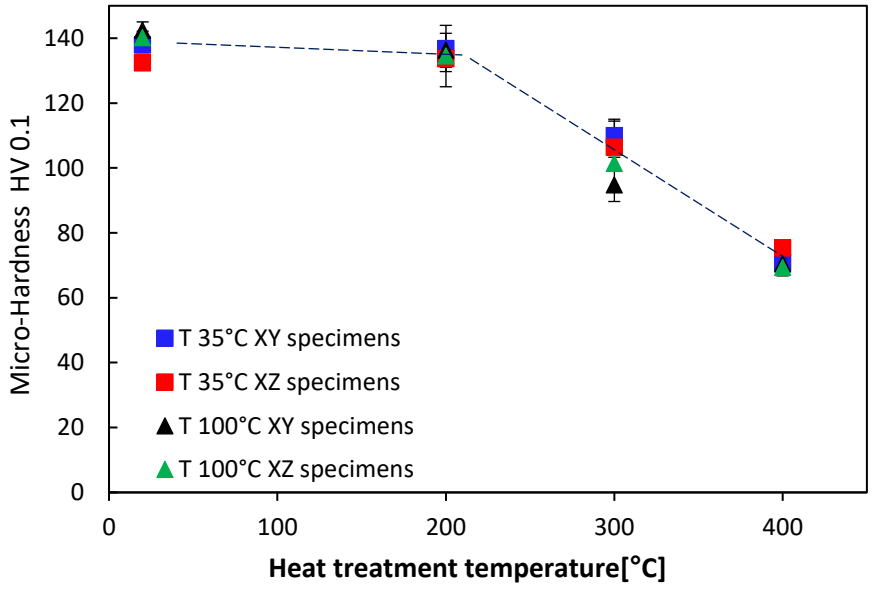

Figure 3-19: Effect of heat treatments on AlSi10Mg microhardness

Scanning kelvin probe force microscope

The result of analysis by SKPFM on XZ UT specimen highlight the typical microstructure formed by melt pools. The melt pool border showed a lower Volta potential than the centre, indicating its anodic behaviour. After the heat treatment at 300°C the different between the centre and the border stay high; the border of the melt pool is still visible. Conversely, the heat treatment at 400°C uniformed the microstructure removing the melt

pools track. The Volta potential map underlined a more homogeneous distribution of potential due to the heat treatment (Figure 3-20).

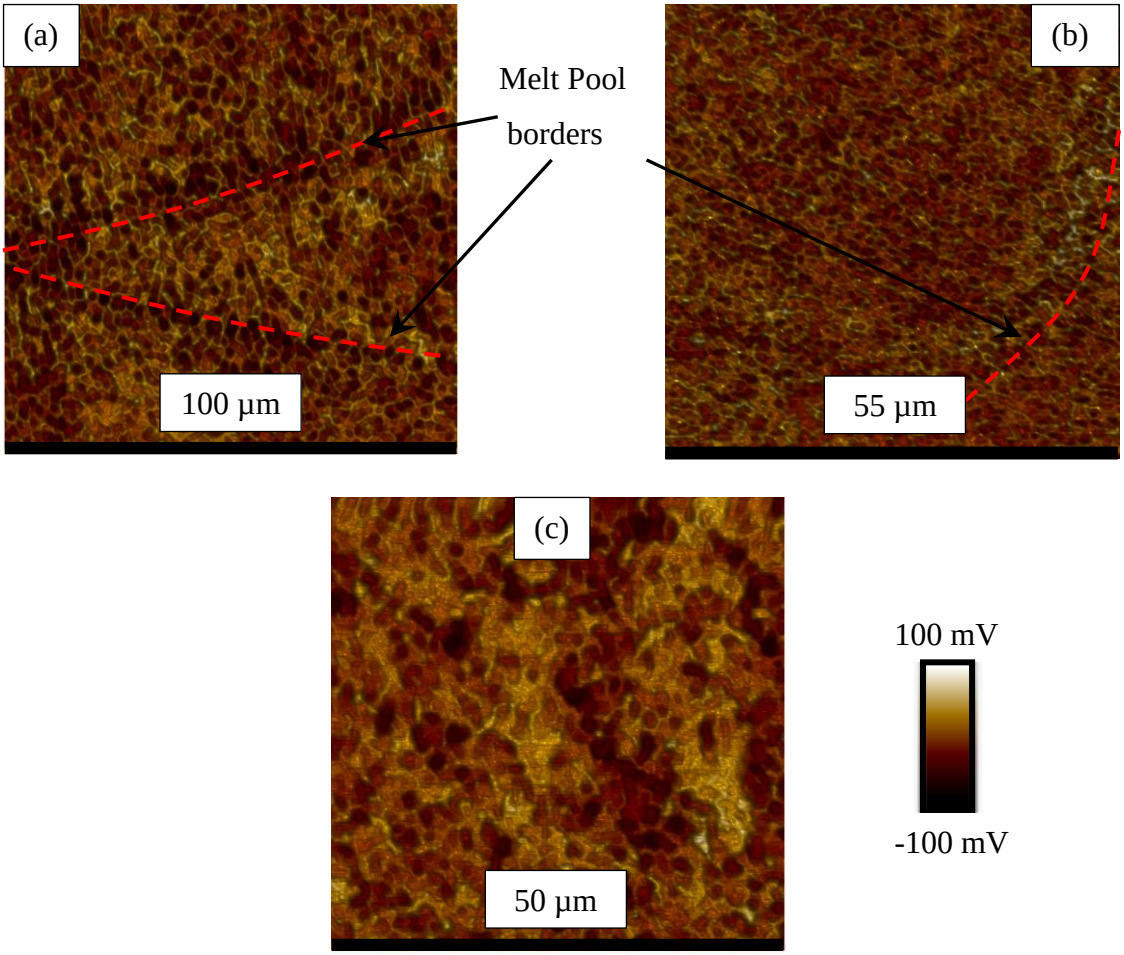

Figure 3-20: SKPFM Volta potential maps for (a) XZ UT, (b) XZ HT 300°C and (c) XZ HT 400°C

Exo-electron emission test

Figure 3-21 shows the effect of heating on the exo-electron emission of the specimens with different heat treatments. The EEE of the not-thermally treated specimens starts from 200 °C and increases with increasing of the temperature. The heat-treated specimens, on the other hand, begin to weakly emit exo-electrons from 250 °C. The specimens stress relieved at 300 °C for 2 hours have an emission peak at about 420 °C. The specimens heat treated at 400 °C maintained a very low emission.

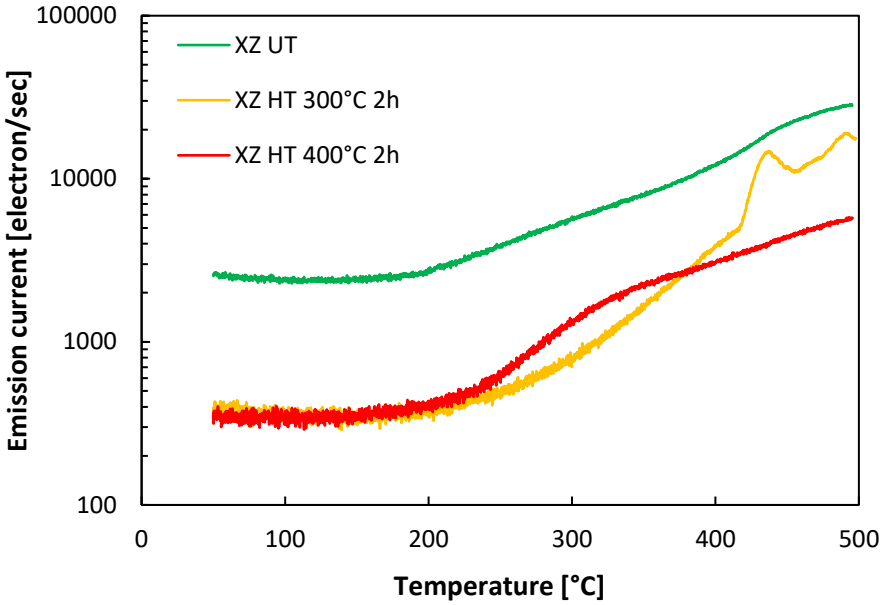

Figure 3-21: Exo-electron emission curves in function of the post processing heat treatment temperatures

3.2 Corrosion mechanism of aluminium

The aluminium alloy is a passive metal with a stable oxide film that have a high impedance. This oxide film is stable in a range of pH between 4 and 9 as reported by the Pourbaix diagram (Figure 3-22).

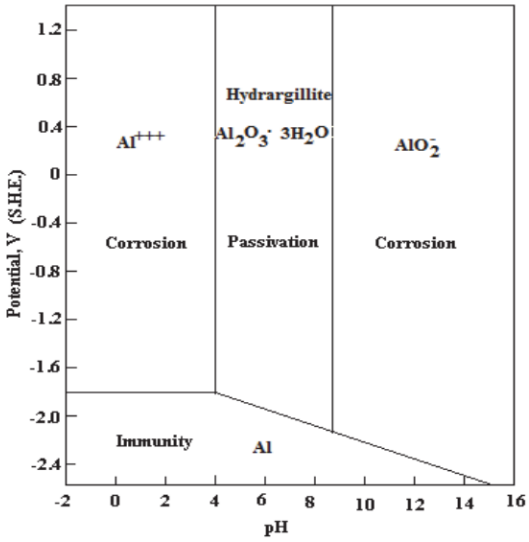

Figure 3-22: Pourbaix diagram for aluminium[107]

However, the localized corrosion can occur during the exposure at the chloride solution. The low reverse potential of aluminium does not allow the re-passivate process leading to high corrosion rate regardless the pH due to the hydrogen cathodic reaction. The second

phases have a main role in the corrosion behaviour that can be anodic such as cupper, iron silicon rich phases or cathodic such as magnesium or zinc.

The corrosion mechanism of pure aluminium in chloride solutions has been described in numerous studies.[83,108–112] According to the McCafferty model,[110,113] the surface of the aluminium passive film assumes a positive charge when it is immersed in a solution with a pH lower than the zero point of charge of its oxide (≈ 8.9–9.2), according to Eq 3.1

$$Al(oxide)OH + H^+ \rightleftarrows Al(oxide)OH_2^+ \quad [3.1]$$

In this reaction, Al(oxide) indicates the metallic Al and the adjacent oxide layer, while OH represents the outer layer of oxide surface hydroxyl groups. The positive charge of the passive film attracts chloride ions from solution, as shown in Eq. [3.2], where n is the number of chloride ions interacting with the surface.

$$Al(oxide)OH_2^+ + nCl^- \rightleftarrows Al(oxide)OH_2Cl_n^{-n+1} \quad [3.2]$$

These ions diffuse for a second time inside the oxide via oxygen vacancies ($V_{O^{\cdot\cdot}}$), according to the reaction:

$$Al(oxide)OH_2Cl_n^{-n+1} + nV_{O^{\cdot\cdot}} \rightarrow Al[n(Cl_{O^{\cdot}})(oxide)]OH_2^+ \quad [3.3]$$

In Eq. [3.3], $Cl_{O^{\cdot}}$ represents the ions occupying the oxygen sites in the oxide lattice and Al $[n(Cl_{O^{\cdot}})(oxide)]OH_2^+$ is the oxide film on the aluminium side where the diffusion of chloride ions takes place; the aluminium at the metal oxide interface is involved in a three stage process, losing three electrons, as described by the overall reaction [3.4]:

$$Al[n(Cl_{O^{\cdot}})(oxide)]OH_2^+ \rightleftarrows Al^{3+}[m(Cl_{O^{\cdot}})(oxide)]OH_2^+ + (n-m)Cl^- + 3e^- \quad [3.4]$$

Frankel[108] demonstrated that the stable propagation of the pit occurs when critical environmental conditions occur that no longer allow repassivation of the metal. Chloride ions prevent repassivation; a critical concentration of Cl^- in the film is therefore necessary to allow propagation of the pit. The total current density (i_a) of the anodic process can be written as a sum of two terms, as shown in Eq. [3.5], where i_u is the current density of the process that takes place uniformly over the passive surface and i_{pit} is the contribution from the formation of localized pits

$$i_a = i_u + i_{pit} \quad [3.5]$$

In addition to transient phenomena related to the potential scanning rate, i_u corresponds to the passivity current. The term i_{pit} is zero under passive conditions, while it assumes a non-zero value when the potential (E) exceeds the pitting potential (E_{pit}) and the attack is initiated. During the propagation phase of pitting corrosion, i_{pit} is significantly larger than i_u. Considering the equilibrium conditions for the reaction shown in Eq. [3.4], McCafferty [109] proposed a relationship between E_{pit} and a_{Cl^-}, valid at constant pH:

$$\left(\frac{dE_{pit}}{dlog[Cl^-]}\right)_{pH} = \frac{-n}{\frac{5}{2}\cdot\left(\frac{E}{2.303RT}\right)} = constant \qquad [3.6]$$

This relationship was verified by observation of a linear trend when plotting the relevant experimental variables on a semi logarithmic scale in several previous studies.[6,113,114] According to Eq. [3.6], the gradient of E_{pit} *vs.* a_{Cl^-} is proportional to the number of chloride ions, n, diffusing into the oxide via oxygen vacancies, following Eq. [3.2] and [3.3]. According to this model, the different gradients are due to the different concentrations of chloride ions required to initiate pitting, where higher slopes correspond to a greater resistance to the initiation of pitting. This relationship is used to study the different parameters that characterize the corrosion behaviour of the aluminium alloy obtained by means of LPBF technology.

3.3 Effect of surface finishing on the pitting potential of AlSi10Mg

Figure 3-23 shows the pitting potentials as a function of the chloride ions activity of the AlSi10Mg specimens after stress relieving at 300°C for 2 hours, with as build surface (AB) (printing and post processing heat treatment) and polished (P) surfaces. The heat treatment at 300°C for 2 hours is the stress relieving treatment suggest to EOS company. The chloride activity is calculated according to Dash et al[115] (Table 3-2). As a matter of fact, the McCafferty model was developed for pure aluminium, whilst AlSi10Mg alloy contains silicon particles more noble than the Al matrix, the linear relationship proposed by McCafferty[109] seems not to strictly fit the data due to relevant scattering.. The galvanic effect of cathodic precipitates promotes pitting and the variations in the local pH caused by the cathodic reaction can affect the passive film stability of aluminium.

The pitting potential can be determined only in the case in which the localized corrosion initiates during the potentiodynamic test after a clear initial passive state. This condition

was observed only for the P specimens at really low chloride concentrations under such circumstances. The experimental pitting potential values (Figure 3-23) decreases with the increasing of the chloride ion activity.

Conversely, when the pitting early initiates during the equilibration time at the beginning of the test, the pitting potential cannot be estimated from potentiodynamic test. The free corrosion potentials for the curves having almost active behaviour are also showed. This condition was observed at very high chloride activity for one P specimen (of a total of three) at a_{Cl^-}=0.05M and for all the P specimens tested in solutions of a_{Cl^-}=0.34 M. The values of these specimens overlapped the trend of the AB specimens, which always showed initiation of pitting during the equilibration time, before starting the potentiodynamic scan.

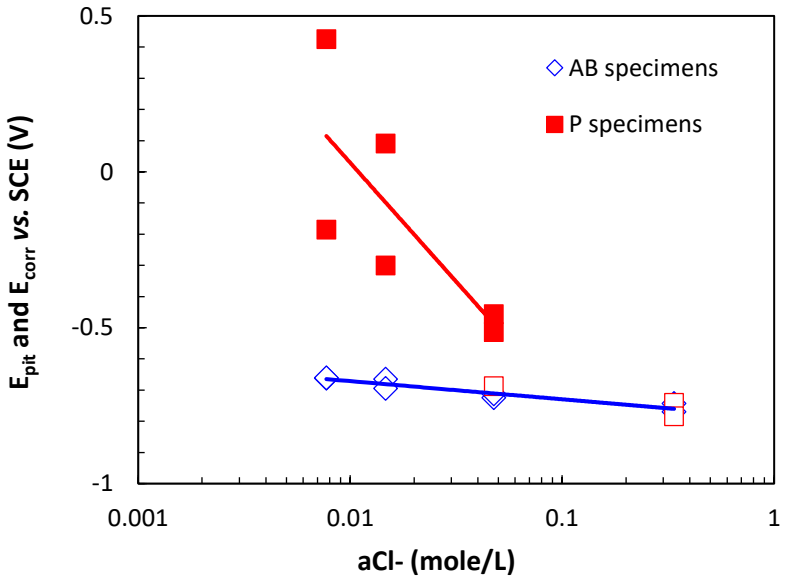

Figure 3-23: Effect of chloride ion activity on the pitting (full symbols) and corrosion potential (empty symbols) of P and AB specimens -heat treated at 300°C- in an aerated NaCl solution at 23 °C. The corrosion potentials were measured when pitting started during the equilibration time, before the potentiodynamic tests.[116]

Table 3-2: Activity of chloride ions

NaCl (g/L)	NaCl (mol/L)	γ_{Cl^-}	aCl- (mol/L)
35	0.6	0.563	0.34
3.5	0.06	0.785	0.05
1	0.02	0.858	0.015
0.5	0.01	0.962	0.008

The higher resistance to the initiation of localized corrosion of the P specimens compared with the AB ones was confirmed by analysis of the of the polarization resistance (Rp) values measured in the range of ± 10 mV *vs.* E_{corr}. The value i_a (Eq. (5)) was calculated, as shown by Evans and Koehler[117] using the Stern–Geary relationship and the polarization resistance:

$$i_u = \frac{k}{R_p}$$

Here, k can be evaluated using the slopes of the polarization curves of the anodic (b_a) and cathodic (b_c) process using the following relationship:

$$k = \frac{b_a b_c}{2.3(b_a + b_c)}$$

If the alloy is passive, the slope of the anodic polarization curve is much higher that of the cathodic one, which was ≈120 mV/decade and coincided with that of the hydrogen cathodic process. This resulted in a k value of 52 mV. In this case, i_{pit} did not contribute to the total anodic current, and i_a coincided with i_u. Figure 3-24 shows the corresponding i_u values as a function of a_{Cl^-} for the P specimens that remained passive during the equilibration time. On the contrary, for the AB specimens, for which the pitting was initiated during the equilibration time, the value of the current density measured by means of the Rp gave the value for i_a (see Eq [3.5]). In this case, a k value of 26 mV/decade is adopted, consistent with an active corrosion process. A linear correlation between i_a and a_{Cl^-} was also observed, with values one order of magnitude higher than those of the P samples. This difference can be ascribed to the difference in the exposed areas (due to the higher roughness of the AB specimens compared to the P specimens), and to the contribution of the active dissolution of the alloy inside the pit.

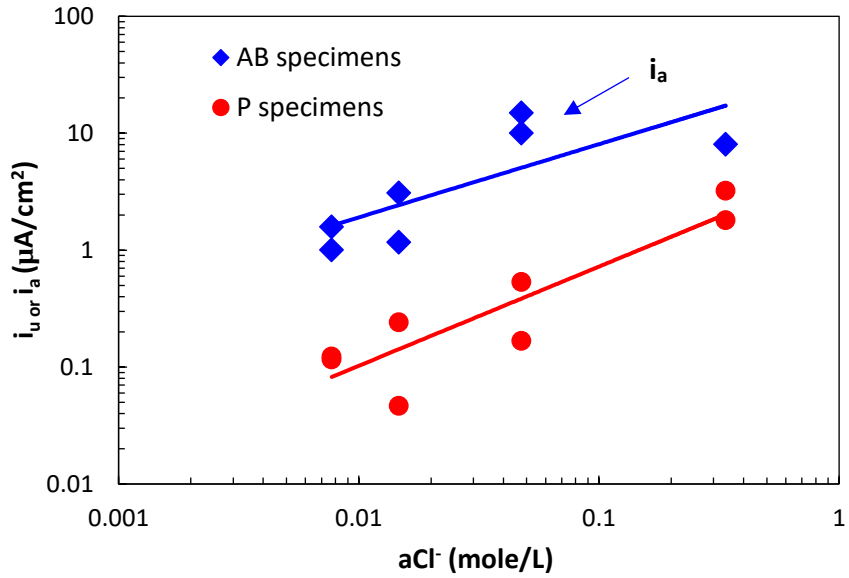

Figure 3-24: Effect of chloride ion activity on the current density i_u of P samples heat treated at 300°C and $i_a=(i_u + i_{pit})$ for AB specimens, evaluated using the polarization resistance.[116]

The different behaviours of the P and AB specimens can be explained considering the different passive film properties, where the former was spontaneously formed in air, and the latter formed during processing and subsequent heat treatment. During the LPBF process, the oxide film was initially formed during solidification in the argon chamber, in an environment with a very low oxygen partial pressure. Subsequently the oxide film grew during the heat treatment – performed in air – used to reduce the residual internal strains introduced during processing. Polishing removed the oxide film present on the AB specimens, which allowed reformation of a film more resistant to the action of the chlorides. Furthermore, as the surface roughness was reduced, the number of critical sites for pitting initiation also decreased. However, polishing cannot completely eliminate residual pores on the surface, which act as preferential sites for pit initiation. The onset of pitting at these sites can explain the experimental data that deviates from the usual behaviour of the polished surface, approximating those obtained on the unpolished as-built surface, as the internal porosity of the P specimens with the passive film was the same as that of the AB specimens.

The composition of the oxides formed on AB and P specimens was investigated using XPS (Figure 3-25 and Figure 3-26).[6]

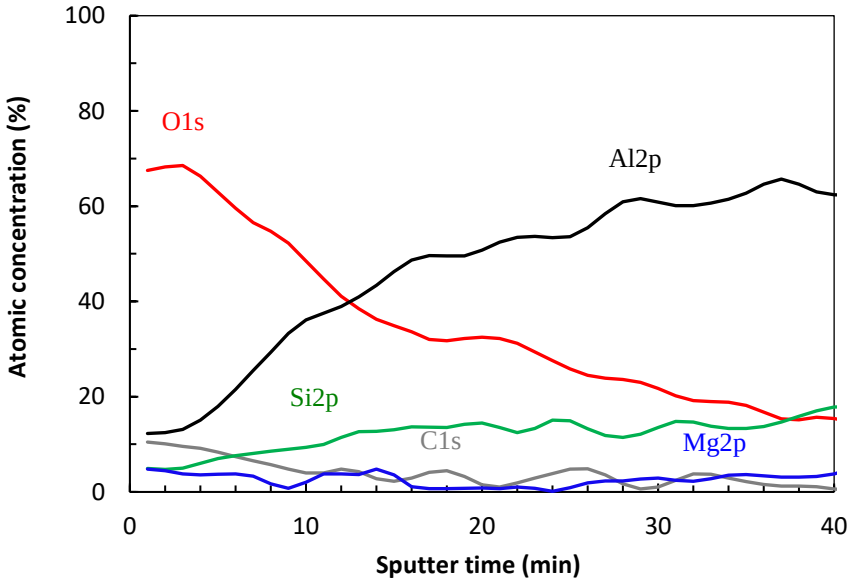

Figure 3-25: XPS spectra measured during milling of the oxide films on the AB specimens.[6]

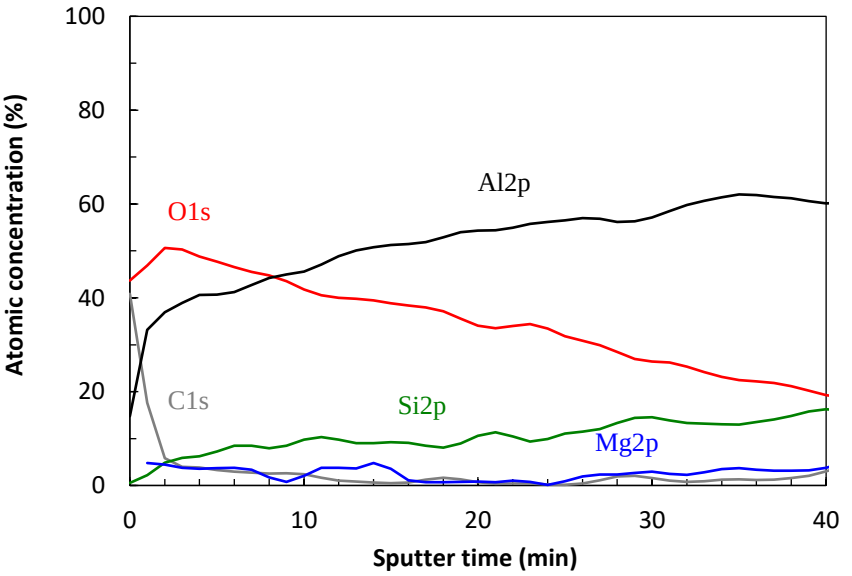

Figure 3-26: XPS spectra measured during milling of the oxide films on the P specimens. [6]

The surface oxides on the AB and P samples had different compositions, but they maintained the same acid–base properties, as noted by Van den Brand et al[117], as oxides formed spontaneously in air or oxidized at high temperature. According to Pech-Canul et al.[118] the oxide formed on the Al-12% alloy incorporates silicon and silicon oxide particles, which makes it more resistant to pitting initiation than pure Al. These particles inhibit chloride from penetrating and diffusing through the film. However, in this case, although the alloy had a Si concentration of ≈10%, significant concentrations of Si were not observed either in the passive film present on the AB specimens, nor in the oxide

spontaneously formed on the P specimens. Vargel[119] described the spontaneous oxide formed in air on Al surfaces as consisting of two layers. The inner layer of about 4 nm thick, present at the metal–oxide interface, acts as a barrier against corrosion, is compact, amorphous, and forms immediately upon contact of the metal surface with air, regardless of the temperature. Its kinetics of formation does not depend on the oxygen partial pressure, while the thickness of the second layer of the film depends on temperature. The latter grows on the barrier layer as a result of the hydration reaction with atmospheric moisture. The final thickness is reached only after several weeks, sometimes even months, and depends on the environment. High-temperature treatment modifies the morphology of the passive film, increasing its thickness and crystallinity, while increasing the porosity and producing microcracks, which decrease the corrosion resistance compared to amorphous films. Such mechanisms may explain the lower E_{pit} values observed for the AB specimens compared to the P specimens.

3.4 Effect of heat treatment on corrosion behaviour of AlSi10Mg

The previous paragraphs report the results about the electrochemical tests in function of the heat treatments. Only the polished surface is considered in order to highlight the effect of microstructure. Figure 3-27 shows pitting potential for the potentiodynamic anodic polarization curves having a clear range of passivity as function of the activity of chloride ions. The free corrosion potential values for the curves having almost active behaviour are also showed.

For the UT condition, the pitting potential values decrease as the chloride activity increases. At the highest chloride ions activity, it approaches free corrosion potential because localized attack initiated since early immersion. After the heat treatment, the specimens show a similar behaviour, but with lower pitting potentials, showing scattering data. The heat treatment at high temperature lead to an active behaviour for concentrations over 0.008 mol/L.

Despite data are very scattered, a logarithmic correlation between pitting potential and activity of the chloride is clearly defined. Such a correlation is emphasized by the model proposed by McCafferty[109]. However, the results show a slope that differs from the value estimated by McCafferty for pure aluminium.

The effect of heat treatment on the corrosion behaviour is underlined in the Figure 3-28, which reported the pitting potential and the free corrosion potential at the lowest chloride ions activity – 0.008 mol/L – as a function of heat treatment temperature.

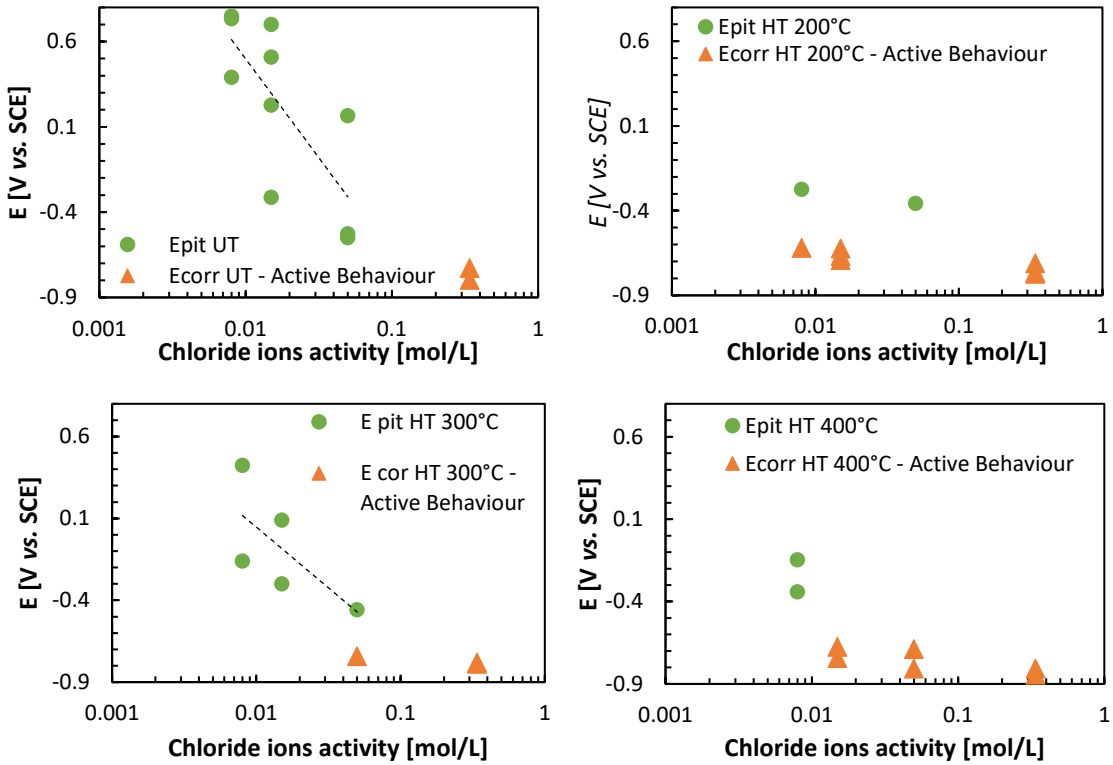

Figure 3-27: Free corrosion potential and pitting potential of LPBF specimens after different heat treatment in relation with the activity of chloride ions.[120]

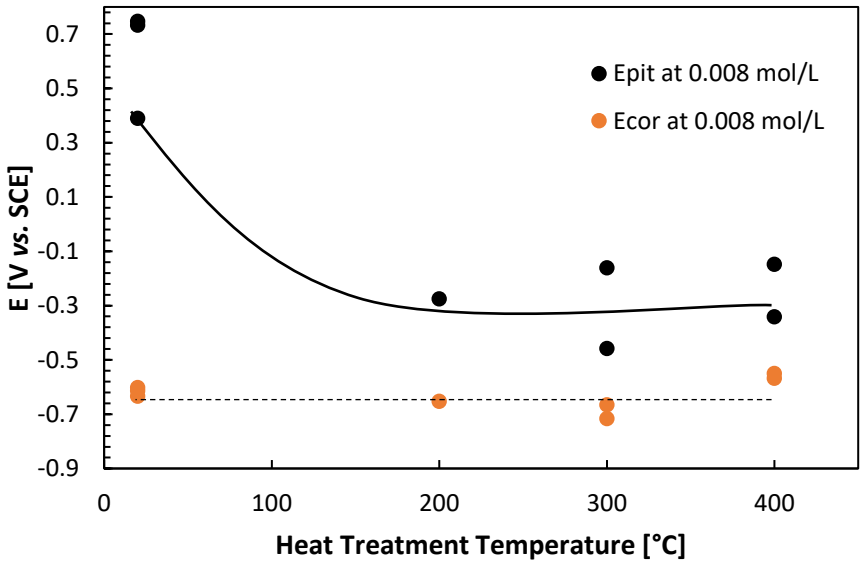

Figure 3-28: Effect of heat treatment on the pitting potential at chloride active equal to 0.008 mol/L[120]

The specimens heat treated in the range 200-400° C for 2 h show a reduction of pitting potential with respect to the UT specimens, with values that approach the free corrosion potential. The lowering of pitting potential denotes a reduction of resistance to localized corrosion after the heat treatment at temperature usually considered for stress relieving.

In order to evaluate post processing heat treatment effect, the stochastic nature of pitting initiation requires a statistical approach,[121] it was done for stainless steels, [122] copper,[123] nickel[124] and aluminium alloys.[125,126]

The scattering minimization was performed maintaining the chloride concentration constant at the value of 0.02 M that allow a large passive range for most specimens permitting the evaluation of pitting potential. A population of 8 specimens for each condition (heat treatment and building direction) was used. In order to analyse the initial conditions of the specimens, between the corrosion potential monitoring and the potentiodynamic tests, the EIS spectra was performed.

The EIS spectra are similar for all the specimens immediately after dipping into the solution. The low-frequency impedance modulus is high, and the phase angle is approaching zero degrees, thus indicating stable passive conditions. Although it does not correspond to the polarization resistance of the specimen, the difference between the impedance modulus at low and high frequencies can nevertheless allow one to estimate the order of magnitude of the oxide resistance and, so, to the protection conferred by the protective film. Figure 3-29 shows these values for different heat treatments. For most specimens, this difference in impedance modulus is between 10^5 to 10^6 Ωcm^2 regardless of the building direction and heat treatment. Such high values indicate the absence of active zones of corrosion. In other words, the just-dipped specimens showed similar values of the impedance modulus regardless of heat treatment and building direction, because the mechanical polishing eliminated any differences in the passive film on the surface, and the oxidation at air formed the same protective film on all the specimens. Polishing, however, does not remove the poorly protective film formed at high temperature during the manufacturing process that still remains inside emerging porosities. In these zones, relatively high current densities can be hypothesized despite the whole surface around the porosity is still passive. This causes a decrease in the impedance modulus.

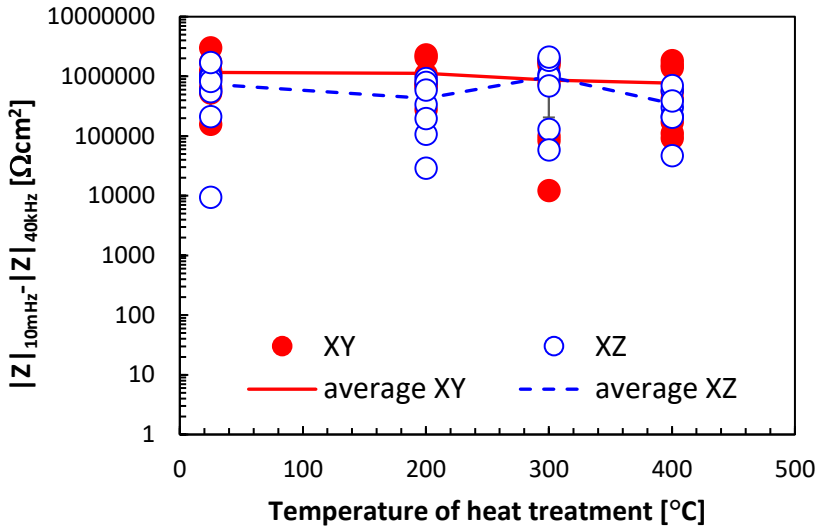

Figure 3-29: Effect of heat treatment temperature on the difference in electrochemical impedance modulus at 10 mHz and 40 kHz in 0.02M NaCl solution at 23 °C.

All the EIS spectra show one time constant, thus indicating passive behaviour of the alloy. In fact, once the localized corrosion is initiated, the attack propagates with the dissolution of the aluminium matrix mainly at the edge of the melt pool created by the laser scan track. This selective corrosion process produces in the EIS spectra a clear separation of the two time constants[106]: one time constant was attributed to the cathodic process on the silicon particles, which are more noble than the aluminium matrix and the passive film on aluminium, while the second time constant is related to the corrosion of the α-Al phase close by Refs.[6,127]

The polarization resistance obtained by the potentiodynamic curves is well correlated to the impedance modulus at low frequency, but unrelated to E_{corr} or E_{pit}, thus confirming the stochastic nature of the localized corrosion initiation.

Statistical data analysis based on analysis of variance technique (ANOVA) was performed. Data were grouped to carry out a two-way analysis with repeated measures, being the building direction and heat treatment the two parameters and the number of repetitions equal to 8 for each condition. The test was chosen to assess whether the populations could be considered as part of the same population (null hypothesis) or they have to be maintained separated (alternative hypothesis) from each other with a confidence level (LOC) of 95%, which equates to declaring statistical significance at the p-value lower than 5%. The analysis of main effects showed that the population significantly differs only by considering the heat treatments with very low p-value, of

about 0.8%. On the contrary, the building direction plays only minor role as the p-value is high, being 33%. Hence, data were grouped by neglecting the different building directions

and they have been analysed based on 16 specimens each heat treatment. No significant interaction between the effects of heat treatment and the building direction on the pitting potential of the alloy was found as the p-value is equal to 7,4%.

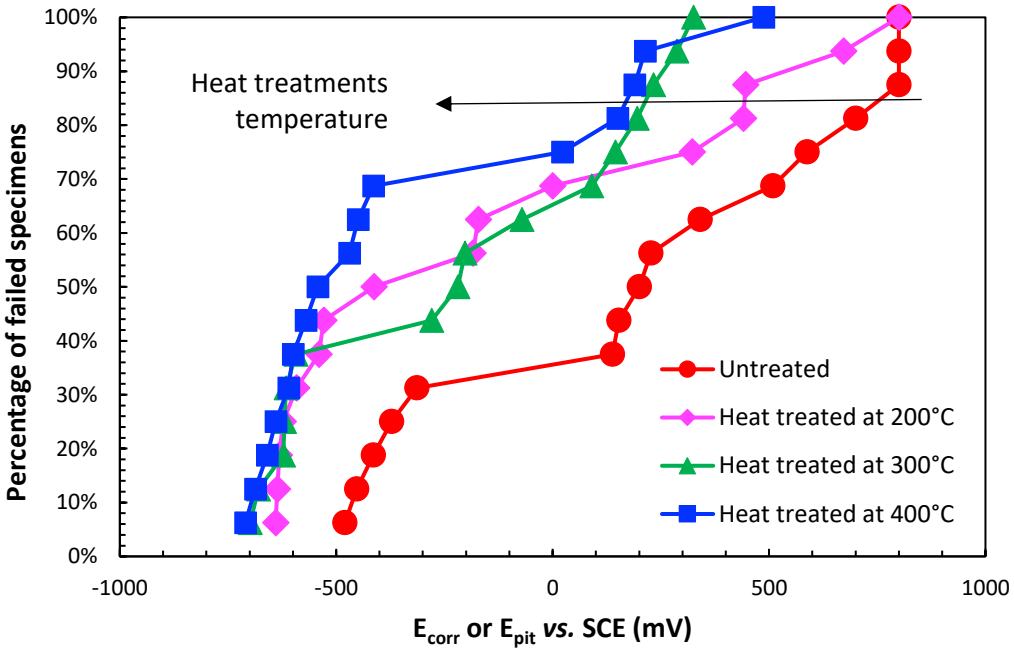

Figure 3-30: Effect of heat treatment temperature on the cumulate frequency of the pitting potentials (16 specimens) (or OCP for the pitting was initiated during the equilibration time) in 0.02M NaCl solution at 23 °C.

A clear negative trend with the heat treatment can be underlined by the cumulative frequency curves of the specimens with different heat-treatment. The pitting potentials UT specimens are between -0.5 and + 0.8 V *vs.* SCE, while the pitting potentials of all other specimens are relatively shifted towards more negative potentials. The specimens heat-treated at 300 °C and 400 °C have similar OCP ranges, between -0.7 V *vs.* SCE and +0.5 V *vs.* SCE. However, the distribution of the specimens treated at 400 °C is more shifted to the right compared to 300 °C, and the average values of the pitting potentials are one hundred millivolt lower than the specimens heat treated at 300 °C (-0.313 ± 0.4 for the specimens heat treated at 400 °C and -0.207 ± 0.4 for the specimens heat treated at 300 °C). The alloy exhibits localized corrosion as the temperature of the heat treatment increases. More complex seems to be the behaviour of the specimens heat treated at 200 °C, that present a very enlarged cumulative frequency distribution.

3.5 Selective attack of LPBF AlSi10Mg

The potentiodynamic tests as well as the intergranular tests evidence the corrosion progresses via selective dissolution of the α-Al matrix, stimulated by the higher nobility of the Si particles, which acted as cathodes (Figure 3-31).[2] The attack preferentially takes place at the melt pool borders and it is more pronounced with heat treatments at 200 and 300 °C. On the contrary the selective dissolution of the border of the melt pool disappears as the heat treatment temperature increase at 400° C or more. The microstructural differences between the border and the edge of the melt pool are strongly dependent on the post processing heat treatment.[61,128–130]

Previous results in Harrison's solution evidenced a selective attack of the edge of the melt pool on specimens stress relieved at 300°C.[7,131] Rubben et al.[128] observed a similar electrochemical behaviour for the alloy in a 0.1 M NaCl solution, independently by the heat treatments (artificial aging at 170 °C for 6 h, a stress relieving at 300 °C for 2 h, and a stress relieving at 250 °C for 2 h), but the corrosion morphologies change from a superficial corrosion attack coupled with micro-cracks along the melt pool boundaries for the untreated specimen and 170 °C aged samples to a more severe penetrating corrosion attack oriented along the melt pool borders. The long-term exposure of the samples to the electrolyte seemed to cause more degradation of the 250 °C and 300 °C heat treated samples than the un-treated ones. Rafieazad et al.[130] investigated the effect of the microstructure of heat treated specimen in the first stage of corrosion; they founded that the corrosion morphology change from a penetrating selective attack along the melt pool boundaries for the untreated and 200 °C heat treated samples to a more localized corrosion in the α-Al matrix along the border of Si particles when the samples were heat treated at 300 °C, ascribed to the uniformity of the microstructure achieved after 300 °C heat treatment.

Preferential attacks at the melt pool borders can be evidenced at the end of intergranular tests, as shown in the 3.1 paragraph. The exposure of both XY and XZ polished specimens allowed for better analysis of the morphology of the attack and enhanced the preferential growth of the attack with respect to the melted pool border. Preferential corrosion of the melt pool border can be attributed to the unique microstructure produced by LPBF process. Analysis of the corrosion morphologies was done at both macro and micro scales. The preferential attack of the melt pool borders could be clearly detected once the melt

pool microstructure was determined by uneven silicon particle precipitation and element segregation.

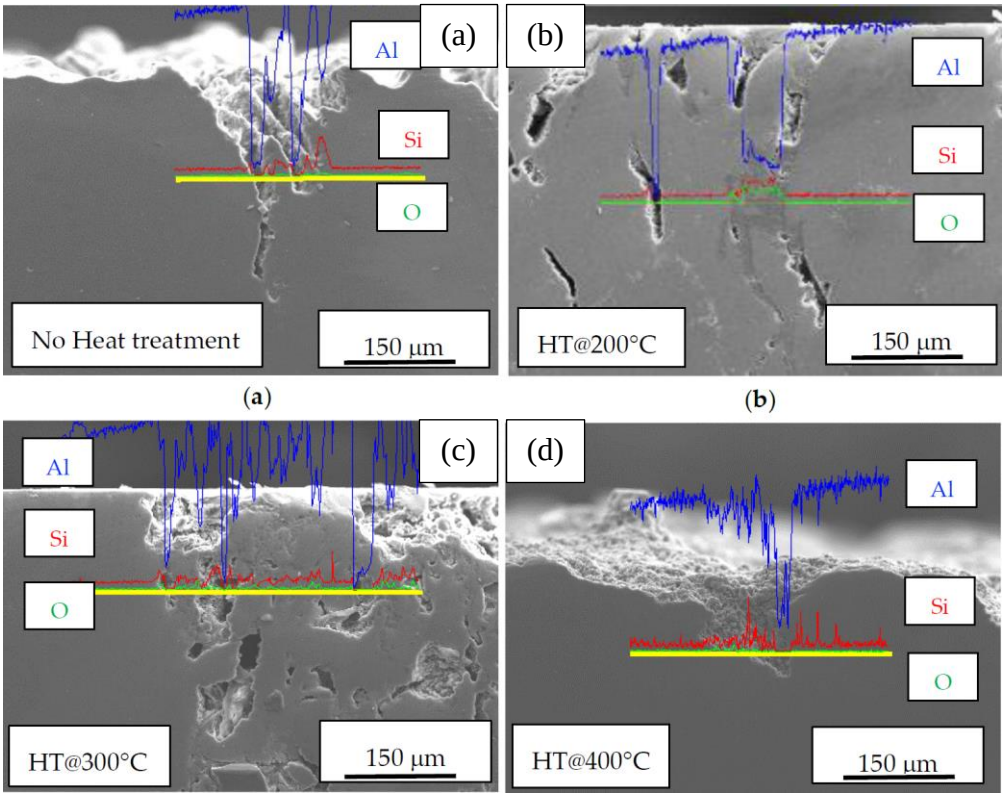

Figure 3-31: Energy dispersive X-ray spectroscopy (EDS) profile of aluminium (blue line), silicon (red line),and oxygen (green line) in the correspondence of attacks on specimens (a) not heat treated; (b) treated at 200°C for 2 h; (c) treated at 300 C for 2 h; (d) treated at 400 C for 2 h.[61]

Cabrini et al.[106] stated that the enhanced content of silicon in the solid solution in the melt pool (due to the rapid solidification and cooling) increases corrosion resistance and the formation of preferential dissolution path in HAZ due to the separation of silicon idiomorphic crystals and produces local galvanic couples. The silicon network that decorates the aluminium dendrites inside the melt pool could partially hinder the aluminium matrix by decelerating the corrosion rate. Conversely, isolated particles in the HAZ stimulate α-Al corrosion. For this reason, the dissolution rate of the melt pool border was higher than the centre. The heat treatments at 200 and 300 °C promoted an increase in size of silicon crystals around the α-Al phase at the border of the melt pool, thus enhancing the intensity of the attacks. When the heat treatment temperature was further increased to 400 °C (Figure 3-32), the melt pools were destroyed and the silicon particle coalescence occurred and rounded second phases were formed. These changes of

microstructure can justify the different corrosion rate after the heat treatment on the specimens.

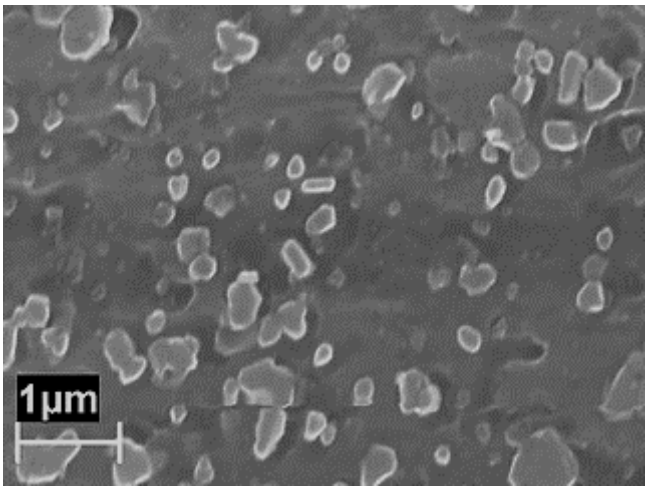

Figure 3-32: Microstructure of the XZ ($T_{platform}$ 35 °C) specimens heat treated at 400 °C

The SKPFM maps of the specimens untreated or thermally treated at 300 and 400 °C showed Volta potential higher for the silicon phase than the α-Al phase. The SKPFM maps reproduced the macrostructure of the specimens, highlighting the different silicon distribution between the centre and edge of the melt pool.

The high-resolution profiles of Volta potential between the centre and the edge of the melt pool evidenced higher differences between the Volta potentials of aluminium and silicon at the border of the melt pool than in the centre both for untreated and stress relieved at 300 °C samples (Figure 3-33-(a)-(b)). It is in agreement with the results presented by Revilla et al.[2] and Rubben et al.[128] The SKPFM map of the specimen heat treated at 400 °C did not present the melt pools, and the differences between aluminium and silicon are lower than the values of the specimens untreated or treated at 300 °C at the border of the melt pool, but not lower than the values inside the melt pool (Figure 3-33-(c)).

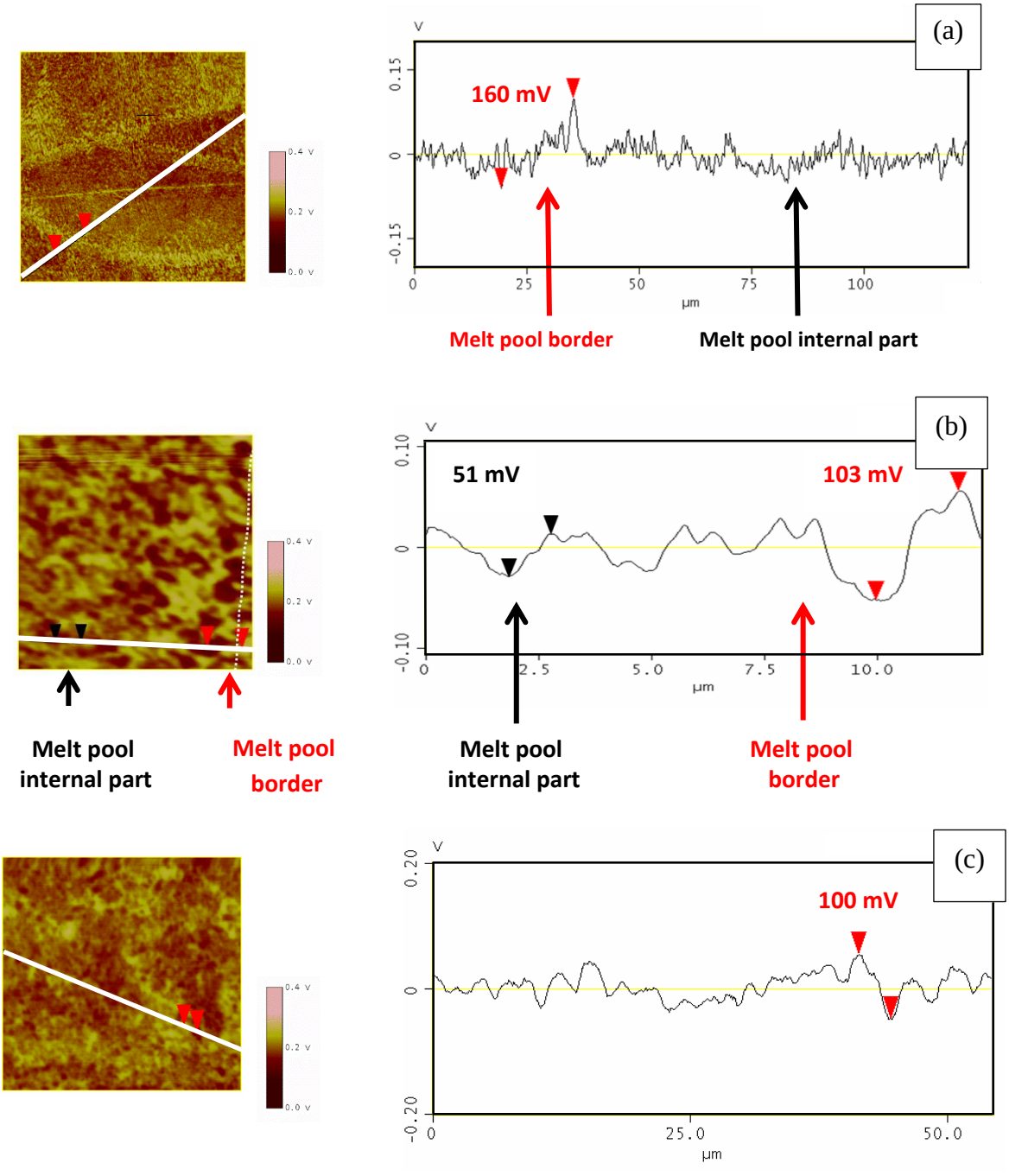

Figure 3-33: Volta potential profiles od (a) XZ UT specimen; (b) XZ heat treated at 300°C for 2 h; (c) XZ heat treated at 400°C for 2 h;

The differences between the Volta potentials of aluminium and silicon in function of the heat treatments temperature can be attributed to the variation of the α-Al potential, due to the distribution of the alloy elements, while the silicon crystals do not solubilize external elements, so their potential can be considered constant. The decrease of silicon in the aluminium matrix should decrease its practical nobility and therefore the difference

between the Volta potential of silicon and aluminium should increase. However, the LPBF microstructure is characterized by strong inhomogeneities with strong local difference composition and the heat treatment homogenize the composition thanks to the solid diffusion. The effect of magnesium precipitates is also considered to explain this behaviour. In fact, although magnesium is an element present in alloy in a concentration much lower than silicon, its difference in nobility with aluminium and silicon is considerable and could significantly change the measured Volta potential values. A similar effect was observed for the alloy 7xxx where the precipitation of $MgZn_2$ increases the Volta potential of aluminium matrix, the effect was confirmed by means of conductibility analysis and TEM observation.[132]

The precipitation of Mg_2Si particles in the Al-Si-Mg alloys, after solubilization and artificial aging, is well known and exploited for the strengthening of the alloy[133] but it is difficult to individuate these particles, owing their nanometric size. In literature are reported controversies on the presence of Mg_2Si precipitates, that could be attributed to the different manufacturing conditions such as the temperature of the building platform.

The EDS maps reported in literature for the alloy printed using a platform temperature of 200 °C, showed an increasing of the concentration of Mg and Fe at the cell boundaries.[134–137] Fousová et al.[136] reported that magnesium, owing to a higher diffusion coefficient with compared to silicon, is located only in the intercellular network where it forms Mg_2Si phase by reaction with Si. Other authors affirmed that the intermetallic phases are mainly $Al_8FeMg_3Si_6$.[66,137–139] Hadadzadeh et al.[140] reported the presence of small quantities of Mg_2Si precipitates in the alloy AlSi10Mg processed with building platform temperature of 200 °C, in form of small precipitates colonies, mostly with needle-shape morphologies. They affirmed that the evolution of Mg_2Si precipitates is not predictable by means of computational thermodynamics under both equilibrium and non-equilibrium solidification conditions, but it seems heating cycles experienced by the material during LPBF process lead to diffusion of Mg and Si atoms through the supersaturated α-Al matrix and formation of Mg_2Si colonies. Moreover, quenched-in dislocations have been also identified as critical sites for nucleation and growth of Mg_2Si.[141] The quenched-in dislocations were formed by means of the ultrafast cooling rates (103–108 K/s) achieved during the process.[140] On the contrary, the absence of phases different from aluminium and silicon was found using a platform temperature of 100 °C.[142–144] In their work,

Maeshima and Ohishi reported an average Mg content in α-Al of 0.1 at%, while the most of the Mg is segregated at eutectic region at the surface of Si particles between α-Al and Si, since there is no solubility of Mg into Si.[144] It is in agreement with other results[134–137] but they did not found Mg_2Si particles, but only Mg clusters and Mg-Si co-clusters in α-Al. Mg clusters and Mg-Si co-clusters in LPBF specimens with the as-built state accelerate the precipitation of Mg_2Si or Si as nuclei by subsequent low temperature and/or short-time heat treatments.[144] Rubben et al[128] using a LPBF equipment without specify the building platform temperature founded a slight accumulation of magnesium in the silicon phase at the border of the α-Al cellular grains of the un treated specimens. For these authors, could indicate the possible formation of Mg_2Si precipitates, although the formation of these precipitates has not been confirmed.

Based on these different results, an effect of the temperature of the building platform on the magnesium distribution could be hypnotized. The different building platform temperatures cause different cooling rates, for which a higher level of oversaturation of magnesium in the aluminium matrix is achieved using low platform temperatures than in the case of high temperatures. In this last case the formation of magnesium precipitates is observed.

Literature data are controversial also on the temperature of precipitation of the Mg_2Si during the post processing heat treatments. Marola et al. [145] reported the results of the DSC analyses of this alloy printed using the platform at 100 °C, with the evidence of exothermic signals, attributed to the precipitation of Mg_2Si around 317 °C and possibly Fe-containing intermetallic around 340 °C. On the contrary, M. Rafieazad et al.[130] reported for the same alloy printed using the platform at 200 °C, the result of DSC analysis, with two pecks, at 232.9 °C and 273.2 °C. The first temperature was attributed to the precipitation of Mg_2Si in β" form, the second peak to the activation of Si interdiffusion in Al, which would typically contribute to the precipitation, coarsening, and spheroidization of Si particles in the alloy.[130] The same author reported that heat treatment at 232.9 °C can initiate the precipitation of the Mg_2Si phase, providing precipitation hardening characteristics for the alloy. The continuous softening in this alloy is induced by further increasing the heat treatment temperature from 200 °C to 350 °C, resulting in a drastic decrease in the microhardness value from 132 ± 2 $HV_{0.1}$ to 69 ± 2 $HV_{0.1}$ owing to the increase of size and spheroidization of the silicon particles [130].

In this thesis, the exo-electron emission (EEE) – performed by the university of Riga – was used to evidence the precipitation of Mg_2Si particles in the alloy.

The EEE is the non-stationary electron emission from solids originating from various external excitations such as mechanical deformation, chemisorption, X-ray irradiation and electron bombardment, which cannot be explained within the framework of the classical photoelectric effect, thermionic emission, secondary electron emission or other well-known processes [146]. T. Górecki and C. Górecki reported EEE in correspondence of phase changes and precipitation of second phases if the specimen is stimulated with appropriate wavelength light.[147–149] Sujak and co-workers investigated the EEE during the early stage of the spontaneous aging (also at room temperature) of the industrial PA-4 alloy, homogenized at 810 K and quenched in ice water.[149] A maximum on the decay curve of the EEE intensity was observed whose position corresponded to the maximum rate of the precipitation of the Mg_2Si phase. The observed decay for the EEE during the precipitation of the Mg_2Si phase can be attributed to the annihilation of the crystal lattice defects created during the quenching procedure.[147]

A similar situation could be supposed for the LPBF process, where the high cooling rate, characterizing the melt pool solidification using a temperature of the building platform of 100 °C, avoids the precipitation of the Mg_2Si. The heat treatment at 300 °C provokes the beginning of the precipitation of these particles from the aluminium matrix, while the spheroidization of silicon particles takes place during the heat treatment at 400 °C. In this way, the EEE of the untreated specimens showed a high exo-electron emission in the temperature range of the precipitation of Mg_2Si, the emission decreases for the heat treated specimens because the precipitation of these particles was mainly during the heat treatment (Figure 3-34).

The presence of Mg_2Si particles could explain the decreases of corrosion resistance of the alloy printed with the building platform temperature of 100 °C, with the heat treatment.

The Mg_2Si particles have a nobleness lower than aluminium and silicon. The corrosion potential of pure aluminium, silicon and Mg_2Si reported by Birbilis and Buchheit in neutral chloride solutions at different concentration, are summarized in Table 3-3.[150]

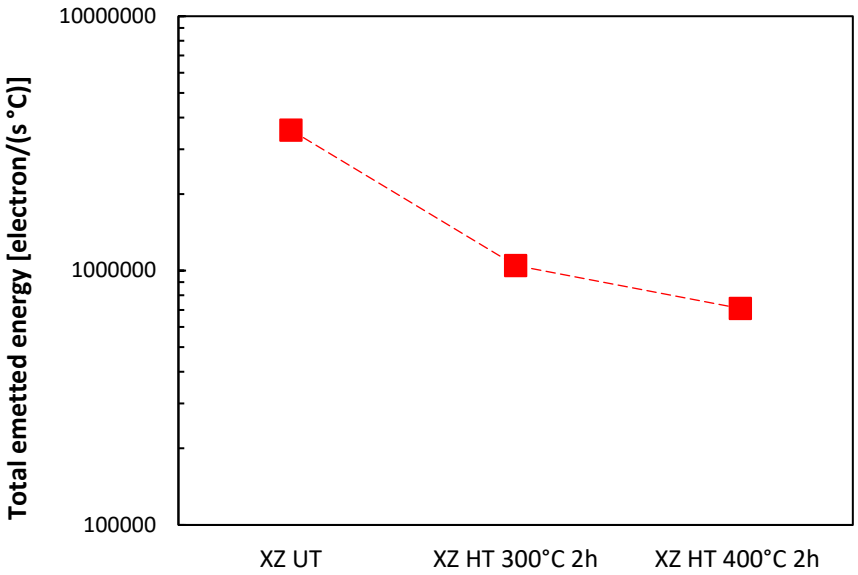

Figure 3-34: Curve integrals of the exo-electron emission for different heat treatment temperatures

Table 3-3: Precipitate corrosion potentials for different chloride content.[150]

Phase	Corrosion potential (mV *vs.* SCE) in neutral NaCl solution at different concentration		
	0.01M	0.1M	0.1M
Pure Al (99.9999)	-679	-823	-849
Pure Si (99.9995)	-450	-441	-452
Mg_2Si	-1355	-1538	-1536

Linardi et al. affirmed that Mg_2Si phase is stable in solutions of pH from 8 to 14, but at pH values lower than 8, it undergoes selective magnesium dealloying.[151]

Silicon has higher practical nobility than aluminium, but it is a bad cathode for the oxygen reduction or hydrogen evolution reaction. In the 6xxx alloys, an optimal ratio between Mg and Si improve the resistance of the alloy to intergranular corrosion because the precipitation of second phases Mg_2Si avoid the segregation of silicon at the grain border, and its stimulation of corrosion. On the other hand, the magnesium rich particles instantaneously react when the alloy is dipped in the aggressive solution with the magnesium preferential dissolution. It is not proven that the reactivity of the magnesium rich particles influences the pitting potential, because their effect run out in few minutes, but the high cathodic activity associated to their anodic dissolution can alkalinizes the aluminium surface and can destabilize its passive film, causing its subsequent corrosion.

The accumulation of Mg_2Si particles at the edge of the melt pool could therefore contribute to its selective corrosion.[152]

The effect of heat treatment at 300 °C on the specimens used in this work (realized on specimens with $T_{platform}$ of 100 °C) is to increase the magnesium precipitation, probably mainly at the edge of the melt pool. In this way, the selective corrosion of this zone increases with the heat treatment.[61,129] Increasing the heat treatment temperature, the silicon particles coalescence decreases this effect. Unfortunately, the size of these particles prevents their determination and more deep analysis, for example at the TEM, should be performed to confirm this hypothesis.

CHAPTER 4

EXPERIMENTAL STUDY OF ALLOY 625

The aim of this chapter is to compare the corrosion resistance of nickel-base alloy 625 (UNS N06625) produced by laser powder bed fusion with hot worked alloy traditionally used in oil and gas plant.

The corrosion assessment was performed at the University of Bergamo by means of electrochemical tests and solution weight loss tests. The specimens were printed and heat treated at the Politecnico di Torino. The characterization of alloy 625 specimens by means of EBSD and SKPFM techniques was conducted at the University of Manchester.

The specimens were printed at the Politecnico di Torino using Eos M270 Dual Mode machine already descripted above. A gas atomized alloy 625 powder provided by EOS GmbH was use. The nominal composition of the powders and the composition of a printed part obtained by Politecnico di Torino via inductively coupled plasma (ICP) and Leco system, were reported in Table 4-1. The distribution if the powders size is within the range with a d_{10} of 16 μm and d_{90} of 48 μm calculated using a laser granulometry diffraction.[153] A traditional hot worked (HW) material provided by a company operating in the oil and gas field, having similar chemical composition, was also used (Table 4-1).

Table 4-1: Nominal chemical composition of alloy 625 powder, of massive LPBF and of Hot Worked material.

Element (%wt)	HW alloy 625	Alloy 625 powder[154]	Alloy 625 measured
C	0.036	≤0.1	0.01
Si	0.25	≤0.5	0.08
Mn	0.19	≤0.5	0.03
P	0.007	≤0.015	< 0.001
S	0.001	≤0.015	0.002
Cr	21.6	20-23	22.4

Mo	8.26	8-10	8.2
Nb	3.66	3.15-4.15	3.73
Ti	0.24	≤0.4	0.18
Al	0.2	≤0.4	< 0.01
Co	0.02	≤1	0.17
Ta	0.01	≤0.05	0.13
Fe	3.1	≤5	0.45
Nb+Ta	3.67	3.2-4-2	3.86

The Table 4-2 shows the mechanical properties of LPBF specimens tested before the post processing heat treatment and the properties of the hot worked one.

Table 4-2: Mechanical properties of LPBF alloy 625

	Building direction	**$R_{p\,0,2}$ [MPa]**	**R_m [MPa]**	**A%**	**Hardness HRC**
LPBF as printed	XY	725 ± 50	990 ± 50	35 ± 5	26,6
	XZ	615 ± 50	900 ± 50	42 ± 5	27,17
Hot worked	--	415	830	30	17,7

Different specimen geometries were used for the corrosion tests:

- Cylindrical specimens with 15 mm diameter and 5 mm height
- Cubic specimens with 15 mm edge
- Tensile specimens for slow strain rate tests
- Flat U-bend specimens

The specimens manufactured via LPBF were tested in two conditions: without heat treatment (named LPBF-UT specimens) and after annealing at 980 °C for 32 minutes followed by water quenching (also known as “grade 1”) as commonly used in the Oil&Gas industry and they are named LPBF-HT specimens. The hot worked specimens were also subjected to the same heat treatment and are named HW.

The LPBF specimens without post processing treatment of surface are named as built (AB); their rough surface obtained under confocal microscope are shown in Figure 4-1.

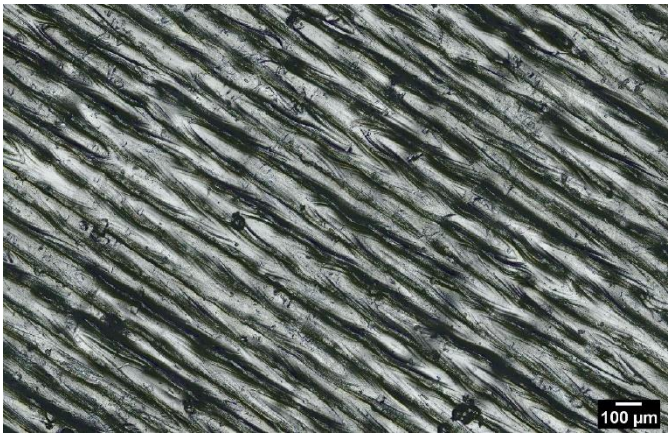

Figure 4-1: Confocal microscope image of the XY as-built surface

The specimens marked as P (Polished) were grinded by abrasive paper and polished by 1 µm diamond past.

After polishing, they were passivated in air for 1 hour before corrosion tests. Before SKPFM and EBSD analysis, colloidal silica was used by polishing of surface for 30 minutes. All specimens were degreased in acetone just before the tests.

Weight loss tests in hot acids

Weight loss tests were carried out according to ASTM G31 in 10 % of hydrochloric acid at 20°C and 60°C and in 50% of sulfuric acid at 50° C, 80° C and boiling temperature.

The specimens were placed in a 1L flask with a reflux condenser. Boiling Chips were used to prevent bumping. The apparatus was heated by used a water bath and the temperature was controlled by thermometer during the tests.

Before the tests, that were repeated twice, all the specimens were grinded using SiC papers up to 1200 grit, one face in XZ direction and one in XY direction were polished with 1 µm diamond paste for scanning electron microscope (SEM) observations. Then, they were weighted 3 times. After 24 hours the specimens were extracted from the solution, washed with water, rinsed in acetone, and weighted again in order to establish the weight loss.

The corrosion rate was calculated by the equation [4.1]:

$$V_{corr} = \frac{(K \cdot W)}{(A \cdot T \cdot D)} \qquad \text{Eq [4.1]}$$

Where:

- K is a constant equal to $8.76 \cdot 10^4$ with corrosion rate in mm/y
- T is the exposure time (h), approximated to 0.01h
- A is the exposed surface (cm^2), approximated to 0.01 cm^2, the contribute of the roughness became negligible after the polished at 1200 grit.
- W is the weight of the sample (g), approximated at least to 1mg
- D material density, that for the alloy 625 is 8.44 g/cm^3

After the exposure, each specimen was observed by SEM.

Intergranular tests

Intergranular corrosion 120h tests in boiling ferric sulphate/sulfuric acid were carried out according to ASTM G28 standard, method A. Before testing, the surface of cubic specimens was grinded up to 1200 grit by silicon carbides emery paper. Two faces of LPBF specimens were ground and polished up to 1 μm diamond paste in order to permit observations of corrosion morphology on main planes. Only the transversal plane to rolling direction was polished on disk specimens. Just before their immersion in the boiling test solution, the specimens were degreased in acetone in ultrasonic bath, rinsed in water and dried. Before and after tests, the specimens were weighed by means of analytic scale to measure the weight loss and corrosion rate. The corrosion rate was calculated by the equation [4.1].

Finally, the specimens were observed by SEM.

Critical Crevice Temperature (CCT) tests

Critical Crevice Temperature (CCT) tests were performed based on the ASTM G48–Method D using a customized Anderson device (Figure 4-2) with elastic ties as employed by other authors.[155] The same methodology was used to test LPBF and HW specimens and the surface exposed was 13 cm^2.

Figure 4-2: Customized Anderson device on the LPBF cubic specimens

Two parallel face cubic specimens were grinded as indicated by the standard.

The tests were conducted in 1L flask using a solution with 6% of $FeCl_3$ and 1% of 37% HCl. After 72 hours, the specimens were extracted from the test solution, scrubbed with a nylon bristle brush under running water and rinsed in acetone in order to remove the incoherent products.

The temperature was controlled with a thermostatic bath and maintained constant throughout each test. Several tests were conducted at different temperatures between 20°C and 40°C with a 5°C increase. All specimens were weighted before and after the tests in order to establish their weight loss. Finally, each specimen was observed by SEM.

Critical pitting temperature test

The tests were carried out according to ASTM G48 using the methodology reported above. The specimens were grounded up to 1200 grit and passivated for 30 minutes in 50% nitric acid at 60°C in order to avoid the crevice corrosion. They were immersed for 72 h with the grounded surface on the top. Then, they were extracted of the test solution, brushed with polymeric brush and rinsed in acetone in order to remove the incoherent products and observed by SEM.

Stress corrosion cracking test

The experimentation was carried out in a 1L flask using magnesium chloride at 155°C according to ASTM G36 and at 170°C. The flat specimens were prepared and stressed, according to ASTM G30(Figure 4-3). The yield stress was maintained by alloy 625 screw. The duration of the tests was 7 days, with intermediate observations of the state of the samples every 24 hours at 50 magnifications to verify the presence of cracks.

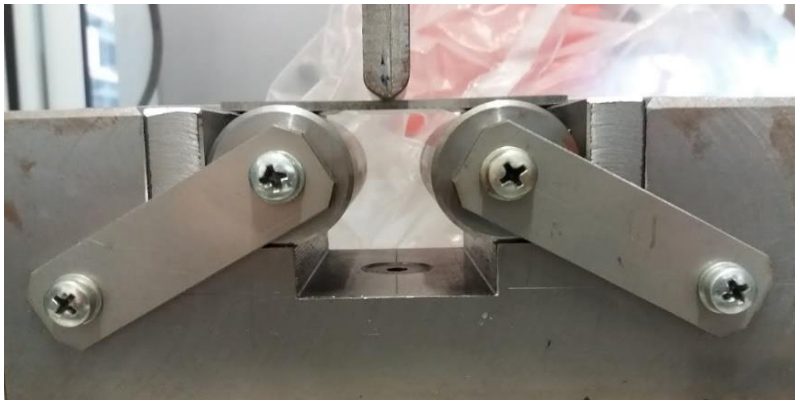

Figure 4-3: Bending of the flat specimens

Potentiodynamic tests

Electrochemical tests were performed by using Ivium Compastact and Metrohm Autolab PGSTAT302.

The potentiodynamic tests were performed in a 1L standard three electrode cell (ASTM G5) using a PTFE sample holder with exposure area of 1 cm^2, a Saturated Calomel Electrode (SCE) and two graphite counter electrodes. Before the test, the solution was de-oxygenated with bubbling of nitrogen. The cell was heated using a water bath and the temperature of the test solution was monitored via a thermometer. Before the cyclic potentiodynamic tests, the open circuit potential (E_{corr}) was monitored for 10 minutes. The potentiodynamic tests were carried out according to ASTM G5 using 10 mV/min as scan rate value. For the solutions do not mentioned by the standard, the polarizations were conducted from 10 mV below the E_{corr} up to 1 V *vs*. SCE or until the anodic current density reached 10 mA/cm^2. Finally, a reverse scan rate was used to returned to the initial open circuit potential value.

The potentiodynamic tests were conducted in three different environments:

1) 0.5 M H_2SO_4 – according to ASTM G5 at 30 °C
2) 35 g/L (0.6 M) NaCl + HCl (10^{-3} M), pH 3 at 40 °C
3) 35 g/L (0.6 M) NaCl, pH 7 at 40 °C

In the end, each specimen was observed by SEM.

Potentiostatic tests

The potentiodynamic setup was also used for potentiostatic tests that they were carried out in 35 g/L (0.6 M) NaCl at pH 7 at +0.2 V or +0.5 V *vs.* SCE for 24 hours, with an acquisition rate of 1 Hz and were repeated twice. Finally, specimens were observed by SEM.

Slow Strain Rate

The Figure 4-4 shows the geometry of the specimens used for slow strain rate tests. The specimens were polished manually with SiC paper up to 1200 grit in order to remove the manufacturing tracks. The tests were conducted in two different setups. In the first experiment setup the specimen was cathodically polarized at -1.1 V *vs.* Ag/AgCl (3M KCl) in sea water (according to ASTM D1141) at 8.2 pH (using 2052 AMEL instrument) and loaded with a strain velocity equal to $3.15*10^{-6}$ s^{-1}. Then, in the second setup the specimen was cathodic charged at -1.1 V *vs.* Ag/AgCl in sea water at 8.2 pH for 16 hours (that is the total duration of the test using the first setup) and after it was loaded using $3.15*10^{-5}$ s^{-1} strain velocity without removed the polarization. All these results were compared to which obtained in air at $3.15*10^{-6}$ s^{-1} strain velocity.

The susceptibility to SCC was expressed in terms of the area reduction percentage (RA%) calculated by the equation [4.2] according to the NACE TM-0198 standard:

$$RA\% = \frac{\left(D_f^2 - D_i^2\right) * 100}{D_i^2} \qquad \text{Eq [4.2]}$$

The area reduction ratio after fracture for the specimen cathodically polarized (RA_{cp}) to the corresponding value determined in the control environment (RA_{air}) was calculated according to the equation [4.3]:

$$SCC = \frac{\mathrm{RA_{cp}}}{\mathrm{RA_{air}}} \qquad \text{Eq [4.3]}$$

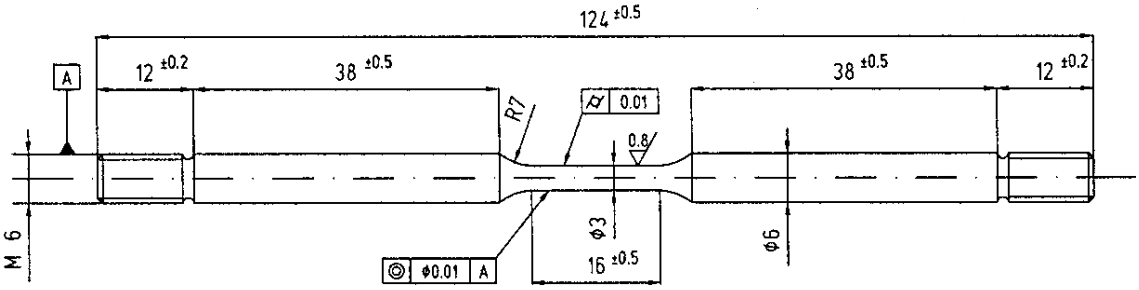

Figure 4-4: Geometry of the SSR specimens

Electron Backscattered diffraction (EBSD)

The microstructure was characterized using SEM-EBSD. Grain orientation maps, with a typical dimension of 1.0 mm x 0.8 mm, were acquired in a FEI Quanta 650 FEG-SEM equipped with a Nordlys EBSD detector from Oxford Instruments. The accelerating voltage used was 20kV and the step size used for the maps was 300nm. The data presented with inversed pole figures (IPF) were processed using HKL Channel 5 software.

Scanning Kevin Probe Force Microscope (SKPFM)

Scanning Kelvin probe force microscopy (SKPFM) was used to obtain maps of the topography and surface potential (Volta potential) of the polished alloy 625 samples. Measurements were performed in a Dimension D3100 AFM using platinum-coated tips (type OSCM-PT) with 25nm tip radius. Acquisition was performed in amplitude modulation with 80nm scan lift height and maps were acquired over 80µm X 80µm regions with 0.1 kHz scan frequency. Each scan was composed of 512 lines, giving a theoretical resolution of approximatively 150 nm per pixel. Measurements were performed at room temperature and humidity.

Hardness tests

The Vickers hardness tests were executed according to UNI EN ISO 6507-1:2018 standard using 2 kg load and 15 s waiting time. Instead, the Rockwell C tests were carried according to UNI EN ISO 6508-1:2016. The tests were repeated 5 times in order to increase the accuracy of the mean values.

4.1 Results on alloy 625

Tests in acid solutions

The Table 4-3 reports the weight loss for the solution containing 10% of HCl at 20 °C and 60 °C. The corrosion rate obtained at 20°C was about 0.13 mm/y for the HT-LPBF specimens, about 0.14 mm/y for the UT-LPBF and 0.15 mm/y for the hot worked. The test carried out at 60 °C showed that the LPBF-UT reduced of 17% the corrosion rate in comparison with the HW. The heat treatment improved the corrosion resistance of 3D alloy allowing the reduction of corrosion rate about 40%.

Table 4-3: Weight loss in 10%HCl for different temperature test

Specimen	Test Temperature [°C]	Specimen n°	Surface exposed [cm^2]	Initial weight* [g]	Final weight* [g]	ΔM [g]	V_{corr} [mm/y]
HW	20	1	6.22	7.90872	7.90650	0.00222	0.15
		2	5.54	5.08706	5.08531	0.00176	0.14
	60	1	6.32	7.97060	7.93582	0.03478	2.38
		2	5.55	5.24564	5.21348	0.03215	2.50
LPBF UT	20	1	13.25	27.5255	27.5213	0.00423	0.14
		2	13.24	27.4436	27.4395	0.00401	0.13
	60	1	13.30	27.8175	27.7541	0.06346	2.06
		2	13.50	27.82110	27.7589	0.06218	2.01
LPBF TT 980°C	20	1	13.18	27.75638	27.7529	0.00350	0.11
		2	13.23	27.27661	27.2725	0.00414	0.14
	60	1	13.44	28.05884	28.0139	0.00450	1.43
		2	13.36	27.53871	27.4938	0.00495	1.46

* average of 3 weights with standard deviation of 0.00001 g

The Figure 4-5(a) reports the morphology of attack observed on LPBF-UT-XY exposed at 20 °C. The presence of emerging porosity (about 30 μm) does not lead to localized attack. Instead at 60 °C, the specimens showed a more intensive but uniform corrosion attack (Figure 4-5(b)). The XZ surfaces underwent similar attack. The test carried out at 60°C highlighted the typical melt pool structure embedded in this technique (Figure 4-6).

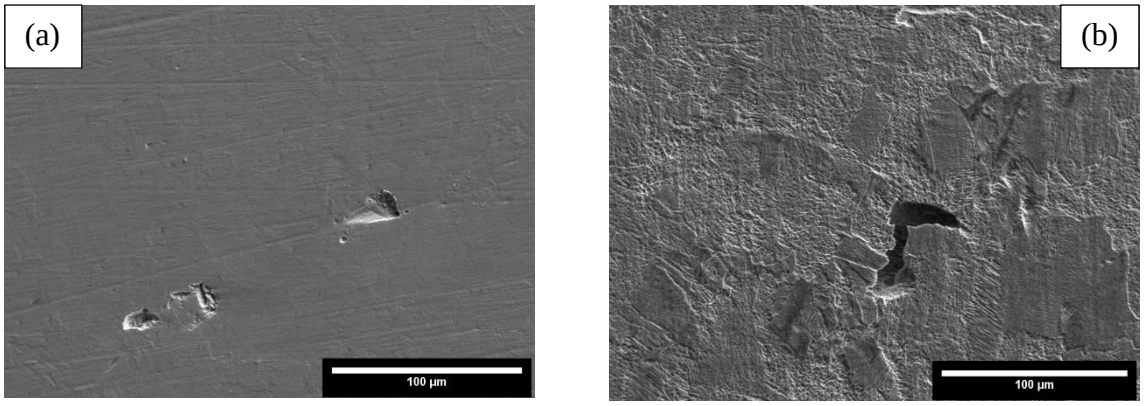

Figure 4-5: Morphology of attack on LPBF-UT-XY specimen after the test at (a) 20°C and (b) 60°C

For the tests carried out, the presence of second phases was not identified.
The specimens obtained from the hot worked bar, after the test at 20 °C, showed a large quantity of second phases at the edge of the austenitic grains, with diverse sizes and shapes as shown in Figure 4-7.

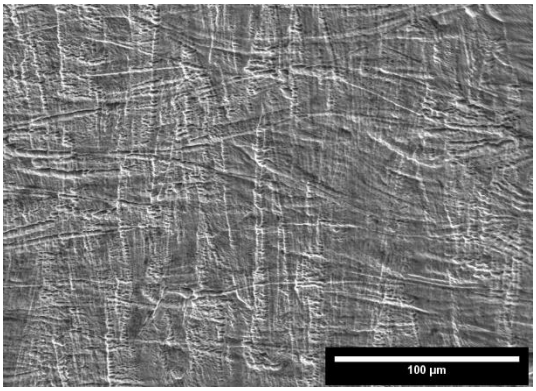

Figure 4-6: Morphology of attack on LPBF-UT-XZ specimen after the test at 60°C

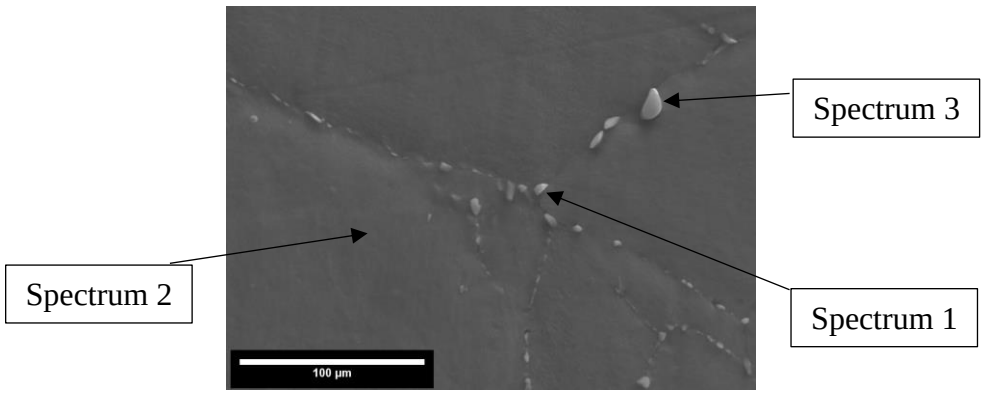

Figure 4-7: Attack morphology after the test in 10% of HCl at 20°C on HW specimen with the indications of EDS analysis

The EDS spectrums were performed at three different points of the specimen, one at the centre of the grain (spectrum 2), one on the largest precipitate (spectrum 3) and finally one on the smaller precipitates (spectrum 1). Table 4-4 shows the chemical composition in weight percentage of the precipitates analysed with respect to the base material at the centre of the grain. The EDS analysis demonstrated that the second identified phases were particularly rich in niobium, molybdenum and carbon.

Table 4-4: EDS spectra on the grain boundary precipitates

Spectrum	C	Si	Ti	Cr	Fe	Ni	Nb	Mo	Total
1	11.13	1.88		15.46	1.68	37.66	10.88	21.32	100.00
2	2.61	0.43	0.24	21.70	2.70	56.62	4.88	10.82	100.00
3	14.61		2.74	3.46	0.34	6.69	72.17		100.00

At the temperature of 60 °C a heavy attack was detected near the precipitates at the grain boundary (Figure 4-8(a)). The corrosive attack of the acid involved even the austenitic matrix. The EDS analysis carried out on the surface showed that the precipitates were rich in titanium, niobium and carbon (Figure 4-8(b)). From Figure 4-8, it is evident that this test temperature leads to a greater dissolution of the metal matrix around these particles.

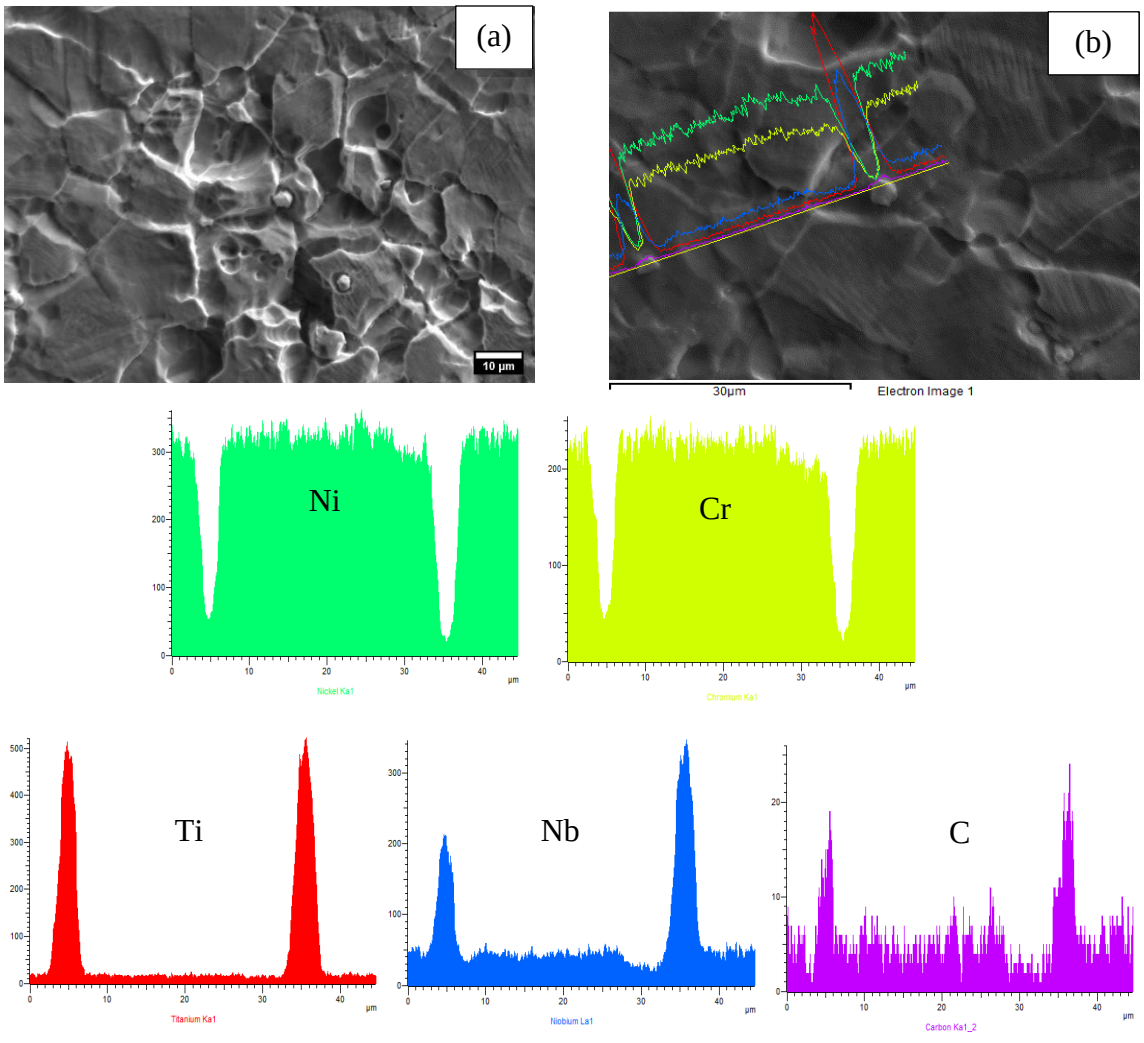

Figure 4-8: Morphology of the hot worked specimen after the test at 60° C (a) and EDS analysis of the precipitates (b)

The SEM analysis of LPBF HT specimens confirmed a stronger attack at 60 °C than 20 °C (Figure 4-9). Figure 4-9(b) denotes the lack of melt pools with comparison to the specimen without heat treatment. No second phases were detected during the SEM analysis of LPBF HT specimens.

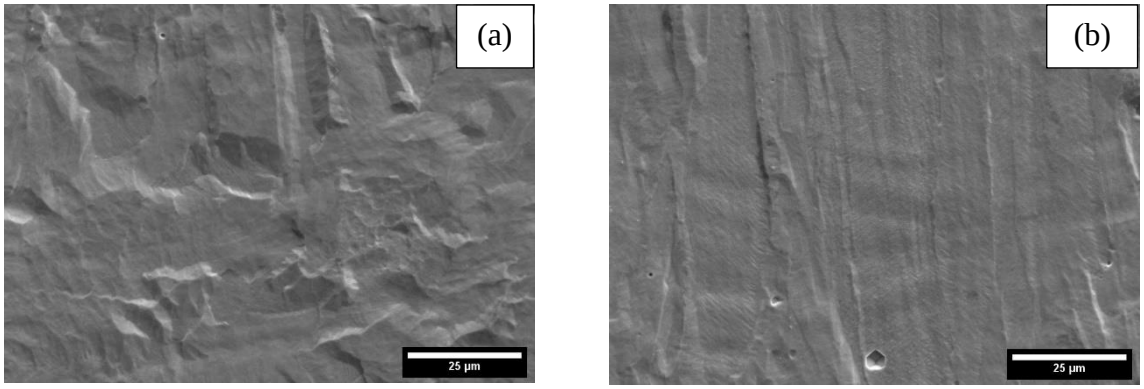

Figure 4-9: Morphology of the (a) LPFB-XY and (b) LPBF-XZ specimens after the test at 60° C

The tests carried out in a 50% solution of sulfuric acid indicated a strong reduction of the corrosion resistance for the LPBF specimens with respect to HW (Table 4-5).

The corrosion rates of the LPBF UT specimen at 50° C was greater than 582% compare with the hot worked one. The heat treatment led to an improvement in the corrosion performance of the 3D printed alloy with values amplified around 405%.

The tests carried out at 80 °C confirmed that the specimens obtained with LPBF were prone to showing corrosion rates well above the hot worked bar. Untreated cubes showed an average value about 7 times higher than HW; the behaviour of the specimens subjected to soft annealing is better, although the corrosion rates remain extremely high, where the ratio was about 5 times.

At boiling temperature, the trend just described was remarked.

After the test at 50°C, the LPBF-UT XY and XZ specimens showed a slight attack that evidence the microstructure constituted by melt pools (Figure 4-10).

At high magnification, columnar and cellular dendritic microstructure was identified for XZ specimen (Figure 4-11). Small particles decorated the border of these structure or they were recorded inside the cellular grain. However, the EDS was not able to distinguish the composition.

Table 4-5: Weight loss in 50% H_2SO_4 for different temperature test (three measure average with standard deviation equal to 0,00001 g)*

Specimens	Temperature [°C]	Specimen n°	Surface [cm^2]	Initial weight* [g]	Final weight* [g]	ΔM [g]	V_{corr} [mm/y]
Hot Worked	50	1	6.22	7.82815	7.82702	0.00113	0.08
		2	5.41	4.96038	4.95873	0.00165	0.13
	80	1	6.25	7.79288	7.77549	0.01739	1.20
		2	5.49	4.91364	4.89847	0.01787	1.41
	126	1	5.12	5.00260	4.53182	0.47078	39.77
		2	5.79	6.66708	6.23011	0.43697	32.62
LPBF UT	50	1	13.38	27.81963	27.79627	0.02336	0.75
		2	13.52	28.47383	28.45735	0.01647	0.53
	80	1	13.22	27.61722	27.27209	0.34513	11.29
		2	13.45	28.32926	28.11942	0.20984	6.75
	126	1	9.88	27.25497	16.90555	10.3494	452.81
		2	12.51	27.20918	24.93778	2.27141	78.50
LPBF HT 980°C	50	1	13.47	28.28090	28.27089	0.01001	0.32
		2	13.41	27.95692	27.93910	0.01782	0.57
	80	1	13.31	27.95211	27.80707	0.14504	4.71
		2	13.27	27.78782	27.57342	0.21440	6.99
	126	1	12.48	27.40367	24.77235	2.63132	91.16
		2	11.93	26.94509	23.33480	3.61029	130.90

* average of 3 weights with standard deviation of 0.00001 g

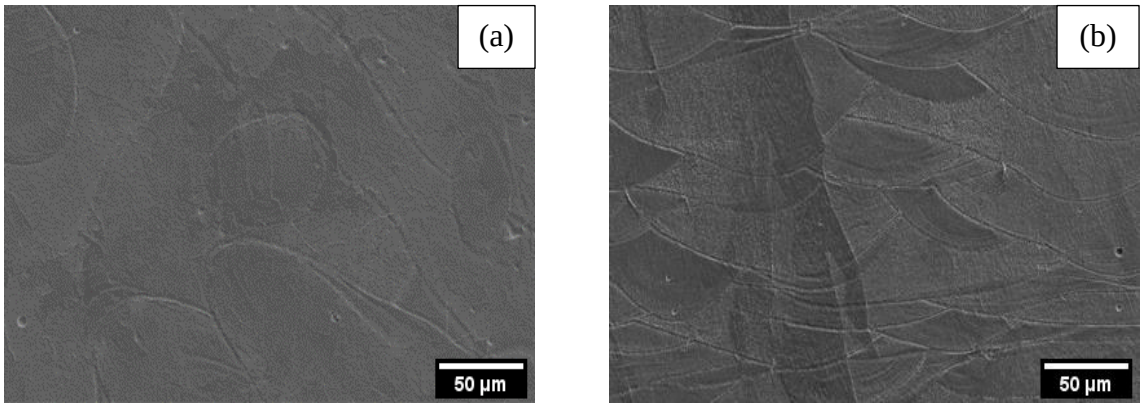

Figure 4-10: Morphology of the corrosion attack after the test for the (a) XY and (b) XZ LPBF UT specimens

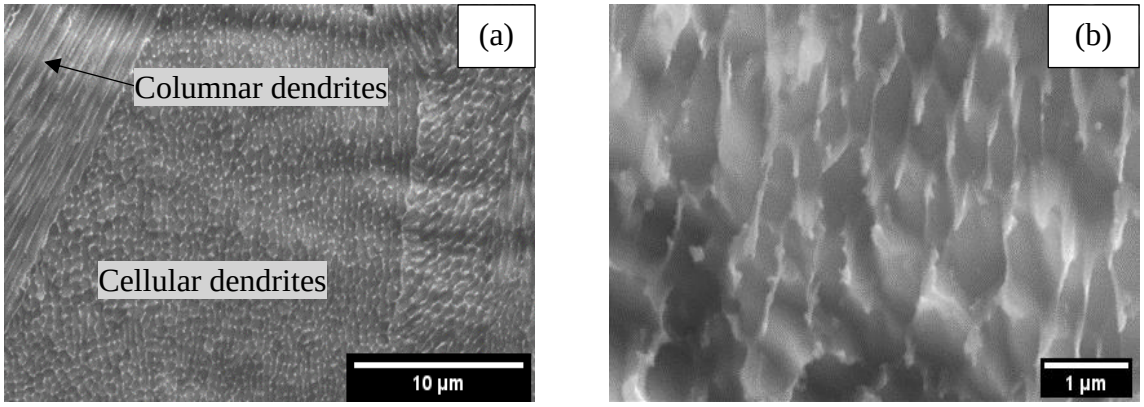

Figure 4-11: (a) Columnar and dendritic structure and (b) particular of cellular grain at high magnification of XZ LPBF UT specimen

A strong damage for the metal matrix was recognized when the temperature reaches the boiling point (126°C) for both the building directions of the untreated LPBF specimens (Figure 4-12).

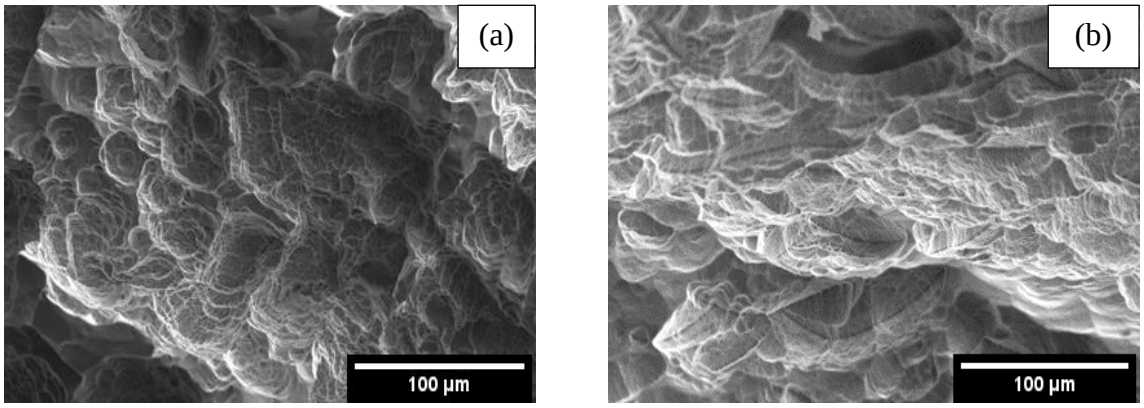

Figure 4-12: LPBF UT (a) XY and (b) XZ morphology after exposure at boiling sulfuric acid

The same test performed on HW specimens at 50°C showed corrosion morphology similar to already observed in HCl with a large number of precipitates (Figure 4-13). The effect of the temperature was to increase the corrosion rate (Figure 4-13(b)). The EDS test was reported in Table 4-6.

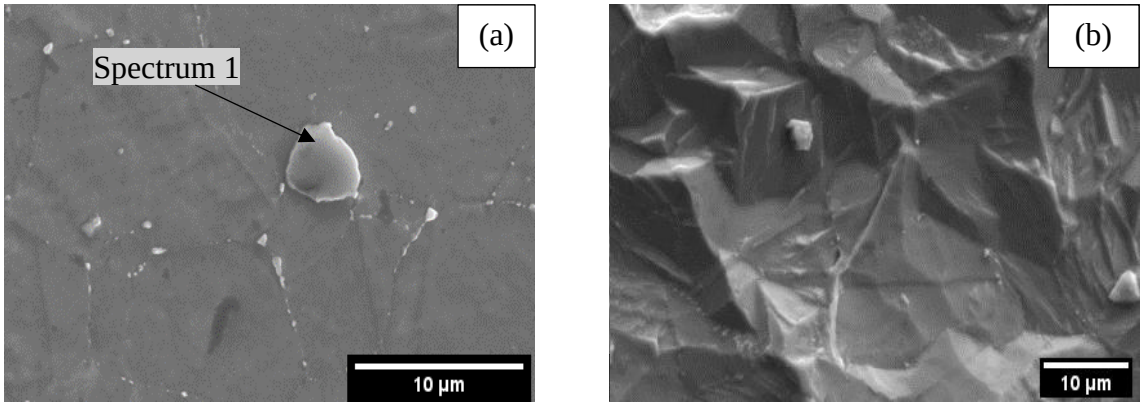

Figure 4-13: Attack morphology after test in H2SO4 performed at (a) 50 °C and (b) boiling point on HW alloy.

Table 4-6: EDS result performed on the particle reported in the previous figure.

Spectrum 1	Ni	Cr	Nb	C	Ti	Fe	Total
% Wt.	9.84	4.16	67.64	15.71	2.12	0.53	100

At the end of test at boiling point, the LPBF specimens after heat treatment presented a morphology similar to the traditional alloy, without the grain boundary precipitates (Figure 4-14).

Regarding to the same specimens after the test at 50°C the corrosion attack was less intensive. The XZ surface showed again columnar structure inside the grain not completely recrystallized (Figure 4-15).

The tests carried out at 80°C for all the samples stayed in intermediate condition.

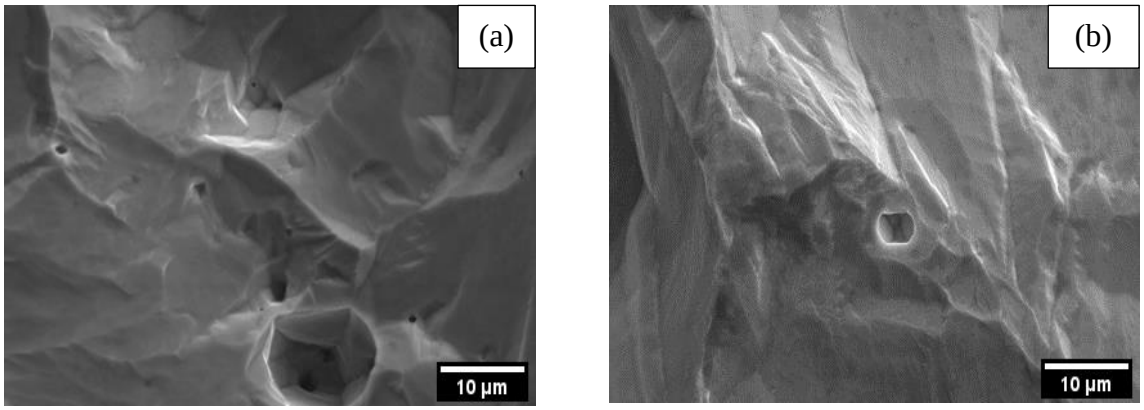

Figure 4-14: LPBF-HT (a) XY and (b) XZ morphology after the test at boiling point.

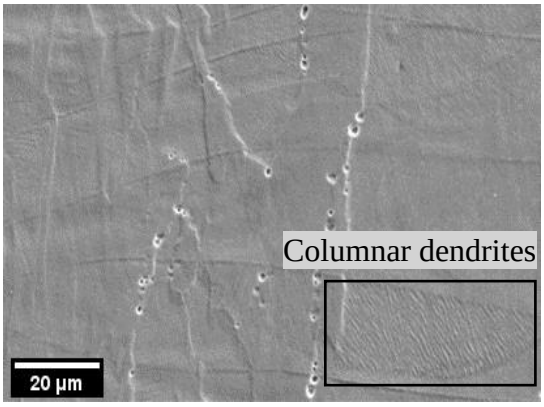

Figure 4-15: Morphology attack after the test at 50°C for the LPBF-HT-XZ specimen with a columnar dendrite inside the grain.

Intergranular corrosion test – ASTM G28

The intergranular corrosion results are reported in the Table 4-7. It is possible notice that the corrosion rate for the traditional alloy was about two times with respect to LPBF UT and about 3 time with respect to LPBF-HT.

Table 4-7: Results after intergranular tests

Specimens	Specimen n°	Surface [cm^2]	Initial weight* [g]	Final weight* [g]	ΔM [g]	V_{corr} [mm/y]
Hot Worked	1	6.04890	6.73923	6.63074	0.10849	1.55
	2	6.12928	7.16643	7.06459	0.10184	1.44
LPBF UT	1	13.50364	28.23744	28.12392	0.11352	0.73
	2	13.34959	27.03907	26.92816	0.11091	0.72
LPBF HT 980°C	1	13.05692	28.24230	28.16770	0.07460	0.49
	2	13.12011	28.34171	28.26959	0.07212	0.48

* average of 3 weights with standard deviation of 0.00001 g

After the tests, the metallographic sections were realized for all the specimens in order to observe the morphology and the penetration of the selective attack. The Figure 4-16 reports the selective attack on the LPBF UT specimen. The attack was very slight as suggest by the very low corrosion rate (Figure 4-16).

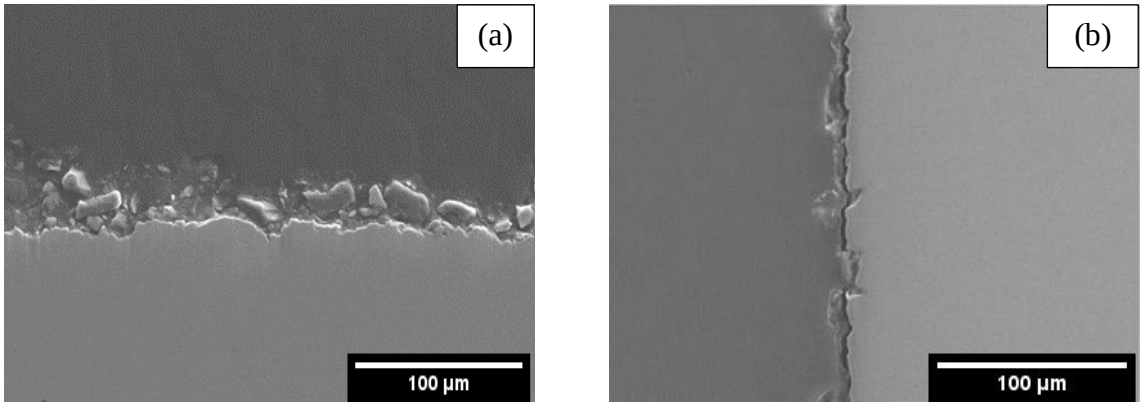

Figure 4-16: Cross section after intergranular test on LPBF UT (a) XY and (b) XZ specimens

The post processing heat treatment improved the resistance of selective attack. The Figure 4-17 shows the cross section after the ASTM G28 test. The LPBF HT had only small attack along the XY plan but the damage remained neglectable.

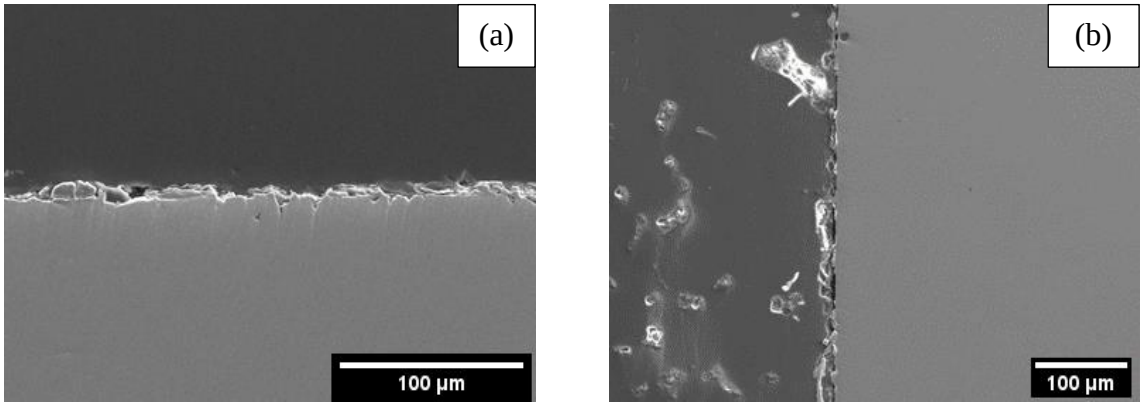

Figure 4-17: Cross section after intergranular test on LPBF HT (a) XY and (b) XZ specimens

The observation on traditional alloy was performed on the cross section realized into a plane parallel to the main direction of the bar. The Figure 4-18 (a) reports a very intensive selective attack that penetrating for 200 µm confirming the analytic corrosion rate. The attack was more intensive at the centre of the bar with comparison to the border. The selective attack corroded the border of austenitic grain, as reported in Figure 4-18 (b) after oxalic acid.

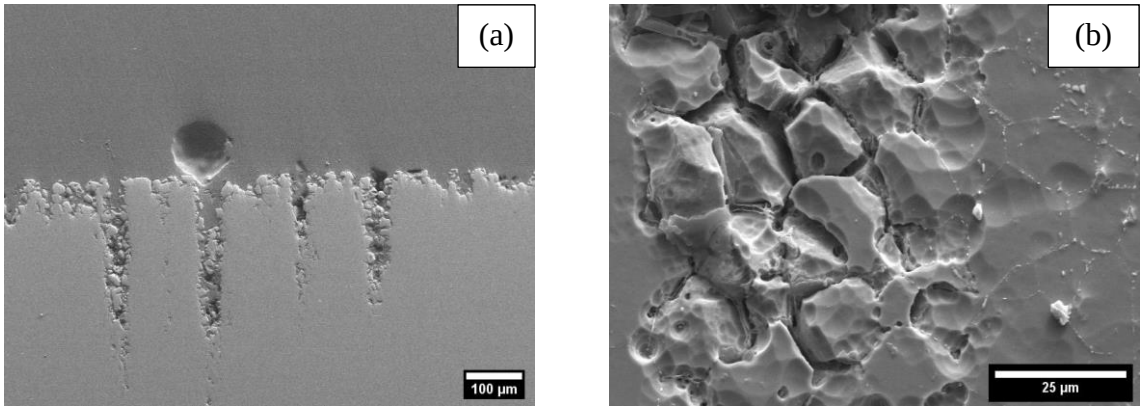

Figure 4-18: (a) SEM image after intergranular test on HW specimens and (b) particular at high magnification of selective attack after oxalic acid .

Critical Crevice Temperature test

The following table reports the results of critical crevice temperature performed at 20, 25, 30 and 40°C. The standard indicates that the attack become considerable if the weight and surface ratio is equal to 0,0001g/cm^2.

Table 4-8: Critical crevice temperature results

Specimens	Temperature	Specimen n°	Surface [cm^2]	Initial weight [g]*	Final weight [g]*	ΔM[g]	N° sector with number	ΔM/Surface [g/cm^2]
LPBF UT	20	1	13.37	27.81113	27.81097	0.00016	1	0.00001
		2	13.49	28.22556	28.22527	0.00028	2	0.00002
	25	1	13.51	28.26928	28.26580	0.00348	3	0.00026
		2	13.46	28.15209	28.15198	0.00010	1	0.00001
	30	1	13.50	28.28908	28.28890	0.00018	0	/
		2	13.47	28.08707	28.08156	0.00550	6	0.00041
	40	1	13.37	27.78046	27.76883	0.01163	7	0.00087
		2	13.14	27.22880	27.20368	0.02513	10	0.00191
Hot Worked	20	1	10.92	23.37711	23.37699	0.00012	1	0.00001
		2	11.60	25.75445	25.75427	0.00017	1	0.00001
	25	1	11.12	24.10286	24.08978	0.01307	7	0.00118
		2	11.51	25.69168	25.67783	0.01385	6	0.00120
	30	1	11.20	24.39887	24.39482	0.00405	2	0.00036
		2	11.40	24.98829	24.94103	0.04726	4	0.00414
	40	1	10.92	23.33335	23.29643	0.03691	4	0.00338
		2	11.08	23.96001	23.85351	0.10650	11	0.00961
LPBF HT 980°C	20	1	13.50	28.25766	28.25740	0.00026	2	0.00002
		2	13.55	28.57210	28.56950	0.00260	0	/
	25	1	13.47	28.33384	28.33339	0.00045	4	0.00003
		2	13.54	28.54620	28.54583	0.00037	2	0.00003
	30	1	13.54	28.53434	28.53026	0.00408	3	0.00030
		2	13.57	28.42263	28.41562	0.00701	6	0.00052
	40	1	13.50	28.20869	28.18991	0.01878	4	0.00139
		2	13.21	27.56083	27.52825	0.03258	12	0.00247

* average of 3 weights with standard deviation of 0.00001 g

The LPBF-UT specimens exhibited a critical crevice temperature of 25 °C. Only one specimen underwent the attack with a value equal to 0.00026 g/cm^2. The same critical temperature was found for hot worked alloy, achieving a value of 0.00120 g/cm^2.The LPBF heat treatment specimen showed a critical crevice temperature of 30 °C.
The Figure 4-19 shows the morphology after the test at 20°C, all the specimens underwent a slight damage far from the crevice attack.

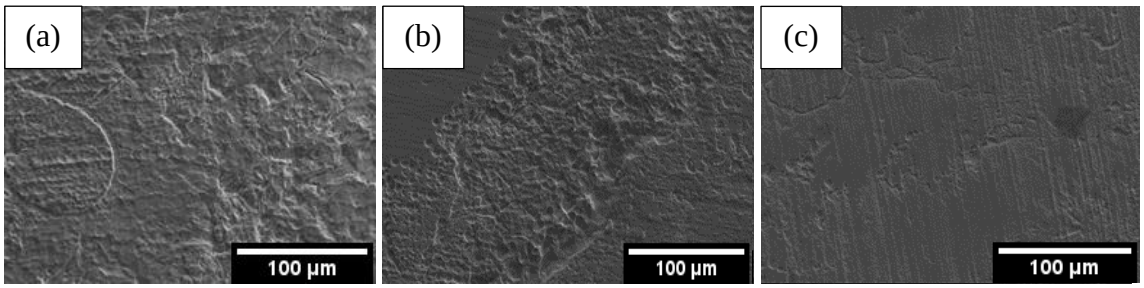

Figure 4-19: Morphology after CCT test at 20°C for (a) LPBF-UT, (b) HW and (c) LPBF-HT

At 25°C, the LPBF-UT specimens underwent the crevice corrosion, as highlighted in the Figure 4-20. Inside the crevice, the typical columnar and cellular structure was found.

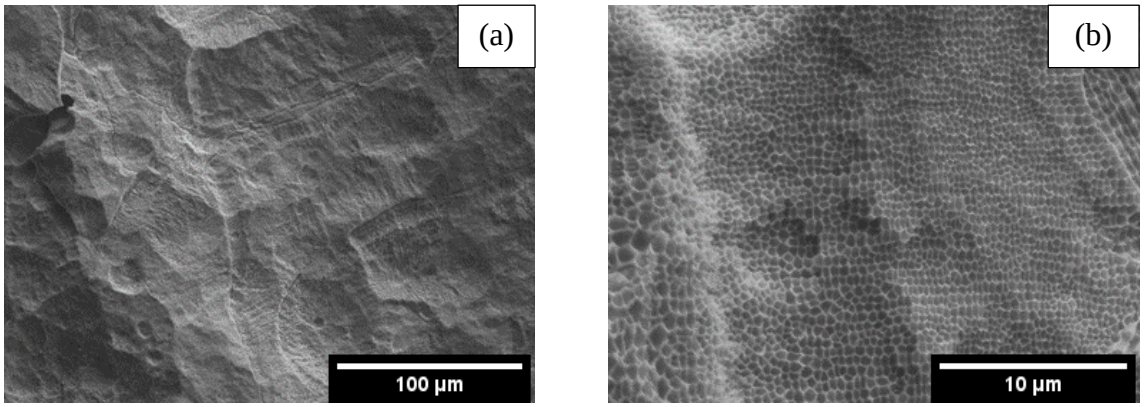

Figure 4-20: Morphology of the attack at 25°C on LPBF UT (a) at low magnification and (b) at high magnification

The traditional material showed a morphology that emphasised the austenitic grains with the precipitates rich in niobium and titanium, as reported in Figure 4-21 and Table 4-9.

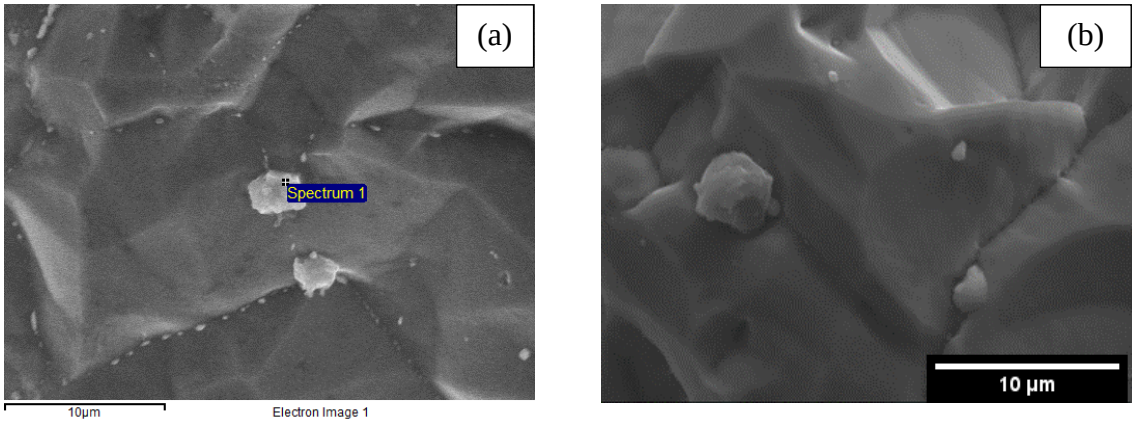

Figure 4-21: (a) EDS scan of precipitate and (b) morphology after test at 25 °C on HW specimen

Table 4-9: EDS of Spectrum 1 shows upstairs

Spectrum 1	Ni	Cr	Nb	Ti	Si	C	O
% wt	19,3	8,4	21,67	24,63	0,25	16,41	8,25

The tests conducted at 30 °C induced a more penetrating attack on the LPBF-UT specimens. The corrosion morphology already found in the lower temperature tests was exhibited. In HW discs, the increase of the temperature produced more penetrating attacks. Figure 4-22reports the morphology of the crevice attack at 30 °C on the LPBF HT cube. The corrosive attack was not limited only to the surface layer, but in some area became more intensive (Figure 4-22 (a)).

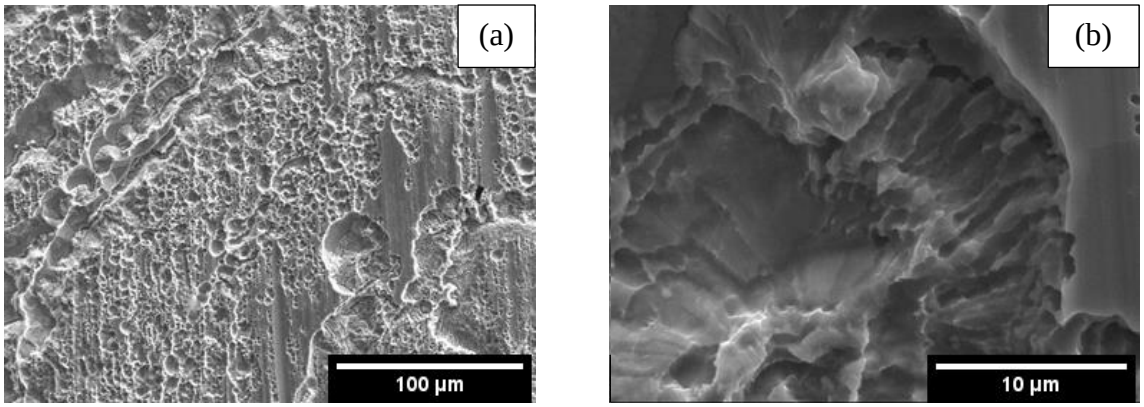

Figure 4-22: (a) LPFB HT specimens after the test at 30°C; (b) morphology at high magnification

By increasing the test temperature up to 40 °C, the materials became more susceptible to localized attack, showing significant damage.

Inside the damage area, the heat-treated LPBF specimens presented areas that are not completely recrystallized (Figure 4 23).

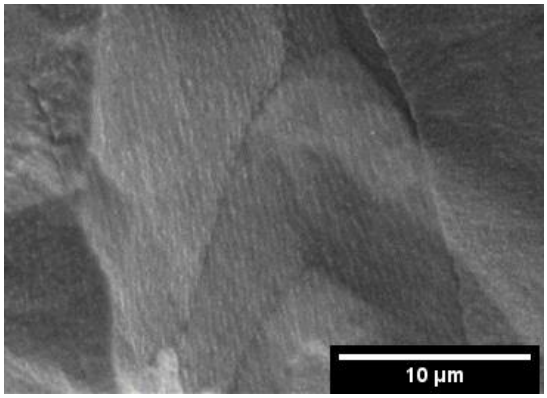

Figure 4-23: Not recrystallized zone inside the damage area for the LPBF-HT after the test at 40°C.

Critical Pitting Temperature test

The first attempt to determine Critical Pitting Temperature (CPT) was performed temperature at 75 °C that was the starting temperature according to the standard. Table 4-10 shows the results of the tests.

Table 4-10: CPT result at 75°C [average of 3 weights with standard deviation of 0.00001 g]*

Specimens	Temperature[°C]	Surface [cm^2]	ΔWeight* [g]	Attack number	ΔM/Surface [g/cm^2]
LPBF UT	75	13.47	1.35707	4	0.10073
HW		11.03	0.00014	0	0.00001
LPBF HT		13.46	0.57790	1	0.04293

After 72 hours of testing, considerable damage was observed on the specimen obtained by LPBF that was not heat treated. The ratio of weight lost compared to the exposed surface was 0.10073 g/cm^2, well above the 0.0001 g/cm^2 declared by the standard to identify the presence or absence of pitting. Conversely, no localized attack was observed on the traditional alloy. The heat treatment of LPBF specimen led to a significant improvement in corrosion performance compared to the untreated one. Only one corrosive attack was observed with a ratio of 0.04293 g/cm^2. However, the damage was still very high. All the attacks highlighted on the LPBF cubes were near to the unpolished edge. For this reason, a second test, using the same condition, was performed on cubes with polished edge in order to understand the effect of the rough surface.

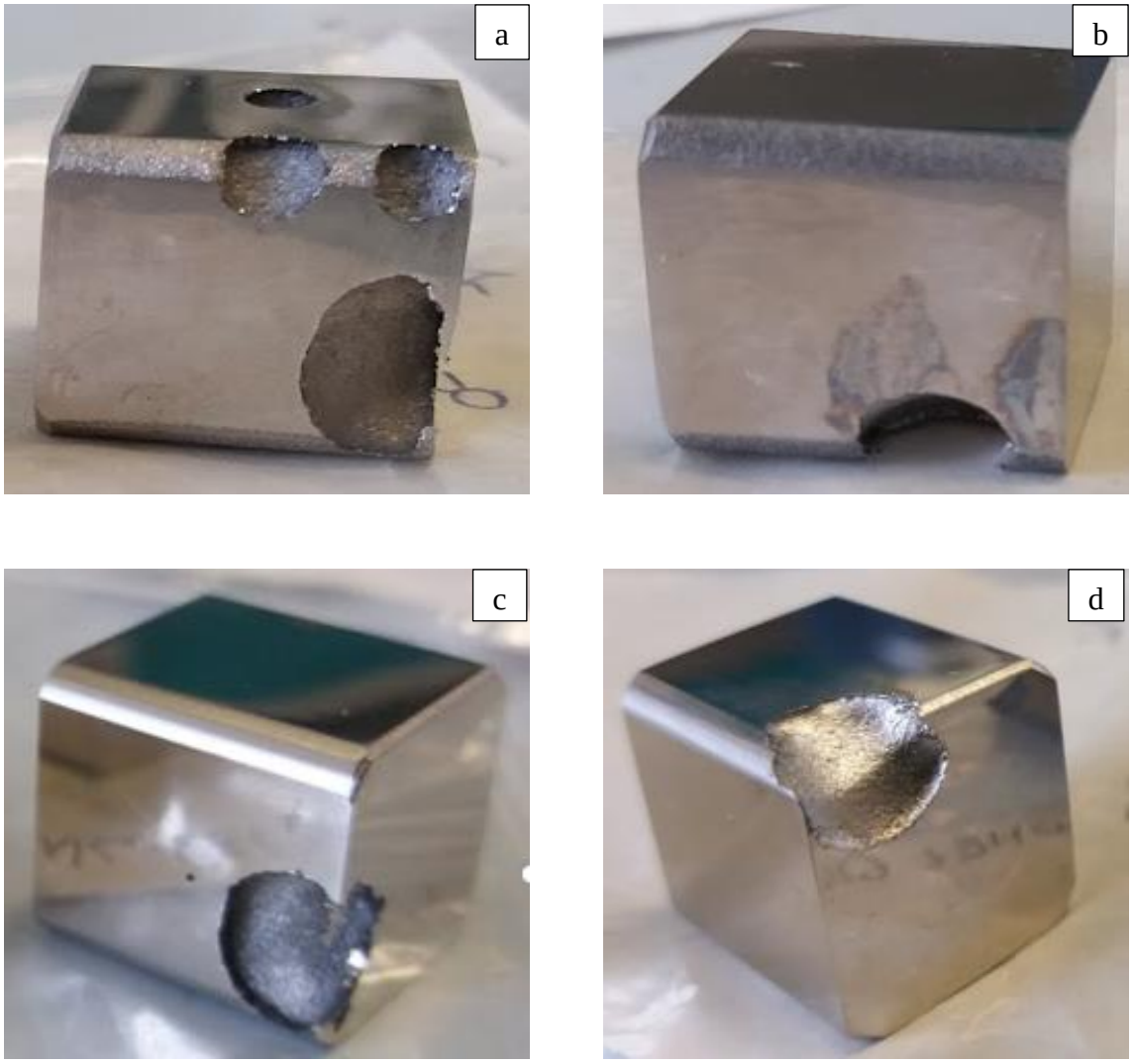

Figure 4-24: Localized attacks after the test at 75°C on (a) LPBF-UT, (b) LPBF-HT, (c) LPBF-UT with polished edge and (d) LPBF-HT with polished edge

The second test results remarked the result obtained with rough edge. (Figure 4-24).
The SEM observation underlined the aggressiveness of the attack on the 3D printed alloy after the exposure at 75°C (Figure 4-25 (a)). The dendritic structure was again recorded (Figure 4-25 (b)). Regarding to the LPBF-HT, second phases rich in niobium and carbon were detected, never recorded before. The corrosion was not stimulated by these phases (Figure 4-25 (c)). The Table 4-11 reports the EDS analysis on this particle.

Table 4-11: EDS spectrum result on the particle recorded on the LPBF-HT specimen

Spectrum 1	Ni	Cr	Mo	Nb	C	O	Al	Ti	Fe	Total
% wt.	40.75	14.64	11.53	9.58	8.27	13.88	0.32	0.6	0.44	100

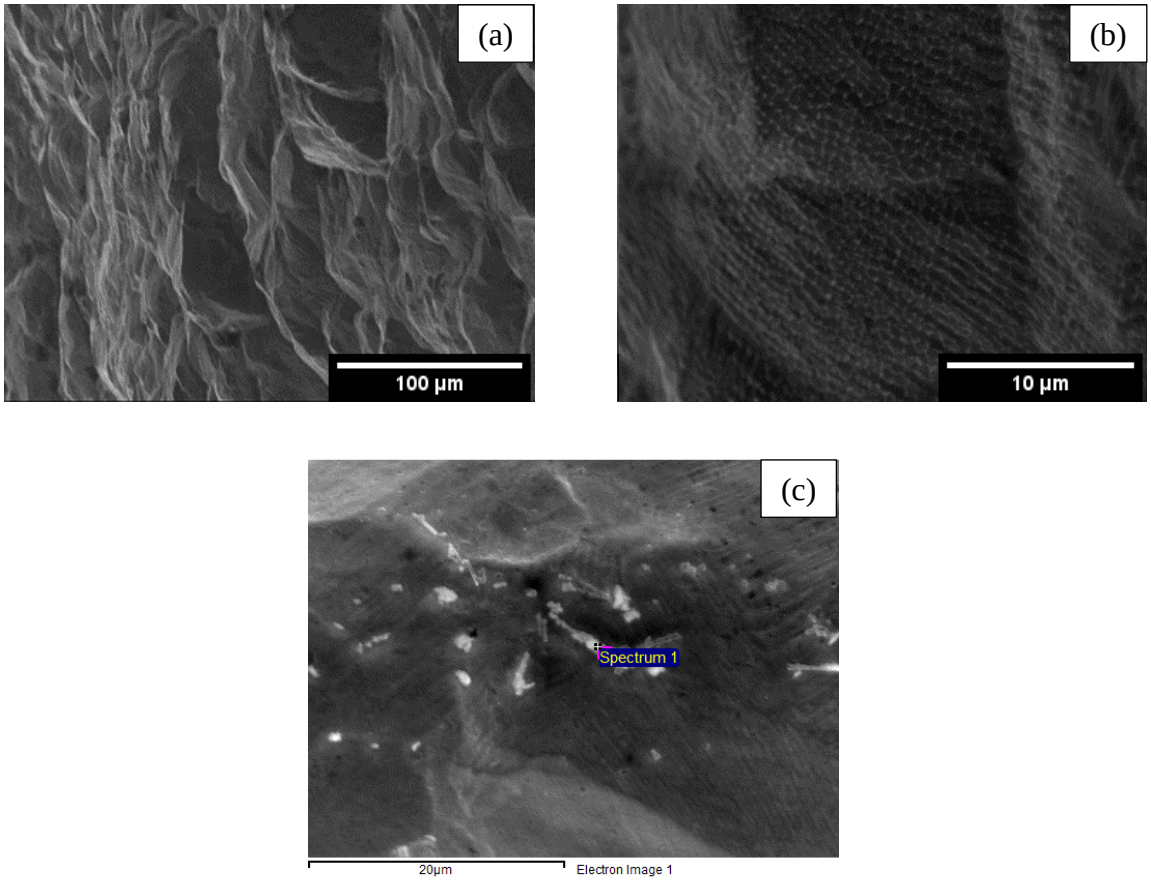

Figure 4-25: (a) Morphology of the attack after CPT test at 75°C and (b) high magnification of morphology attack on LPFB-UT;(c) EDS spectrum on LPBF-HT

A third test using 60°C was performed. The LPBF-UT specimens presented a slight corrosion not considered sufficient by the standard.

The pit observed at 60 °C was large about 400 µm as shown in Figure 4-26. At high magnification the melt pool structure was observed inside the pit (Figure 4-26 (b)).

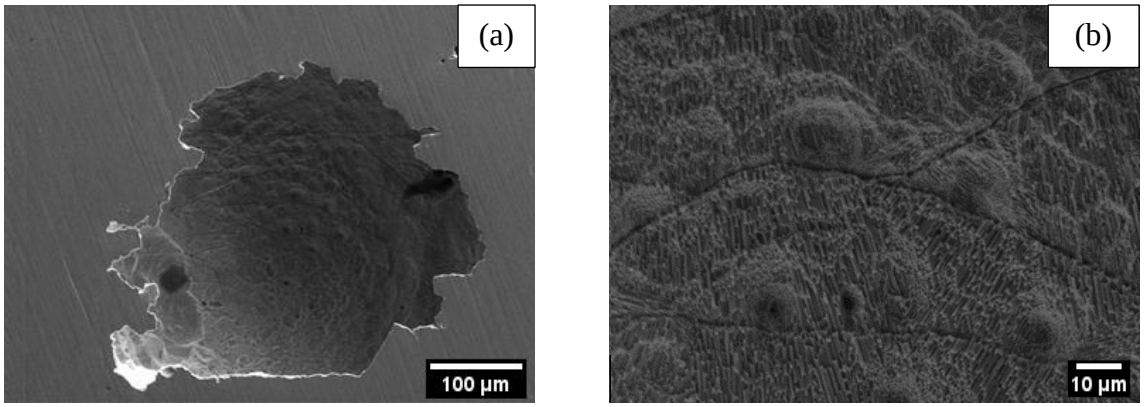

Figure 4-26: (a) Pit recorded on LPBF-UT after the test at 60°C; (b) microstructure inside the pit

Stress Corrosion Cracking test

Stress corrosion cracking (SCC) tests were conducted on LPBF-UT specimens at temperatures of 155 °C and 170 °C, for 168 hours. Both building directions did not show the stress corrosion cracks. The replication of the tests at 170 ° C on the U-bend remarked the same results. The heat treatment does not affect the corrosion resistance. The Table 4-12 reports all the results.

Table 4-12: SCC at 155 and 170°C results

Specimen	Temperature [°C]	Building direction	Specimen number	Initial weight * [g]	Final Weight * [g]	ΔM [g]	Crack	Immersion type
U-bend LPBF UT	155	XY	1	29.80806	29.80671	0.00134	NO	Full immersion
		Z	1	27.21266	27.20922	0.00344	NO	
U-bend LPBF UT	170	XY	1	27.16713	27.16435	0.00278	NO	
			2	26.90112	26.89606	0.00507	NO	
		Z	1	31.46677	31.46087	0.00591	NO	
			2	31.46682	31.46087	0.00596	NO	
U-bend LPBF HT 980°C	170	XY	1	27.85226	27.84929	0.00297	NO	
			2	28.27807	28.27352	0.00455	NO	
		Z	1	28.59065	28.58455	0.00610	NO	
			2	28.76252	28.58455	0.17797	NO	

Slow strain rate tests (SSR)

The results of SSR for the LPBF untreated specimens is shown in the Figure 4-27.

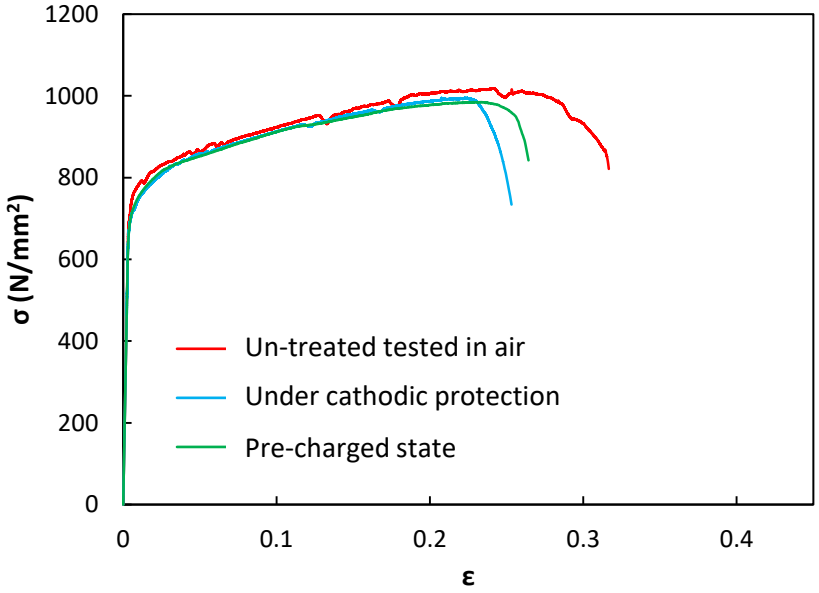

Figure 4-27: SSR results of LPBF-UT at 3.15 10^{-6} s^{-1} (red line) in air, at 3.15 10^{-6} s^{-1} (red line) under cathodic protection (blue line) and at 3.15 10^{-5} s^{-1} (green line) after hydrogen charging

The alloy tested in air at 3.15 10^{-6} s^{-1} showed a very pronounced plastic region achieving 1018 MPa of ultimate stress and 0.316 of strain to rupture. The same alloy under cathodic protection presented a reduction of strain to rupture achieving a value equal to 0.25. The condition with hydrogen pre-charged and strain velocity of 3.15 10^{-5} s^{-1} showed an intermediate behaviour.

The Figure 4-28 shows the SSR result obtained using LPBF-HT specimens. The air test indicated a very large plastic region. The specimens reached maximum stress of 953 Mpa and strain of 0.425. The cathodic protection at -1.1 V *vs.* Ag/AgCl strongly reduced the plastic region led to a strain equal to 0.189 and stress of 893. Again, the pre-charging represented an intermediate condition, close to the test in air, leading to a strain of 0.381.

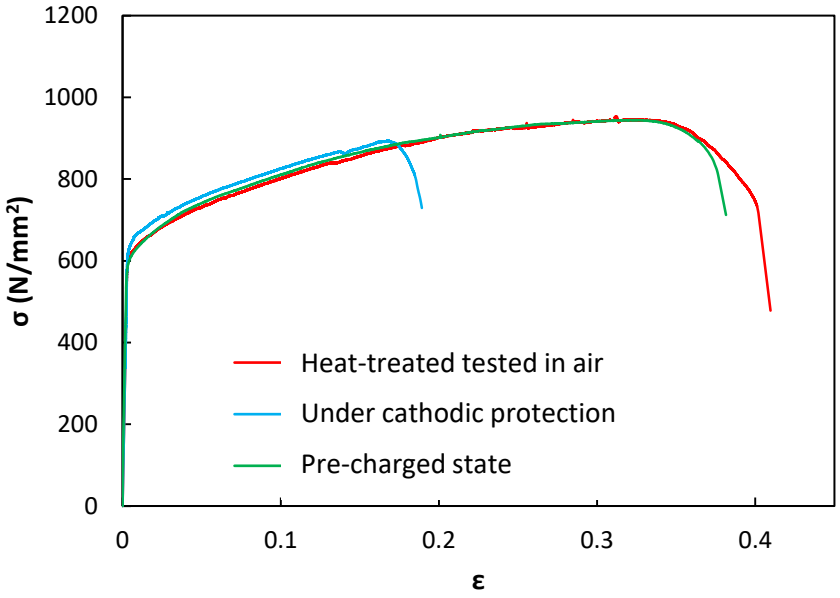

Figure 4-28: SSR results of LPBF-HT at 3.15 10^{-6} s^{-1} (red line) in air, at 3.15 10^{-6} s^{-1} (red line) under cathodic protection (blue line) and at 3.15 10^{-5} s^{-1} (green line) after hydrogen charging

The fractography exam was carried out for all the specimens by SEM. The fracture surface after the test carried out in air showed clearly a typical ductile surface characterized by the dimples (Figure 4-29 (a)). Moreover, defects inside the specimens was detected that can decrease the mechanical strength (Figure 4-30).

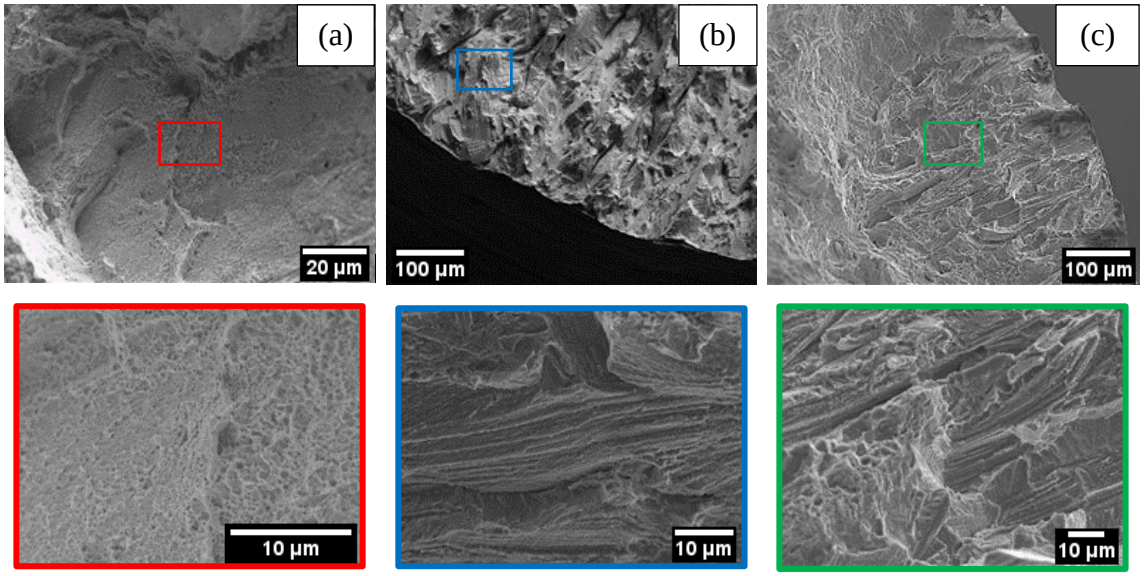

Figure 4-29: Images of fracture zone for the LPBF UT specimens (a) at 3.15 10^{-6} s^{-1} in air, (b) at 3.15 10^{-6} s^{-1} under cathodic protection and (c) at 3.15 10^{-5} s^{-1} after hydrogen charging

The LPBF-UT specimen under cathodic protection showed a different fracture surface with flat zone differently oriented. The pre-charged LPBF-UT specimen presented the same morphology with a limited extension (Figure 4-29-(b)-(c)). For these specimens the dimples area is delineated only in the specimen centre.

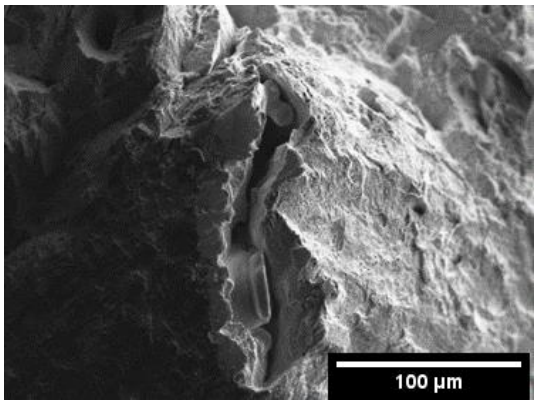

Figure 4-30: Internal defect recorded into the SSR specimen

After the test in air, the LPBF heat treated specimen showed a fracture surface with dimples indicating the ductile character of this material (Figure 4-31-(a)). Under cathodic protection the fracture morphology completely changes showing a fibrous zone preferentially directed to the centre of the specimen (Figure 4-31-(b)). The pre charged condition is an intermediate condition with a mixed fracture morphology between the two previously discussed.

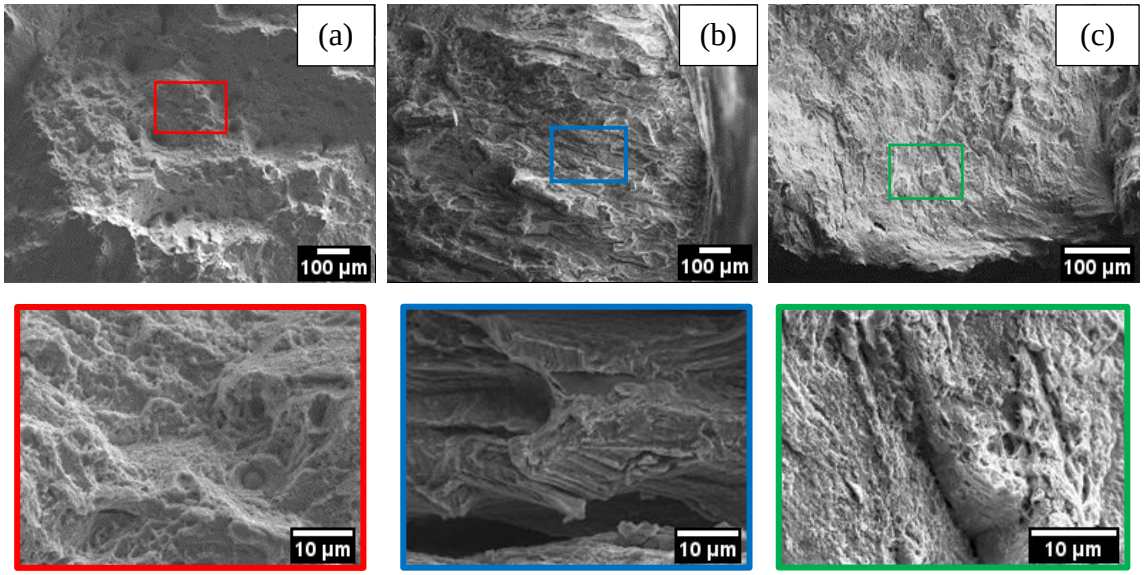

Figure 4-31: Images of fracture zone for the LPBF HT specimens (a) at 3.15 10^{-6} s^{-1} in air, (b) at 3.15 10^{-6} s^{-1} under cathodic protection and (c) at 3.15 10^{-5} s^{-1} after hydrogen charging

Potentiodynamic tests

The Figure 4-32 shows the average E_{corr} recorded before the potentiodynamic tests, calculated over 600 seconds. After the specimens were immersed in the solution, they reached a steady state E_{corr} within a few tens of seconds. The E_{corr} values were always higher than the equilibrium potentials of hydrogen. Furthermore, the E_{corr} decreased with increasing the pH. No differences in terms of E_{corr} of LPBF-UT-P and HW-P specimens were noticed, although the LPBF-HT-P samples had slightly lower E_{corr}.

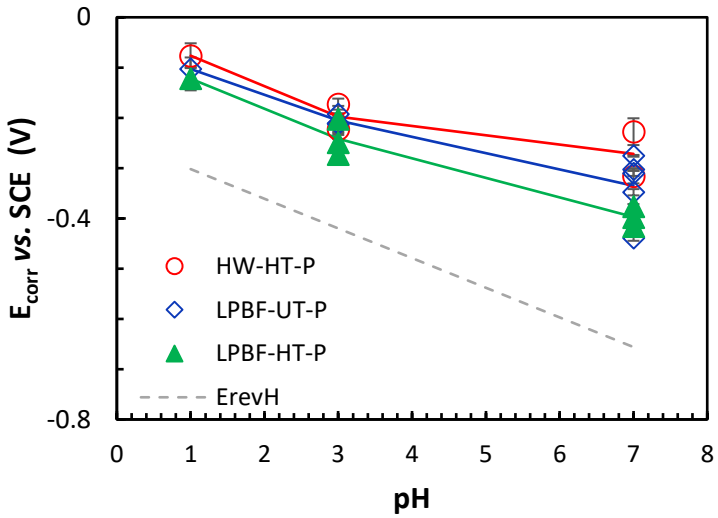

Figure 4-32: OCP (average values on 600 s) of the specimens before the potentiodynamic tests in H2SO4 0.5 M solution at pH 1, in 0.6 M NaCl acidified at pH 3 solution and in neutral NaCl 0.6 M at pH 7[156]

Some examples of the cyclic potentiodynamic curves are shown in Figure 4-33. Figure 4-33 (a) shows the potentiodynamic (PD) curves obtained in H_2SO_4 0.5 M solution for every condition. All the specimens presented a passive behaviour over a wide range of potential thus confirming the very high corrosion resistance of the alloy 625. A similar behaviour was observed in NaCl 0.6 M solution acidified with HCl to pH 3 (Figure 4-33 (b)). In these solutions, no localized attack (pitting or crevice) was observed. Conversely, the presence of crevice attacks was detected on some specimens after the potentiodynamic test in neutral NaCl 0.6 M solution as indicated by the hysteresis loop in the potentiodynamic curve (Figure 4-33 (c)).

The potentiodynamic curves of LPBF specimens with as-built surface (AB) were showed in the Figure 4-34. The passive range was limited with comparison to the polished specimens, the current density for the passive range was 1.2 µA/cm^2 for the untreated alloy and 2.7 for the heat-treated ones. Furthermore, the curve for the LPBF-UT showed a lot of anodic spikes.

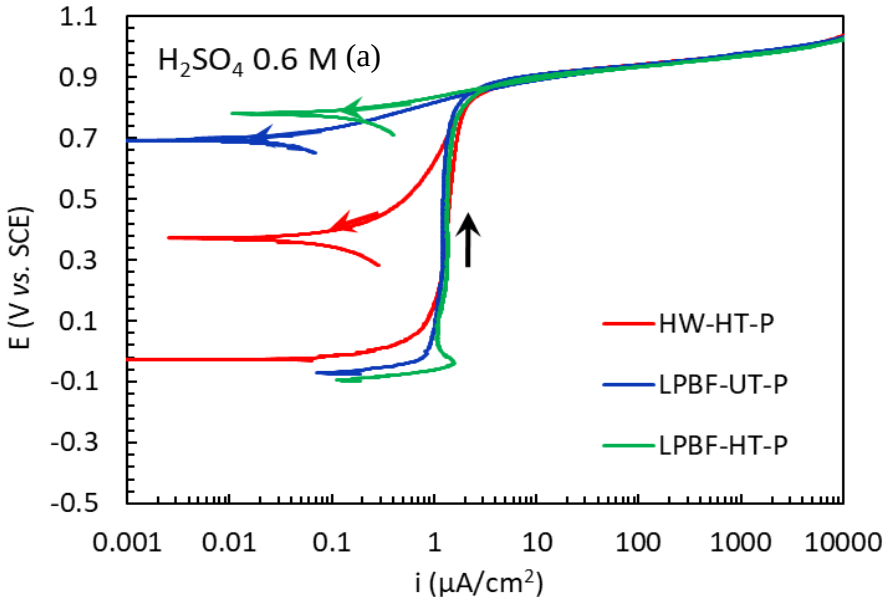

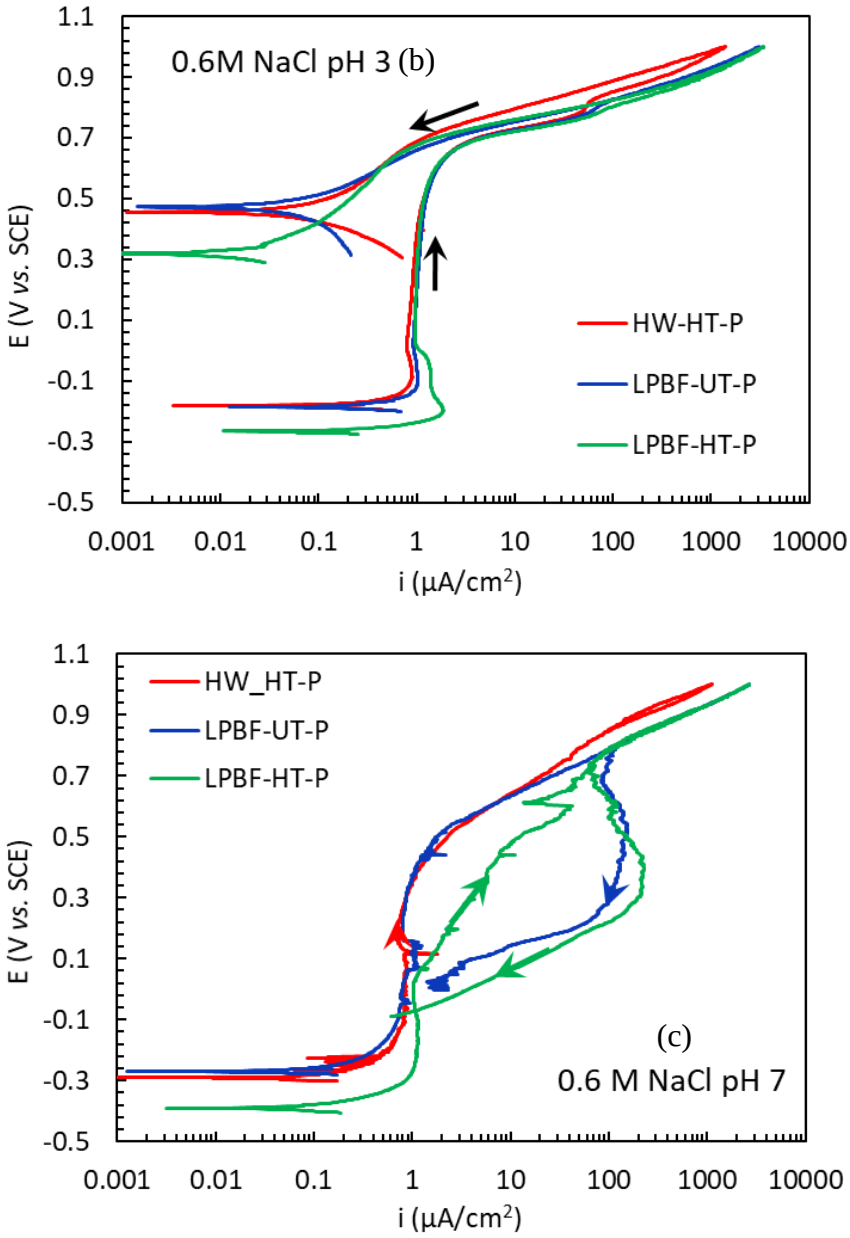

Figure 4-33: Potentiodynamic polarization curves of the HW and LPBF specimens (a) in H2SO4 0.5 M solution; (b) in 0.6 M NaCl acidified at pH 3 solution and (c) in neutral NaCl 0.6 M solution [156]

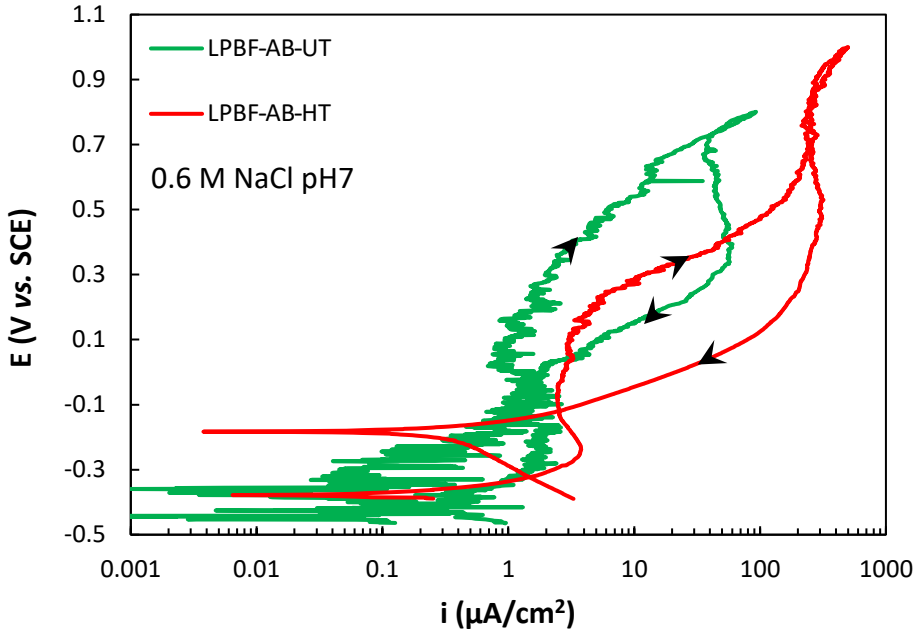

Figure 4-34: Potentiodynamic curves of the LPBF-UT specimens and LPBF-HT specimens with as-built (AB) surfaces, in NaCl 0.6 M solution.

Potentiostatic tests

The Figure 4-35 shows the result of potentiostatic test carried out at +200 mV *vs.* SCE in 0.6 M NaCl at pH 7. The LPBF untreated showed a passive behaviour with a passive current of 0.1 µA/cm^2 after about 13 h. The heat treatment on the same alloy did not change the corrosion resistant and the specimens LPBF-HT had passive current equal to 0.2 µA/cm^2. Instead, the hot-worked alloy showed a corrosion attack after few minutes after the immersion. Only one test showed a passive behaviour for this alloy with anodic current density of 0.1 µA/cm^2.

The Figure 4-36 reports the curves obtained at +500 mV *vs.* SCE. In the first test LPBF-UT showed a stable passive behaviour with anodic current density of 1.5 µA/cm^2, instead in the second test a temporary breakdown of passive film was recorded. Concerning the LPBF-HT, all the tests reported that the alloy underwent localized corrosion, but one specimen was able to re-passivate. The HW alloy evidenced a trend similar to the LPBF-HT.

The morphology inside the crevice of the HW specimens evidenced the austenitic grains and the preferential corrosion of the niobium rich precipitates on their borders (Figure 4-37 (a) and (b)).

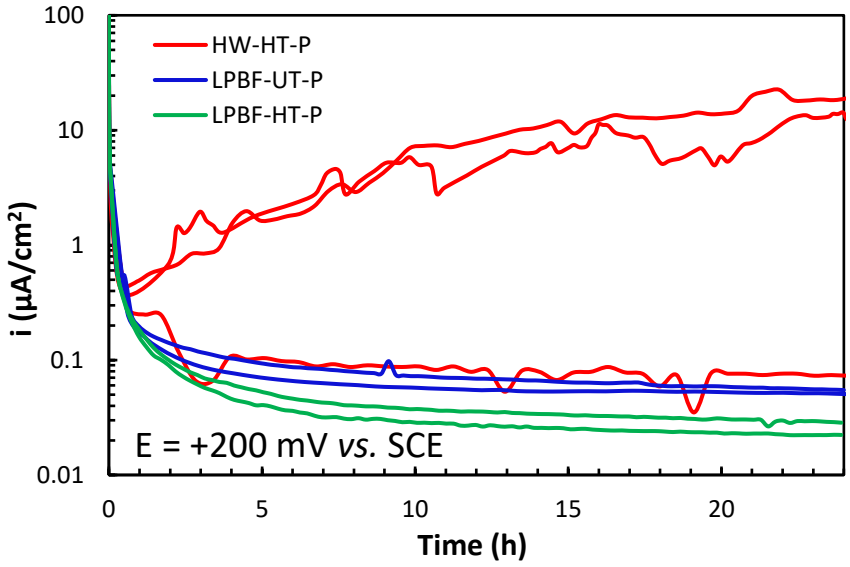

Figure 4-35: Current density vs. time curve in potentiostatic tests at + 200 mV vs. SCE in NaCl 0.6N solution at pH 7

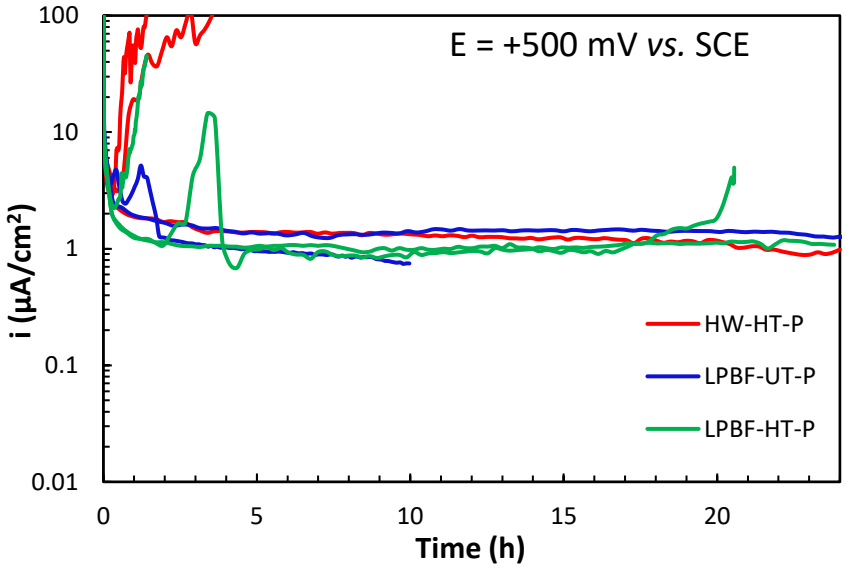

Figure 4-36: Current density vs. time curve in potentiostatic tests at + 500 mV vs. SCE in NaCl 0.6N solution at pH 7

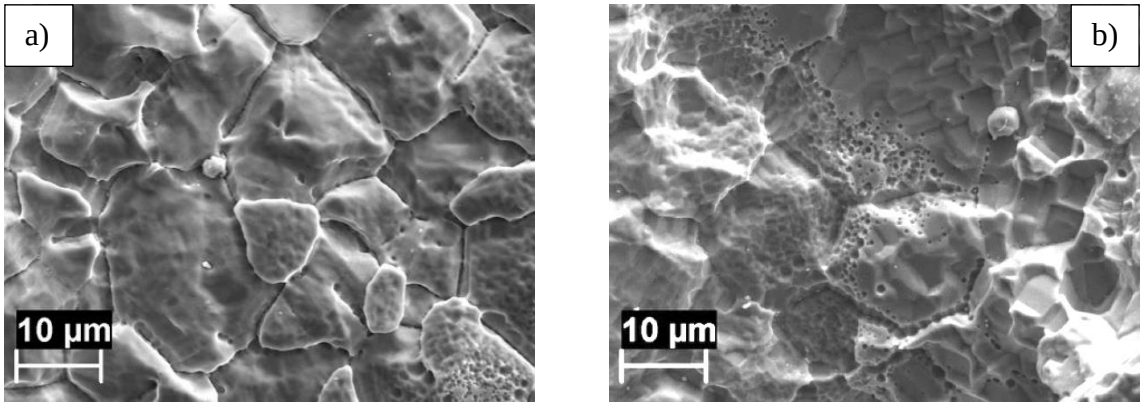

Figure 4-37: SEM images of the corrosion morphology inside the crevice of a HW-HT specimen after the potentiostatic tests in NaCl 0.6N solution at a) E = +0.2 V *vs*. SCE; b) + 0.5 V *vs*. SCE

Conversely, the corrosion attack observed on the LPBF-UT after the potentiostatic tests at +500 mV *vs*. SCE took place preferentially along the edge of the melt pools (Figure 4-38 (a) and (b)).

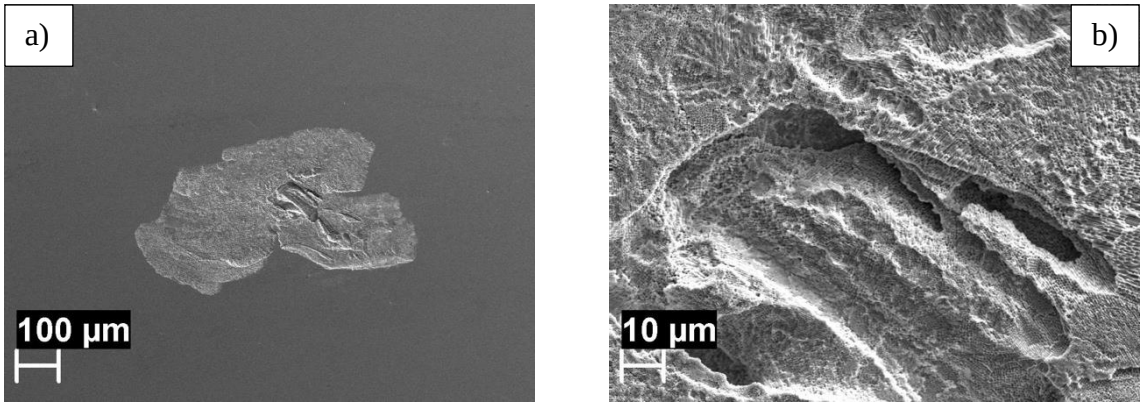

Figure 4-38: SEM images of the morphology of corrosion inside a shallow attack of a LPBF-UT-P specimen after the potentiostatic tests in NaCl 0.6N solution at + 0.5 V vs. SCE; (b) close-up at higher magnifications

Finally, LPBF-HT specimens showed an intermediate microstructure inside the attack: the re-crystallized equiaxed grains showed a morphology of corrosion similar to HW, but the absence of macro precipitates did not promote the selective attack (Figure 4-39 (a) (b)).

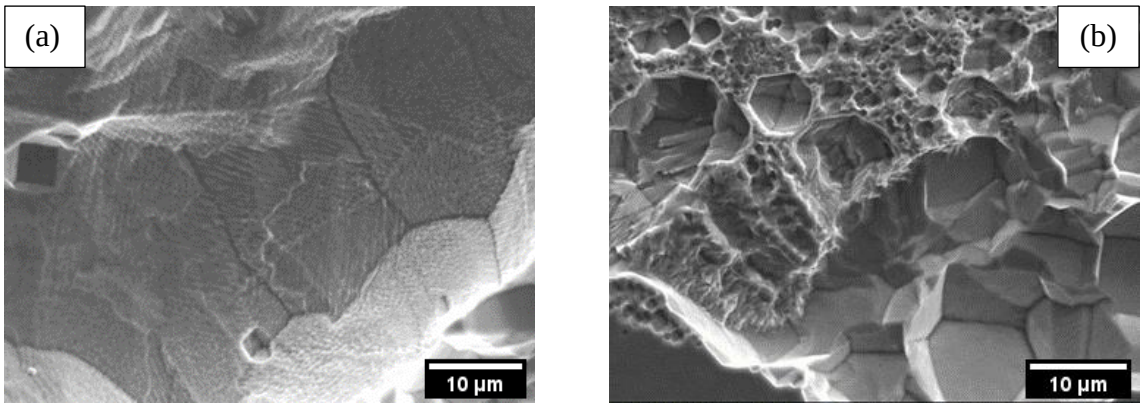

Figure 4-39: SEM images of the morphology inside the crevice of a LPBF-HT-P specimen after the potentiostatic tests in NaCl 0.6N solution at + 0.5 V vs. SCE; (a) intergranular attack in a zone fully re-crystalized of the specimen and (b) mixed morphology in a zone of the same specimen not fully re-crystalized

Electron backscattered diffraction (EBSD)

The Figure 4-40 (a, b, c, d) shows the Inverse Pole Figure (IPF) Z maps come from EBSD map for the LPBF specimens. The LBPF untreated specimens showed a microstructure preferentially oriented in {001} direction (red colour) with irregular crystallographic structures that had dimension larger than the melt pool. The heat treatment changes the morphology and the orientation of the grain. Geometrical forms with small colour variation was also detected.

Equiaxed grains in an average size of 20 µm and some annealing twins were observed in the traditional alloy 625, as shown in Figure 4-40 (e)

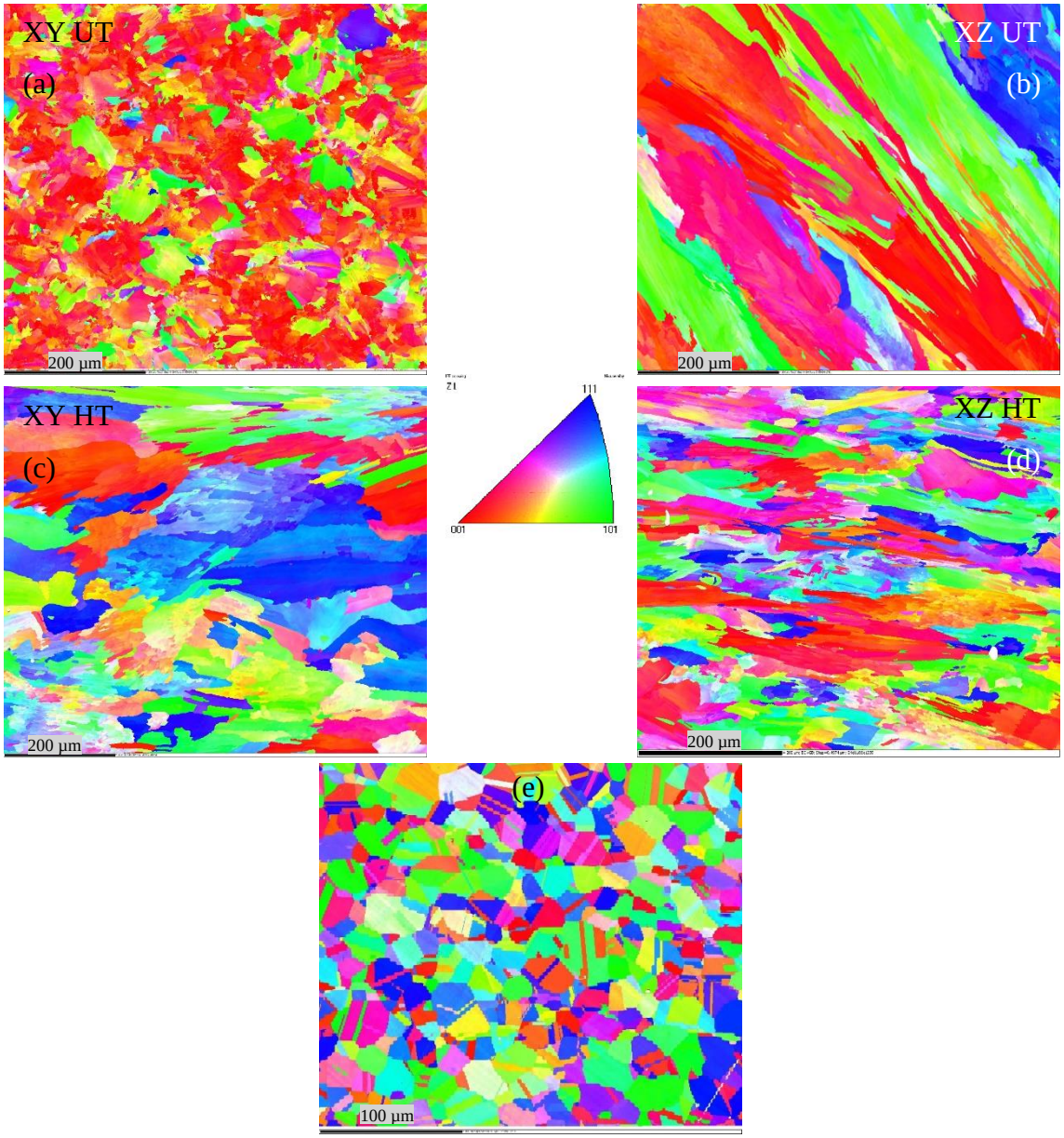

Figure 4-40: (a,b) EBSD IPF Z maps for the LPBF UT specimens in function of the building direction; : (c,d) EBSD IPF Z maps for the LPBF HT specimens in function of the building direction; (e) : EBSD IPF Z maps for the hot worked alloy 625

Scanning Kelvin Probe Force Microscope (SKPFM)

The Figure 4-41 reports the Volta potential maps obtained form SKPFM for the LPBF alloy 625. For all the specimens regardless the heat treatment, the microstructure had uniform potential without relevant different between the melt pool.

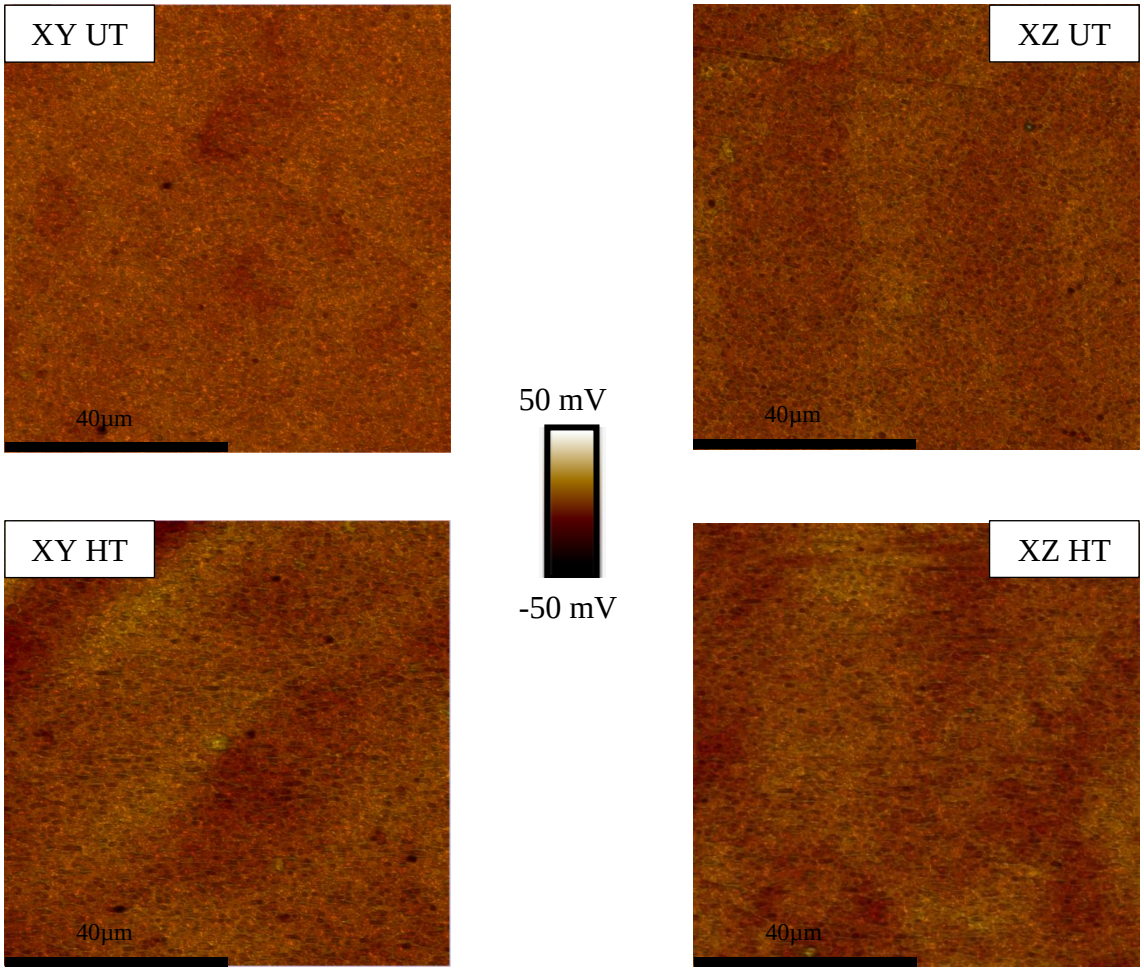

Figure 4-41: SKPFM Volta potential maps for alloy 625 processed by LPBF

Instead, the traditional alloy presented cathodic macro precipitates. On the same precipitates the EDS analysis showed that the particles were formed preferentially by Nb and Ti or Ti, Nb, and N (Figure 4-42 and Table 4-13).

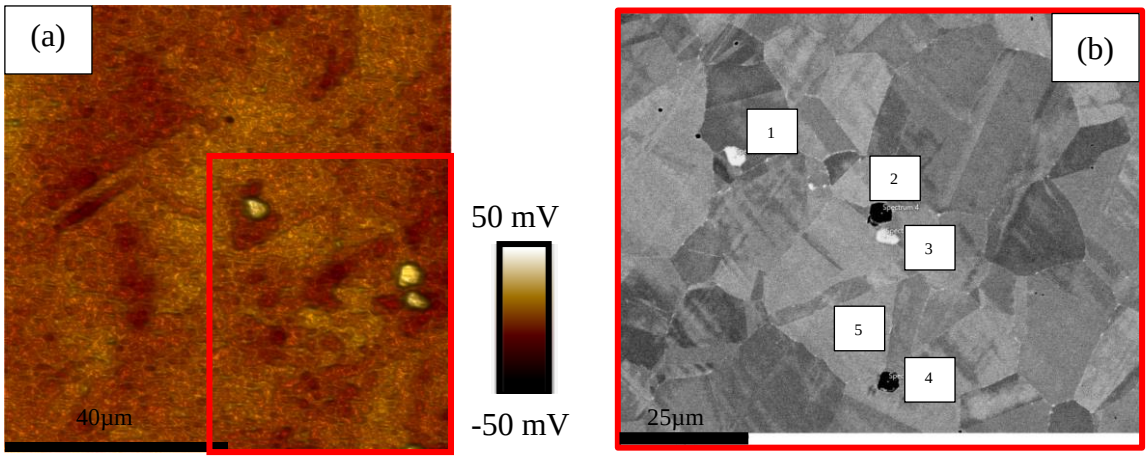

Figure 4-42: (a) Volta potential map of hot worked alloy; (b) EDS on the same precipitates with the compositions.

Table 4-13: EDS analysis of precipitates

	Weight %					
EDS spectra	Nb	Ti	Ni	Cr	N	Mo
1	91.5	4.9	2.7	0.9		
2	29.3	50.9	1.7	1.8	14.6	
3	92	4.4	2.5	1.1		
4	32.3	47.5	2.7	2.1	15.2	
5	3.3		62.6	22.6		8.5

Rockwell and Vickers tests

The Figure 4-43 reports the mean values of the Vickers hardness tests. The LPBF untreated alloy showed values of 300 HV. The heat treatment does not strongly modify the values of hardness that achieve 310 HV. Instead the hot worked specimens showed values of 230 HV with high dispersion. Figure 4-44 shows the Rockwell C hardness values. The LPBF untreated and heat treated had 27 HRC while the hot worked had 18 HRC with higher dispersion than the LPBF alloys. The trend presented of the two techniques it is the same.

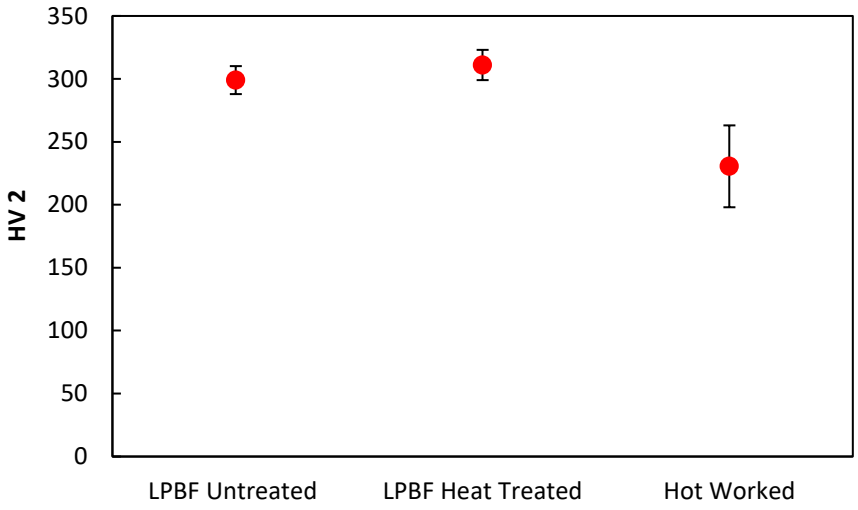

Figure 4-43: Vickers values for LPBF and HW specimens

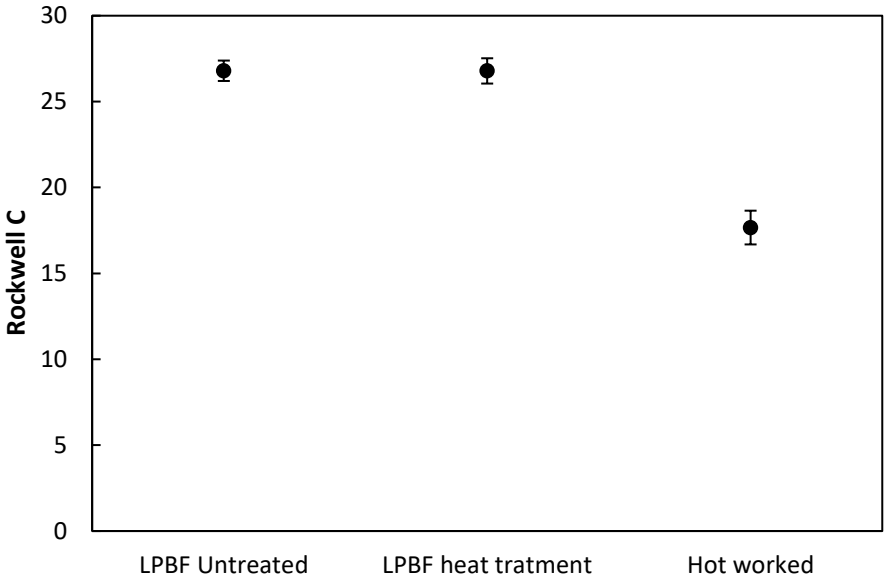

Figure 4-44: Rockwell C values for LPBF and HW specimens

4.2 Generalized corrosion in acid solutions

The Figure 4-45 reports the Haynes® map of iso-corrosion given for the alloy with comparable chemical composition used in Oil&gas field.[157] The experimental data obtained are completely in accordance with this iso-corrosion map. The LPBF-UT alloy showed a stronger resistance to generalized corrosion if compared with the hot worked ones. Instead, the Figure 4-46 reports the iso-corrosion map for the sulfuric acid and it highlights the opposite trend with respect to the previous environmental.[157]

The nickel alloys have higher corrosion resistance than austenitic stainless steels thanks to the higher solubility of the chromium and molybdenum into the austenitic lattice. Cr and Mo are elements that increases the stability of the passive film. Lloyd et al. showed that high-Cr alloys develop thick oxides with a layered structure consisting of an inner Cr-Ni oxide layer and an outer Mo-W oxide. The effect of the chromium is to reduce the corrosion rate in oxidant environment. The molybdenum increases the resistance to localized corrosion, improves the repassivation kinetic and the corrosion resistance in acidic reducing environments.[158,159]

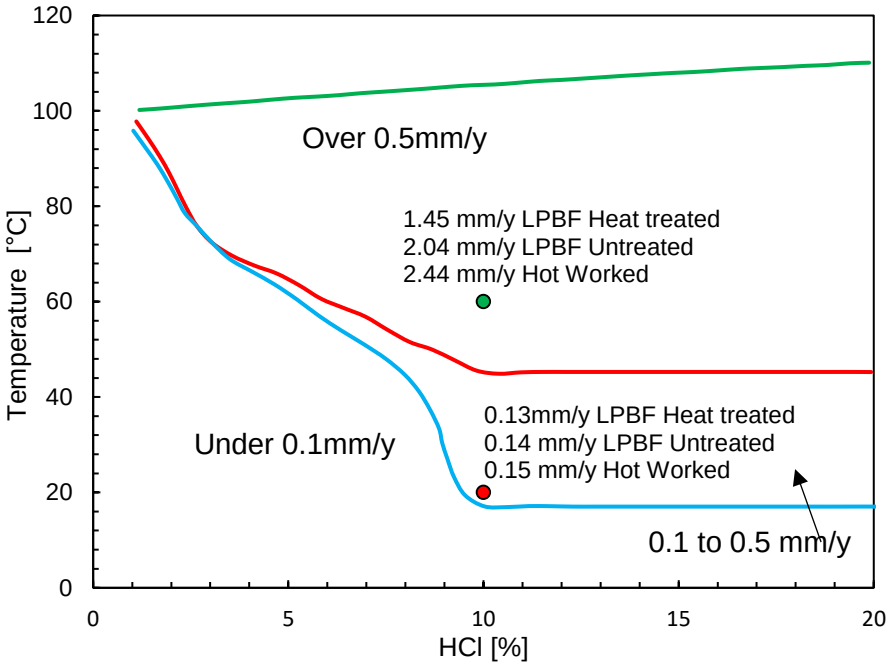

Figure 4-45: Hydrochloric iso-corrosion map for alloy 625.[157]

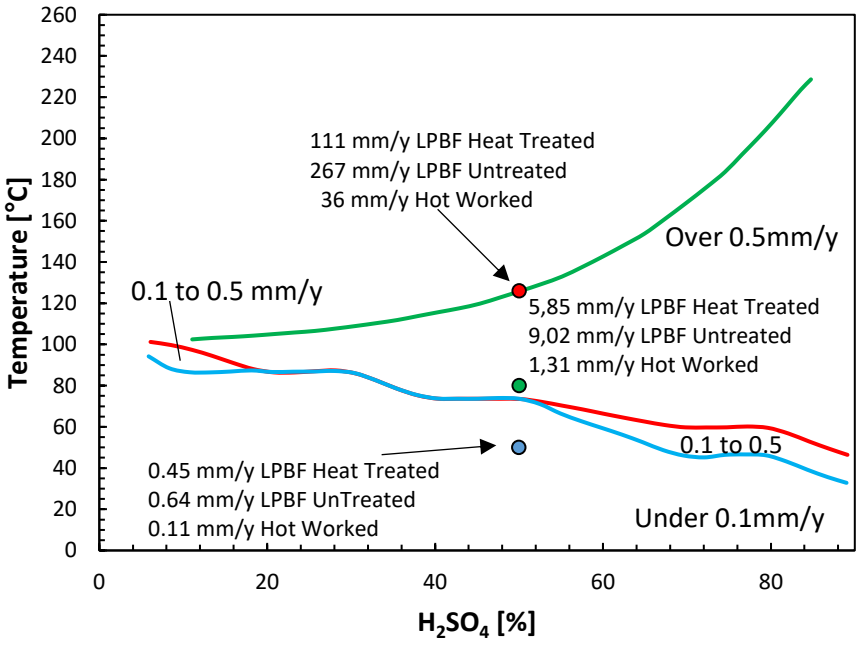

Figure 4-46: Sulfuric iso-corrosion map for alloy 625.[157]

The HW specimens present equiaxed grains with second phases precipitates along the grain boundaries. The EDS analysis of the precipitates evidenced the presence of niobium and molybdenum in the micro-precipitate at the grain boundaries which is consistent with MC carbides and Ni_3Nb phase; moreover, titanium and nitrogen in the macro-precipitates

was also identified (Figure 4-47). The SKPFM map show clearly the cathodic nature of precipitates with respect to the matrix.

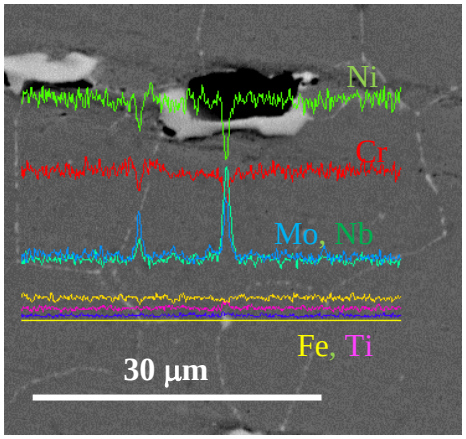

Figure 4-47: EDS line scan on macro precipitates of HW-HT specimen

The specimens obtained via LPBF have different microstructures than those specimens produced via conventional hot working, with nano-size second phases uniformly distributed between the microdendrites.[160–162] The very high cooling rates generate a supersaturated solution leading to high segregation of some elements (e.g. Nb, C) that remain entrapped in the dendritic core, as reported in literature for the LPBF process.[56,163] The supersaturated state is also denote by the presence of very fine Nb-rich MC carbides within the dendritic core.

The heat treatment at 980 °C of the LPBF specimens homogenises the microstructure. The melt pools are no longer detected, as well as macro precipitates of Nb and Mo (Figure 4-48).

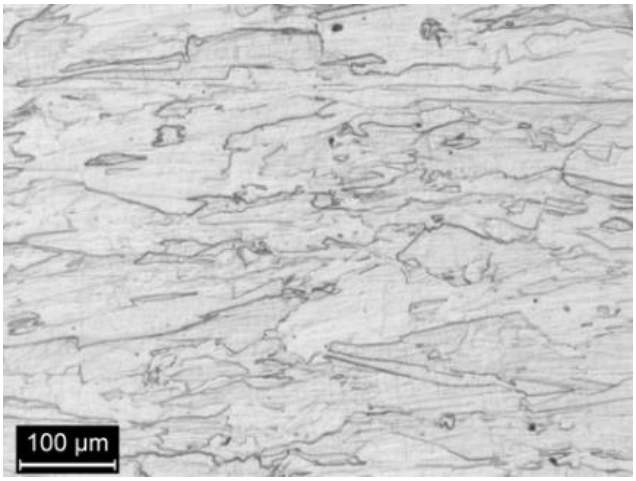

Figure 4-48: Microstructure of the LPBF-HT specimens after metallographic etching

Furthermore, the dendritic structures are not fully re-crystallized, and the LPBF-HT has columnar grains which are aligned along the building direction confirmed also by the EBSD analysis. In fact, the Figure 4-49 shows an elaboration of EBSD map of LPBF heat treated alloy 625. It indicates that using a low angle grain boundary value of 2, a large part of the microstructure is not fully re-crystalized.

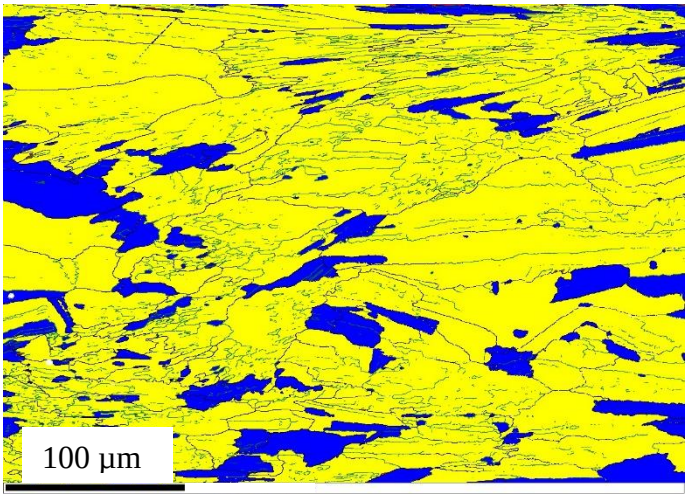

Figure 4-49: EBSD processing map on LPBF heat treated alloy 625 (blue grain → recrystalized structure; yellow grain → substructure)

A mechanism bases on the effects of precipitates could be hypnotize. Yao et al[164] reported that under severe conditions, the Laves phase in T-400 can be preferentially attacked in highly oxidizing environments and the matrix phase preferentially attacked under highly reducing conditions. Nikiforov el al[165,166] underlined the important contribute of the molybdenum for the corrosion resistance and other authors highlight the role of niobium precipitates that can be promote the corrosion rate. The role of Nb rich precipitates in the corrosion of alloy 625 alloy was underlined by Tawancy et al.[70] Authors made tests in boiling 10% nitric acid on alloy 625 annealed and aged at different time and temperature. They concluded that Ni_3Nb phase formed during aging is preferentially corroded owing the lower chromium content compared to the surrounding matrix.

The Figure 4-50 shows the AISI316L anodic behaviour in presence of strong oxidant agent (Fe^{3+} ions) and in reducing conditions. The anodic curves strongly change with the concentrations of chlorides ions.[167] It could be hypotized that increasing the test temperature the anodic curves of the alloy 625 becomes similar than those reported for stainless steel.

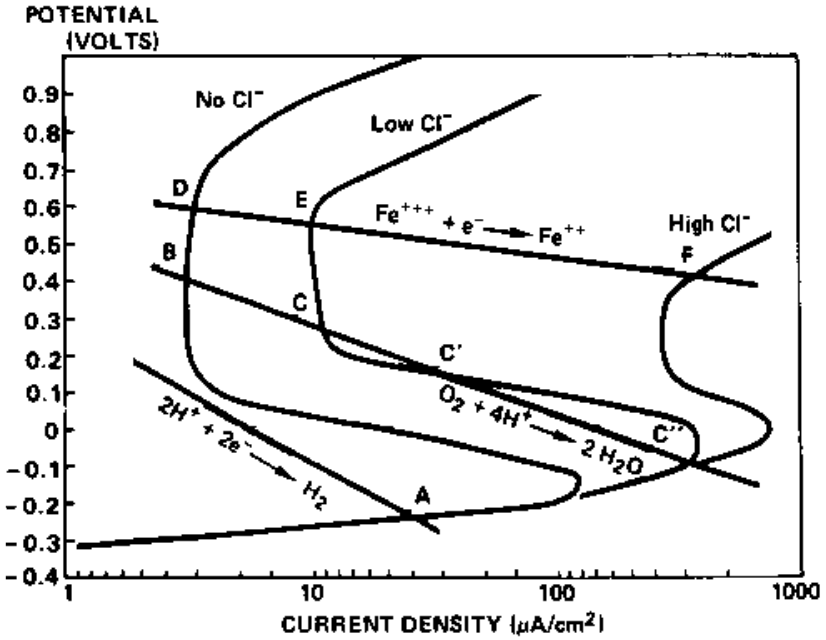

Figure 4-50: Effect of oxidizing agents and chlorides on the anodic curves for AISI 316L[167]

The tests performed in HCl can be analyse considering the central curve in the Figure 4-50 due to the higher corrosion resistance of nickel alloy than AISI 316L and the presence of small part of oxygen into the solution.

For this condition, the anodic curve intercepts the cathodic curve in 3 point leading to 3 different corrosion rates. The first point is the maximum of the nose (c''), the second in the middle of the anodic nose (c') and the last intercepts the anodic curve in the passive zone (c). The corrosion rate is the mean of the 3 values. It is possible to hypothesize that the alloy without precipitates work close to the C point with a small corrosion rate thanks to the passive behaviour. While, the zone near at the precipitate particles the alloy work in the C'' point due to the molybdenum depletion. The specimens exposed to HCl environmental have low corrosion rate but can show a localized attack stimulated by the second phase precipitates. For tests carried out in the H_2SO_4 acid the cathodic curve is based on the hydrogen reduction leading to an active behaviour for the specimens. With the increase of the temperature, the anodic curves change as shown in Figure 4-51 causing very high corrosion rates. These tests underline the galvanic effect of the niobium precipitates. The corrosion rate is proportional to the ratio between the anodic area and the cathodic area. The HW specimens have a low anodic/cathodic area ratio and the presence of precipitates is localized at the grain boundaries limiting the active corrosion.

Conversely, the LPBF alloy have nanometric precipitates homogeneously distributed between the micro dendrites. This microstructure amplifies strongly the corrosion. The heat treatment shows an intermediate behaviour thanks to the intermediate microstructure.

The Streicher tests carried out on the alloy 625 used concentrate H_2SO_4 acid with ferric sulphate achieving oxidizing condition and they are design for the intergranular corrosion. This condition corresponds to the curve at high nobility condition (Figure 4-50). The Cr and Mo content in the alloy 625 allow passivity condition in this environmental (D point) but the zone with a depletion of Mo -due to the second phase precipitated- work in transpassive zone (F point). This situation leads to a very penetrating attacks as shown by the HW specimen, while the LPBF alloy does not show a selective attack.

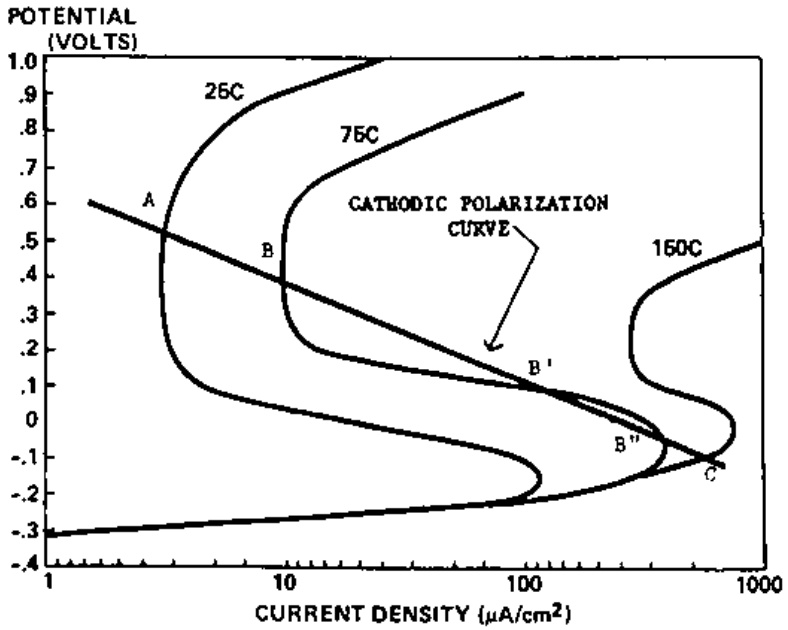

Figure 4-51: Different anodic curves in H_2SO_4 acid in function of the temperature for AISI316L[167]

4.3 Localized corrosion

The behaviour in dilute solutions has been studied through electrochemical tests due to the passive condition that leads to corrosion morphology that cannot be evaluated by gravimetric methods. In these environments the alloy, regardless of the production technology, is passive, even if in neutral chloride environmental there are phenomena of crevice corrosion.

The potential at which the current started rapidly increasing could be associated with crevice (E_c), transpassivity (E_t) or oxygen evolution reaction (OER). These phenomena are discriminated depending on whether hysteresis occurred when the scan was reversed as expected for crevice corrosion. The distinction between transpassivity and oxygen evolution reaction is done on a thermodynamic basis, where the OER potential is calculated according to the Nernst equation. The results shown in Figure 4-47 indicate the potentials associated with OER (dotted line), crevice (empty symbols) and transpassivity (full symbols).

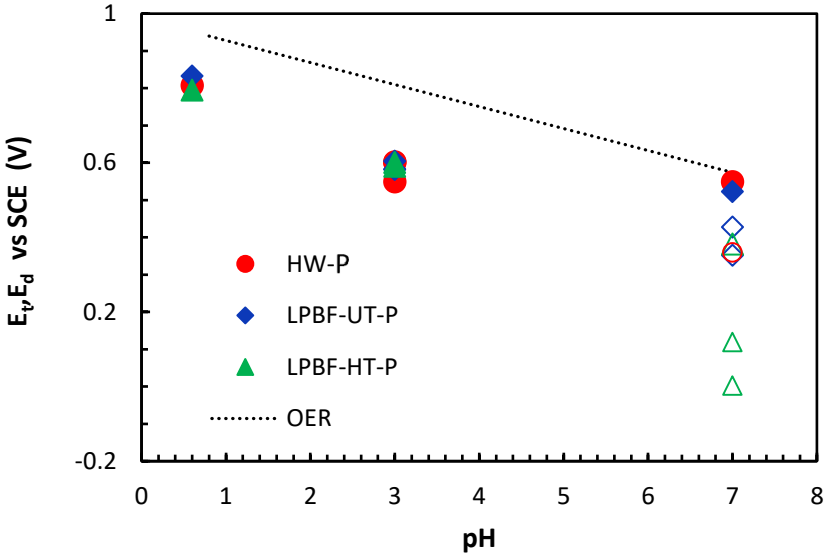

Figure 4-52: Transpassive potentials (Et) (full symbols) and damage potential (Ed) (empty marks) as a function of pH for the HW and LPBF specimens[156]

It is worth noting that sometimes, the specimens showed a passive behaviour until the OER, but during the reverse scan the presence of a hysteresis loop was detected and it is consistent with results reported in the licterature.[168,169] In this case, it is reasonable to assume that the crevice potential was close to the OER and that the local acidification associated with OER promoted the localized attack. [170]

The corrosion current densities i_{corr} are also calculated by means Stern and Geary relation in the range of ± 10 mV *vs.* E_{corr} using a typical value of 52 mV/decade for passive systems as electrochemical constant B. The values of i_{corr}, shown in Figure 4-53, are slightly higher for all the samples tested in acidic and chloride containing solutions than for those

tested in sulfuric acid or in neutral chloride solutions; however the difference between i_{corr} of all the specimens (LPBF and HW) is negligible.

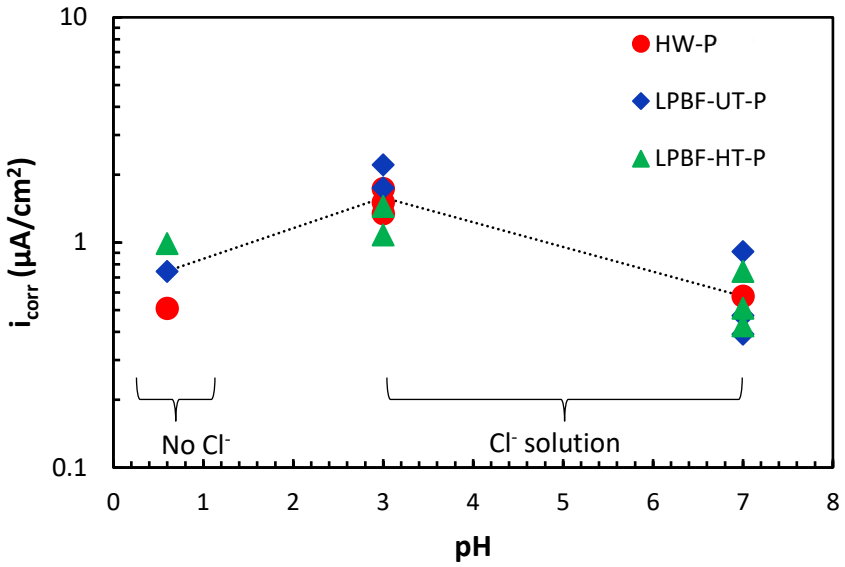

Figure 4-53: Corrosion current density (from Rp data) as a function of the pH of the solution

Moreover, the value of the current densities in the passive range (i_p) are calculated as an average over a potential range between -50 and 400 mV *vs.* SCE, or between -50 mV and E_c if the specimens presented localized corrosion, as shown in Figure 4-54.

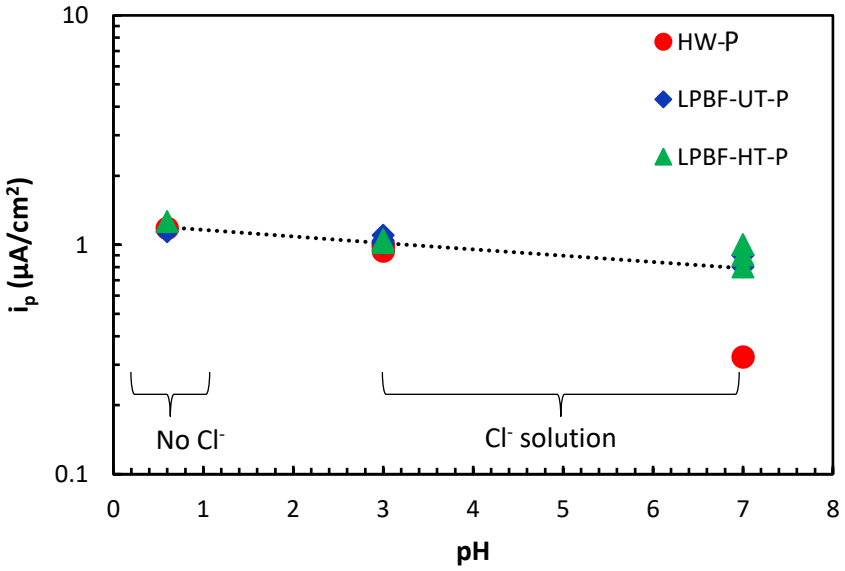

Figure 4-54: Average current density in the passive range of potentials of the potentiodynamic tests as a function of the pH of the solution

The values of i_p are very similar in all the solutions for all the specimens. However, noting that crevice corrosion was found in neutral condition but not in slightly acidic solution.

Even though the potentiodynamic tests did not highlight any significant differences between the corrosion resistance of the HW alloy and the LPBF-UT specimens, the evidence shows the possibility of crevice corrosion susceptibility in NaCl neutral solution, mainly for the LPBF-HT specimens.

The results of the potentiostatic tests underline that the LPBF alloy 625 has a similar, if not higher, corrosion resistance than the HW alloy. None of the alloys displayed pitting initiation during the electrochemical tests, although in some cases crevice was observed; this is consistent with what is reported in the literature in chloride containing solutions on alloy 625.[168,171,172]

The mass loss as a function of test temperature after the immersion tests is reported in Figure 4-55 and it was used to evaluate the CCT. According to ASTM G48, CCT is defined as the temperature above which the mass loss is greater than 0.0001 g/cm^2.

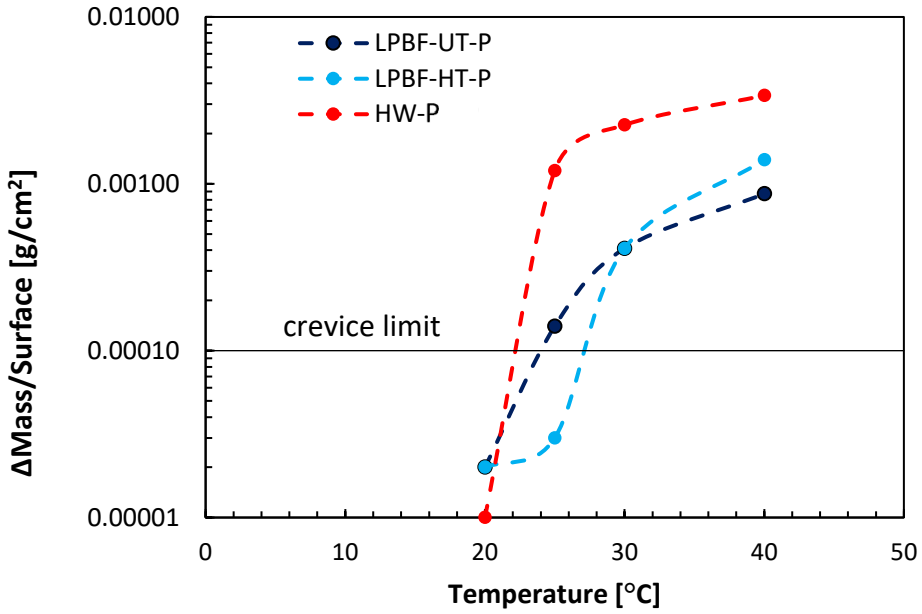

Figure 4-55: Mass loss a function of time according to the ASTM G48 used to calculate the critical crevice temperature

Figure 4-55 provides a more comprehensive description of the crevice susceptibility of these samples. It is also worth noting that at 40°C, which is the same temperature used for the potentiostatic and potentiodynamic tests, the most corrosion resistant specimens were LPBF-UT ones, whilst the HW-HT specimens has the worst behaviour with a mass loss five times greater than the LPBF specimens. Moreover, whilst CCT results appears to contradict the result from the potentiodynamic tests, they are in perfect agreement with the potentiostatic result.

The effect of the surface on the localized corrosion was also studied by potentiodynamic tests in 0.6M NaCl at pH 7 on specimens with rough surface.

The transpassive and damage potentials shown in Figure 4-56 highlight that the passive film on the AB specimens was less protective than the air formed one.

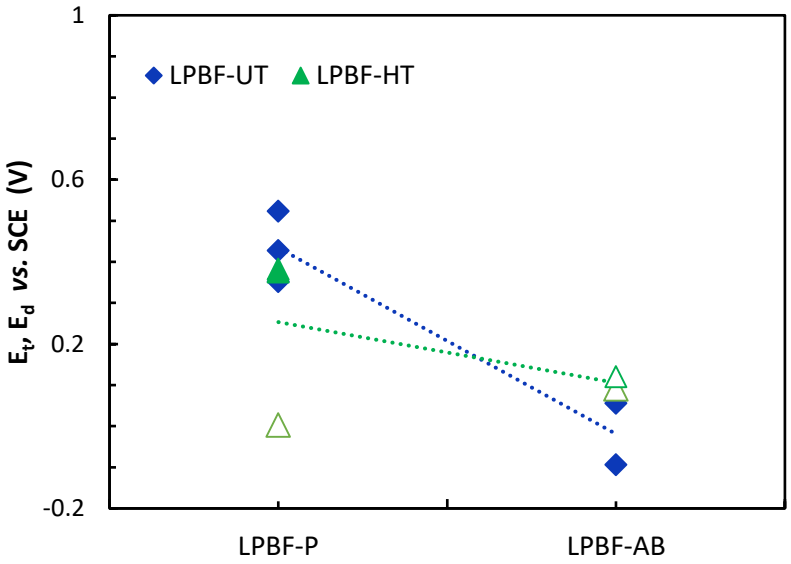

Figure 4-56: Transpassive potentials (Et) (fully marks) and damage potential (Ed) (empty marks) for LPBF specimens with polished (P) or as-built (AB) surfaces

Moreover, the AB surface conditions lead to have a passive current density higher than polished ones due to the high roughness (Figure 4-57).

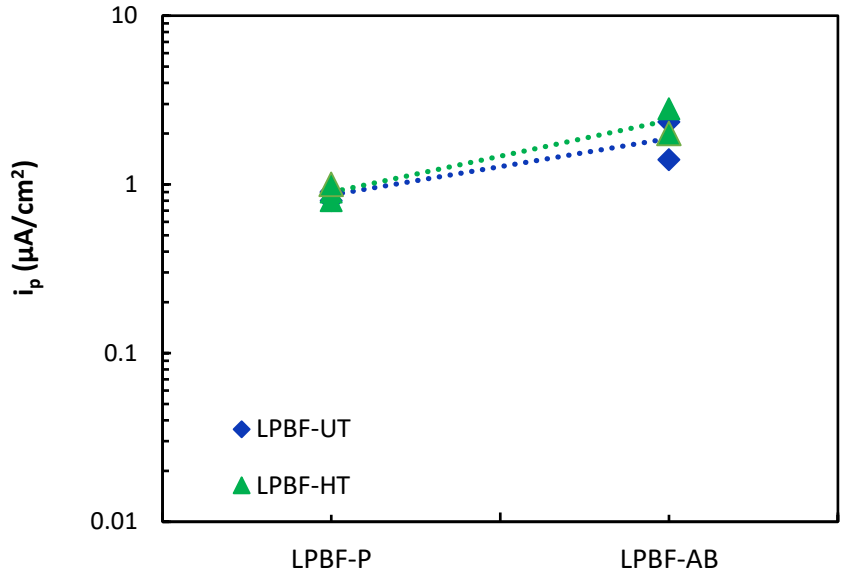

Figure 4-57: Passive current density (average value in the passive range of potential) for LPBF specimens with polished (P) or as-built (AB) surfaces

4.4 Environmental assisted cracking

The NACE MR0175 standard limits the hardness to 35 HRC to avoid stress corrosion cracking for oil and gas service. Despite the LBPF specimen showed hardness below this limit, an EAC characterization has been performed due to the higher hardness values of the LPBF than the HW ones. Many literature works report that the alloy 625 is free from chloride stress corrosion cracking.[173] The results in this thesis underline the strong corrosion resistance for this type of corrosion and they highlight that also using an environmental more corrosively with comparison to the standard one the alloy 625 does not show any form of corrosion.

Conversely, the stress corrosion tests under cathodic protection show a susceptibility of alloy 625 to the hydrogen embrittlement cracking for high cathodic potential. The Figure 4-58 reports the SCC factor calculated by means of NACE TM-0198 that describe the ratio between reduction area of the specimens exposed in corrosive environmental and the reduction area of the specimens exposed in air. This parameter – equal to 0.36 for the UT specimen and 0.44 for the HT – indicates that the union of slow strain rate in the magnitude of 10^{-6} and a cathodic overprotection lead to a reduction below the 50% regardless the heat treatment of the specimens. Conversely, the cathodic pre-charge and

the strain rate in the magnitude of 10^{-5} is a less dangerous condition and it is a detrimental condition only for the LPBF un-treated specimen.

The literature data report the hydrogen embrittlement phenomenon for alloy 625 during cathodic protection. Kane et al.[174] performed constant load tests on cold-deformed alloy 625 specimens in acid solutions, analysing the cathodic potential effect. Failure times decreased from thousands of hours to tens of hours upon application of cathodic current in the l0 mA/cm^2 range. Aging at 500 °C decreased the failure time by almost two orders of magnitude regardless of the applied potential. The worst corrosion behaviour for the LPBF untreated specimens -that show the hydrogen embrittlement even in the less aggressive condition- could be explain with the EBSD maps. In fact, the maps reveal that the untreated specimens had a major crystal orientation in the {001} direction with compared to the heat-treated alloy. Baker et. al.[175] found that CMSX-2 nickel alloy fracture occurs in the embrittled region parallel to {001} planes while the fracture occurs along {111} slip planes by ductile shearing of the matrix.

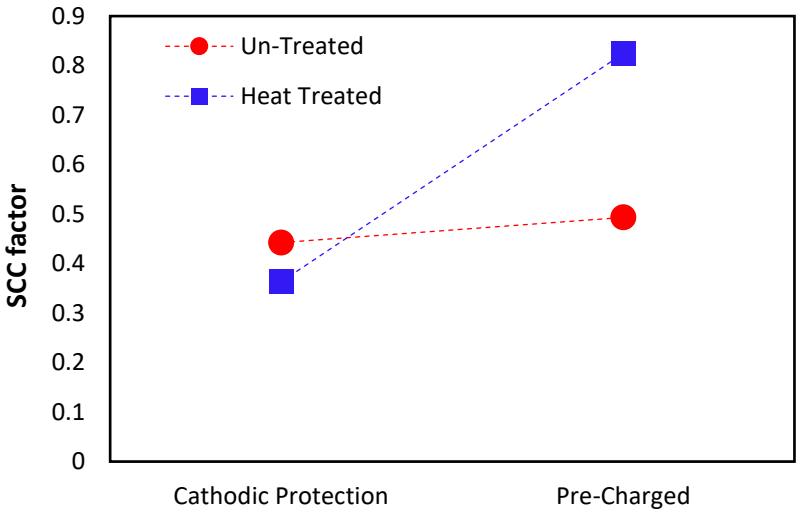

Figure 4-58: SCC factor for the LPBF specimens after SSR tests.

CHAPTER 5

EXPERIMENTAL STUDY OF Ti6Al4V

A gas atomized Ti6Al4V powder with 50 µm of average size, provided by EOS GmbH, was used. The material was printed by Politecnico di Torino.

The nominal chemical composition is reported in Table 5-1. A traditional wrought material, with a similar chemical composition of powder, was also used.

Table 5-1: Normal Chemical composition of Ti6Al4V powder

Element (%wt)	Al	V	O	N	H	Fe	C	Y
Powder	6.11	4.03	0.13	0.008	0.002	0.18	0.013	<0.001

For the corrosion tests, cylindrical specimens with 15 mm diameter and 5 mm height were used. Even for titanium specimens the same orientations, reported in chapter 3 and 4, were adapted.

The specimens manufactured via LPBF were tested in two conditions: without heat treatment (named LPBF-UT specimens) and after soft annealing at 680°C for 4h in vacuum condition followed by the cooling inside the oven. Argon atmosphere was used during the pick operation.

The LPBF specimens without post processing treatment of surface are named as built (AB); the high rough surface obtained by confocal microscope are shown in Figure 5-1

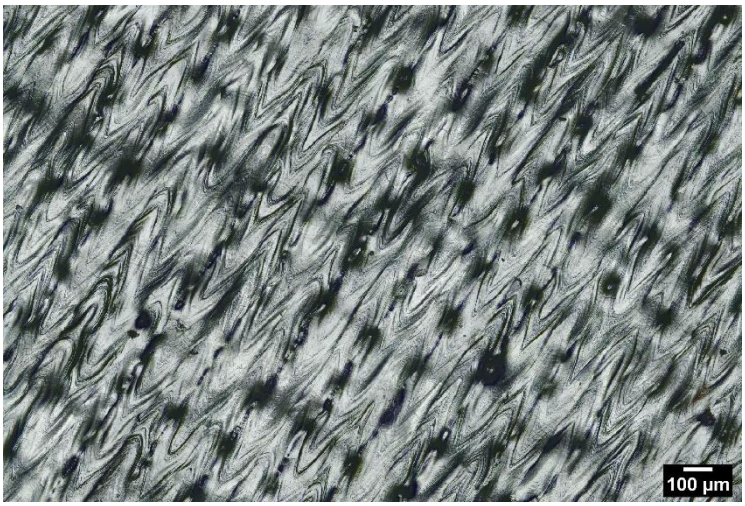

Figure 5-1: Confocal microscope image of the XY as-built surface of titanium sample

The specimens marked as P (Polished) were grinded with 4000 grit abrasive paper and polished with 1 µm diamond past. They were passivated in air for 1 hour before tests. Some specimens were also pickled with acid (25% HNO_3 e 2.5% HF) for 60 seconds at room temperature. All specimens were degreased in acetone before the tests.

Potentiostatic test

These tests were carried out in simulated body solution (SBF) with NaCl 8.74 g/L, $NaHCO_3$ 0.35 g/L, $Na_2HPO_4 \cdot H_2O$ 0.075 g/L, $NaH_2PO_4 \cdot H_2O$ 0.069 g/L at 38°C de-oxygenated with nitrogen for 1 hour. The potentiostatic tests were carried out in a 3 electrode ASTM G5 cell using a PTFE holder sample with the exposed surface equal to 1 cm^2. The specimens were polarized at +0.5 V *vs.* SCE for 60 hours. A nitrogen bubbling was used during the test. The tests were performed using the Ivium Compastat.

Potentiostatic test at the same potential and in the same solution and condition were carried out for 6000 hours using 8 samples, one reference and 1 counter electrode into a 25 litres cell. The specimens were anodic polarized using the 2052 AMEL instrument. The data were collect using a 2000 Keithley combined with 7001 Keithley that read the ohmic drop of Shunt resistances. The values these resistances, equal to 10,1000 end 20000 Ω, were adapted in order to minimize the effect on the ohmic drop. A Matlab program read the values for each channel with different acquisition frequency.

5.1 Passivation kinetics of Ti6Al4V

The Figure 5-2 reports some of the anodic curves in SBF for different LPBF condition compare with the curve obtain for the wrought specimens. The LPBF as built specimens present many spikes and a current density higher than the other specimens. Conversely, the polished and pickled ones showed the minimum value of current after 60 hours with comparison to the traditional wrought material. All the curves marked a negative exponential law. The other curves are located at the annex A.

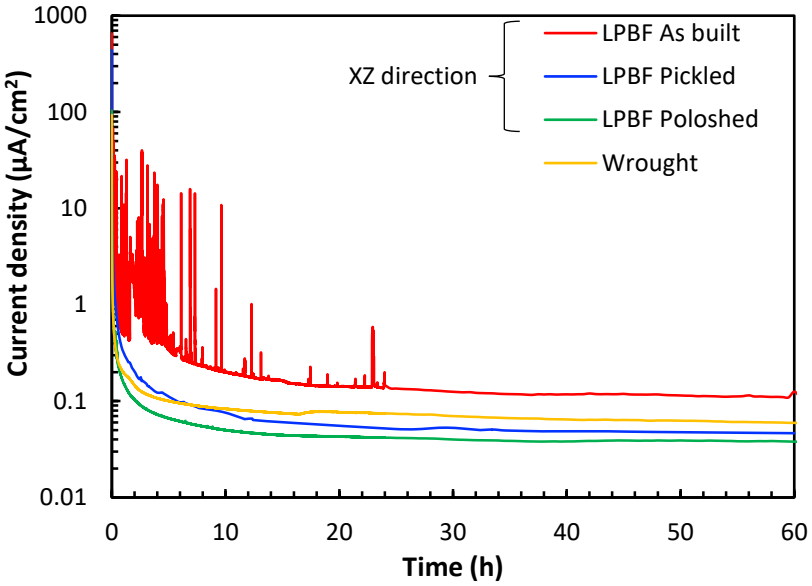

Figure 5-2: Short time potentiostatic curves at +500mV in simulated body solution for different Ti6Al4V specimens

The specimens with surface AB presented many spikes and a higher current density than the other specimens, due to the presence of partially-melted powder and re-solidified drops (balling)[176] which cannot be separated through sonication in acetone (Figure 5-3).

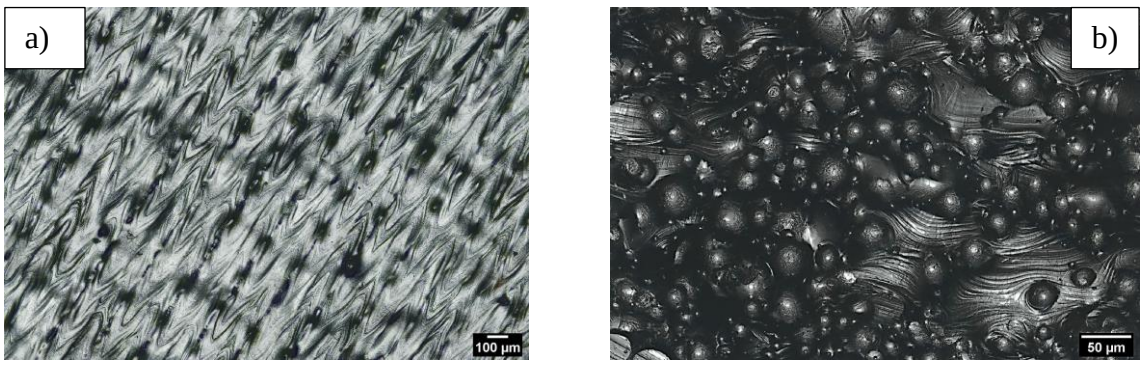

Figure 5-3: Laser images of (a) XY and (b) XZ LPBF Ti6Al4V specimens in as built condition

The 3D surface reconstruction performed on the LPBF as built specimens confirmed the presence of partially melted powder on the XZ specimens (Figure 5-4).

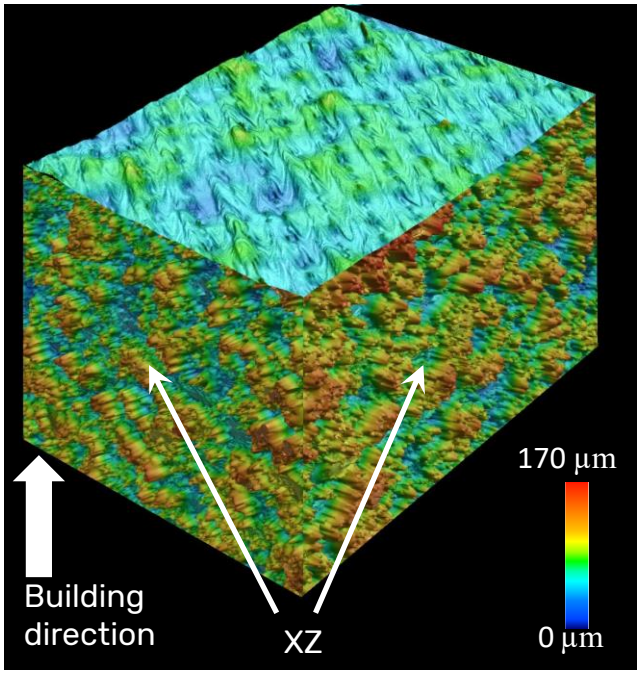

Figure 5-4: 3D reconstruction of Ti6Al4V LPBF specimen.

In a hypothetical use of this alloy in the biomedical field, the presence of small particles of molten powder or balling is not admissible. Therefore, a cleaning treatment (chemical or mechanical) is essential for their use.

In this way, the capability of hydrofluoric-nitric solution was investigated. After the exposure for 60 second in acid solution the reconstruction of the same surfaces was carried out again showing the reduction of the balling phenomenon without smooth excessively the roughness (Ra) that change from 14.5 to 11.5 µm (Figure 5-5). The reducing of the balling and un-melted powder by pickling permits to partially remove the spikes, but they are totally avoided only after mechanical polishing.

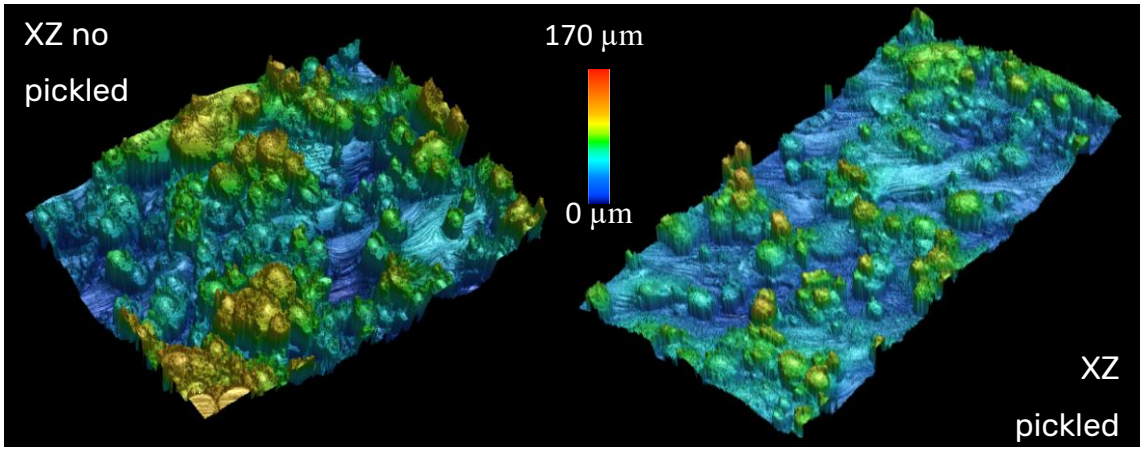

Figure 5-5: Effect of pickled on the balling phenomenon for the XZ LPBF surface

Regardless the spikes, the trend of the anodic current with respect to time at constant potential is limited in the earliest moments of polarization by the ohmic drop between the sample and the Luggin capillary probe, then it is possible to observe an exponential trend between the current density and the time.[177] The passivation kinetics can therefore be expressed with a relation of the type:

$$i = i_p + i_0(\frac{t}{t_0})^{-n}$$

Where i_0 represents the current in the first moments of polarization associated with the time t_0, i_p the passivity current at equilibrium and n the coefficient of the passivation kinetics. The values of i_0 and n were calculated from the extrapolation of the potentiostatic curves as shown in Figure 5-6. The specimens with surface AB have initial values of i_0 higher than the other specimens (Figure 5-7). A possible worse behaviour of the passive film formed during the LPBF process can be supposed. After the chemical pickling, the specimens show initial currents lower than the as build samples, but higher than polished specimens. The ability of the pickling to remove the poorly protective film and the partially melted particles on the surface can be hypothesized. The high initial current density values are attributed to the greater exposed surface that is not eliminated by the chemical treatment.

Furthermore, the value of n is similar for all the samples, around 0.95, indicating that the superficial condition does not influence the kinetic of the film growth in environment.

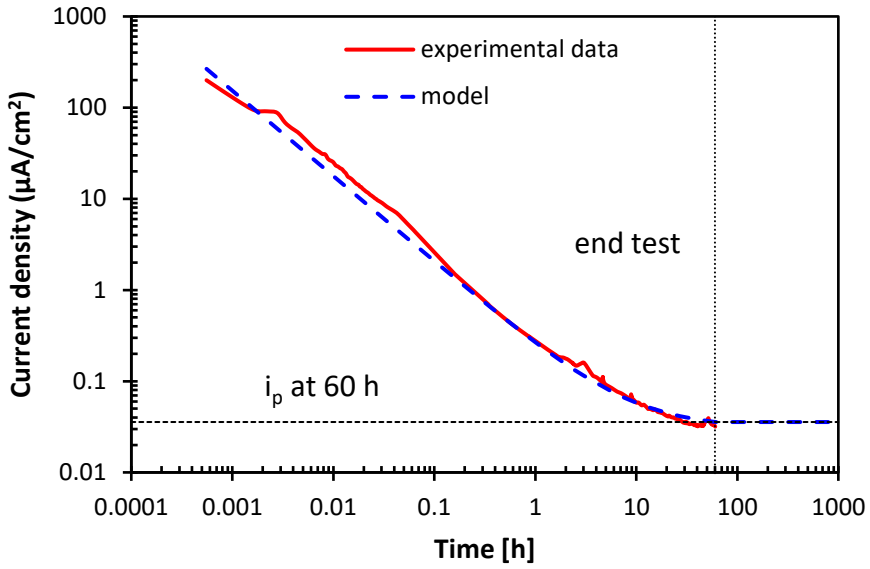

Figure 5-6: Example of fitting of the data (sample LPBF XZ UT pickled)

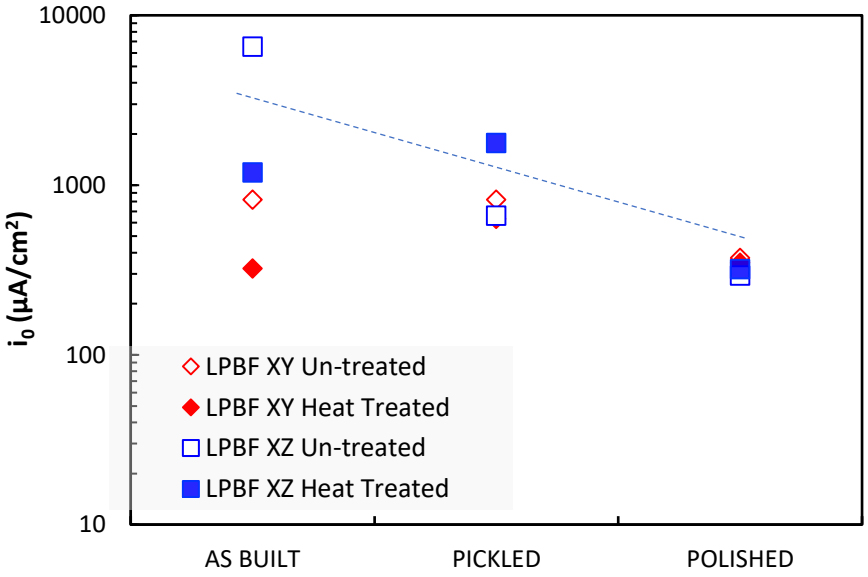

Figure 5-7: Initial current density as function of superficial conditions

The i_p determination requires long time that was not compatible with this experiment setup. In the first instance, the values in the last hour of the tests have very low standard deviation, indicating a quasi-stable state. This value of current, called i_{p60h}, is used to compare the equilibrium behaviour of the samples.

Figure 5-8 and Figure 5-9 report the effect of the surface finishing on i_{p60h}. The XZ specimens with as built surface showed current values higher than the XY specimens (average i_{p60h} of 2.3 µA/cm^2 for heat treated specimens and 0.11 µA/cm^2 for the

untreated). These differences become neglectable for polishing samples. A slight decrease of i_{p60h} is observed for the XZ specimens in function of the surface finishing, whereas the XY specimens showed similar values to the AB and P.

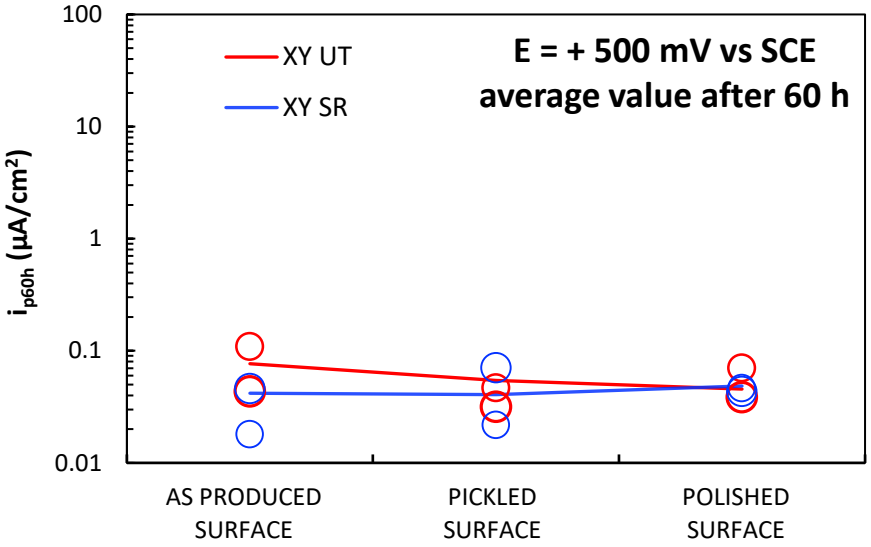

Figure 5-8: Average current density after 60h for untreated and heat treated XY-LPBF specimens as function of surface conditions

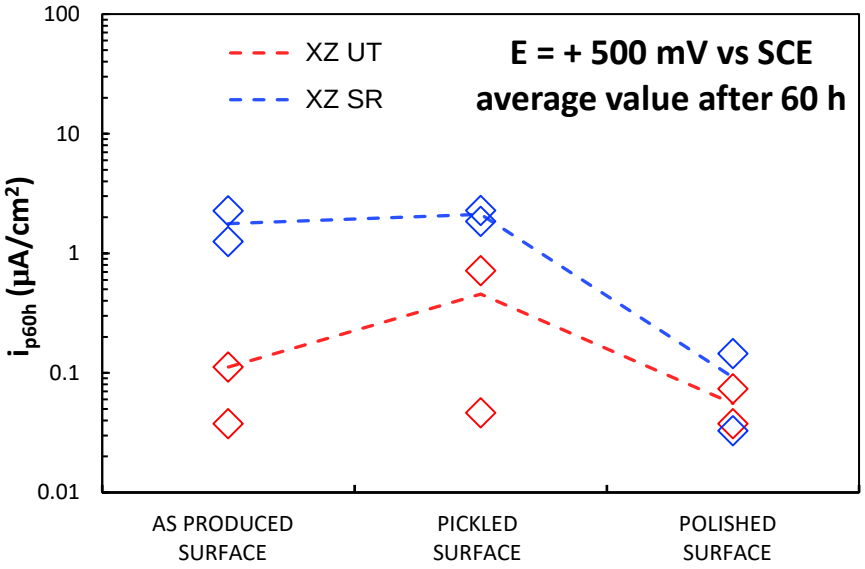

Figure 5-9: Average current density after 60h for untreated and heat treated XZ-LPBF specimens as function of surface conditions

Chen et al.[178] using different equipment and scan strategy, observed that the sample growth perpendicular to the building platform shows a lower corrosion resistance than the samples parallel to the building platform in Hank's solution at 37°C. They affirmed

that the parallel specimens had more artefact holes due to the zigzag laser scanning strategy. A worst corrosion behaviour of the XZ samples with respect to XY was also observed by Dai et al.[179] in HCl 1M that supposed the formation of "weaker" passive layer on the planes perpendicular to the building platform.[1]

Differences in the hardness[180], in tensile resistance and ductility[181] were founded between the materials built in perpendicular or parallel directions. Conversely, no differences between the building direction were founded by Chandramohan et al.[182]

The values of i_{p60h} of the polished specimens are reported in Figure 5-10 as a function of the metallurgical state (wrought, LPBF-UT and LPBF-HT).

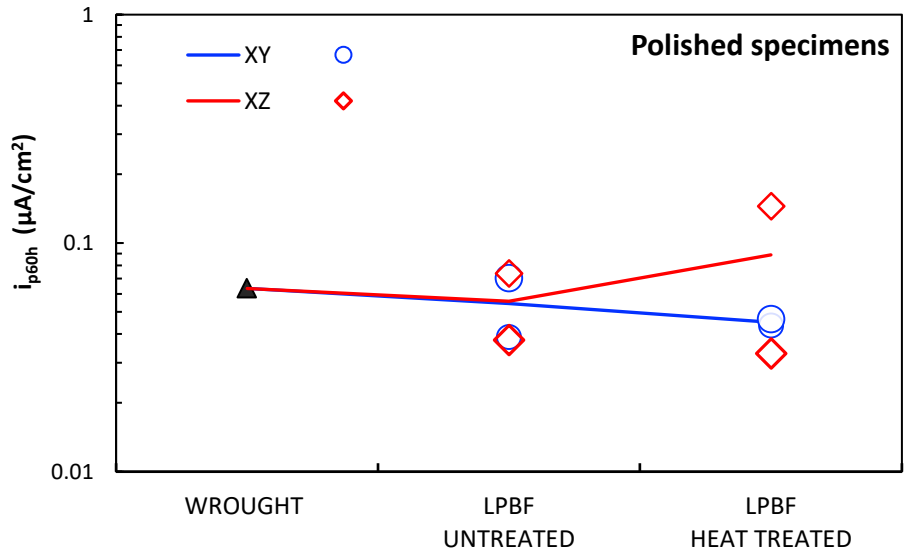

Figure 5-10: Average current density after 60h for the polished specimens as function of metallurgical conditions

The i_{p60h} of the LPBF-UT polished specimens are comparable to the value of the wrought alloy. A slight increase of the current density is observed for the XZ-LPBF-HT specimens, whereas the XY-LPBF-HT specimens showed similar values of i_{p60h} than the UT and wrought ones. This effect could be due to the higher emerging porosity, not removed by the mechanical polishing.

The effect of post processing heat treatment is controversial. Dai et al.[179] reported that the heat treatment of LPBF Ti6Al4V (2 h at 500 °C, 850 °C, and 1000 °C) was detrimental to passivation in 3.5 wt% NaCl. Similar results were reported by Chandramohan et al.[182] Conversely, different results were presented by Xu et al.[11] in SBF and by Yang et al. in NaCl 3.5% solution.[183] They found that the LPBF Ti6Al4V specimens after heat

treatment exhibited inferior corrosion resistance compared to the commercial wrought alloy.

Probably, the scan strategy and the equipment used for the printing influenced the microstructure of the alloy and its modification with the heat treatments. Similar results were found on AlSi10Mg described in the chapter 3 or by other authors on CoCr alloy.[184] On the contrary a beneficial effect of heat treatment was observed for AISI316L[185,186]and 17-4 PH.[187]

The passivity current values are consistent with the values reported in literature. The corrosion rate of the traditional wrought alloy in neutral Hank's reported by Alves et al.[188] is in the range of 0.03-0.33 $\mu A/cm^2$, De Assis et al.[189] obtained 0.019 ±0.0009 $\mu A/cm^2$ while in neutral Ringer solution Vasilescu et al. reported higher values, from 0.2 to 21 $\mu A/cm^2$ depending on the metallurgical condition.[190] These values were obtained by means of potentiodynamic and electrochemical impedance spectroscopy techniques and depend from the time of immersion. On the contrary, long-time immersion potentiostatic tests on the same wrought alloy, given lower corrosion rate than the values reported above.[191] It could suppose that an exposure time longer than 60 hours is necessary to reach a steady state condition.

The passive current density after long time exposure was evaluated by means of multi-samples potentiostatic tests. The Figure 5-11 shows an example of the results at +500mV *vs.* SCE in SBF for pickled and polished LPBF Ti6Al4V specimens. For these tests the As Built surface has been avoid due to the anodic spikes and superficial defects (balling) that make unusable in biomedical field this surface. All the results are summarized in the annex A.

The curves showed clearly that during the first hours, the polarization is far from the set point due to the Shunt resistance. Furthermore, noise was detected during the test.

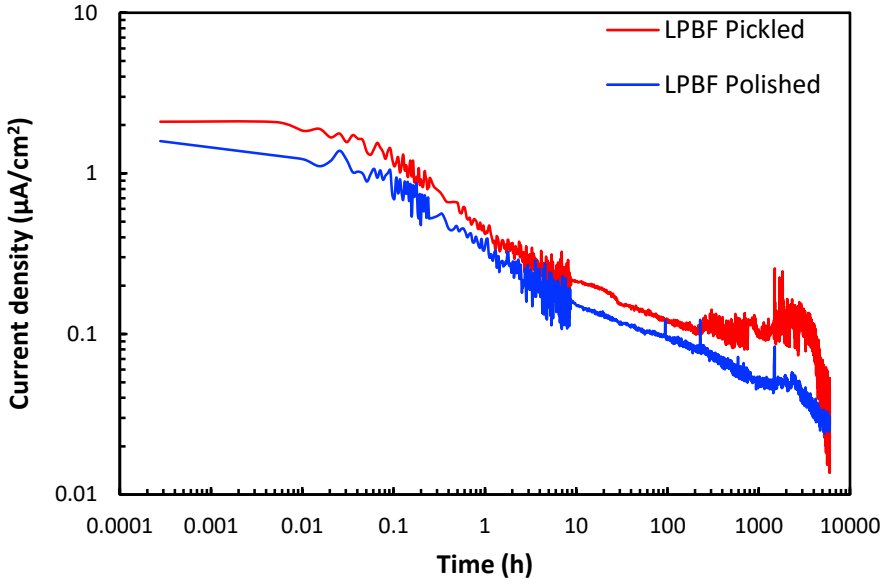

Figure 5-11: Long time potentiostatic curves at +500mV in simulated body solution for different XZ UT Ti6Al4V specimens[192]

The Figure 5-12 shows the comparison between some values -as example- of i_p after 60 hours and after 6000 hours. The current density after 60h is obviously higher than the current density after 6000h. Therefore, based on the comparison between the current density values obtained by the model applied to the short time tests and those obtained from the long period tests, it is possible to observe a slight difference, as shown in Figure 5-13.

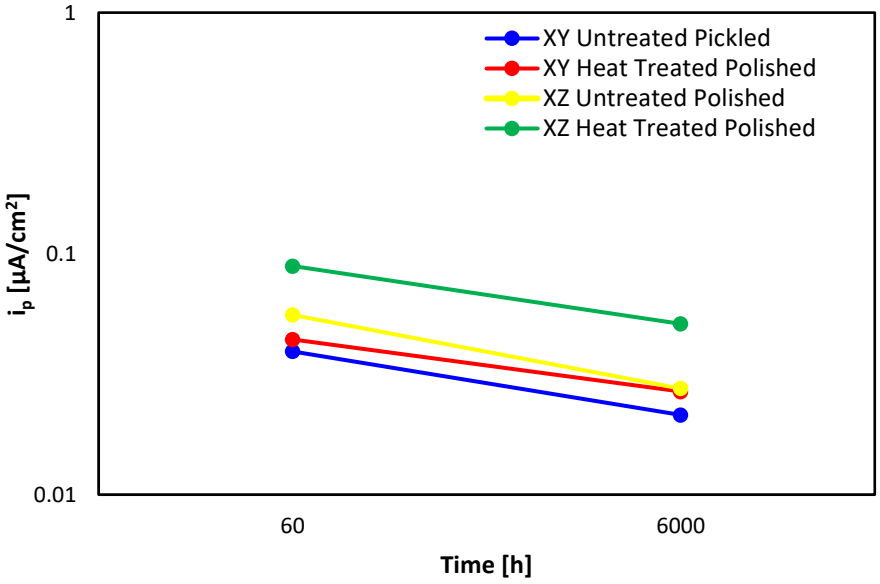

Figure 5-12: Anodic current density of LPBF specimen after 60h and 6000h

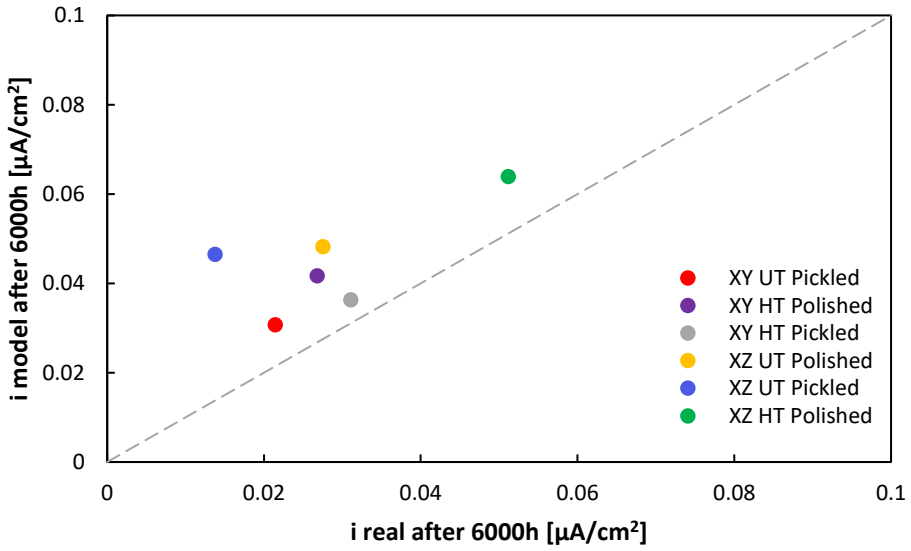

Figure 5-13: Comparison between the real current after 6000h and the value obtain by means of the model

In any case the work confirms the excellent resistance to corrosion of the Ti6Al4V alloy in SBF environment, also for the rough surface produced by LPBF. High roughness is particularly indicated to support the growth of bone cells at the interface between the prosthesis and the diaphyseal canal.[193] The pickling treatment permits to remove the initial spikes of current, but the time of treatments has to be increased to be sure to remove all the un-melt powders or the balling formed during the 3D printing.

CHAPTER 6

CONCLUSIONS

This PhD thesis presents the research carried out on three different corrosion resistant alloys –AlSi10Mg, alloy 625, and Ti6Al4V– processed by Laser Powder Bed Fusion (LPBF). The studies concern both the generalized and localized corrosion and the environmental assisted cracking comparing the results with the tests carried out on the commercial traditional alloys. The effects of microstructure and post processing treatment on the corrosion resistance are investigated.

The corrosion resistance of the alloys obtained by means of additive manufacturing techniques depend on different parameter. Only recently, international organizations, such as The Wielding Institute, have issued some guidelines to outline the standardization of these processes.

The LPBF process produces high surface roughness with oxide created during the printing process different compared to that formed spontaneously in the air. The oxide layer formed during the LPBF process decreases the AlSi10Mg corrosion resistance leading to penalization of pitting potential for this passive alloy. The film naturally formed, after a post processing treatment of the surface such as mechanical polishing, is more resistant to the corrosion presenting higher pitting potentials. However, emerging porosity may be present. Inside the porosity the poor film cannot be removed and therefore represent a critical point where the corrosion can initiate.

The oxide formed during the LPBF process affect the corrosion resistance of alloy 625. The alloy 625 analysed in this work presents a lower resistance of localized corrosion when used with surface as produced by the process. Under this condition, the material

shows lower damage potentials and higher corrosion current density than the traditional alloy. The alloy 625 with oxide formed in air achieves at least comparable performance with respect to the traditional material or exceeds them. The alloy regardless the manufacturing process shows high corrosion rates in reducing acid environments. In oxidizing solutions, the LPBF alloy present a good corrosion resistance with comparison to the hot worked one.

The Ti6Al4V shows similar electrochemical behaviour and it seem not be affected by the nature of the surface oxide in the test solution used, which is not very corrosive. However, the phenomenon of balling compromises the usability of the rough surface. The balling causes spikes in the corrosion current that are correlated with higher ionic release of substances harmful to the human body in the case of biochemical use. The acid pickling post processing can be adopted to remove the partially melted particles of powders in order to limit the balling phenomenon without compromise the roughness necessary for osseointegration of prostheses.

The microstructural modification plays a fundamental role in corrosion resistance. The heat treatment post processing is necessary to remove the internal stress due to the rapid cooling rate, but it leads to a microstructure different from the start condition. The LPBF alloy is formed by melt pools which are the fusion tracks left by the laser. Within this microstructure, micro-dendrites are located. The effect of heat treatment on the AlSi10Mg alloy is modified the microstructure of the melt pools changing the distribution of the silicon between the centre and the border of the melt pool. This effect can stimulate the selective corrosion leading to a penetrating attack on the border of the melt pools. The stress relieving heat treatment suggested by the EOS company results to be very detrimental for the corrosion. In this way, no heat treatment is recommended. For the critical application, where the heat treatment is mandatory, a temperature above 400 °C is recommended, which leads to less penetrating corrosion but worse mechanical resistance.

No standard deals about the heat treatment for the alloy 625 processed by means of LPBF. The heat treatment “grade 1” is adopted in this thesis as a common heat treatment in the oil and gas field. This heat treatment dissolve partially the melt pools avoiding the second phases precipitation. The heat treated specimens show in some cases a better corrosion behaviour that the untreated ones. However, a decrease in the corrosion resistance has

been noted with intermediate performances between the untreated LPBF specimens and the hot worked specimens. The possibility of hydrogen embrittlement on heat treated specimens under slow stress rate and cathodic overprotection is detected.

A specific heat treatment for the alloy 625 processed by means of LPBF could lead to a good combination between the mechanical resistance and the corrosion performance.

The heat treatment adopted for Ti6Al4V does not change the corrosion resistance in a simulated body fluid.

A global analysis of the results suggests the need to standardize all the parameters of the LPBF process starting from the powders to the post processing treatments. These rules are necessary to govern all the parameters that can influence the final properties of the additive manufacturing part.

BIBLIOGRAPHY

1. Sander G, Tan J, Balan P, et al. Corrosion of additively manufactured alloys: A review. *Corrosion*. 2018;74(12):1318-1350. doi:10.5006/2926

2. Revilla RI, Liang J, Godet S, De Graeve I. Local Corrosion Behavior of Additive Manufactured AlSiMg Alloy Assessed by SEM and SKPFM. *J Electrochem Soc*. 2017;164(2):C27-C35. doi:10.1149/2.0461702jes

3. Leon A, Shirizly A, Aghion E. Corrosion Behavior of AlSi10Mg Alloy Produced by Additive Manufacturing (AM) vs. Its Counterpart Gravity Cast Alloy. *Metals (Basel)*. 2016;6(7):148. doi:10.3390/met6070148

4. Leon A, Aghion E. Effect of surface roughness on corrosion fatigue performance of AlSi10Mg alloy produced by Selective Laser Melting (SLM). *Mater Charact*. 2017;131:188-194. doi:10.1016/J.MATCHAR.2017.06.029

5. Cabrini M, Lorenzi S, Pastore T, et al. Corrosion resistance of direct metal laser sintering AlSiMg alloy. *Surf Interface Anal*. 2016;48(8):818-826. doi:10.1002/sia.5981

6. Cabrini M, Lorenzi S, Pastore T, et al. Effect of heat treatment on corrosion resistance of DMLS AlSi10Mg alloy. *Electrochim Acta*. 2016;206:346-355. doi:10.1016/j.electacta.2016.04.157

7. Cabrini M, Lorenzi S, Pastore T, et al. Evaluation of corrosion resistance of Al-10Si-Mg alloy obtained by means of Direct Metal Laser Sintering. *J Mater Process Technol*. 2016. doi:10.1016/j.jmatprotec.2015.12.033

8. Prashanth KG, Debalina B, Wang Z, et al. Tribological and corrosion properties of Al-12Si produced by selective laser melting. *J Mater Res*. 2014;29. doi:10.1557/jmr.2014.133

9. Sarmiento Klapper H, Molodtsov N, Burns M, Wangenheim C. Critical Factors Affecting the Pitting Corrosion Resistance of Additively Manufactured Nickel Alloy in Chloride Containing Environments. In: *NACE Corrosion Conference 2017*. ; 2017.

10. de Damborenea JJ, Arenas MA, Larosa MA, Jardini AL, de Carvalho Zavaglia CA, Conde A. Corrosion of Ti6Al4V pins produced by direct metal laser sintering. *Appl Surf Sci*. 2017;393:340-347. doi:10.1016/J.APSUSC.2016.10.031

11. Xu Y, Lu Y, Sundberg KL, Liang J, Sisson RD. Effect of Annealing Treatments on the Microstructure, Mechanical Properties and Corrosion Behavior of Direct Metal Laser Sintered Ti-6Al-4V. *J Mater Eng Perform*. 2017;26(6):2572-2582. doi:10.1007/s11665-017-2710-y

12. DebRoy T, Wei HL, Zuback JS, et al. Additive manufacturing of metallic components – Process, structure and properties. *Prog Mater Sci*. 2018. doi:10.1016/j.pmatsci.2017.10.001

13. Milewski JO. *Additive Manufacturing of Metals*. Vol 258. Cham: Springer International Publishing; 2017. doi:10.1007/978-3-319-58205-4

14. Sames WJ, List FA, Pannala S, Dehoff RR, Babu SS. The metallurgy and processing science of metal additive manufacturing. *Int Mater Rev*. 2016;61(5):315-360. doi:10.1080/09506608.2015.1116649

15. Körner C. Additive manufacturing of metallic components by selective electron beam melting — a review. *Int Mater Rev*. 2016;61(5):361-377. doi:10.1080/09506608.2016.1176289

16. Herzog D, Seyda V, Wycisk E, Emmelmann C. Additive manufacturing of metals. *Acta Mater*. 2016;117:371-392. doi:10.1016/J.ACTAMAT.2016.07.019

17. Bourell DL. Perspectives on Additive Manufacturing. *Annu Rev Mater Res*. 2016;46(1):1-18. doi:10.1146/annurev-matsci-070115-031606

18. King WE, Anderson AT, Ferencz RM, et al. Laser powder bed fusion additive manufacturing of metals; physics, computational, and materials challenges. *Appl Phys Rev*. 2015;2(4):041304. doi:10.1063/1.4937809

19. Gu DD, Meiners W, Wissenbach K, Poprawe R. Laser additive manufacturing of metallic components: materials, processes and mechanisms. *Int Mater Rev*. 2012;57(3):133-164. doi:10.1179/1743280411Y.0000000014

20. Collins PC, Brice DA, Samimi P, Ghamarian I, Fraser HL. Microstructural Control of Additively Manufactured Metallic Materials. *Annu Rev Mater Res*. 2016;46(1):63-91. doi:10.1146/annurev-matsci-070115-031816

21. Lewandowski JJ, Seifi M. Metal Additive Manufacturing: A Review of Mechanical Properties. *Annu Rev Mater Res*. 2016;46(1):151-186. doi:10.1146/annurev-matsci-070115-032024

22. Olakanmi EO, Cochrane RF, Dalgarno KW. A review on selective laser sintering / melting (SLS / SLM) of aluminium alloy powders : Processing , microstructure , and properties. *J Prog Mater Sci*. 2015;74:401-477. doi:10.1016/j.pmatsci.2015.03.002

23. Imran MK, Masood SH, Brandt M, Bhattacharya S, Mazumder J. Direct metal deposition (DMD) of H13 tool steel on copper alloy substrate: Evaluation of mechanical properties. *Mater Sci Eng A*. 2011;528(9):3342-3349. doi:10.1016/J.MSEA.2010.12.099

24. Ding D, Pan Z, Cuiuri D, Li H. Wire-feed additive manufacturing of metal components: technologies, developments and future interests. *Int J Adv Manuf Technol*. 2015;81(1-4):465-481. doi:10.1007/s00170-015-7077-3

25. Xiong J, Lei Y, Chen H, Zhang G. Fabrication of inclined thin-walled parts in multi-layer single-pass GMAW-based additive manufacturing with flat position deposition. *J Mater Process Technol*. 2017;240:397-403. doi:10.1016/J.JMATPROTEC.2016.10.019

26. Gibson I, Rosen D, Stucker B. *Additive Manufacturing Technologies: 3D Printing, Rapid Prototyping, and Direct Digital Manufacturing, Second Edition*.; 2015.

doi:10.1007/978-1-4939-2113-3

27. Ultrasonic Additive Manufacturing - Inside Metal Additive Manufacturing. https://www.insidemetaladditivemanufacturing.com/blog/ultrasonic-additive-manufacturing. Accessed August 26, 2019.

28. Binder Jetting | Additive Manufacturing Research Group | Loughborough University. https://www.lboro.ac.uk/research/amrg/about/the7categoriesofadditivemanufacturing/binderjetting/. Accessed August 26, 2019.

29. Brecher C, ed. *Integrative Production Technology for High-Wage Countries*. Berlin, Heidelberg: Springer Berlin Heidelberg; 2012. doi:10.1007/978-3-642-21067-9

30. High Level Processes: Directed Energy Deposition. https://www.bintoa.com/directed-energy-deposition/. Accessed September 20, 2019.

31. Rieder H, Dillhöfer A, Spies M, Bamberg J, Hess T. *Online Monitoring of Additive Manufacturing Processes Using Ultrasound*. www.ndt.net/?id=16533. Accessed September 20, 2019.

32. Dehoff RR, Babu SS. Characterization of interfacial microstructures in 3003 aluminum alloy blocks fabricated by ultrasonic additive manufacturing. *Acta Mater*. 2010;58(13):4305-4315. doi:10.1016/J.ACTAMAT.2010.03.006

33. Laser Melting - Additively. https://www.additively.com/en/learn-about/laser-melting. Accessed August 26, 2019.

34. Bourell D, Kruth JP, Leu M, et al. Materials for additive manufacturing. *CIRP Ann - Manuf Technol*. 2017. doi:10.1016/j.cirp.2017.05.009

35. Edwards P, Ramulu M. Fatigue performance evaluation of selective laser melted Ti–6Al–4V. *Mater Sci Eng A*. 2014;598:327-337. doi:10.1016/J.MSEA.2014.01.041

36. Niendorf T, Leuders S, Riemer A, Richard HA, Tröster T, Schwarze D. Highly Anisotropic Steel Processed by Selective Laser Melting. *Metall Mater Trans B*. 2013;44(4):794-796. doi:10.1007/s11663-013-9875-z

37. Murr LE, Martinez E, Hernandez J, et al. Microstructures and Properties of 17-4 PH Stainless Steel Fabricated by Selective Laser Melting. *J Mater Res Technol*. 2012;1(3):167-177. doi:10.1016/S2238-7854(12)70029-7

38. Xin X, Xiang N, Chen J, Xu D, Wei B. Corrosion characteristics of a selective laser melted Co–Cr dental alloy under physiological conditions. *J Mater Sci*. 2012;47(12):4813-4820. doi:10.1007/s10853-012-6325-2

39. Parimi LL, A. RG, Clark D, Attallah MM. Microstructural and texture development in direct laser fabricated IN718. *Mater Charact*. 2014;89:102-111. doi:10.1016/J.MATCHAR.2013.12.012

40. Cabrini M, Lorenzi S, Pastore T, et al. Corrosion behavior of aluminum-silicon

alloys obtained by Direct Metal Laser Sintering. In: *EUROCORR 2017 - The Annual Congress of the European Federation of Corrosion, 20th International Corrosion Congress and Process Safety Congress 2017*. ; 2017.

41. Anderson IE, Figliola RS, Morton H. Flow mechanisms in high pressure gas atomization. *Mater Sci Eng A*. 1991;148(1):101-114. doi:10.1016/0921-5093(91)90870-S

42. Yin JO, Chen G, Zhao SY, et al. Microstructural characterization and properties of Ti-28Ta at.% powders produced by plasma rotating electrode process. *J Alloys Compd*. 2017;713:222-228. doi:10.1016/J.JALLCOM.2017.04.195

43. Mukherjee T, Zhang W, DebRoy T. An improved prediction of residual stresses and distortion in additive manufacturing. *Comput Mater Sci*. 2017;126:360-372. doi:10.1016/J.COMMATSCI.2016.10.003

44. Mukherjee T, Zuback JS, De A, DebRoy T. Printability of alloys for additive manufacturing. *Sci Rep*. 2016;6(1):19717. doi:10.1038/srep19717

45. Brice C, Shenoy R, Kral M, Buchannan K. Precipitation behavior of aluminum alloy 2139 fabricated using additive manufacturing. *Mater Sci Eng A*. 2015;648:9-14. doi:10.1016/J.MSEA.2015.08.088

46. Brice CA, Rosenberger BT, Sankaran SN, Taminger KM, Woods B, Nasserrafi R. Chemistry Control in Electron Beam Deposited Titanium Alloys. *Mater Sci Forum*. 2009;618-619:155-158. doi:10.4028/www.scientific.net/MSF.618-619.155

47. Gaytan SM, Murr LE, Medina F, Martinez E, Lopez MI, Wicker RB. Advanced metal powder based manufacturing of complex components by electron beam melting. *Mater Technol*. 2009;24(3):180-190. doi:10.1179/106678509X12475882446133

48. Carlton HD, Haboub A, Gallegos GF, Parkinson DY, MacDowell AA. Damage evolution and failure mechanisms in additively manufactured stainless steel. *Mater Sci Eng A*. 2016;651:406-414. doi:10.1016/J.MSEA.2015.10.073

49. Jia Q, Gu D. Selective laser melting additive manufacturing of Inconel 718 superalloy parts: Densification, microstructure and properties. *J Alloys Compd*. 2014;585:713-721. doi:10.1016/J.JALLCOM.2013.09.171

50. Rahmati S, Vahabli E. Evaluation of analytical modeling for improvement of surface roughness of FDM test part using measurement results. *Int J Adv Manuf Technol*. 2015;79(5-8):823-829. doi:10.1007/s00170-015-6879-7

51. Lewis GK, Schlienger E. Practical considerations and capabilities for laser assisted direct metal deposition. *Mater Des*. 2000;21(4):417-423. doi:10.1016/S0261-3069(99)00078-3

52. Mercelis P, Kruth J. Residual stresses in selective laser sintering and selective laser melting. *Rapid Prototyp J*. 2006;12(5):254-265. doi:10.1108/13552540610707013

53. David SA, Vitek JM. Correlation between solidification parameters and weld microstructures. *Int Mater Rev*. 1989;34(1):213-245.

doi:10.1179/imr.1989.34.1.213

54. Kou S. *Welding Metallurgy*. Vol 73. 2nd ed. John Wiley & Sons, Inc.; 2012.

55. Wei HL, Elmer JW, DebRoy T. Origin of grain orientation during solidification of an aluminum alloy. *Acta Mater*. 2016;115:123-131. doi:10.1016/J.ACTAMAT.2016.05.057

56. Li S, Wei Q, Shi Y, et al. Microstructure Characteristics of Inconel 625 Superalloy Manufactured by Selective Laser Melting. *J Mater Sci Technol*. 2015;31(9):946-952. doi:10.1016/j.jmst.2014.09.020

57. Manfredi D, Calignano F, Ambrosio EP, et al. Direct Metal Laser Sintering: An additive manufacturing technology ready to produce lightweight structural parts for robotic applications. *Metall Ital*. 2013;105(10):15-24. doi:10.1016/j.jallcom.2016.10.285

58. Kim US, Park JW. High-Quality Surface Finishing of Industrial Three-Dimensional Metal Additive Manufacturing Using Electrochemical Polishing. *Int J Precis Eng Manuf Technol*. 2019;6(1):11-21. doi:10.1007/s40684-019-00019-2

59. Hot Isostatic Pressing | GE Additive. https://www.ge.com/additive/additive-manufacturing/materials/apc-homepage/hot-isostatic-pressing. Accessed August 29, 2019.

60. Miller W., Zhuang L, Bottema J, et al. Recent development in aluminium alloys for the automotive industry. *Mater Sci Eng A*. 2000;280(1):37-49. doi:10.1016/S0921-5093(99)00653-X

61. Cabrini M, Calignano F, Fino P, et al. Corrosion Behavior of Heat-Treated AlSi10Mg Manufactured by Laser Powder Bed Fusion. *Materials (Basel)*. 2018;11(7):1051. doi:10.3390/ma11071051

62. Kempen K, Thijs L, Van Humbeeck J, Kruth JP. Mechanical Properties of AlSi10Mg Produced by Selective Laser Melting. In: *Physics Procedia*. ; 2012. doi:10.1016/j.phpro.2012.10.059

63. Cabrini M, Calignano F, Fino P, et al. Corrosion behavior of heat-treated AlSi10Mg manufactured by laser powder bed fusion. *Materials (Basel)*. 2018;11(7). doi:10.3390/ma11071051

64. Frazier WE. Metal additive manufacturing: A review. *J Mater Eng Perform*. 2014;23(6):1917-1928. doi:10.1007/s11665-014-0958-z

65. Prashanth KG, Scudino S, Klauss HJ, et al. Microstructure and mechanical properties of Al-12Si produced by selective laser melting: Effect of heat treatment. *Mater Sci Eng A*. 2014. doi:10.1016/j.msea.2013.10.023

66. Takata N, Kodaira H, Sekizawa K, Suzuki A, Kobashi M. Change in microstructure of selectively laser melted AlSi10Mg alloy with heat treatments. *Mater Sci Eng A*. 2017. doi:10.1016/j.msea.2017.08.029

67. Murray JL, McAlister AJ. The Al-Si (Aluminum-Silicon) system. *Bull Alloy Phase Diagrams*. 1984. doi:10.1007/bf02868729

68. Thijs L, Kempen K, Kruth JP, Van Humbeeck J. Fine-structured aluminium products with controllable texture by selective laser melting of pre-alloyed AlSi10Mg powder. *Acta Mater*. 2013;61(5):1809-1819. doi:10.1016/j.actamat.2012.11.052

69. Li S, Wei Q, Shi Y, Zhu Z, Zhang D. Microstructure Characteristics of Inconel 625 Superalloy Manufactured by Selective Laser Melting. *J Mater Sci Technol*. 2015;31(9):946-952. doi:10.1016/J.JMST.2014.09.020

70. Tawancy HM, Allam IM, Abbas NM. Effect of Ni3Nb precipitation on the corrosion resistance of Inconel alloy 625. *J Mater Sci Lett*. 1990. doi:10.1007/BF00725845

71. Craig B. Materials for deep oil and gas well construction. *Adv Mater Process*. 2008;166(5):33-35.

72. Brownlee JK, Flesner KO, Riggs KR, Miglin BP. Selection and Qualification of Materials for HPHT Wells. In: *SPE High Pressure/High Temperature Sour Well Design Applied Technology Workshop*. Society of Petroleum Engineers; 2005. doi:10.2118/97590-MS

73. Kane RD, Anand T, Biswas A, Ellis PF, Srinivasan S. New approach to H<inf>2</inf>S limits for high-pressure, high-temperature petroleum production wells. *Mater Perform*. 2014;53(1).

74. Kolts J, Wu J, Manning P, Asphahani A. Highly Alloyed Austenitic Material for Corrosion Resistance. *Corros Rev*. 1986;6:279-326.

75. Scarberry R, Graver D, Stephens C. Alloying for Corrosion Control. *Mater Prot*. 1967:54-57.

76. Kritzer P, Boukis N, Dinjus E. Review of the corrosion of nickel-based alloys and stainless steels in strongly oxidizing pressurized high-temperature solutions at subcritical and supercritical temperatures. *Corrosion*. 2000;56(11):1093-1104. doi:10.5006/1.3294394

77. Hwang SS, Kim HP, Lee DH, Kim UC, Kim JS. The mode of stress corrosion cracking in Ni-base alloys in high temperature water containing lead. *J Nucl Mater*. 1999;275(1):28-36. doi:10.1016/S0022-3115(99)00111-7

78. Sun H, Wu X, Han EH. Effects of temperature on the protective property, structure and composition of the oxide film on Alloy 625. *Corros Sci*. 2009;51(11):2565-2572. doi:10.1016/j.corsci.2009.06.043

79. Kritzer P. Corrosion in high-temperature and supercritical water and aqueous solutions: A review. *J Supercrit Fluids*. 2004;29(1-2):1-29. doi:10.1016/S0896-8446(03)00031-7

80. Geddes B, Leon H, Huang X. *Superalloys : Alloying and Performance*. ASM International; 2010. https://www.asminternational.org/search/-/journal_content/56/10192/05300G/PUBLICATION. Accessed August 30, 2019.

81. Anam A, Dilip JJS, Pal D, Stucker B. Effect of Scan Pattern on the Microstructural Evolution of Inconel 625 during Selective Laser Melting. *Int Solid Free Fabr Symp*

– *An Addit Manuf Conf*. 2014:363-376. doi:10.13140/2.1.1256.6089

82. Vilaro T, Colin C, Bartout JD, Nazé L, Sennour M. Microstructural and mechanical approaches of the selective laser melting process applied to a nickel-base superalloy. *Mater Sci Eng A*. 2012;534:446-451. doi:10.1016/j.msea.2011.11.092

83. Arısoy YM, Criales LE, Özel T, Lane B, Moylan S, Donmez A. Influence of scan strategy and process parameters on microstructure and its optimization in additively manufactured nickel alloy 625 via laser powder bed fusion. *Int J Adv Manuf Technol*. 2017;90(5-8):1393-1417. doi:10.1007/s00170-016-9429-z

84. Marchese G, Garmendia Colera X, Calignano F, et al. Characterization and Comparison of Inconel 625 Processed by Selective Laser Melting and Laser Metal Deposition . *Adv Eng Mater*. 2016. doi:10.1002/adem.201600635

85. Manfredi D, Calignano F, Krishnan M, Canali R, Ambrosio EP, Atzeni E. From powders to dense metal parts: Characterization of a commercial alsimg alloy processed through direct metal laser sintering. *Materials (Basel)*. 2013;6(3):856-869. doi:10.3390/ma6030856

86. Kreitcberg A, Brailovski V, Turenne S. Elevated temperature mechanical behavior of IN625 alloy processed by laser powder-bed fusion. *Mater Sci Eng A*. 2017. doi:10.1016/j.msea.2017.06.045

87. Cabrini M, Lorenzi S, Testa C, et al. Microstructure and Selective Corrosion of Alloy 625 Obtained by Means of Laser Powder Bed Fusion. *Materials (Basel)*. 2019;12(11):1742. doi:10.3390/ma12111742

88. Antonsson T, Fredriksson H. The effect of cooling rate on the solidification of INCONEL 718. *Metall Mater Trans B-Process Metall Mater Process Sci*. 2005. doi:10.1007/s11663-005-0009-0

89. Marchese G, Lorusso M, Parizia S, et al. Influence of heat treatments on microstructure evolution and mechanical properties of Inconel 625 processed by laser powder bed fusion. *Mater Sci Eng A*. 2018;729. doi:10.1016/j.msea.2018.05.044

90. Xu FJ, Lv YH, Xu BS, Liu YX, Shu FY, He P. Effect of deposition strategy on the microstructure and mechanical properties of Inconel 625 superalloy fabricated by pulsed plasma arc deposition. *Mater Des*. 2013;45:446-455. doi:10.1016/j.matdes.2012.07.013

91. Dupont JN, Robino C V., Marder AR, Notis MR. Solidification of Nb-bearing superalloys: Part II. Pseudoternary solidification surfaces. *Metall Mater Trans A Phys Metall Mater Sci*. 1998. doi:10.1007/s11661-998-0320-x

92. Hack H, Link R, Knudsen E, Baker B, Olig S. Mechanical properties of additive manufactured nickel alloy 625. *Addit Manuf*. 2017;14:105-115. doi:10.1016/J.ADDMA.2017.02.004

93. EOS. IN625 - Material data sheet - EOS. http://ip-saas-eos-cms.s3.amazonaws.com/public/d1327facdca0e32a/373a60ec4f5c891b7dbcdf572

e37d3b0/EOS_NickelAlloy_IN625_en.pdf. Accessed August 30, 2019.

94. Wang K. The use of titanium for medical applications in the USA. *Mater Sci Eng A*. 1996. doi:10.1016/0921-5093(96)10243-4

95. *BIOMATERIALS IN CLINICAL PRACTICE : Advances in Clinical Research and Medical*. SPRINGER INTERNATIONAL PU; 2018.

96. Thijs L, Verhaeghe F, Craeghs T, Humbeeck J Van, Kruth J-P. A study of the microstructural evolution during selective laser melting of Ti–6Al–4V. *Acta Mater*. 2010;58(9):3303-3312. doi:10.1016/J.ACTAMAT.2010.02.004

97. Herzog D, Seyda V, Wycisk E, Emmelmann C. Additive manufacturing of metals. *Acta Mater*. 2016;117:371-392. doi:10.1016/J.ACTAMAT.2016.07.019

98. Lütjering G (Gerd), Williams JC (James C. *Titanium*. Springer; 2007. https://books.google.it/books?hl=it&lr=&id=c9iR1Lm43GEC&oi=fnd&pg=PA4&ots=aIsTv6K7N4&sig=HekY9gfLzKujaVrPdjJp4W6YrH0&redir_esc=y#v=onepage&q&f=false. Accessed September 5, 2019.

99. Donachie MJ. *Titanium : A Technical Guide*. ASM International; 2000. https://books.google.it/books?hl=it&lr=&id=HgzukknbNGAC&oi=fnd&pg=PR7&ots=K04-ji8E0O&sig=rTZpwd6fSqwT7tz2MfcBFphShuw&redir_esc=y#v=onepage&q&f=false. Accessed September 5, 2019.

100. Vilaro T, Colin C, Bartout JD. As-Fabricated and Heat-Treated Microstructures of the Ti-6Al-4V Alloy Processed by Selective Laser Melting. *Metall Mater Trans A*. 2011;42(10):3190-3199. doi:10.1007/s11661-011-0731-y

101. Facchini L, Magalini E, Robotti P, Molinari A, Höges S, Wissenbach K. Ductility of a Ti-6Al-4V alloy produced by selective laser melting of prealloyed powders. *Rapid Prototyp J*. 2010;16(6):450-459. doi:10.1108/13552541011083371

102. Wycisk E, Siddique S, Herzog D, Walther F, Emmelmann C. Fatigue Performance of Laser Additive Manufactured Ti–6Al–4V in Very High Cycle Fatigue Regime up to 109 Cycles. *Front Mater*. 2015;2:72. doi:10.3389/fmats.2015.00072

103. Trevisan F, Calignano F, Lorusso M, et al. Effects of heat treatments on A357 alloy produced by selective laser melting. In: *World Powder Metallurgy 2016 Congress and Exhibition, World PM 2016*. DISAT-Dipartimento Scienza Applicata e Tecnologia, Politecnico di Torino, Corso Duca degli Abruzzi 24, Torino, 10129, Italy: European Powder Metallurgy Association (EPMA); 2016. https://www.scopus.com/inward/record.uri?eid=2-s2.0-85035349398&partnerID=40&md5=48aa84963180825772d298441b5f9ca0.

104. Calignano F, Manfredi D, Ambrosio EP, Iuliano L, Fino P. Influence of process parameters on surface roughness of aluminum parts produced by DMLS. *Int J Adv Manuf Technol*. 2013;67(9-12):2743-2751. doi:10.1007/s00170-012-4688-9

105. Melitz W, Shen J, Kummel AC, Lee S. Kelvin probe force microscopy and its application. *Surf Sci Rep*. 2011;66:1-27. doi:10.1016/j.surfrep.2010.10.001

106. Cabrini M, Lorenzi S, Pastore T, et al. Evaluation of corrosion resistance of Al-

10Si-Mg alloy obtained by means of Direct Metal Laser Sintering. *J Mater Process Technol*. 2016;231:326-335. doi:10.1016/j.jmatprotec.2015.12.033

107. Mutombo K, du M. Corrosion Fatigue Behaviour of Aluminium 5083-H111 Welded Using Gas Metal Arc Welding Method. In: *Arc Welding*. ; 2011. doi:10.5772/25991

108. Frankel GS. Pitting Corrosion of Metals. *J Electrochem Soc*. 1998;145(6):2186. doi:10.1149/1.1838615

109. McCafferty E. The electrode kinetics of pit initiation on aluminum. *Corros Sci*. 1995;37(3):481-492. doi:10.1016/0010-938X(94)00150-5

110. Natishan PM, O'Grady WE. Chloride Ion Interactions with Oxide-Covered Aluminum Leading to Pitting Corrosion: A Review. *J Electrochem Soc*. 2014;161(9):C421-C432. doi:10.1149/2.1011409jes

111. Foley RT. Localized Corrosion of Aluminum Alloys—A Review. *CORROSION*. 1986;42(5):277-288. doi:10.5006/1.3584905

112. Galvele JR, de De Micheli SM. Mechanism of intergranular corrosion of Al-Cu alloys. *Corros Sci*. 1970;10(11):795-807. doi:10.1016/S0010-938X(70)80003-8

113. Böhni H, Uhlig HH. Environmental Factors Affecting the Critical Pitting Potential of Aluminum. *J Electrochem Soc*. 1969;116(7):906. doi:10.1149/1.2412167

114. Stirrup BN, Hampson NA, Midgley IS. Pit formation in relation to the etching of aluminium in chloride solutions. *J Appl Electrochem*. 1975;5(3):229-235. doi:10.1007/BF01637273

115. Debasmita Dash, Shekhar Kumar, C.Mallika and UK. New Data on Activity Coefficients of Potassium, Nitrate, and Chloride Ions in Aqueous Solutions of KNO3 and KCl by Ion Selective Electrodes. *ISRN Chem Eng*. 2012;2012:1-5. doi:10.5402/2012/730154

116. Cabrini M, Lorenzi S, Pastore T, et al. Corrosion behavior of AlSi10Mg alloy produced by laser powder bed fusion under chloride exposure. *Corros Sci*. 2019;(November 2018):0-1. doi:10.1016/j.corsci.2019.03.010

117. J. van den Brand *,†, P. C. Snijders ‡, W. G. Sloof §, H. Terryn † and, J. H. W. de Wit† §. Acid−Base Characterization of Aluminum Oxide Surfaces with XPS. 2004. doi:10.1021/JP037877F

118. Pech-Canul MA, Pech-Canul MI, Bartolo-Pérez P, Echeverría M. The role of silicon alloying addition on the pitting corrosion resistance of an Al-12 wt.%Si alloy. *Electrochim Acta*. 2014;140:258-265. doi:10.1016/J.ELECTACTA.2014.05.034

119. Vargel C. *Corrosion of Aluminium*. Elsevier; 2004.

120. Cabrini M, Lorenzi S, Pastore T, et al. Corrosion resistance in chloride solution of the AlSi10Mg alloy obtained by means of LPBF. *Surf Interface Anal*. 2018;(September):6-11. doi:10.1002/sia.6601

121. Shibata T. Statistical and Stochastic Approaches to Localized Corrosion. *Corros Sci*. 1996;52(11):813-830. doi:10.5006/1.3292074

122. Wang J, Qian S, Li Y, Macdonald DD, Jiang Y, Li J. Passivity breakdown on 436 ferritic stainless steel in solutions containing chloride. *J Mater Sci Technol*. 2019;35(4):637-643. doi:10.1016/J.JMST.2018.10.030

123. Kong D, Dong C, Wei X, et al. Size matching effect between anion vacancies and halide ions in passive film breakdown on copper. *Electrochim Acta*. 2018;292:817-827. doi:10.1016/J.ELECTACTA.2018.10.004

124. Al-Sahli A, Ghanbari E, Macdonald DD. Effect of tungsten alloying on passivity breakdown of nickel. *Mater Corros*. 2019. doi:10.1002/maco.201810121

125. Pride ST. Metastable Pitting of Aluminum and Criteria for the Transition to Stable Pit Growth. *J Electrochem Soc*. 2006. doi:10.1149/1.2059275

126. AZIZ PM. Application of the Statistical Theory of Extreme Values To the Analysis of Maximum Pit Depth Data for Aluminum. *CORROSION*. 2014. doi:10.5006/0010-9312-12.10.35

127. Buchheit RG. A Compilation of Corrosion Potentials Reported for Intermetallic Phases in Aluminum Alloys. *J Electrochem Soc*. 1995;142(11):3994. doi:10.1149/1.2048447

128. Rubben T, Revilla RI, De Graeve I. Influence of heat treatments on the corrosion mechanism of additive manufactured AlSi10Mg. *Corros Sci*. 2019;147:406-415. doi:10.1016/j.corsci.2018.11.038

129. Cabrini M, Lorenzi S, Testa C, et al. Statistical approach for electrochemical evaluation of the effect of heat treatments on the corrosion resistance of AlSi10Mg alloy by laser powder bed fusion. *Electrochim Acta*. 2019;305:459-466. doi:10.1016/j.electacta.2019.03.103

130. Rafieazad M, Mohammadi M, Nasiri AM. On microstructure and early stage corrosion performance of heat treated direct metal laser sintered AlSi10Mg. *Addit Manuf*. 2019;28:107-119. doi:10.1016/j.addma.2019.04.023

131. EOS. EOS GmbH - Electro Optical Systems, Material Data Sheet: EOS Aluminium AlSi10Mg.

132. Andreatta F. Local electrochemical behaviour of 7xxx aluminium alloys. 2004. https://repository.tudelft.nl/islandora/object/uuid:a0692f2f-59e3-4d2f-9816-3c70211ca87e/. Accessed September 4, 2019.

133. Gupta AK, Lloyd DJ, Court SA. Precipitation hardening in Al-Mg-Si alloys with and without excess Si. *Mater Sci Eng A*. 2001;A 316:11-17. doi:10.1016/S0921-5093(01)01247-3

134. Xiong ZH, Liu SL, Li SF, Shi Y, Yang YF, Misra RDK. Role of melt pool boundary condition in determining the mechanical properties of selective laser melting AlSi10Mg alloy. *Mater Sci Eng A*. 2019;740-741:148-156. doi:10.1016/j.msea.2018.10.083

135. Liu M, Takata N, Suzuki A, Kobashi M. Microstructural characterization of cellular AlSi10Mg alloy fabricated by selective laser melting. *Mater Des*. 2018;157:478-491. doi:10.1016/j.matdes.2018.08.005

136. Fousová M, Dvorský D, Michalcová A, Vojtěch D. Changes in the microstructure and mechanical properties of additively manufactured AlSi10Mg alloy after exposure to elevated temperatures. *Mater Charact*. 2018;137:119-126. doi:10.1016/j.matchar.2018.01.028

137. Hadadzadeh A, Amirkhiz BS, Li J, Odeshi A, Mohammadi M. Deformation mechanism during dynamic loading of an additively manufactured AlSi10Mg_200C. *Mater Sci Eng A*. 2018;722:263-268. doi:10.1016/j.msea.2018.03.014

138. Takata N, Kodaira H, Suzuki A, Kobashi M. Size dependence of microstructure of AlSi10Mg alloy fabricated by selective laser melting. *Mater Charact*. 2018;143:18-26. doi:10.1016/j.matchar.2017.11.052

139. Hadadzadeh A, Baxter C, Amirkhiz BS, Mohammadi M. Strengthening mechanisms in direct metal laser sintered AlSi10Mg: Comparison between virgin and recycled powders. *Addit Manuf*. 2018;23:108-120. doi:10.1016/j.addma.2018.07.014

140. Hadadzadeh A, Amirkhiz BS, Mohammadi M. Contribution of Mg2Si precipitates to the strength of direct metal laser sintered AlSi10Mg. *Mater Sci Eng A*. 2019;739:295-300. doi:10.1016/j.msea.2018.10.055

141. Fallah V, Korinek A, Ofori-Opoku N, et al. Atomic-scale pathway of early-stage precipitation in Al-Mg-Si alloys. *Acta Mater*. 2015;82:457-467. doi:10.1016/j.actamat.2014.09.004

142. Chen B, Moon SK, Yao X, et al. Strength and strain hardening of a selective laser melted AlSi10Mg alloy. *Scr Mater*. 2017;141:45-49. doi:10.1016/j.scriptamat.2017.07.025

143. Bai Y, Yang Y, Xiao Z, Zhang M, Wang D. Process optimization and mechanical property evolution of AlSiMg0.75 by selective laser melting. *Mater Des*. 2018. doi:10.1016/j.matdes.2017.11.045

144. Maeshima T, Oh-ishi K. Solute clustering and supersaturated solid solution of AlSi10Mg alloy fabricated by selective laser melting. *Heliyon*. 2019;5:e01186. doi:10.1016/j.heliyon.2019.e01186

145. Marola S, Manfredi D, Fiore G, et al. A comparison of Selective Laser Melting with bulk rapid solidification of AlSi10Mg alloy. *J Alloys Compd*. 2018;742:271-279. doi:10.1016/J.JALLCOM.2018.01.309

146. Klar F, Bansmann J, Glaefeke H, Fitting HJ, Meiwes-Broer KH. Exoelectron emission from magnesium surfaces. *Surf Sci*. 1999;442(3):477-484. doi:10.1016/S0039-6028(99)00965-6

147. Górecki T, Górecki C. Exoelectron emission accompanying phase changes in age-hardenable aluminium alloys. *Jpn J Appl Phys*. 1985;24(Supplement 24-4):102-

105. doi:10.7567/JJAPS.24S4.102

148. Górecki T. Exoelectron Emission During Phase Transformations in Metallic Materials. *Rev Latinoam Metal y Mater*. 1987;7(1):3-17.

149. Sujak B, Górecki T, Malkiewicz M, Stepriowski I. No Title. *Acta Phys Pol*. 1966;30:51.

150. Birbilis N, Buchheit RG. Electrochemical characteristics of intermetallic phases in aluminum alloys : An experimental survey and discussion. *J Electrochem Soc*. 2005;152(4):B140. doi:10.1149/1.1869984

151. Linardi E, Haddad R, Lanzani L. Stability Analysis of the Mg2Si Phase in AA 6061 Aluminum Alloy. *Procedia Mater Sci*. 2012;1:550-557. doi:10.1016/j.mspro.2012.06.074

152. Eckermann F, Suter T, Uggowitzer PJ, Afseth A, Schmutz P. The influence of MgSi particle reactivity and dissolution processes on corrosion in Al-Mg-Si alloys. *Electrochim Acta*. 2008;54(2):844-855. doi:10.1016/j.electacta.2008.05.078

153. Marchese G, Parizia S, Rashidi M, et al. The role of texturing and microstructure evolution on the tensile behavior of heat-treated Inconel 625 produced via laser powder bed fusion. *Mater Sci Eng A*. 2020;769:138500. doi:10.1016/j.msea.2019.138500

154. *Technical Data General Process Data*.

155. Oldfield JW. Test techniques for pitting and crevice corrosion resistance of stainless steels and nickel-base alloys in chloride-containing environments. *Int Mater Rev*. 2012;32(1):153-172. doi:10.1179/095066087790150313

156. Cabrini M, Lorenzi S, Testa C, et al. Evaluation of Corrosion Resistance of Alloy 625 Obtained by Laser Powder Bed Fusion. *J Electrochem Soc*. 2019;166(11):C3399-C3408. doi:10.1149/2.0471911jes

157. Haynes International. Haynes International. https://www.haynesintl.com/alloys/alloy-portfolio_/High-temperature-Alloys/HAYNES625Alloy/iso-corrosion-diagrams.

158. Lloyd AC, Shoesmith DW, McIntyre NS, Noël JJ. Effects of Temperature and Potential on the Passive Corrosion Properties of Alloys C22 and C276. *J Electrochem Soc*. 2003;150(4):B120. doi:10.1149/1.1554914

159. Lloyd AC, Noël JJ, McIntyre S, Shoesmith DW. Cr, Mo and W alloying additions in Ni and their effect on passivity. *Electrochim Acta*. 2004;49(17-18):3015-3027. doi:10.1016/J.ELECTACTA.2004.01.061

160. Dinda GP, Dasgupta AK, Mazumder J. Laser aided direct metal deposition of Inconel 625 superalloy: Microstructural evolution and thermal stability. *Mater Sci Eng A*. 2009;509(1-2):98-104. doi:10.1016/j.msea.2009.01.009

161. Paul CP, Ganesh P, Mishra SK, Bhargava P, Negi J, Nath AK. Investigating laser rapid manufacturing for Inconel-625 components. *Opt Laser Technol*. 2007;39(4):800-805. doi:10.1016/j.optlastec.2006.01.008

162. Paul CP, Mishra SK, Premsingh CH, Bhargava P, Tiwari P, Kukreja LM. Studies on laser rapid manufacturing of cross-thin-walled porous structures of Inconel 625. *Int J Adv Manuf Technol*. 2012;61(5-8):757-770. doi:10.1007/s00170-011-3742-3

163. Harrison NJ, Todd I, Mumtaz K. Reduction of micro-cracking in nickel superalloys processed by Selective Laser Melting: A fundamental alloy design approach. *Acta Mater*. 2015. doi:10.1016/j.actamat.2015.04.035

164. Yao MX, Wu JBC, Yick S, Xie Y, Liu R. High temperature wear and corrosion resistance of a Laves phase strengthened Co-Mo-Cr-Si alloy. *Mater Sci Eng A*. 2006;435-436:78-83. doi:10.1016/j.msea.2006.07.054

165. Nikiforov A V., Petrushina IM, Christensen E, Tomás-García AL, Bjerrum NJ. Corrosion behaviour of construction materials for high temperature steam electrolysers. *Int J Hydrogen Energy*. 2011;36(1):111-119. doi:10.1016/j.ijhydene.2010.09.023

166. Davis JR (Joseph R., ASM International. Handbook Committee. *Nickel, Cobalt, and Their Alloys*. ASM International; 2000. https://www.asminternational.org/search/-/journal_content/56/10192/06178G/PUBLICATION. Accessed August 1, 2019.

167. *The Corrosion Resistance of Nickel-Containing Alloys in Sulfuric Acid and Related Compounds*.; 1983. https://www.nickelinstitute.org/media/1829/thecorrosionresistanceofnickel_containingalloysinsulphuricacidandrelatedcompounds_1318_.pdf. Accessed September 6, 2019.

168. Postlethwaite J, Scoular RJ, Dobbin MH. LOCALIZED CORROSION OF MOLYBDENUM-BEARING NICKEL ALLOYS IN CHLORIDE SOLUTIONS. *Corrosion*. 1988;44(4):199-203. doi:10.5006/1.3583925

169. Asphahani AI. LOCALIZED CORROSION OF HIGH PERFORMANCE ALLOYS. *Mater Perform*. 1980;19(8):9-21. http://www.scopus.com/inward/record.url?eid=2-s2.0-0019045963&partnerID=40&md5=1c5f0a84a4ef8e0da3028df01749a1c6.

170. Man IC, Su HY, Calle-Vallejo F, et al. Universality in Oxygen Evolution Electrocatalysis on Oxide Surfaces. *ChemCatChem*. 2011;3(7):1159-1165. doi:10.1002/cctc.201000397

171. McCafferty E, Bogar FD, Thomas ED, Creegan CA, Lucas KE, Kaznoff AI. Crevice Corrosion Propagation on Alloy 625 and Alloy C276 in Natural Seawater. *Corros*. 1997;53(10):755-761. doi:10.5006/1.3290259

172. Kritzer P, Boukis N, Dinjus E. Corrosion of Alloy 625 in Aqueous Solutions Containing Chloride and Oxygen. *Corrosion*. 1998;54(10):824-834. doi:10.5006/1.3284802

173. Rebak RB. Stress corrosion cracking (SCC) of nickel-based alloys. In: *Stress Corrosion Cracking*. Elsevier; 2011:273-306. doi:10.1533/9780857093769.3.273

174. KANE RD. Accelerated Hydrogen Charging of Nickel and Cobalt Base Alloys.

CORROSION. 1978;34(12):442-445. doi:10.5006/0010-9312-34.12.442

175. Baker CL, Chene J, Bernstein IM, Williams JC. Hydrogen effects in [001] oriented nickel-base superalloy single crystals. *Metall Trans A*. 1988;19(1):73-82. doi:10.1007/BF02669816

176. Townsend A, Senin N, Blunt L, Leach RK, Taylor JS. Surface texture metrology for metal additive manufacturing: a review. *Precis Eng*. 2016;46:34-47. doi:10.1016/J.PRECISIONENG.2016.06.001

177. Beck TR. Initial Oxide Growth Rate on Newly Generated Surfaces. *J Electrochem Soc*. 1982;129(11):2500. doi:10.1149/1.2123591

178. Chen LY, Huang JC, Lin CH, et al. Anisotropic response of Ti-6Al-4V alloy fabricated by 3D printing selective laser melting. *Mater Sci Eng A*. 2017. doi:10.1016/j.msea.2016.11.061

179. Dai N, Zhang LC, Zhang J, et al. Distinction in corrosion resistance of selective laser melted Ti-6Al-4V alloy on different planes. *Corros Sci*. 2016. doi:10.1016/j.corsci.2016.06.009

180. Guzanová A, Ižaríková G, Brezinová J, Živčák J, Draganovská D, Hudák R. Influence of build orientation, heat treatment, and laser power on the hardness of Ti6Al4V manufactured using the DMLS process. *Metals (Basel)*. 2017. doi:10.3390/met7080318

181. Simonelli M, Tse YY, Tuck C. Effect of the build orientation on the mechanical properties and fracture modes of SLM Ti-6Al-4V. *Mater Sci Eng A*. 2014. doi:10.1016/j.msea.2014.07.086

182. Chandramohan P, Bhero S, Obadele BA, Olubambi PA. Laser additive manufactured Ti–6Al–4V alloy: tribology and corrosion studies. *Int J Adv Manuf Technol*. 2017. doi:10.1007/s00170-017-0410-2

183. Yang J, Yang H, Yu H, Wang Z, Zeng X. Corrosion Behavior of Additive Manufactured Ti-6Al-4V Alloy in NaCl Solution. *Metall Mater Trans A Phys Metall Mater Sci*. 2017. doi:10.1007/s11661-017-4087-9

184. Alifui-Segbaya F, Lewis J, Eggbeer D, Williams RJ. In vitro corrosion analyses of heat treated cobalt-chromium alloys manufactured by direct metal laser sintering. *Rapid Prototyp J*. 2015. doi:10.1108/RPJ-11-2012-0110

185. Ganesh P, Giri R, Kaul R, et al. Studies on pitting corrosion and sensitization in laser rapid manufactured specimens of type 316L stainless steel. *Mater Des*. 2012. doi:10.1016/j.matdes.2012.03.011

186. Chen X, Li J, Cheng X, Wang H, Huang Z. Effect of heat treatment on microstructure, mechanical and corrosion properties of austenitic stainless steel 316L using arc additive manufacturing. *Mater Sci Eng A*. 2018. doi:10.1016/j.msea.2017.10.002

187. Stoudt MR, Ricker RE, Lass EA, Levine LE. Influence of Postbuild Microstructure on the Electrochemical Behavior of Additively Manufactured 17-4 PH Stainless Steel. *JOM*. 2017. doi:10.1007/s11837-016-2237-y

188. Alves VA, Reis RQ, Santos ICB, et al. In situ impedance spectroscopy study of the electrochemical corrosion of Ti and Ti-6Al-4V in simulated body fluid at 25 °C and 37 °C. *Corros Sci*. 2009. doi:10.1016/j.corsci.2009.06.035

189. De Assis SL, Wolynec S, Costa I. Corrosion characterization of titanium alloys by electrochemical techniques. In: *Electrochimica Acta*. ; 2006. doi:10.1016/j.electacta.2005.02.121

190. Vasilescu E, Drob P, Raducanu D, et al. Effect of thermo-mechanical processing on the corrosion resistance of Ti6Al4V alloys in biofluids. *Corros Sci*. 2009. doi:10.1016/j.corsci.2009.08.014

191. Cigada A, Cabrini M, Pedeferri P. Increasing of the corrosion resistance of the Ti6Al4V alloy by high thickness anodic oxidation. *J Mater Sci Mater Med*. 1992. doi:10.1007/BF00701236

192. Testa C, Cabrini M, Lorenzi S, et al. Comportamento alla corrosione di una lega Ti6Al4V per applicazione biomediche ottenuta tramite additive manufacturing. *LA Metall Ital*. 2020;112:6-11.

193. Boyan BD, Hummert TW, Dean DD, Schwartz Z. Role of material surfaces in regulating bone and cartilage cell response. *Biomaterials*. 1996;17(2):137-146. doi:10.1016/0142-9612(96)85758-9

Annex A

Aluminium alloy:

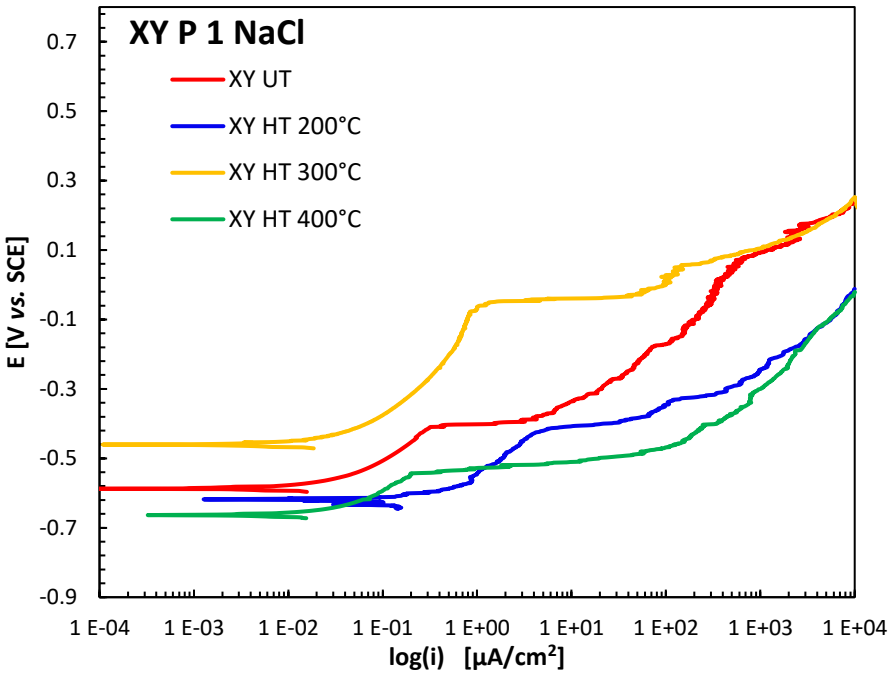

Figure A-1: Potentiodynamic tests on XY polished specimens in 1 g/L NaCl in function of the heat treatment temperature

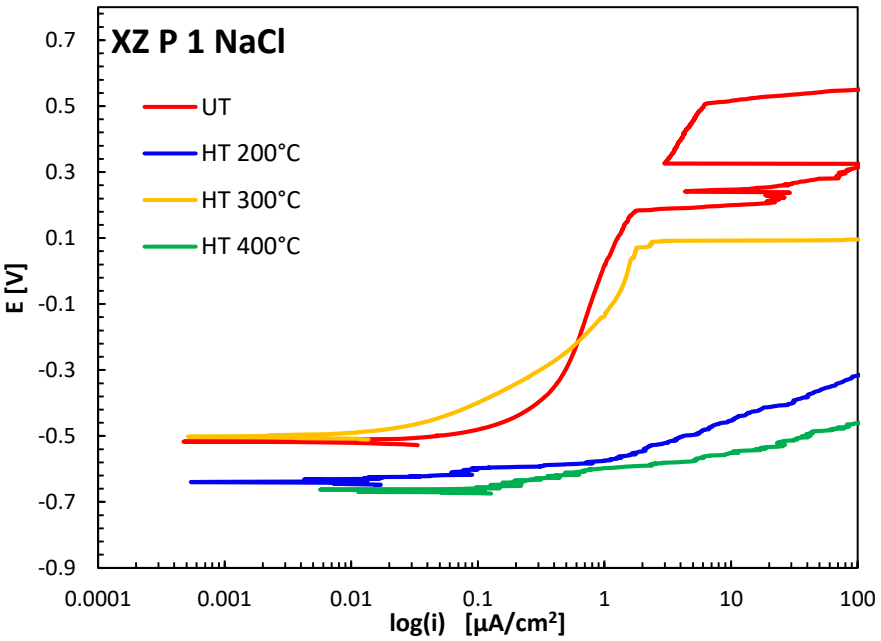

Figure A-2: Potentiodynamic tests on XZ polished specimens in 1 g/L NaCl in function of the heat treatment temperature

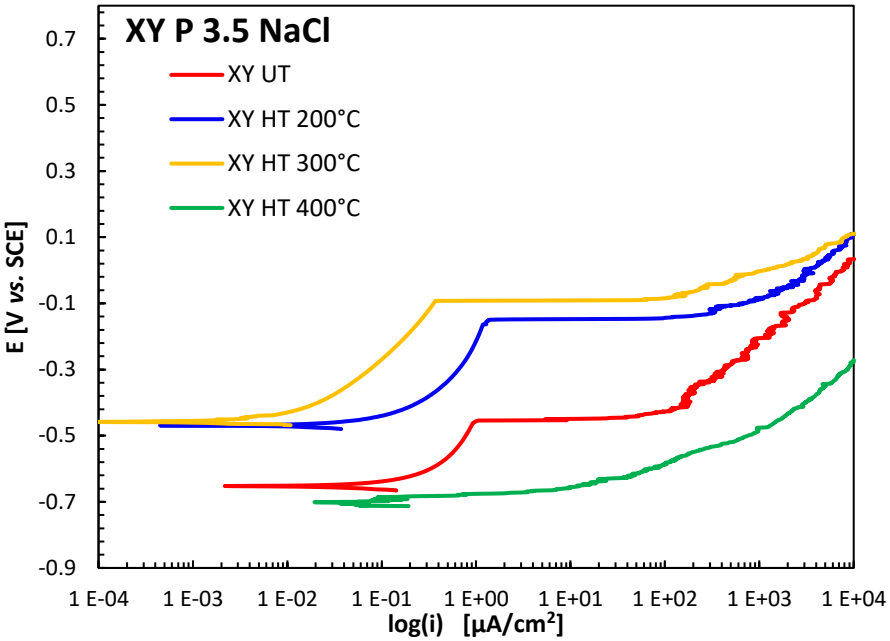

Figure A-3: Potentiodynamic tests on XY polished specimens in 3.5 g/L NaCl in function of the heat treatment temperature

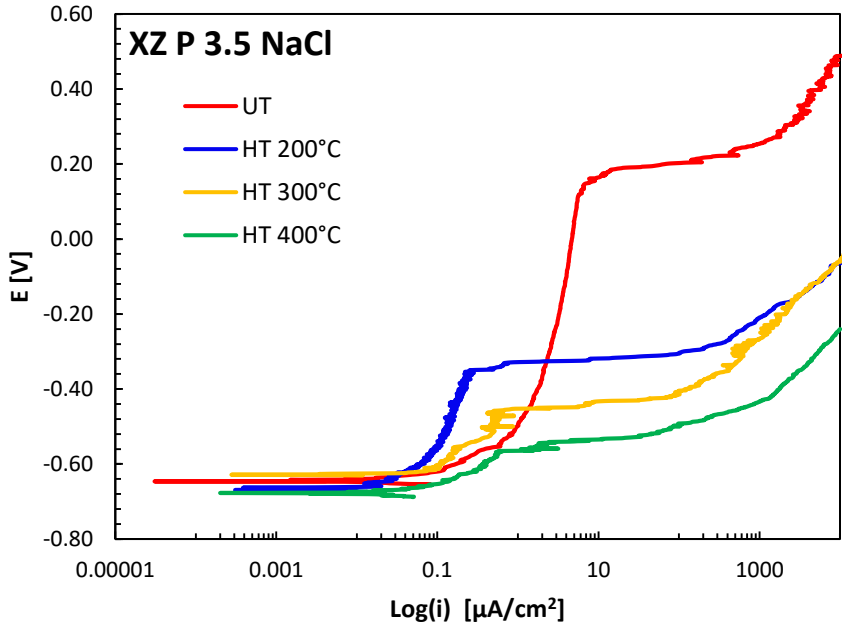

Figure A-4: Potentiodynamic tests on XZ polished specimens in 3.5 g/L NaCl in function of the heat treatment temperature

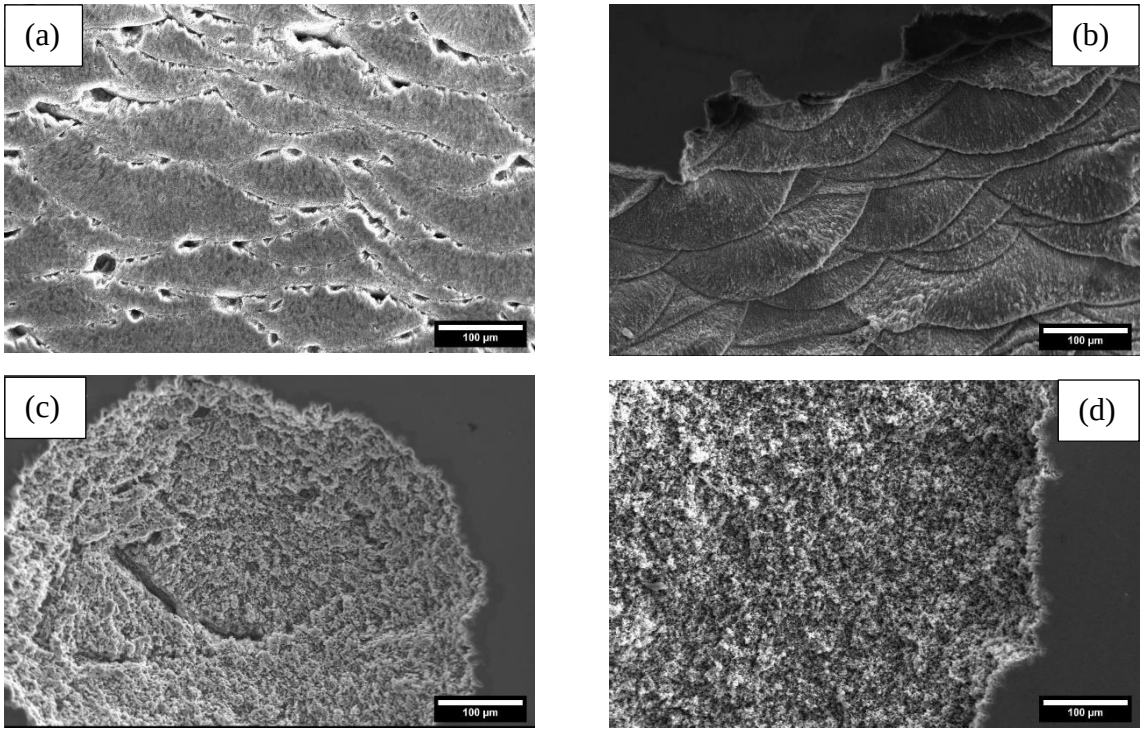

Figure A-5: Localized attack on polished surface exposed in 3.5 g/L NaCl for (a) the XZ un-treated specimen, (b) the XZ specimen heat treated at 200°C, (c) the XZ specimen heat treated at 300°C and (d) the XZ heat treated at 400°C.

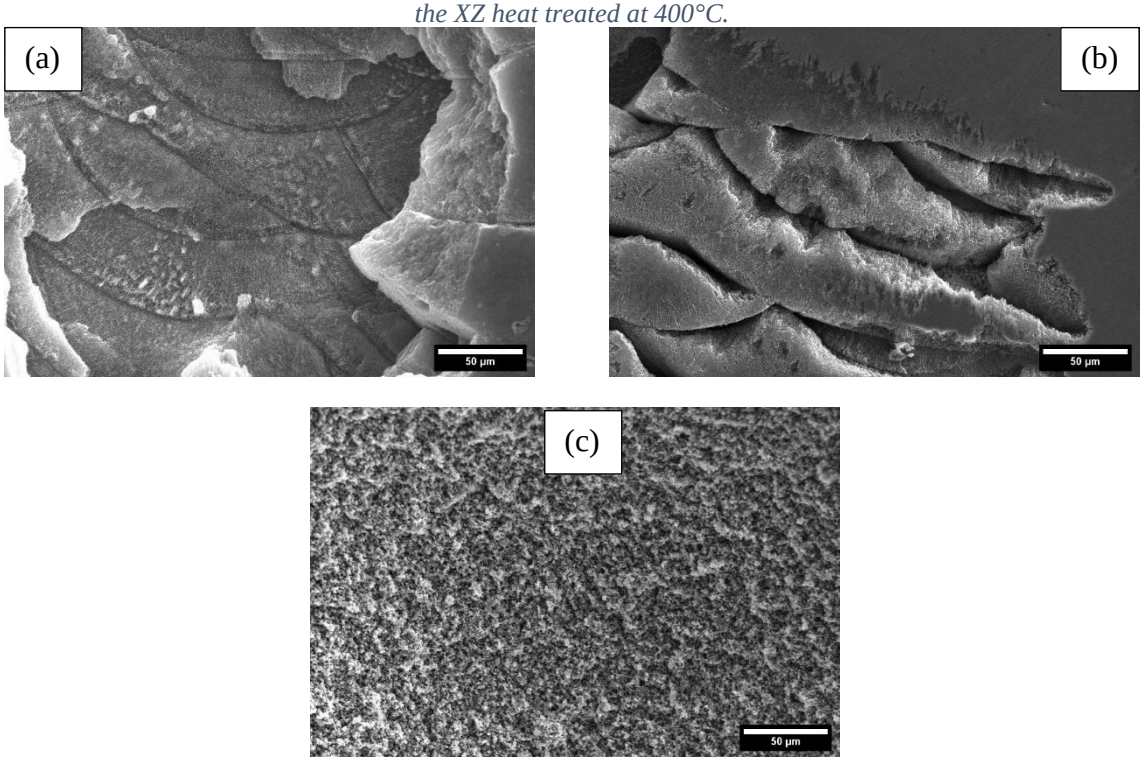

Figure A-6: Localized attack in 0.5 g/L NaCl for (a) the XZ un-treated specimen, (b) the XZ heat treated at 200°C and (C) the XZ heat treated at 400°C.

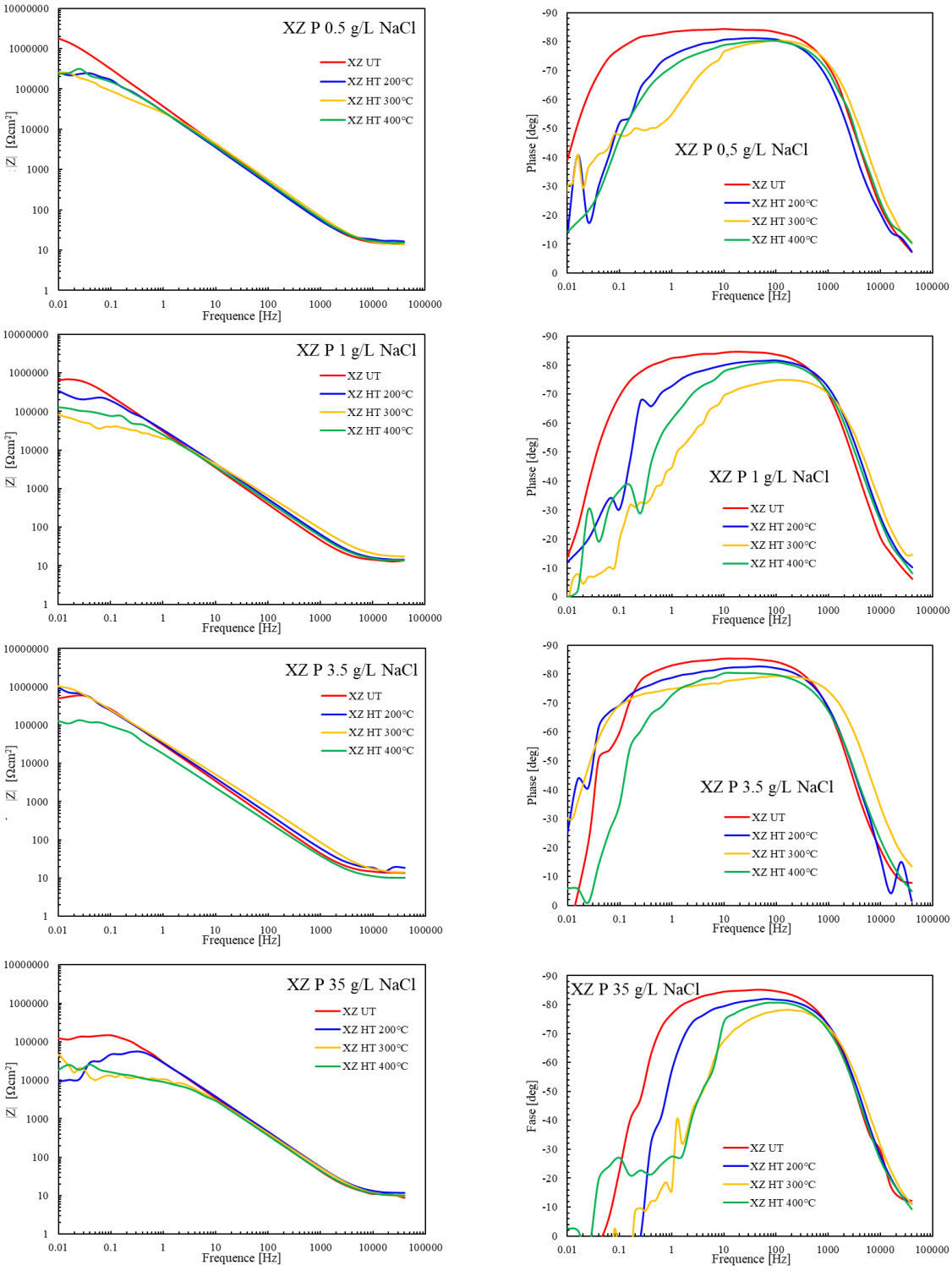

Figure A-7: Bode diagram of XZ P specimens in function of chloride content

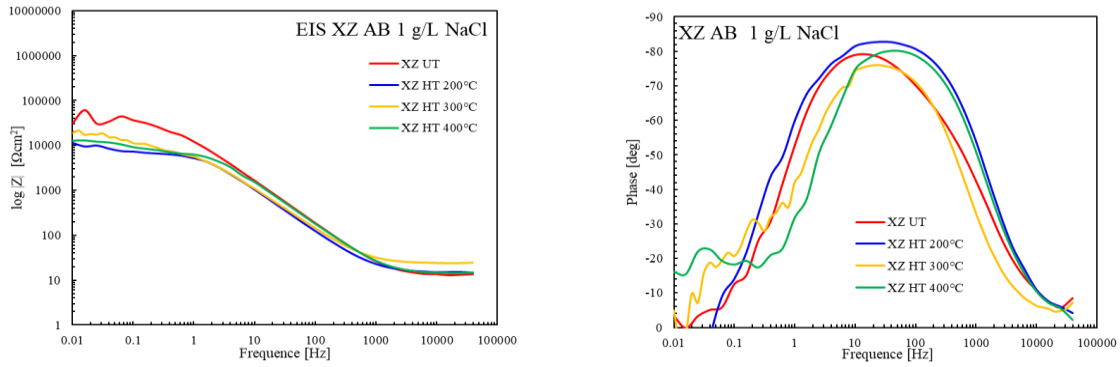

Figure A-8: Bode diagram of XY AB specimens

Table A-1: E_{corr} and E_{pit}, the impedance modulus, and the polarization resistance extrapolated from EIS and potentiodynamic tests

		XY specimens							
HTT*	test	1	2	3	4	5	6	7	8
UT	$\|Z\|_{40000}$ [ohm·cm^2]	14	13	14	164	12	16	12	19
	$\|Z\|_{0.01}$ [ohm·cm^2]	6.6E+05	1.3E+06	1.6E+05	5.3E+05	3.0E+06	9.0E+05	1.1E+06	1.7E+06
	Rp [ohm]	6.1E+05	7.2E+05	1.7E+05	5.5E+05	7.0E+06	1.6E+06	1.1E+06	1.7E+06
	E_{pit} [V *vs.* SCE]	0.341	0.414	0.480	0.453	0.138	0.800	0.588	0.800
	E_{corr} [V *vs.* SCE]	-0.741	0.587	0.639	0.577	0.569	0.550	0.597	0.661
200°C	$\|Z\|_{40000}$ [ohm·cm^2]	18	16		12	12	22	25	20
	$\|Z\|_{0.01}$ [ohm·cm^2]	7.7E+05	2.8E+05		2.3E+06	1.1E+06	2.1E+06	6.7E+05	7.0E+05
	Rp [ohm]	8.1E+04	2.6E+05	4.9E+05	3.5E+06	1.3E+06	1.9E+06	8.8E+05	8.8E+05
	E_{pit} [V *vs.* SCE]	-0.413	-0.184	0.000	0.441	0.322	0.800	0.446	-0.172
	E_{corr} [V *vs.* SCE]	-0.661	-0.641	-0.627	-0.587	-0.675	-0.526	-0.573	-0.600
300°C	$\|Z\|_{40000}$ [ohm·cm^2]		20	18	18	8	9	19	19
	$\|Z\|_{0.01}$ [ohm·cm^2]		8.4E+04	1.8E+06	7.7E+05	1.6E+06	1.7E+06	1.2E+04	9.9E+04
	Rp [ohm]	7.1E+05	2.2E+05	2.9E+06	6.5E+05	2.0E+06	2.3E+06	2.9E+05	1.1E+05
	E_{pit} [V *vs.* SCE]	-0.071	-0.699	0.145	0.233	-0.203	0.325	-0.620	-0.622
	E_{corr} [V *vs.* SCE]	-0.461	-0.704	-0.497	-0.547	-0.480	-0.450	-0.639	-0.652
400°C	$\|Z\|_{40000}$ [ohm·cm^2]	13	10	18	13	13	7	6	13
	$\|Z\|_{0.01}$ [ohm·cm^2]	1.7E+05	5.6E+05	1.6E+06	1.8E+06	1.4E+06	9.2E+04	4.2E+05	1.1E+05
	Rp [ohm]	4.6E+05	7.0E+05	1.7E+06	2.0E+06	9.0E+05	5.0E+05	1.8E+07	1.1E+06
	E_{pit} [V *vs.* SCE]	-0.610	-0.543	-0.470	0.150	0.022	-0.450	-0.610	-0.660
	E_{corr} [V *vs.* SCE]	-0.652	-0.663	-0.485	-0.557	-0.489	-0.613	-0.660	-0.735

* HTT= Heat treatment temperature

		XZ specimens							
HTT*	test	1	2	3	4	5	6	7	8
UT	$\|Z\|_{40000}$ [ohm·cm^2]	14	13	15	14	12	12	12	12
	$\|Z\|_{0.01}$ [ohm·cm^2]	5.9E+05	5.6E+05	9.4E+03	2.1E+05	1.0E+06	9.6E+05	8.3E+05	1.7E+06
	Rp [ohm]	4.7E+05	6.4E+05	8.3E+03	7.9E+05	1.6E+06	1.2E+06	9.7E+05	1.4E+06
	E_{pit} [V *vs.* SCE]	- 0.314	0.700	0.227	0.509	0.800	0.200	0.372	0.153
	E_{corr} [V *vs.* SCE]	- 0.694	- 0.628	-0.592	-0.518	- 0.574	- 0.617	-0.577	-0.648
200°C	$\|Z\|_{40000}$ [ohm·cm^2]	14	14	-	15	15	35	13	15
	$\|Z\|_{0.01}$ [ohm·cm^2]	3.4E+05	9.3E+05		2.9E+04	1.1E+05	8.0E+05	2.0E+05	5.9E+05
	Rp [ohm]	2.1E+05	8.3E+05	6.7E+05	4.4E+05	2.1E+06	1.1E+06	8.1E+05	5.0E+05
	E_{pit} [V *vs.* SCE]	-0.623	-0.632	-0.540	-0.636	-0.592	0.672	-0.640	-0.529
	E_{corr} [V *vs.* SCE]	-0.670	-0.641	-0.663	-0.726	-0.647	-0.557	-0.675	-0.536
300°C	$\|Z\|_{40000}$ [ohm·cm^2]		17	17	15	17	25	13	20
	$\|Z\|_{0.01}$ [ohm·cm^2]		1.1E+06	1.0E+06	1.9E+06	2.1E+06	1.3E+05	5.9E+04	7.0E+05
	Rp [ohm]	2.4E+05	1.1E+06	1.1E+06	2.2E+06	1.9E+06	1.4E+05	6.3E+04	3.6E+05
	E_{pit} [V *vs.* SCE]	-0.270	0.090	0.195	-0.219	0.287	-0.593	-0.680	-0.616
	E_{corr} [V *vs.* SCE]	-0.746	-0.501	-0.526	-0.595	-0.486	-0.624	-0.676	-0.638
400°C	$\|Z\|_{40000}$ [ohm·cm^2]	14	11	17	12	17	17	13	13
	$\|Z\|_{0.01}$ [ohm·cm^2]	3.0E+05	4.7E+04	2.1E+05	2.1E+05	5.9E+05	7.0E+05	3.9E+05	9.8E+05
	Rp [ohm]	7.6E+04	8.0E+04	7.3E+06	5.3E+06	3.2E+07	4.2E+07	1.6E+07	7.1E+04
	E_{pit} [V *vs.* SCE]	-0.600	-0.710	0.189	-0.687	-0.414	0.214	0.487	-0.570
	E_{corr} [V *vs.* SCE]	-0.664	-0.722	-0.724	-0.775	-0.487	-0.729	-0.528	-0.570

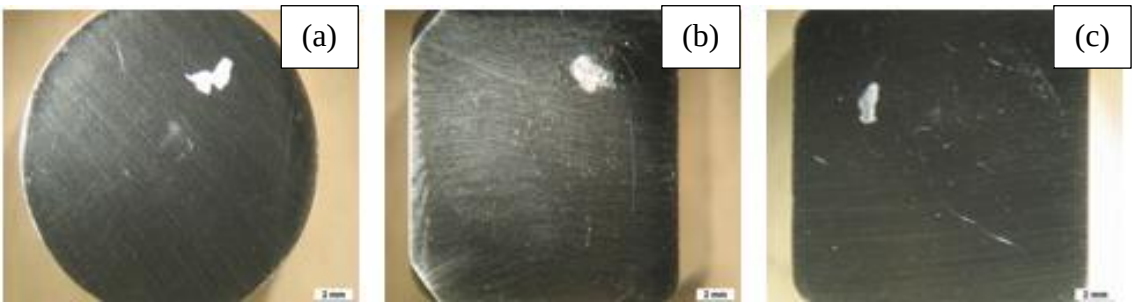

Figure A-9: Macro image of attacks after the test at 20°C on (a) HW, (b) LPBF UT and (c) LPFB HT

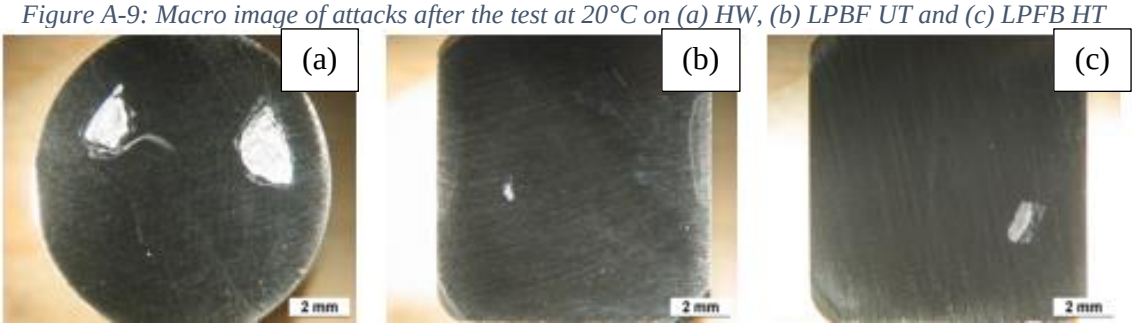

Figure A-10: Macro image of attacks after the test at 25°C on (a) HW, (b) LPBF UT and (c) LPFB HT

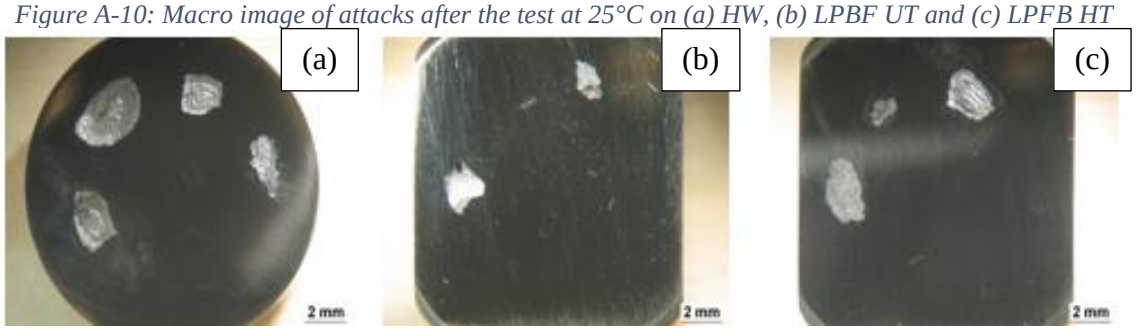

Figure A-11: Macro image of attacks after the test at 30°C on (a) HW, (b) LPBF UT and (c) LPFB HT

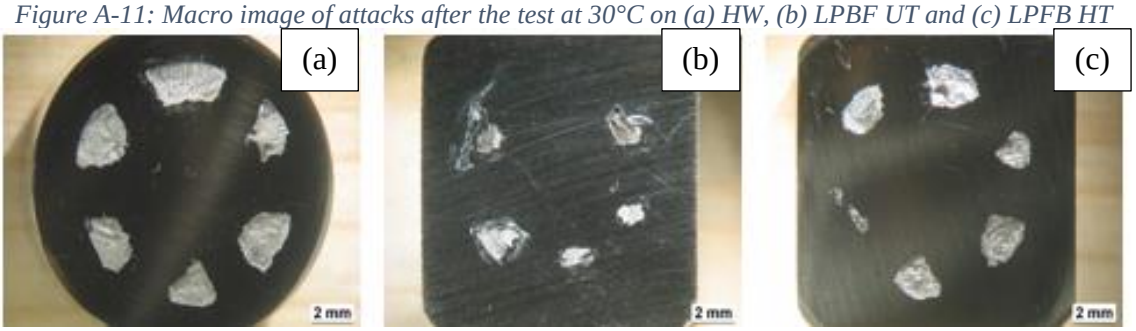

Figure A-12: Macro image of attacks after the test at 40°C on (a) HW, (b) LPBF UT and (c) LPFB HT

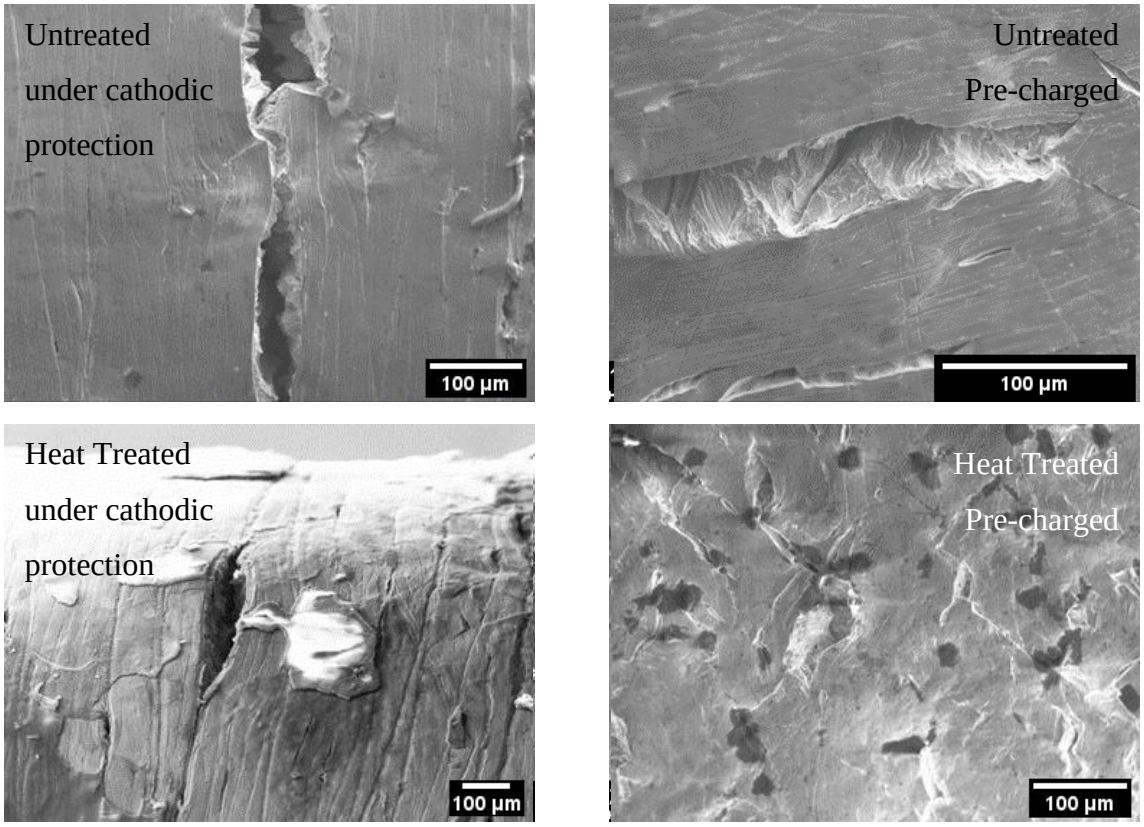

Figure A-13: SEM observations after SSR stress at -1.1 V vs. Ag/AgCl

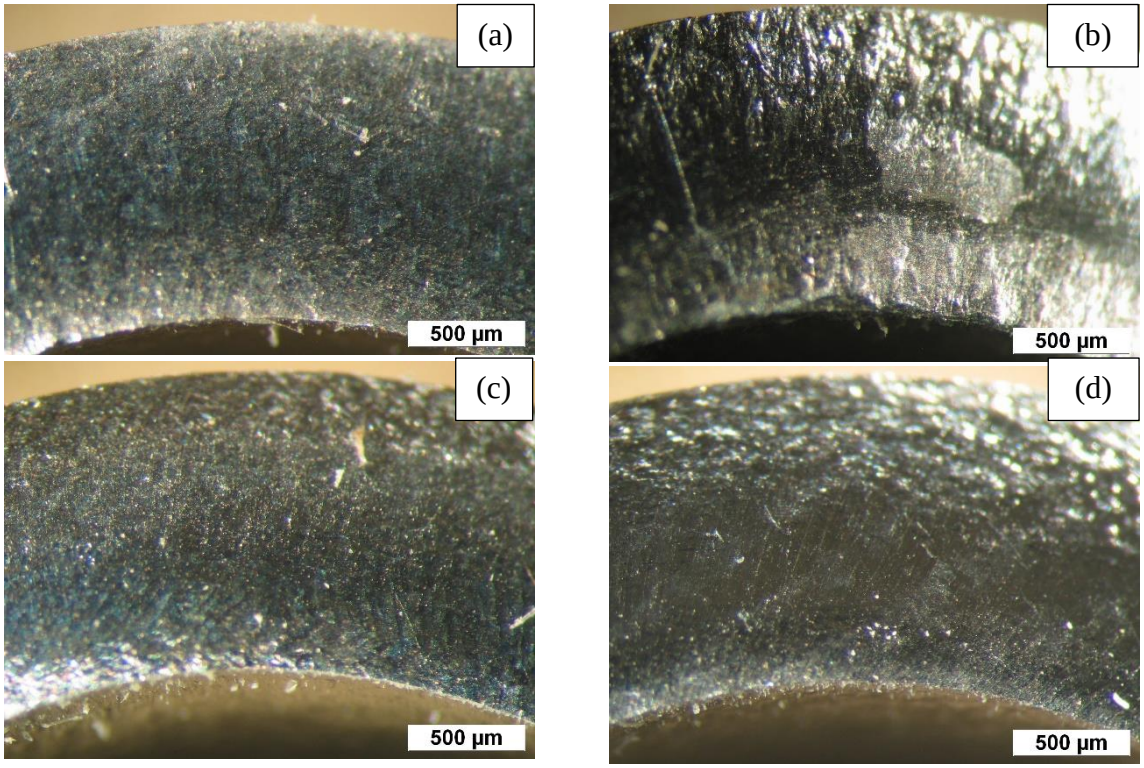

Figure A-14: Thickness status before the test for (a) LPBF-UT and (c) LPBF-HT; thickness status after the test for (b) LPBF-UT and (d) LPBF-HT

Table A-2: E_{corr} values before potentiodynamic tests

Environment	Sample	Surface condition	Heat treatment condition	Average E_{corr} (V *vs.* SCE)
0.6 M NaCl pH 7	LPBF	P	UT	-0.276
				-0.439
				-0.303
		AB		-0.368
				-0.443
				-0.195
				-0.491
				-0.164
		P	HT	-0.416
				-0.398
				-0.377
		AB		-0.373
	HW	P		-0.228
				-0.316
0.6 M NaCl pH 3	LPBF	P	UT	-0.211
				-0.212
			HT	-0.249
				-0.273
				-0.192
	HW	P	HT	-0.203
				-0.173
				-0.222
0.5 M H_2SO_4	LPBF	P	UT	-0.103
	LPBF	P	HT	-0.122
	HW	P	HT	-0.076

Table A-3: i_{corr}, i_p and E_t or E_c calculated after potentiodynamic tests

Sample	**i_{corr} (µA/cm²)**			**i_p (µA/cm²)**			**E_t and E_c (V *vs.* SCE)**		
	0.6 M NaCl pH7	0.6 M NaCl pH3	0.5 M H_2SO_4	0.6 M NaCl pH7	0.6 M NaCl pH3	0.5 M H_2SO_4	0.6 M NaCl pH7	0.6 M NaCl pH3	H_2SO_4 0.5 M
HW-HT	0.58	1.74	0.51	0.32	0.98	1.18	0.55	0.55	0.81
	Not determinable	1.51		0.7	1.00		0.36*	0.60	
		1.35			0.94			0.60	
LPBF-UT-P	0.47		0.74	0.80	1.01	1.14	0.35*	0.61	0.83
	0.39	2.21		0.90	1.04		0.43*	0.58	
	0.91	1.75		0.90	1.10		0.52	0.58	
LPBF-HT-P	0.74	1.08	0.99	0.80	1.02	1.26	0.38*	0.60	0.80
	0.51	1.44		0.90	1.05		0.00*	0.59	
	0.43			1.00			0.12*		
LPBF-UT-AB	Not determinable			1.4			0.06*		
				2.34			-0.09*		
LPBF-HT-AB	0.47			2.80			0.09*		
	0.93			2.00			0.12*		

** indicates the crevice potential (E_c)*

Table A-4: Summary of the types of corrosion morphology observed in the potentiostatic tests in LPBF and HW Alloy 625 alloy

Sample	**E = +0.2V *vs.* SCE**			**E = +0.5 V *vs.* SCE**		
	Test 1	Test 2	Test 3	Test 1	Test 2	Test 3
HW	Crevice	No attack	Crevice	Crevice	No attack	Crevice
LPBF-UT	No attack	No attack	-	Crevice + repassivation	No attack	-
LPBF-HT	No attack	No attack		Crevice	Crevice + repassivation	Crevice

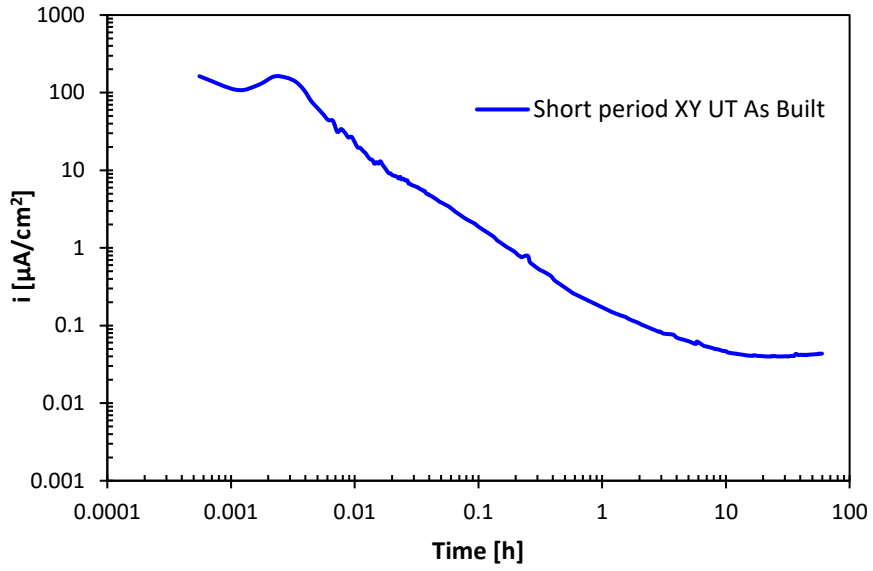

Figure A-15: Potentiostatic curve of LPBF untreated As Built specimens

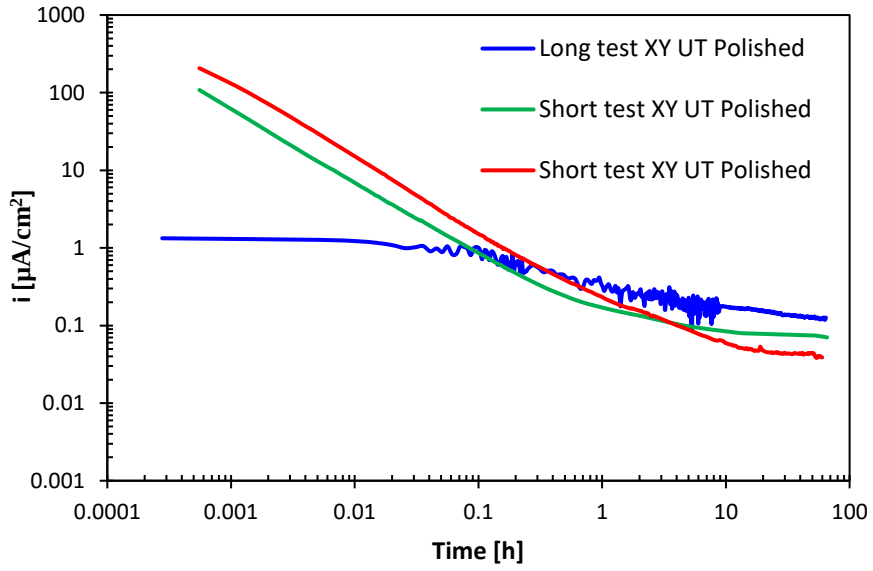

Figure A-16: Potentiostatic curves of XY LPBF untreated polished specimens

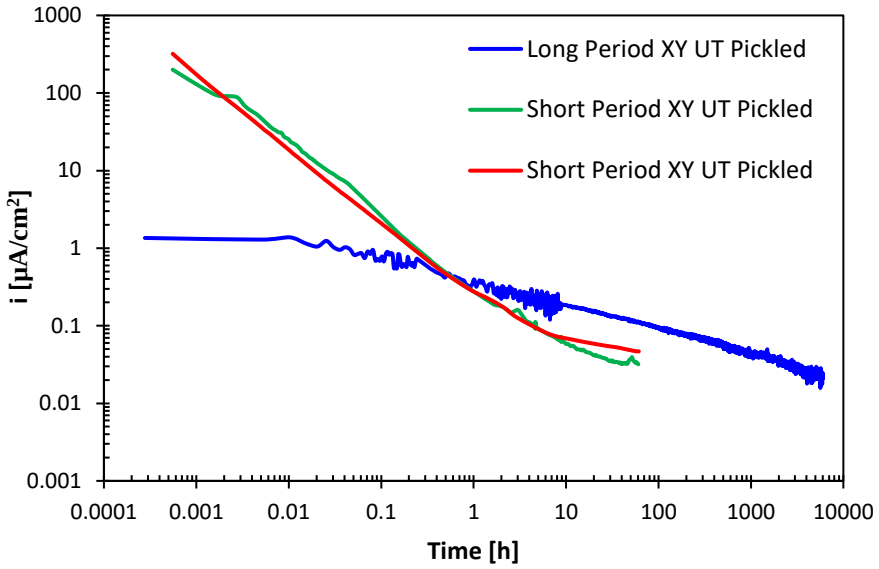

Figure A-17: Potentiostatic curves of XY LPBF untreated pickled specimens

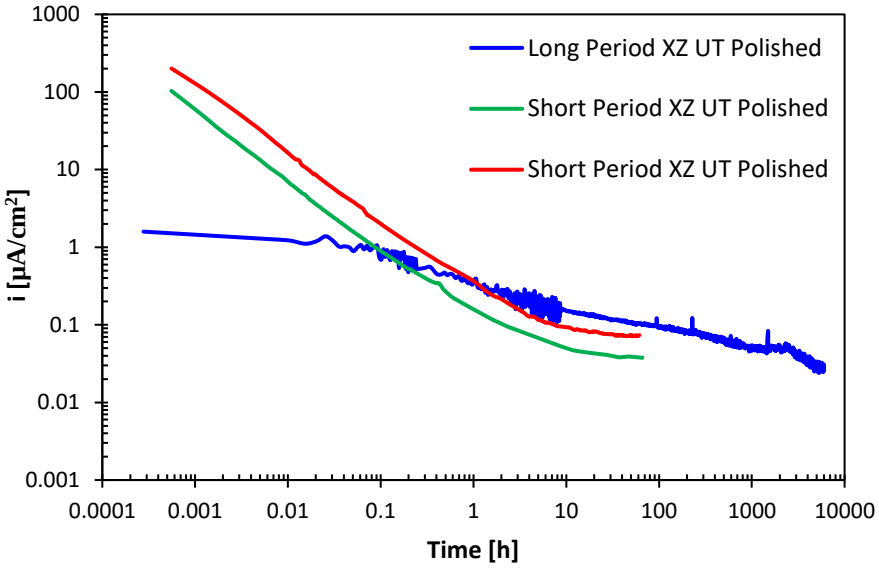

Figure A-18: Potentiostatic curves of XZ LPBF untreated polished specimens

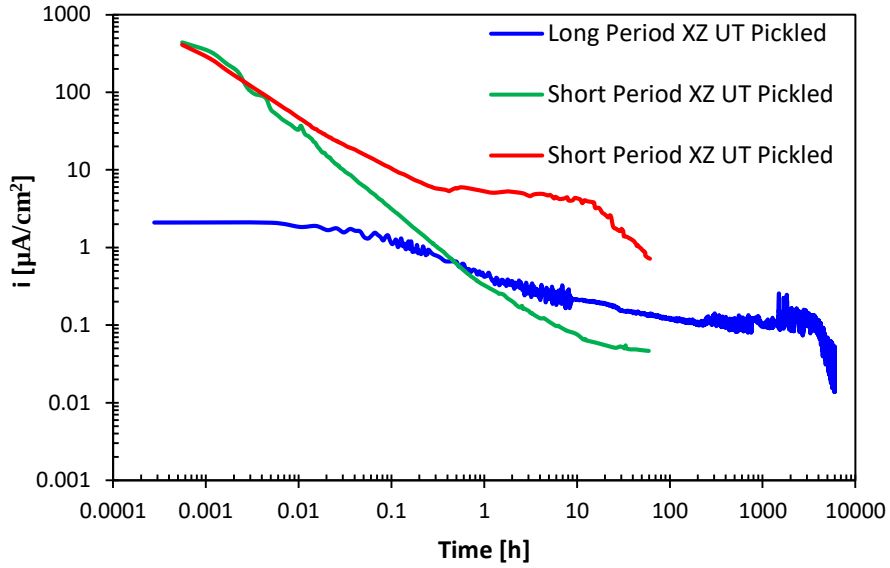

Figure A-19: Potentiostatic curves of XZ LPBF untreated pickled specimens

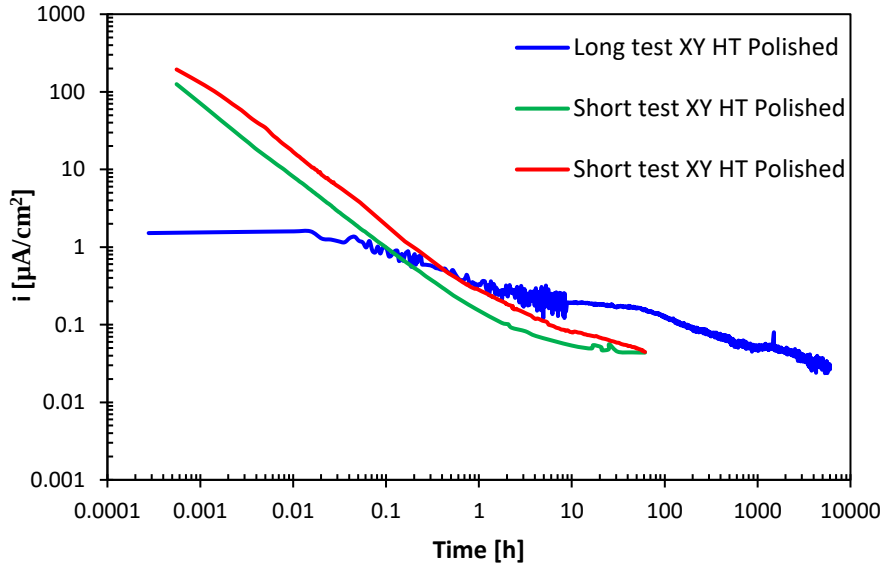

Figure A-20: Potentiostatic curves of XY LPBF heat-treated polished specimens

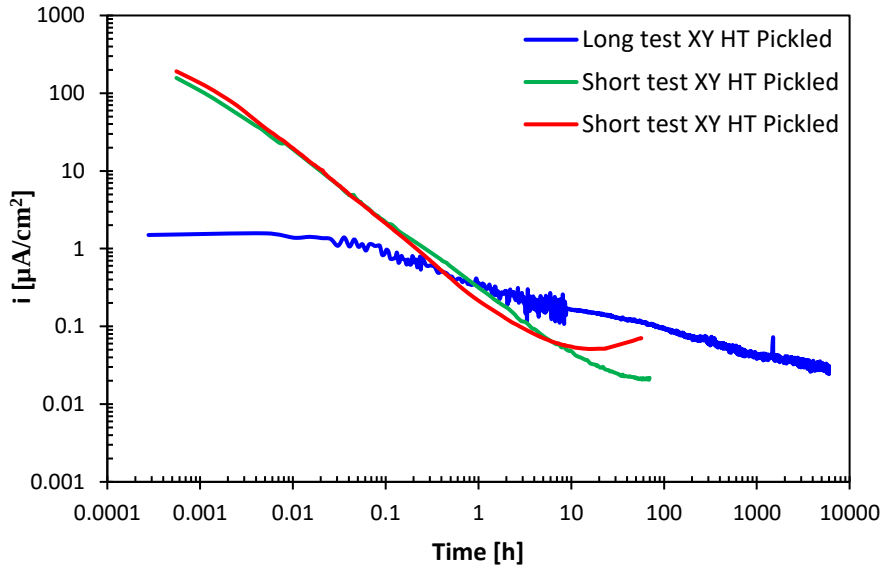

Figure A-21: Potentiostatic curves of XY LPBF heat-treated pickled specimens

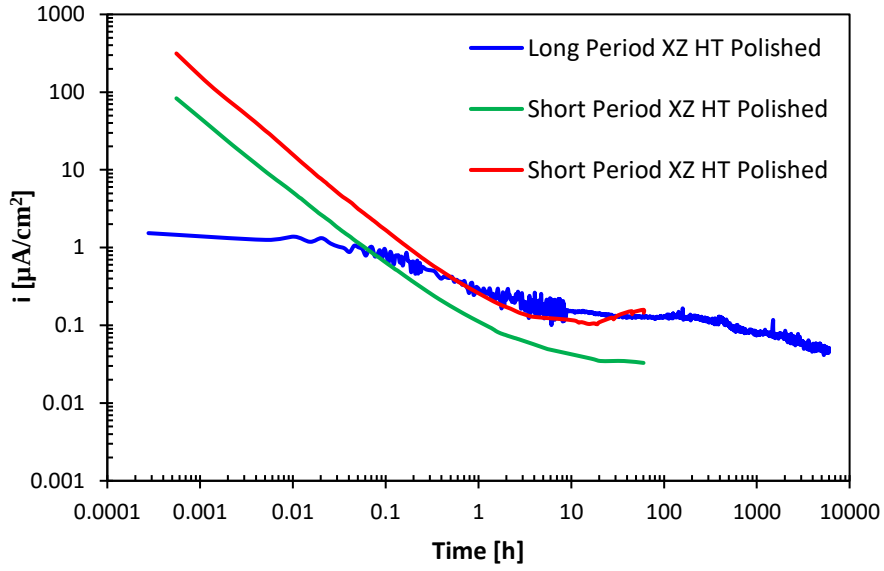

Figure A-22: Potentiostatic curves of XZ LPBF heat-treated polished specimens

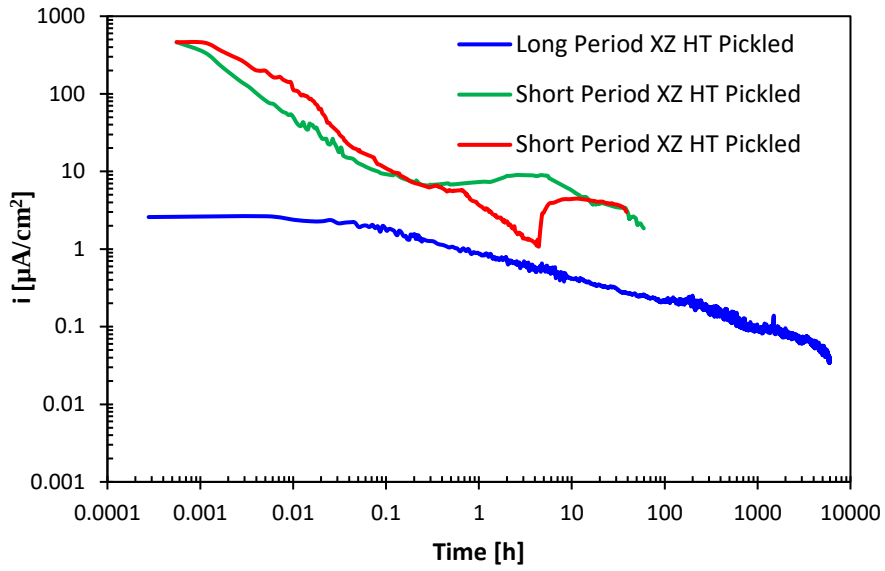

Figure A-23: Potentiostatic curves of XZ LPBF heat-treated pickled specimens

Table A-5: Values of real current after 6000h and of extrapolated current from the model after 6000h

	i_{real} after 6000 hours [µA/cm²]	i_{model} after 6000 hours [µA/cm²]
XY UT Pickled	0.0214	0.0307
XY HT Polished	0.0268	0.0417
XY HT Pickled	0.0311	0.0363
XZ UT Polished	0.0275	0.0482
XZ UT Pickled	0.0137	0.0466
XZ HT Polished	0.0512	0.0639
XZ HT Pickled	0.0406	0.1029

Table A-6: Values of i_p after 60h and after 6000h

i_p [µA/cm²]							
Time (h)	XY UT Pickled	XY HT Polished	XY HT Pickled	XZ UT Polished	XZ UT Pickled	XZ HT Polished	XZ HT Pickled
60	0.0393	0.0441	0.0264	0.0557	0.3818	0.0889	2.0597
6000	0.0214	0.0268	0.0707	0.0275	0.0455	0.0511	0.0406